BNL-211142-2019-TECH
NSLSII-ASD-TN-168

NSLS-II SR Commissioning Report

G. Wang,

April 2015

Photon Sciences
Brookhaven National Laboratory

U.S. Department of Energy
USDOE Office of Science (SC), Basic Energy Sciences (BES) (SC-22)

DISCLAIMER

NSLS II TECHNICAL NOTE BROOKHAVEN NATIONAL LABORATORY	NUMBER **NSLSII-ASD-TN-168**
AUTHOR: G. Wang, T. Shaftan, F. Willeke, G. Bassi, A. Blednykh, E. Blum, W. Cheng, J. Choi, M. Davidsaver, L. Doom, R. Fliller, G. Ganetis, F. Gao, W. Guo, Y. Hidaka, H. Hseuh, P. Ilinski, Y. Li, W. Louie, J. Mead, B. Podobedov, J. Rose, S. Seletskiy, O. Singh, T. Summers, Y. Tian, B. Wahl, Z. Xia, X. Yang, L. Yang, L. Yu, F. Zafonte	DATE 04/18/2015
TITLE: **NSLS-II SR Commissioning Report**	

NSLS-II SR Commissioning Report

G. Wang, T. Shaftan, F. Willeke, G. Bassi, A. Blednykh, E. Blum, W. Cheng, J. Choi, M. Davidsaver, L. Doom, R. Fliller, G. Ganetis, F. Gao, W. Guo, Y. Hidaka, H. Hseuh, P. Ilinski, Y. Li, W. Louie, J. Mead, B. Podobedov, J. Rose, S. Seletskiy, O. Singh, T. Summers, Y. Tian, B. Wahl, Z. Xia, X. Yang, L. Yang, L. Yu, F. Zafonte

Contents

Summary

The NSLS-II linear accelerator has been commissioned in 2012 reaching the design specifications (0.5/12 nC per bunch/ bunch train, emittance of 70 nm rad at 200 MeV). The facility commissioning has restarted in November 2013 with the booster start-up. In two and half months the booster system has been tested with beam and to this date booster is delivering 1 nC to 10 nC of electron beam at 3 GeV per shot at the rate of 1 Hz. The extracted beam emittances are 37/8 nm·rad (horizontal and vertical correspondingly) and relative energy spread is about 0.1%.

Prior to the beam commissioning we carried out a comprehensive training program focusing on education of the commissioning team in the specifics of the injector and storage ring subsystems, device controls, interlocks and beam study tools. The schedule of courses that were presented to the Accelerator Physics, Beam Operations, Injector and Storage Ring Coordination groups is listed in the table below.

Date	**Meeting Time**	**Courses**	**#**
Mon 3/10/2014	8-10am	Vacuum system (Alexei), Power Supplies (Guimei), RF system (Guimei), Timing system (Guimei, M.D.), Pulsed magnets (Tasha)	I
	1:30-3:30pm	BtS TL HLAs (Guimei, Xi)	
Tue 3/11/2014	8-10am	Diagnostics (Reid), TMS (Weixing), IOC status (Tasha), Utilities (Tasha)	I
	1:30-3:30pm	MASAR, Data Browser, Alarm system (Guobao, Tasha), Orbit HLAs, Beta-function measurements (Lingyun and Weixing), SR Chromaticity control (Lingyun)	
Wed 3/12/2014	8-10am	Vacuum system (Alexei), Power Supplies (Guimei), RF system (Guimei), Timing system (Guimei, M.D.), Pulsed magnets (Tasha)	II
	1:30-3:30pm	PyLatt notebook (Yongjun)	
Thur 3/13/2014	8-10am	Diagnostics (Reid), TMS (Weixing), IOC status (Tasha), Utilities (Tasha)	II
	1:30-3:30pm	Injection and 1st turn steering (Sergei), Coupling control, beam-based alignment (Lingyun)	
Mon 3/17/2014	8-10am	EPS (Buda), PPS (Tasha), Operator Aids+ MSG and Op Wiki + Commissioning Database (Emil and Tasha, Jinhuyk), Injector controls (Eric)	I
Wed 3/19/2014	8-10am	EPS, PPS, Operator Aids, Injector controls (Tasha)	II

Another part of the preparation of the commissioning team was in training of Scientific and Lead operators in safety, programmatic and conduct of operations procedures (at https://ps.bnl.gov/docs/Pages/MSG.aspx) developed by the Photon Science Directorate staff.

Scheduled On-the-Job Trainings (OJTs) and practical lessons eased learning of operating in a new environment and using new complex tools for the machine operations.

Following the injector commissioning the NSLS-II storage ring start-up took place in April-May 2014. NSLS-II Storage Ring Commissioning Sequence (Photon Sciences Directorate procedure PS-C-ASD-PRC-066) presents the scope and progression path for the commissioning activities. The Sequence includes the following steps:

1. First Commissioning with Beam and Injection Studies
2. Initial Functionality Test of the Beam Instrumentation
3. Establish Stored Beam
4. Beam Accumulation
5. Orbit, Chromaticity and Coupling Correction
6. Verification of Beam Emittance and Beam Stability
7. Higher Intensity Studies

All of these steps were completed during beam commissioning. Running 24 hours / 7 days a week we followed the Commissioning Sequence observing its hold points for the radiation fault studies. Every step of the Commissioning sequence was illustrated by a Commissioning module, which was printed and kept in the Control Room as well as posted at the commissioning website (http://lsasd2.ls.bnl.gov:8000/sr/). These modules proved to be very helpful during initial days of the commissioning when the team was on a steep learning curve and working on basic calibrations of the elements, while comparing beam measurement results with the design values. The details of these modules are listed in the following table:

Title	Objectives
Commission BtS TL-II with beam	A) Measure beam energy / energy spread / emittance. (**G. Wang**, X. Yang) B) Measure beam envelopes (**G. Wang**, A. Blednykh). C) Center beam on TL axis (**G. Wang**, A. Blednykh). D) Commission ICT interlock. (O. Singh, S. Buda, **R. Fliller**) E) Info on B1-B2 interlock (S. Buda, **R. Fliller**). F) Optimize matching to the entrance of the AC SR septum (G. Wang, **S. Seletskiy**).
Commission injection elements in SR	A) Commission launching through the AC SR septum (**S. Seletskiy**, G. Wang). B) Develop a dogleg with kickers 1 and 2 (**E. Blum**, S. Seletskiy). C) Test IS diagnostics with beam (**W. Cheng**, S. Seletskiy). D) Optimize kicker and septum timing (**E.Blum**, W. Cheng). E) Info on SR dipole interlock (S. Buda, **B. Podobedov**).

First turn steering	A) Adjust injection positions and angles (hor/vert) using injection elements including 2 BtS TL correctors (**G. Wang**, A. Blednykh). B) Correct the orbit on the first turn using a first turn steering algorithm (**S. Seletskiy**, Y. Li). C) Fine tune the SR BPM TBT settings (**W. Cheng**, O. Singh). D) Adjust SR dipole magnet as to minimize energy offset or horizontal corrector offset (**Y. Hidaka**, J. Choi, W. Guo). E) Optimize corrector settings at the end of the first turn turn (**J. Choi**, A. Blednykh).
Circulating and Stored beam	A) Commission on-axis injection (S. Seletskiy, W. Guo, Y. Li), A) Achieve circulating beam (**W. Guo**). B) Optimize BPM performance in FA mode (**W. Cheng**). C) Commission RF System with the beam (J. Rose, **B. Podobedov**, G. Bassi). D) Optimize capture efficiency for a single injection shot (J. Rose, **B. Podobedov**, G. Bassi). E) Measure fsynchr and energy acceptance (W. Cheng, **J. Choi**, G. Bassi).
Accumulation Injection	A) Optimize kicker amplitudes and timing (**E. Blum**, G. Wang). B) Optimize closed bump at injection (**W. Guo**). C) Commission beam accumulation into the same RF bucket (E. Blum, **S. Seletskiy**). D) Test bunch select system (W. Cheng, **G. Bassi**).
Fault studies	4 modules according to SR Commissioning Sequence and SR Radiation Fault Study Sequence. Prepare local injection bumps for damping beam at designated locations as per Rad Fault Study sequence. (W. Guo, **R. Fliller**)
Instrumentation test	A) Observe beam on SR diagnostics devices. B) Optimize performance of BPMs, tune measurement system, visible SR diagnostics, DCCT, Loss control & monitor systems with scrapers, IS beam flag, Bunch-to-bunch current monitor (**W. Cheng** (visible) P. Ilinski (x-ray), O. Singh, G. Wang, Y. Hidaka, S. Kramer).
Orbit correction	A) Test / Measure Response Matrix (**L. Yang**, X. Yang, J. Choi) B) Correct orbit (**L. Yang**, X. Yang). C) Minimize corrector strengths (**L. Yang**, X. Yang) D) Test control over local orbit bumps (**L. Yang**, X. Yang) E) Dipoles contribution to orbit distortion (**J. Choi**) F) Measure orbit circumference (**J. Choi**)
Chromaticity correction	A) Commission control over beam energy (**G. Wang**). B) Measure momentum compaction **(B. Podobedov)**. C) Measure and correct chromaticity (**W. Guo**). D) Test Chrom correction matrix (**W. Guo**).
Beam characterization	A) Measure beam emittance (**W. Cheng**, P. Ilinski). B) Quantify beam stability and orbit motion (including injection transient and long-term motion) (**W. Cheng,** J. Choi). C) Measure spectrum of orbit jitter (**W. Cheng**, A. Blednykh). D) Identify sources of orbit jitter (**B. Podobedov**, J. Bengtsson).

Beam Optics correction	A) Measure and correct Twiss functions (W. Cheng, X. Yang, **J. Choi**, Y. Li). B) Measure and correct X/Y coupling (**W. Guo**, W. Cheng, X. Yang, J. Choi, Y. Li). C) Create Coupling correction knobs (**W. Guo**, W. Cheng, X. Yang, J. Choi, Y. Li) D) Perform beam-based alignment. (**L. Yang**)
Dynamic aperture assessment	A) Commission DA measurements using injection kicker (E. Blum, **J. Bengtsson**, Y. Hidaka). B) Measure size of the horizontal DA (**W. Guo**, Y. Hidaka). C) Analyze spectrum of the "pinged" orbit and characterize nonlinear peaks (**J. Bengtsson**, Y. Hidaka, W. Cheng). D) Optimize DA (**W. Guo**, J. Bengtsson, Y. Hidaka, L. Yang, Y. Li). E) Test lattices with high(er) chromaticity (**W. Guo**, J. Bengtsson, Y. Hidaka, Y. Li, L. Yang).
Commission orbit and BBB feedbacks	A) Commission slow orbit feedback (**L.H. Yu**, Y. Tian). B) Characterize orbit jitter residuals (**W. Cheng**, G. Bassi) C) Commission bunch-by-bunch feedback (**W. Cheng**, G. Bassi).
Inject >25mA. Study multibunch effects.	A) Accumulate current of 25 mA (**A. Blednykh**, G. Bassi, B. Podobedov). B) Measure beam lifetime (W. Cheng, **L. Yang**). C) Characterize potential collective effects (**G. Bassi**, A. Blednykh, B. Podobedov). D) Mitigate their impact on the beam (W. Cheng, **G. Bassi**, A. Blednykh, B. Podobedov). E) Test lattices with higher chromaticity (**W. Guo**, Y. Li, Y. Hidaka).

At the end of commissioning the lattice data was saved and we measured orbit, tunes, chromaticity, DA, beta- and phase-beat. The data is located at control network folder//epics/op/apps/apscripts/Operation_result.

In summary, the scope of the storage ring commissioning planned in PS-C-ASD-PRC-066 has been accomplished, machine performance was demonstrated and recorded at the required level, all safety requirements were fulfilled. The following table summarizes the accomplished scope of the beam commissioning in April-May 2014.

Project goals		
	required by SR Commissioning sequence	**accomplished**
	Beam parameters	
Beam energy	3 GeV	2.980 GeV
Beam current	25 mA	25 mA
Betatron tunes x/y	33.24 / 16.18	33.24 / 16.18
Orbit flatness x/y		<0.2 mm / < 0.2 mm RMS
Beta beat		<3% / < 3% RMS
Dispersion beat		~20% RMS
Chromaticity x/y	2 / 2	1.7 / 2.4
Momentum compaction	3.64e-4	not measured
Coupling		2.10%
Estimate on DA	>15 mm	X DA measured as 14 mm

1. Introduction

The NSLS-II storage ring (SR) phase I commissioning has been successfully completed in May 12, 2014. In accordance to the project milestone, 25 mA average current was achieved in the storage ring with PETRA III 500 MHz 7-cell PETRA-III RF cavity but w/o ID's and Landau cavities. In about 5 weeks we delivered a 3 GeV beam to the ring injection straight section, made the 1st turn around the ring, achieved hundreds of turns optimizing injection, stored beam having sextupoles and RF turned ON. Injection efficiency was achieved 95%, close orbit rms value is ~100 um, tune and chromaticity were measured and adjusted as desired, and beam lifetime was a few hours depending on the stored beam current.

This report consists of a summary, a chronological part, the injector system performance in Ch3, SR commissioning experience in Ch4 and the outlook of remaining work in Ch5.

The SR commissioning experience includes the software experience, hardware (timing, diagnostics, RF, vacuum, PS) operation experience, the strategy for initial injection beam to the stored beam, measurement of the linear optics and control to the desired value, nonlinear beam dynamics study, beam instability study, the subsystem reliability and fault study at different scenarios.

2. Chronological part

Below we list a set of excerpts from elog outlining progress during beam commissioning Mar 26th to May 10th. The list does not pretend to be complete and self-inclusive, its purpose to illustrate rapid progress with the beam commissioning, its milestones and difficulties met along the way.

Id	CreateTime	Description	Shift ID
9037	Wed, 26 Mar 2014 00:22:36	Tasha, Phil, I authorize the start of linac beam operation. Emil	['209']
9118	Wed, 26 Mar 2014 21:53:39	Accelerated 2.5 mA in the booster.	['211']
9126	Wed, 26 Mar 2014 23:15:46	Authorization from Emil and Ferdinand to start storage ring commissioning has been given: Timur, I approve the shift plan. Good Luck! Ferdinand	['211']
9145	Thu, 27 Mar 2014 08:59:12	Beam is delivered to BtS P8	[]
9207	Fri, 28 Mar 2014 04:34:47	Storage ring phase-I fault studies complete	['215']
9243	Fri, 28 Mar 2014 21:15:22	SR Scrapers are fully open; sending beam around the ring	['217']
9259	Sat, 29 Mar 2014 01:58:09	Beam is seen at the exit of cell 30 (injection straight).	['217']
9350	Sun, 30 Mar 2014 05:13:49	Beam is seen on Cell 03 BPM 06.	['220']
9366	Sun, 30 Mar 2014 08:51:57	1st turn around SR is complete.	[]
9453	Mon, 31 Mar 2014 06:56:46	3 turns	[]
9536	Tue, 01 Apr 2014 12:18:21	Maintenance mode is in effect for Linac, Booster, SR Pentants 1,2,5.	['228']
9636	Wed, 02 Apr 2014 17:14:15	Visible light monitor shows small signal - first light!	['231']
9673	Thu, 03 Apr 2014 01:09:28	Wrong kicker polarity is fixed	['232']
9680	Thu, 03 Apr 2014 02:00:24	Circulating beam, about 14 turns	['232']
9772	Fri, 04 Apr 2014 04:21:09	Circulating beam, about 50 turns	['235']
9817	Fri, 04 Apr 2014 20:12:00	The Fault Study SR commissioning phase II complete.	['237']

9843	Sat, 05 Apr 2014 04:21:29	Beam up to 200 turns. Turned on the sextupoles, retuned the BTS and orbit, the beam goes to almost 300 turns. Turned ON RF.	[]
9851	Sat, 05 Apr 2014 05:44:12	Reduced the X-tune by 0.05 and we have 10000+ turns	[]
9999	Mon, 07 Apr 2014 05:09:54	First reliable tune measurements with TBT and kicker	['245']
10039	Tue, 08 Apr 2014 04:01:30	Injecting up to about 0.25mA (70% injection efficiency)	['247']
10106	Wed, 09 Apr 2014 04:53:20	Begun testing orbit bumps	['251']
10164	Wed, 09 Apr 2014 21:19:48	Maintenance Day 2: 11 main dipole connections were replaced in fixing current leak problem; dipole wth jammed leads is fixed.	['254']
10247	Fri, 11 Apr 2014 00:02:23	Today is the first day the tune measurement system is working. Horizontal: 0.44 -- corrected tp 0.24 Vertical: 0.15 -- corrected to 0.26	['257']
10407	Sun, 13 Apr 2014 03:16:35	Moving from on-axis to off-axis injection. We now see accumulation with low rate.	['263']
10685	Wed, 16 Apr 2014 14:56:08	0.5mA one-shot injection with on-axis injection	['274']
10713	Wed, 16 Apr 2014 20:09:07	Accumulated >2.6mA	['274']
10752	Thu, 17 Apr 2014 08:01:06	We have hit a maximum of 4.6mA.	['276']
10806	Fri, 18 Apr 2014 04:25:36	Leads to Dipole C05G3 shorted.	['278']
10856	Fri, 18 Apr 2014 18:18:03	Closed orbit X <0.4mm and Y <1mm p2p	['281']
10860	Fri, 18 Apr 2014 19:10:11	We... got the ring stored current up to 5 mA with a lifetime of ~3 hours!	['281']
11079	Tue, 22 Apr 2014 05:22:16	BBA tests for 50 quads	['291']
11144	Wed, 23 Apr 2014 05:31:31	Local vertical bump in BPMs 62/63 shown an obstacle in vacuum chamber	['294']
11155	Wed, 23 Apr 2014 10:30:15	SOFB is tested and brings the orbit back to the reference orbit in 1-2 cycles (0.5Hz feedback cycle).	[]
11166	Wed, 23 Apr 2014 11:34:01	Scheduled maintenance	['295']
11287	Fri, 25 Apr 2014 00:15:01	After opening up the 3rd bellows, and an RF contact spring was found in cell10.	['298']
11420	Sat, 26 Apr 2014 03:15:51	5mA average current beam stored in the storage ring. Fault studies complete.	['298']

11698	Tue, 29 Apr 2014 03:56:08	Filled to 10.1 mA, Vac avg 3.6E-9, lifetime about 1.3hr	['307']
11707	Tue, 29 Apr 2014 04:41:45	Filled to 15.1 mA, Vac avg 3.1E-9, lifetime about 1.5hr	['308']
11734	Tue, 29 Apr 2014 08:02:22	25 mA!	['308']
11816	Tue, 29 Apr 2014 20:10:32	Uniform fill pattern has been tested. Orbits were corrected, the rms of two planes are 0.3mm/0.1mm.	['309']
11825	Tue, 29 Apr 2014 21:23:02	Fault study IV for 25mA have been carried out.	['309']
11872	Wed, 30 Apr 2014 11:58:24	First LOCO measurements.	['310']
11961	Thu, 01 May 2014 11:46:11	Bunch length is measured: ~ 35.8ps FWHM @ 0.22mA; ~ 57.7ps FWHM @ 0.89mA.	['313']
12067	Fri, 02 May 2014 12:19:34	Complete set of the BBA data taken	[]
12151	Sat, 03 May 2014 01:00:24	92% Injector efficiency	['319']
12359	Sun, 04 May 2014 00:33:09	Optics correction by using phase advance response matrix (6.8% beta-beat in x-plane, 7.8% beta-beat in y-plane) after one iteration.	['321']
12467	Sun, 04 May 2014 19:21:31	Beta beat is corrected down to 2.7% in rms horizontally, and 3.1% in rms vertically. Coupling calculated based upon loco fitted lattice is 2.1%	['323']
12588	Tue, 06 May 2014 03:57:44	The accumulated current is 3.84mA at chromaticity 4.6&+4.6.	['327']
12666	Wed, 07 May 2014 00:57:10	Commissioning bunch-by-bunch feedback	['331']
12763	Wed, 07 May 2014 22:58:30	25 mA filled uniformly over 80% of machine.	['333']
12842	Thu, 08 May 2014 09:14:36	compare lifetime before and after coupling correction: I(mA) Lifetime (hrs) before 4.18 9.03 after 4.14 5.38	['335']
12917	Fri, 09 May 2014 04:16:48	Coupling is 0.32%. Injection efficiency is near 100%.	['338']
12956	Fri, 09 May 2014 18:34:56	Transverse bunch-by-bunch feedback system has been commissioned successfully. It helps to cure single bunch instability as well as coupled bunch instability. Fast ion instabilities were observed with long bunch train filling, as expected.	[]
	Sun, 11 May 2014	Commissioning complete	

3. Injector performance

3.1 Linac

The NSLS-II linac was commissioned in the spring of 2012. After an initial period of integrated testing and RF conditioning, commissioning started on March 26, 2012, and ended June 18, 2012. The linac was restarted on November 27, 2013 for booster commissioning. After an initial period of checkout and fault studies, the linac beam was successfully transported into the booster on December 7, 2013.

Much of the following information is covered in References 3.1.1 through 3.1.3. Table 3.1.1 is a summary of the parameters achieved in the linac to date.

Parameter	Specification	Single Bunch Mode	Multi Bunch Mode
Energy	200 MeV	200 MeV	200 MeV
Charge	>0.5 nC Single Bunch Mode >15 nC per train Multi Bunch Mode	0.5 nC	15 nC
Bunch Train Length	160 – 300 ns MultiBunch Mode	N/A	30-300 ns demonstrated
Bunch Train Uniformity	<10% MultiBunch Mode	N/A	25%
Energy Spread	<0.5% rms	0.14% FWHM, with 80% of charge within 0.5%	150ns - 0.32% FWHM, with 88% of charge within 0.5% 300 ns - 0.47% FWHM, with 85% of charge within 0.5%
Emittance	<38 nm rms - design <70 nm rms - acceptance	X: 58 nm, Y: 63 nm	X: 56 nm, Y: 47 nm

Table 3.1.1: Comparison of Linac Specifications and Measurements Bunch charge was measured at the end of the linac using an Integrating Current Transformer (LB-IT1).

Energy measurements were performed by centering the beam in the dispersive beamline using the calibrated dipole LB-B1 and reading the beam position on the downstream flag. Energy spread measurements were performed by focusing the beam on the same flag using the triplet upstream of the dipole. The dispersion at the flag is 864 mm, so 1 mm of horizontal beam size corresponds to 0.11% momentum spread.

Emittance measurements were performed using a quadrupole scan. The flag is an OTR screen located 6.5m downstream of the quadrupoles used in the scan. Once the energy and energy spread were optimized, the beam was steered into the straight section and the scan initiated via an automated script. The beam would be scanned through its focus and the emittance determined via a fit to

$$\sigma_{x2}(I_q)^2 = \sigma_{x1}{}^2 M(I_q)_{11}{}^2 + 2\sigma_{xx'1} M(I_q)_{11} M(I_q)_{12} + \sigma_{x'1}{}^2 M(I_q)_{12}{}^2.$$

Where I_q is the current in the scanning quadrupole, $M(I_q)_{ab}$ is the abth matrix element of the transport matrix between the flag and the start of the quadrupole. The beam size at the flag is σ_{x2} and $\sigma_{x1}, \sigma_{xx'1}, \sigma_{x'1}$ are the beam size, correlation, and divergence at the start of the quadrupole. The square root of the determinant of the beam matrix at the start of the quadrupole is the emittance.

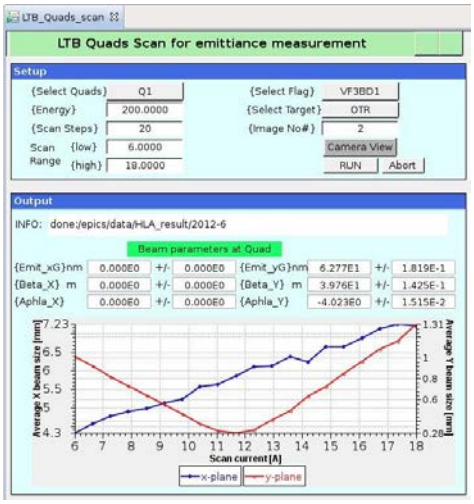

During the restart of the linac, the 3 GHz prebuncher cavity was found to have a mutlipactoring problem. Conditioning the cavity did not yield any improvement so it was decided not to use the cavity. This cavity improves the capture efficiency of the buncher cavity. Therefore only 70% charge transport efficiency from the gun to the ICT was obtained.

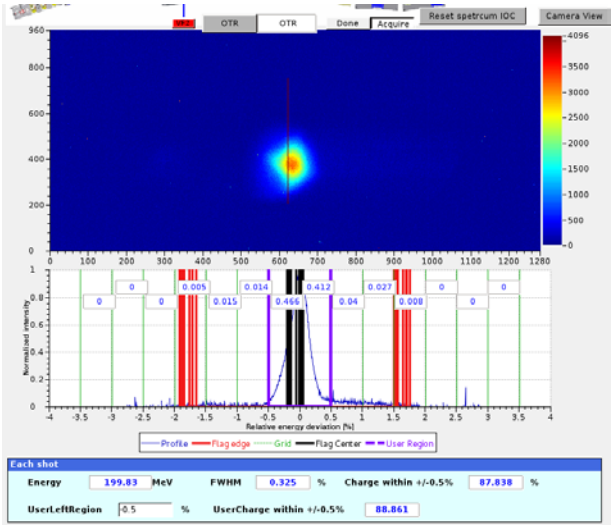

Figure 3.1.2: Beam Loading Compensation of 70 Bunches

Beam loading compensation was not commissioned during the initial stage of linac commissioning, but was completed during storage ring commissioning. The energy spread values in Table 3.1.1 above for Multi Bunch Mode reflect the achieved energy spread with compensation on. On May 12, 2014 a 300 ns long train was successfully injected into the

booster with all bunches surviving. Issues in the booster did not allow fully optimizing injection.

Figure 3.1.3: Injection of 150 bunches into the booster

Reference:

[1] R. Fliller, et al., "Results of NSLS-II Linac Commissioning". International Particle Accelerator Conference 2013, Shanhai, China. WEPWA083.

[2] K. Dunkel. Site Acceptance Test Protocol. RI Report Number 3200-BP-9291-0

[3] R. Fliller. "Comparision of the NSLS-II Linac Model to Measurments" International Particle Accelerator Conference 2014, Dresden, Germany.

3.2 Booster

3.2.1 Introduction

During Booster acceptance testing measurements of all major parameters of the electron beam were taken. Charge, beam energy and energy spread, emittance and beam sizes were measured using diagnostics line in Booster-to-Storage Ring transport line. The transport line layout is presented in the next figure.

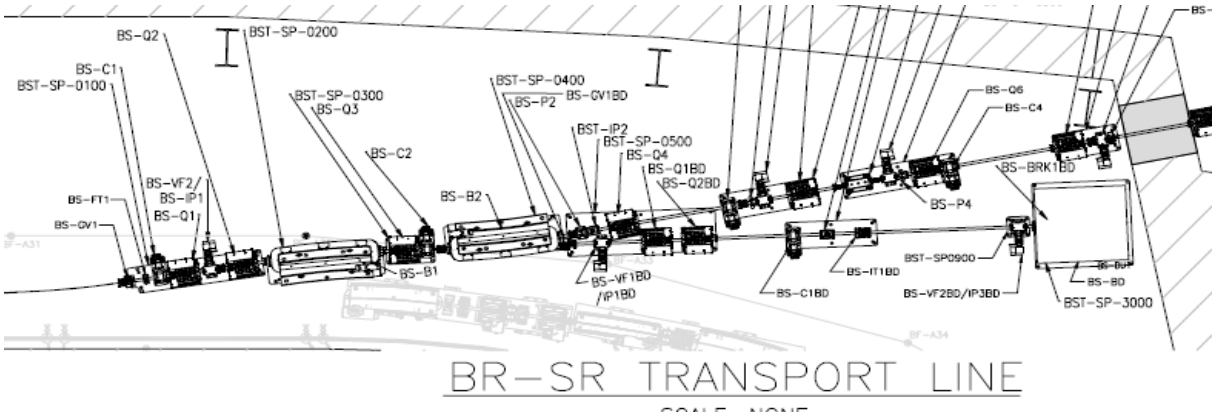

Figure 3.2.1 Booster-to-Storage Ring diagnostics line

The transport line is equipped with several beam screens, Fast Current Transformer (FCT), Faraday cup and Beam Position Monitors (BPMs). Using these diagnostics the booster output has been tested for several 8-hour shifts.

Studies on the booster optics were performed. Twiss functions were measured using 36 BPMs. Circulating beam emittance along the energy rump was obtained by recording synchrotron light images and retrieving emittance using model beta-functions.

Charge transmission was recorded using Integrated Current Transformer in Linac-to-Booster transport line, booster DC current Transformer and FCT in Booster-to-Storage Ring transport line. As a result of the acceptance testing the machine performance correspond to the design parameters and comply with the project requirements.

3.2.2 Charge and Bunch Pattern

The following figure demonstrates the capability of measuring the filling pattern and total charge extracted from the booster in long pulse mode using the FCT in the booster-to-storage ring transport line.

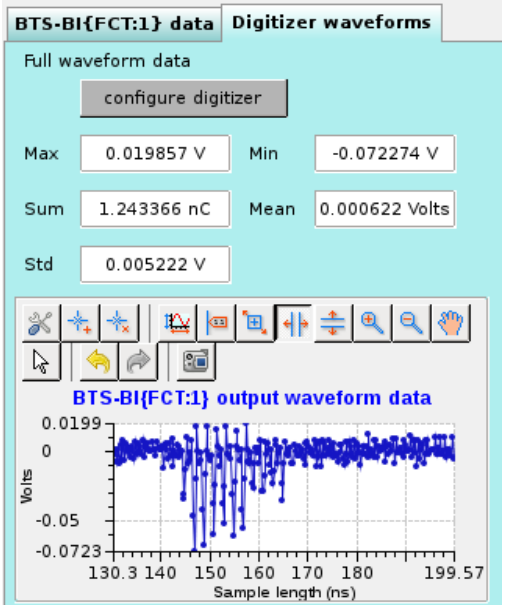

Figure 3.2.2 Signal from Booster-to-Storage Ring FCT showing bunch pattern andcharge in short pulse mode.

The following figure shows the filling pattern as measured on the booster FCT during long pulse mode.

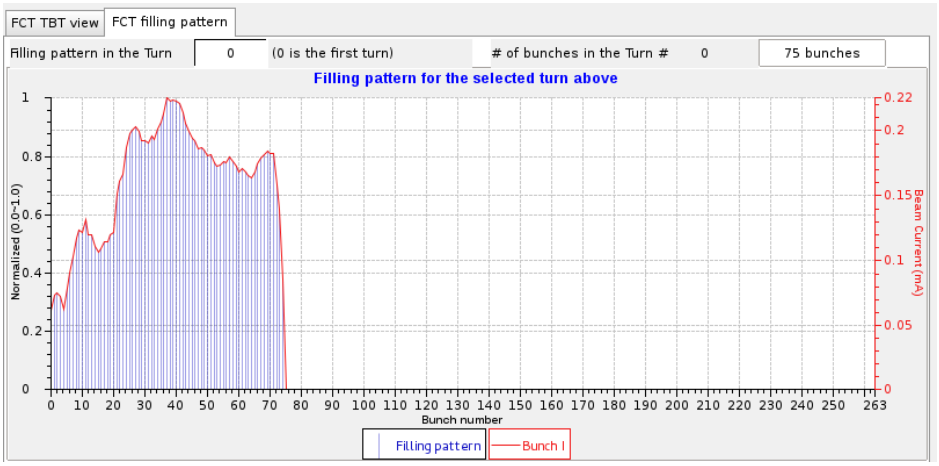

Figure 3.2.3 Signal from Booster FCT showing bunch pattern in long pulse mode.

The following figure, produced in long pulse mode, demonstrate the ability to measure charge and current in the linac, booster, and transport lines during the entire injection cycle.

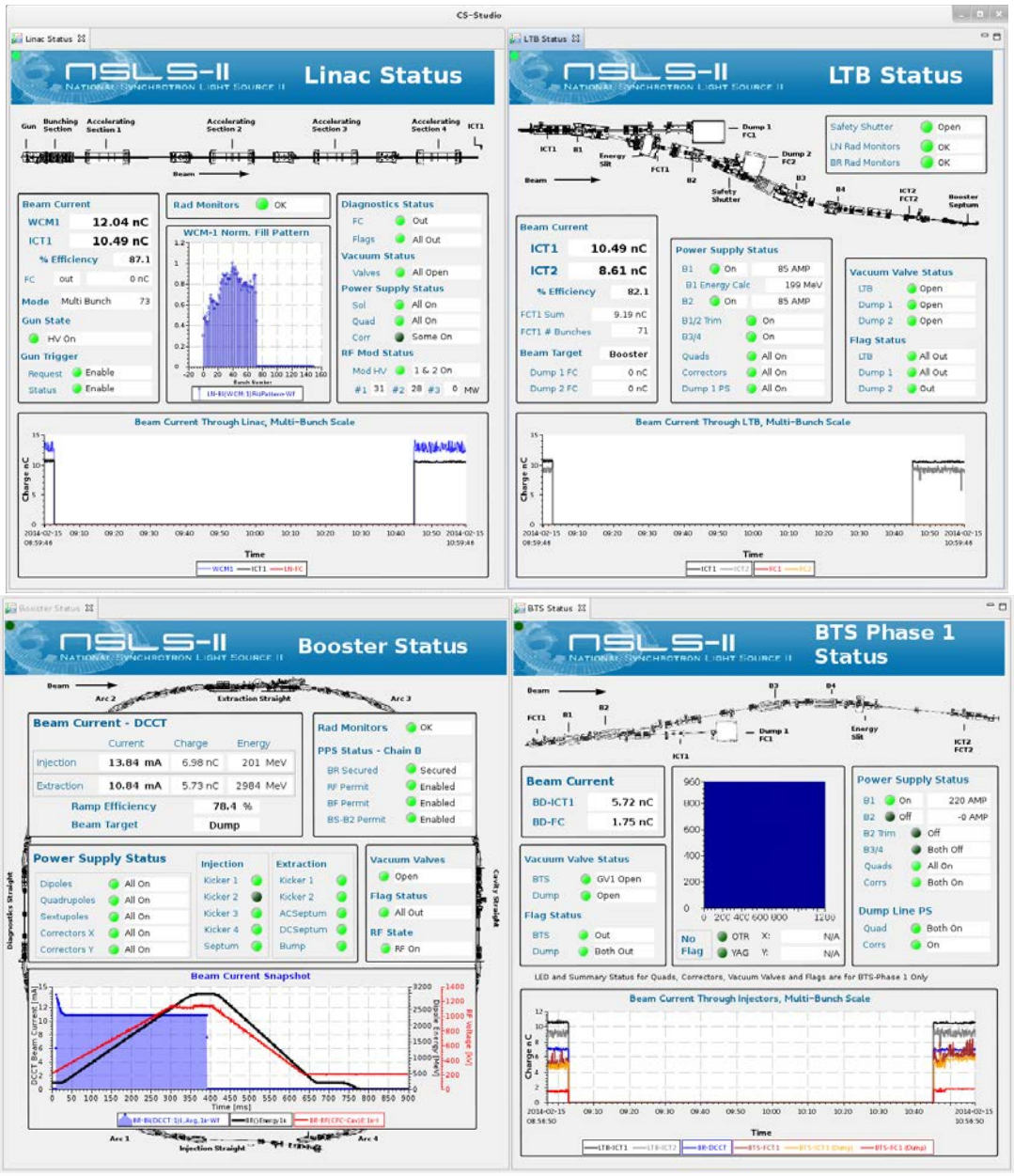

Figure 3.2.4. Status displays showing the performance of the NSLS-II injector complex in long bunch mode.

The display at the top left shows the charge of the electrons in the linear accelerator. The top right left plot shows the charge in the linac-to-booster transport line, the bottom right shows the charge in the booster at injection at extraction, and the bottom right shows the charge extracted from the booster in the box labeled BD-ICT1.

3.2.3 Booster Energy

Method A:

Booster energy at extraction as derived from booster dipole currents.There are three families of dipoles in the booster: BD1, BD2, and BF. At extraction the dipole currents were IBD1= IBD2=739.24 A and IBF=854.1 A. The dipoles have magnetic lengths LBD1= LBD2=1.29945 m and LBF=1.24076 m. There are 16 BD1 dipoles, 16 BD2 dipoles, and 28 BF dipoles in the Booster. To second order in current, the magnetic field of the dipoles are:

$$B_{BD1,2}[T] = -0.14741 + 2.022 \cdot 10^{-3} \cdot I_{BD1,2} - 4.089 \cdot 10^{-7} \cdot I_{BD1,2}{}^{2}$$

$$B_{BF}[T] = 2.200 \cdot 10^{-4} + 5.336 \cdot 10^{-4} \cdot I_{BF} - 1.626 \cdot 10^{-9} \cdot I_{BF}{}^{2}$$

Derived from the dipole set-points and assuming that the ring RF frequency is as per design, the booster energy is given by:

$$E[GeV] = \frac{0.2997925}{2 \cdot \pi}\left(16 \cdot B_{BD1} \cdot L_{BD1} + 16 \cdot B_{BD2} \cdot L_{BD2} + 28 \cdot B_{BF} \cdot L_{BF}\right)$$

or E=2983.8 MeV.

Method B:

Booster energy at extraction as derived from B1 bending magnet in the booster-to-storage ring transport line.

The extracted beam from the booster is transported to a dump through magnet BS-B1 which deflects it by an angle of θ=0.1148 rad. The magnet current was I=219 A. The magnetic rigidity for this magnet, Bρ, is given by

$$B\rho[Tm] = 0.59923038 + 0.004974837I$$

The beam energy is given by:

$$E[MeV] = \frac{B\rho}{.0033357\theta}$$

or E=3001.6 MeV. The two measurements agree within 0.7%.

3.2.4 Energy Spread

The energy spread was inferred from the spot width of the synchrotron light seen on one of the synchrotron light monitors using measured or calculated values of emittance, beta, and dispersion. Consequently, an energy spread of order 0.1% was estimated from BR-A3SLM where the dispersion at the source point is 0.18 m. This measurement is not very accurate because the profile that is measured is confused by a wide background caused by reflections from the vacuum chamber walls.

3.2.5 Emittance

Method A:

Emittance as derived from spot of the synchrotron light. The BR-A1SLM output port is located close to the DS straight section, in a region with minimal dispersion. Synchrotron light is mitted from the BR-A1BD8 dipole magnet. Using operating machine currents, Twiss parameters at the source are estimated to be βx = 5.8 m, βy = 23.8 m, and ηx=0.1 m. At extraction energy the measured emittances were ε_x=33 nm and ε_y=4nm.

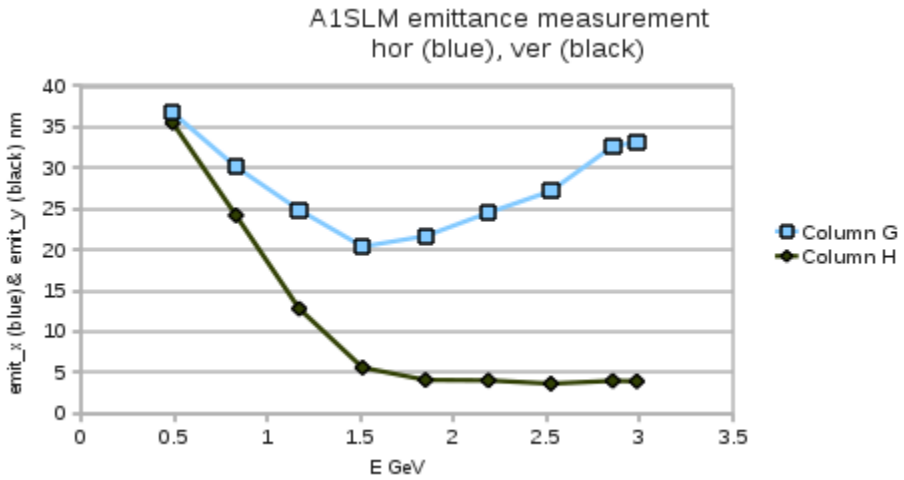

Figure 3.2.5 Horizontal and vertical emittance during the acceleration cycle as determined by the profile of the synchrotron light seen by the BR-A1SLM monitor.

Method B:

Emittance from quadrupole scan in the Booster-to-Storage Ring Transport LineVertical emittance was measured by scanning quadrupole BS-Q2BD and observing the profile on the BS-VF2BD flag in the Booster-to-Storage Ring dump line. An emittance of 8 nm was obtained using Twiss parameters at the entrance of the quadrupole of βy=18.3m and αy=14.8. The flag has a YAG screen which usually over-estimates the beam size by 25% compared to an Optical Transition Radiation (OTR) screen.

A horizontal emittance measurement was made by scanning quadrupole BS-Q3 while observing flag BS-VF1BD. The measurement showed a horizontal emittance of 32 nm. Twiss parameters at Q3 were β_x=2.79 m, α_x=2.247, with BS-Q1 set to 50A and BS-Q2 set to108 A. Note that this measurement cannot be viewed as definitive because of dispersion in the transport line at Q3. Dispersion-free region quads Q4 to Q8 should be used in the future for emittance measurements.

3.2.6 Twiss Parameters

Injection kicker 1 was used to excite the beam. Trigger delay of the kicker and the beam position monitor turn-by-turn (TBT) offset are adjusted such that excited BPM TBT data are saved at different times during the booster ramp.

As an example, the beam was excited at 290ms in booster ramp and all BPM TBT data were saved. MIA (Model Independent Analysis) technique was used to find all spatial modes and temporal modes. The pair modes were picked for the lattice analysis. Twiss parameters, β_x, β_x, n_x, and n_y were plotted at all BPM locations. In the figures that follow the red curves were calculated from the live magnet currents and the blue ones are from TBT data. They agree reasonably well.

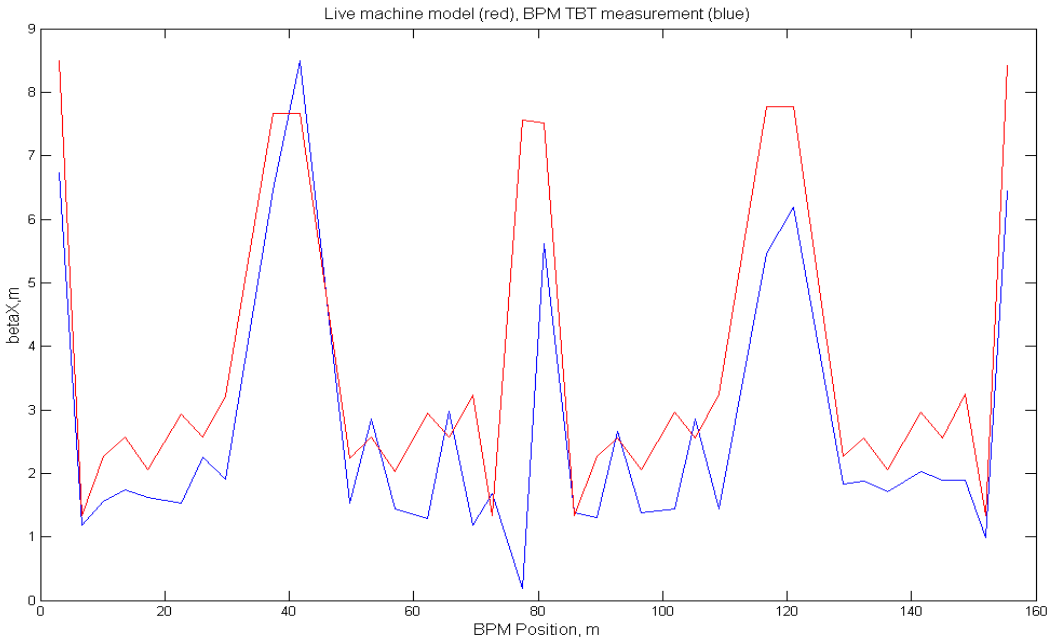

Figure 3.2.6 Horizontal beta functions

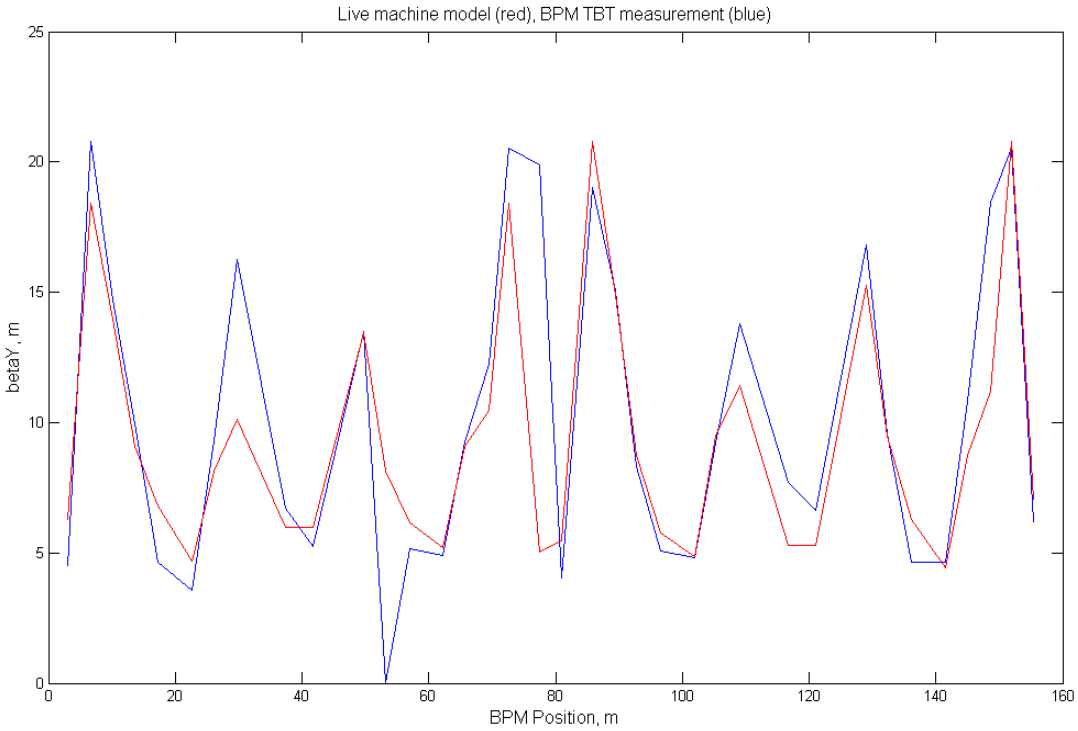

Fig. 6. Vertical beta functions.

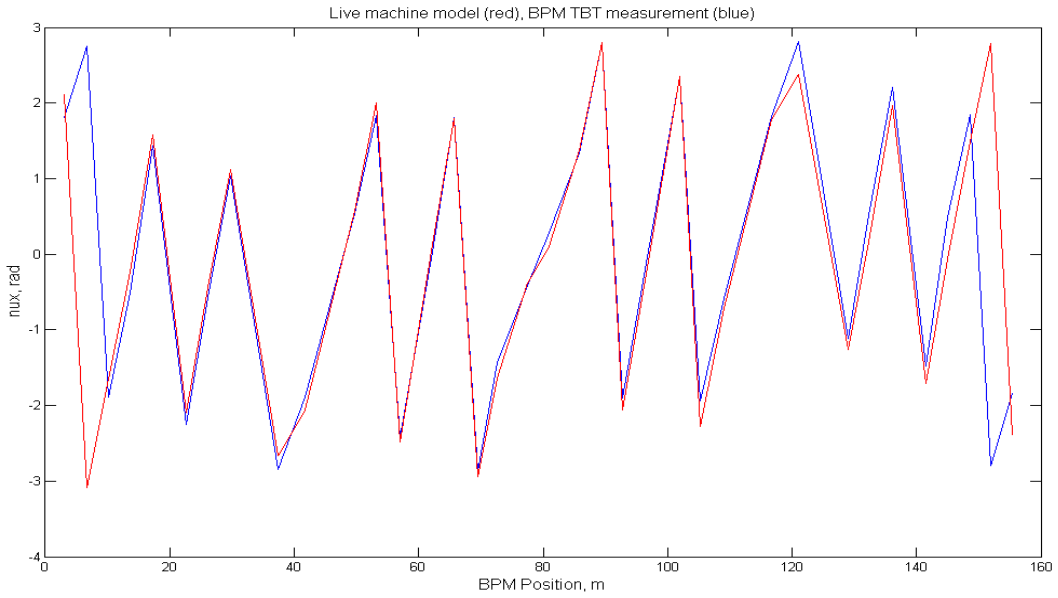

Fig. 7. Horizontal phase advance.

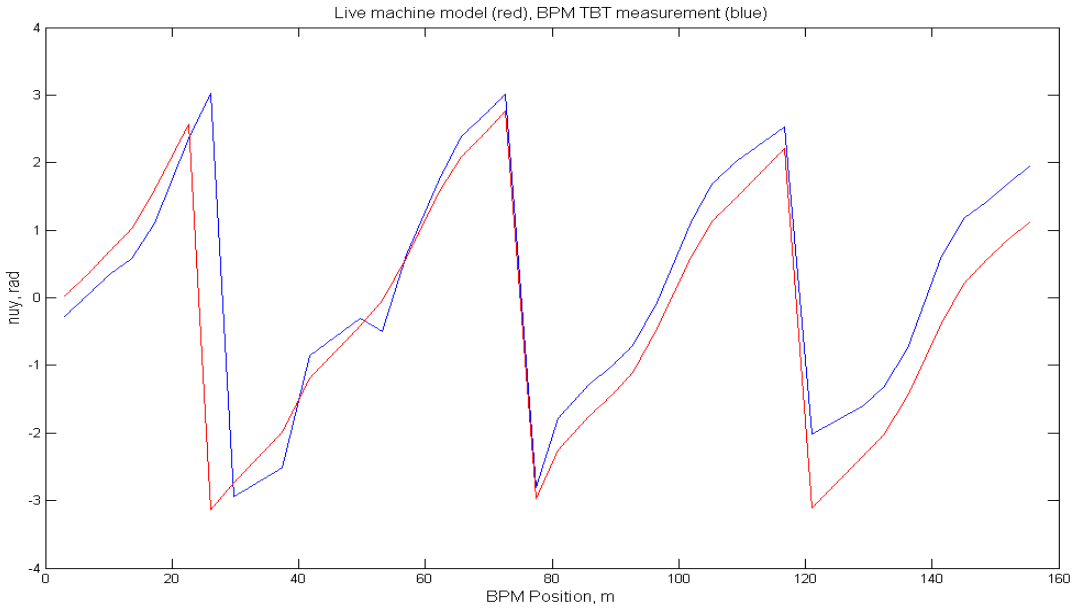

Fig. 8. Vertical phase advance.

3.2.7 Stability Tests

A. Short pulse mode:

The following figure shows the current in the booster during 7 hours of continuous operation with 2 nC as seen on ICT1 in the linac. The current delivered from the booster was nearly constant.

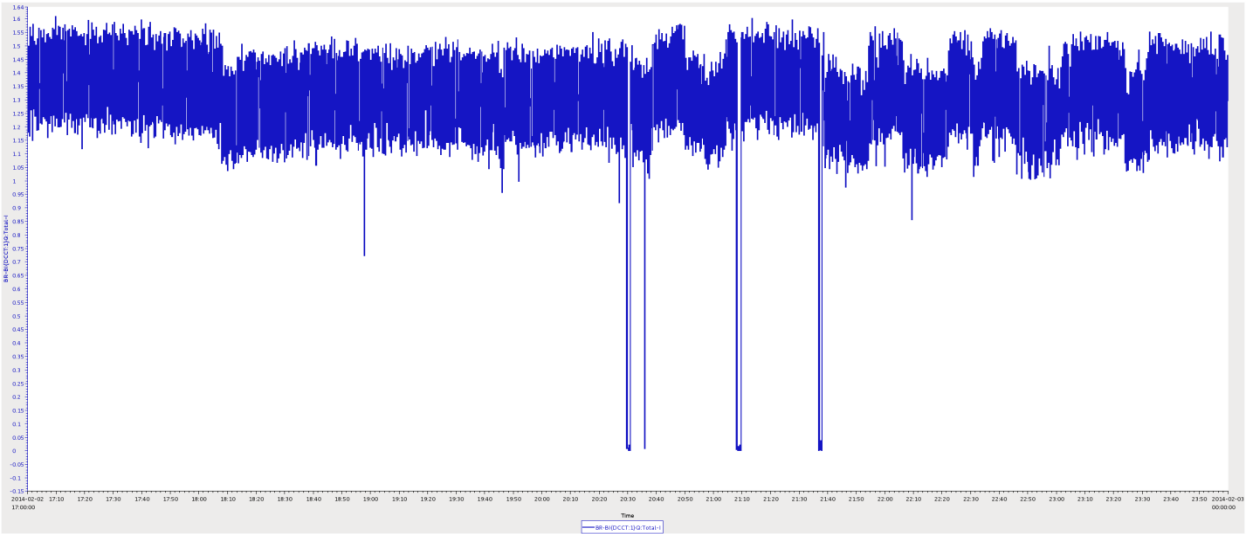

Fig. 9. Booster current in short pulse mode during a 7 hour run.
The vertical scale on the graph is -0.15 to 1.64 mA.

B. Long pulse mode:

The following figure shows the booster current during a 4 hour period of continuous operation in long pulse mode. The linac charge was 10 nC per shot at a repetition rate of 0.2 Hz.

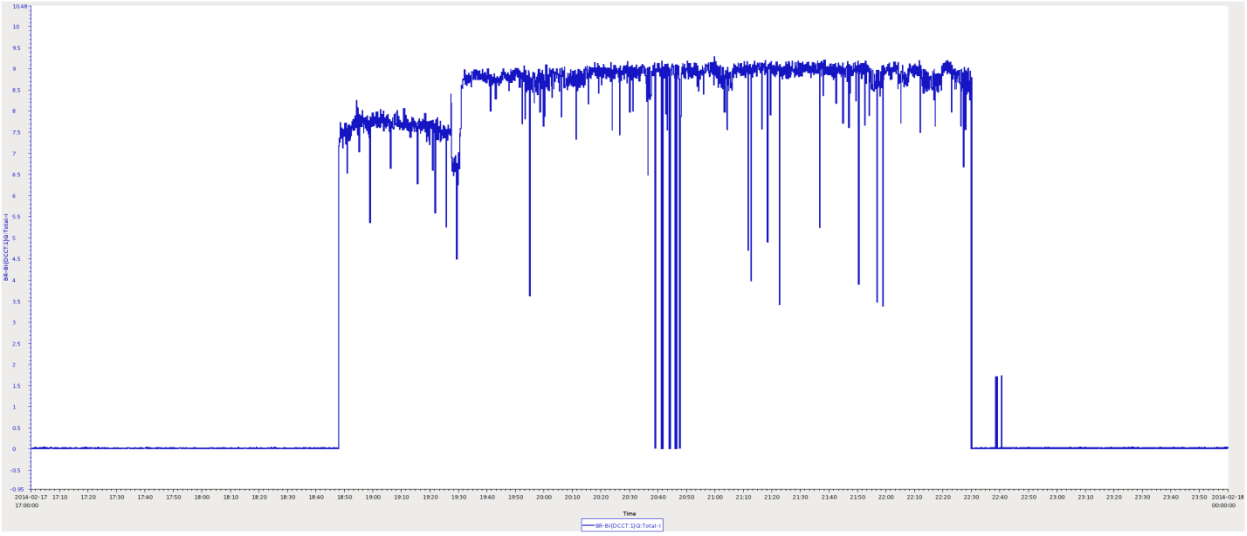

Fig. 10. Booster current in long pulse mode during a 7 hour run. The vertical scale on the graph is -0.95 to 10.48 mA.

3.2.8 Transmission

The following figure shows the current in the Linac-To-Booster transport line, in the booster and in the Booster-to-Storage Ring transport line at a repetition rate of 1/3 Hz.

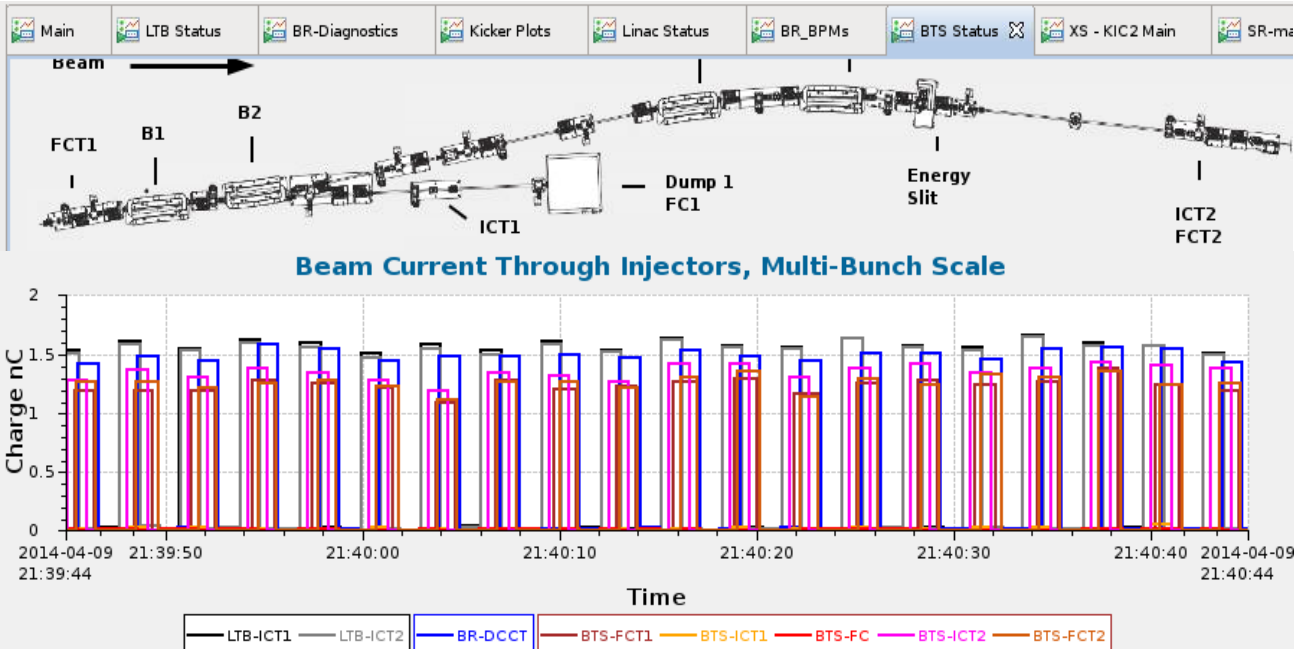

Fig. 11. The current in the Linac-To-Booster transport line, in the booster and in the Booster-to-Storage Ring transport line at a repetition rate of 1/3 Hz.

The charge transport efficiency between ICTs in LB and BSR TL is around 85%

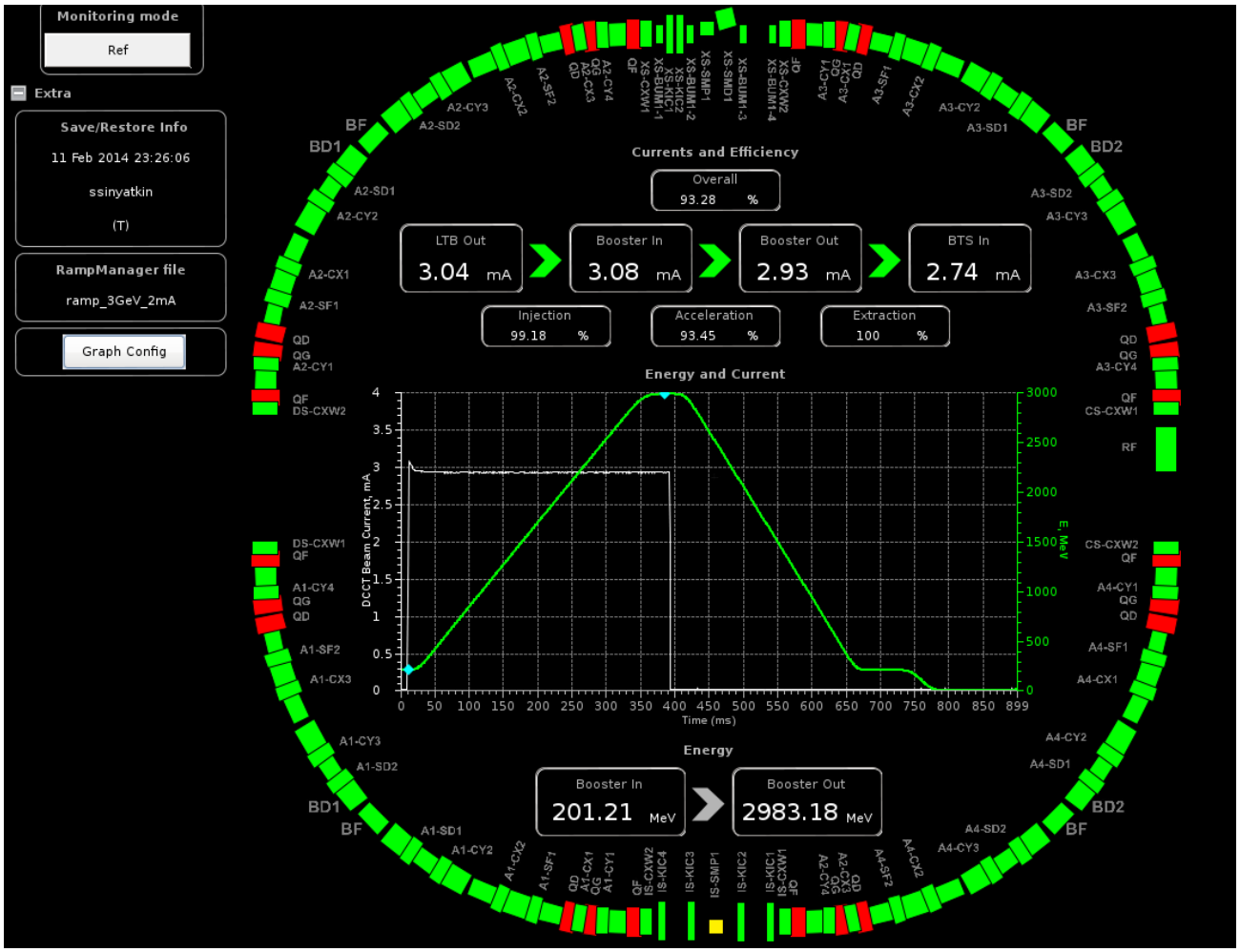

Fig. 12. I Booster Status Screen displaying currents in the Linac-To-Booster transport line, the booster ring and in the Booster-to-Storage Ring transport line.

The transmission between LtB and BsT is shown in the box labelled “Overall”.

3.2.9 Extraction Stability

The output beam stability was observed via sampling the transverse spot stability on the BTS screen VF2.

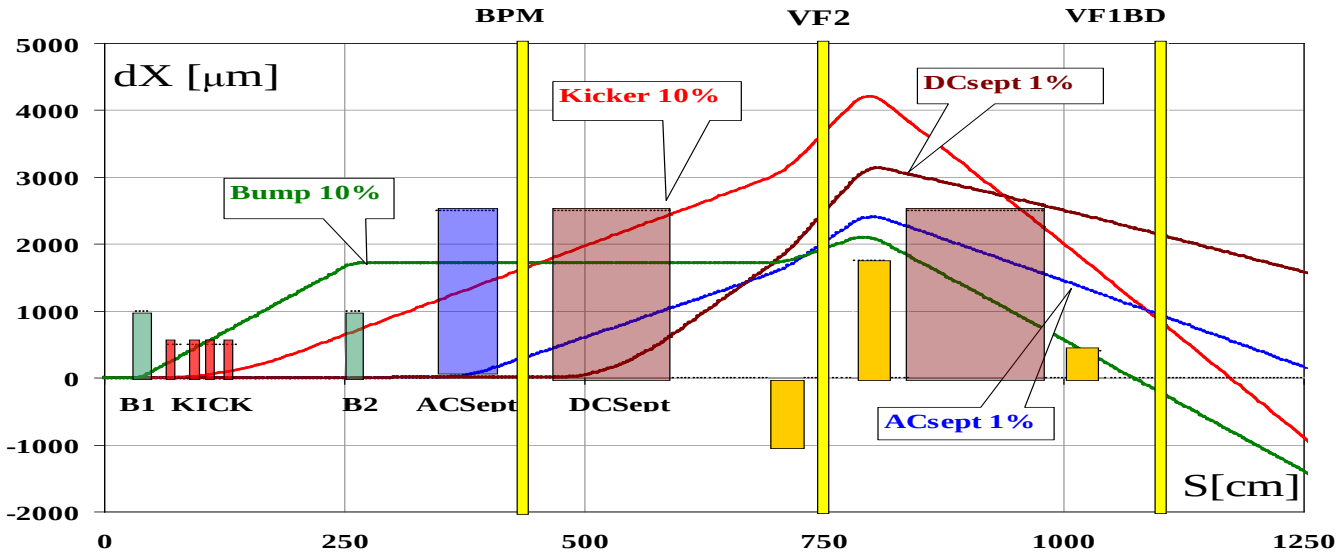

Fig. 13. Beam trajectories in the booster extraction along the BTS diagnostics line.

Extraction subsystem	Bump	Kicker	AC septum	DC septum	BD, BF (dE)
Maximum deviation of the magnet field amplitude [%] (according to the design requirements on the extraction system)	± 0.02	± 0.2	± 0.02	± 0.02	± 0.01
Corresponding maximum deviation on beam screen VF2, dX [μm]	± 4	± 50	± 45	± 62	± 35 (η_x=0.35m)
Total estimated stability better than, [μm] : ±150 μm					

In reality, during the acceptance testing during 1 hour at the repetition rate of 1 Hz we observed transverse beam stability better than dX ≈ ± 27 μm.

3.2.10 Conclusion on the Acceptance Testing

During the acceptance testing that was going on for 10 days, we measured all major beam parameters and tested machine performance. The machine was tested in both short- and long-pulse modes and the following beam parameters were achieved and recorded:

	Design	**Measured**
Beam energy	3+/-0.15 GeV	~3 GeV
Bunch charge	0.5…15 nC	0.5…10 nC
Bunch train	1 / 80…160 bunches	1 / 75 bunches
Beam energy spread @3GeV	0.08%	0.10%
Beam emittance X	38 nm rad	33 nm rad
Beam emittance Y	4 nm rad	4…8 nm rad
Charge transport efficiency between ICTs in LB and BSR TL	>75%	~80% as seen between LtB and BsT FCTs

In conclusion we found that the NSLS-II 3-GeV booster-synchrotron has passed the acceptance testing and the machine performance closely corresponds to the project requirements.

3.3 BTS TL

The booster to storage ring transfer line layout is shown in Figure 1. It consists of the extraction section, an achromatic transport section, and the matching section into the storage ring. There is a diagnostic beamline that allows for commissioning, troubleshooting, and beam studies. It also allow for the booster to operate with maintenance activities are ongoing in the storage ring vault. The BtS main line allows for injection into the storage ring while maintaining the beam emittance from the booster. It contains an energy selection slit to limit the energy acceptance of the transport line. The optics of the transport line allow for matching of the beam via the quadrupoles and flags in the straight section penetrating through the wall. The follow section describes beam parameters measurement in the transfer line.

Figure 1: Layout Booster to Storage Ring Transfer Line

3.3.1 Measure the beam energy, energy spread and emittance

Energy: Booster beam energy at the extraction is calibrated using two independent methods:

- Beam energy at the extraction can be determined from the Booster dipole ramping curve. Keep the dipole current-to-field calibration to the 2^{nd} order and sum all the dipoles' contributions: E=2983.8 MeV. [1]
- Spectrometer dipole at BSR transfer line (TL) for the beam energy measurement:
  Beam energy is calibrated using BSR-B2 dipole. The beam energy is retrieved from the dipole B2 current and the geometrical angle (0.154rad).
  Energy = (0.004974837*I+0.059923038)/0.154/0.0033357, I=292.5A.
  Energy = 2949.33MeV.

The difference between these two independent measurements is 1.16%. It is larger than the estimated measurement accuracy ~0.8%.

Energy spread: It is calibrated using BR-A3SLM. The horizontal dispersion in A3SLM is 0.18m. Due to the ambient light and not optimized focusing, we have to cut-off the background light. The estimated energy spread is ~10^{-3}.

Emittances:
Booster beam emittance at the extraction by synchrotron radiation monitor (SLM): The BR-A1SLM output port is located close to the diagnostic straight section (DS), in a plane with minimal dispersion. Synchrotron radiation (SR) is emitted from the BR-A1BD8 dipole magnet.

The twiss at the SR source is *estimated* using online live machine model, β_x=5.8m, β_y=23.8m, η_x=0.1m. Therefore, ε_x=33nm and ε_y=4nm at the top of the Booster ramp [1].

Quadrupole scan method in BSR dump line: Vertical emittance is measured using BSR-Q2BD and the YAG screen of BSR-VF2BD flag in the dump line. The result is ~8 nm. Compared to OTR screen, YAG screen often 25% over-estimates the beam size; therefore the emittance ε_y is corrected to ~6nm. β_y=18.3m, α_y=14.8 at the entrance of BSR-Q2BD quad.
Horizontal emittance is measured using the BSR-Q3 scan and the OTR screen of BSR-VF1BD, ε_x=32nm. β_x=2.79m, α_x=2.247, at BSR-Q1=50A and BSR-Q2=108A. It can only be used as the reference since the beam comes out of the Booster with dispersion at the quadrupole. Dispersion free region quads, Q4 to Q8, should be used in the emittance and twiss measurement.

Quadrupole scan in the main BSR TL:
The horizontal twiss functions were measured at BSR-Q5 in the shift of March 28th 2014. Table 1 summarizes the result of the scan, as shown in Fig.1. The emittance is compared to synchrotron light monitor measurements in the Booster.

Parameter	Expected	Measured
β_x	86.3 m	64.4 ±2.8m
α_x	-22.0	-19
ε_x	33 nm	37 ± 1.6 nm

Table 1: Summary of Quadrupole Scan Measurement in the BtS.

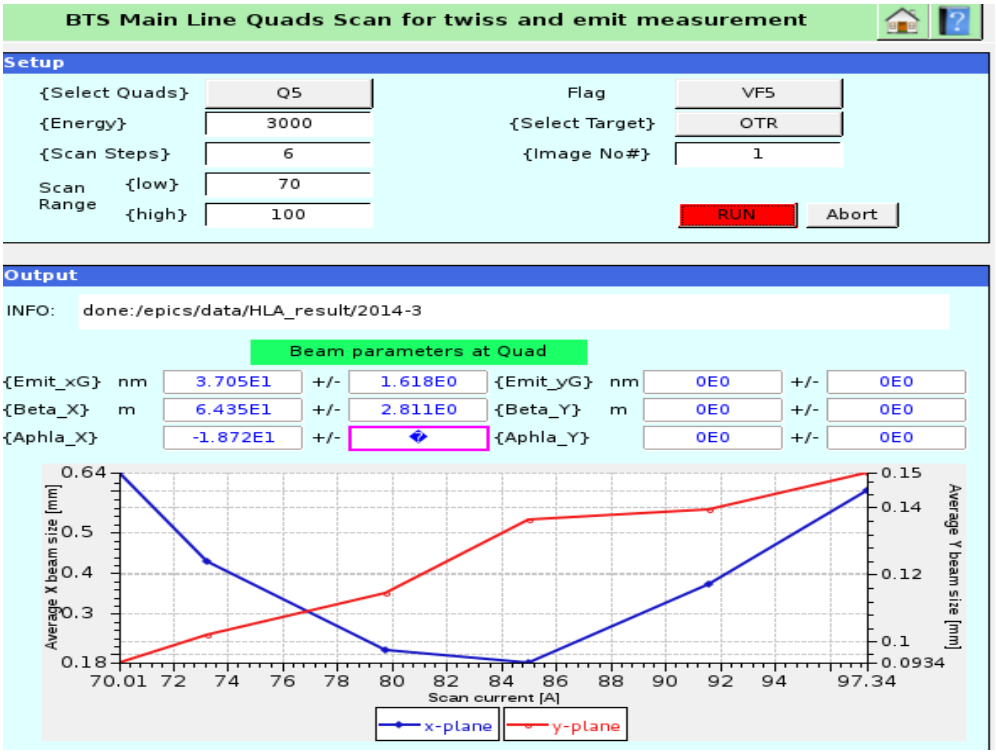

Fig.1 BSR quad scan for the emittance and twiss measurement. BSR-Q5 was scanned in the range of 70-100A; OTR screen of flag BSR-VF5 was used for the beam size measurement.

3.3.2 BSR-online model

The program reads magnet settings in BSR TL, starting from the exit of the last QF magnet in the Booster ring, including all dipoles and quads in BSR line, and also Booster extraction magnets, AC septum, DC septum, slow bump 1 and 2, fast kicker 1,2,3,4, and storage ring injection magnet DC and AC septa, injection bump 3 and 4. Only quad settings are used in the online model calculation; other magnet settings, including physics and hardware units, are displayed in the table.

After converting the machine setting into the physics unit in BSR line, elegant is called to calculate the live machine twiss, as shown in Fig.2. The twiss, beam emittance, and beam energy and energy spread at the start of BSR line is obtained from the Booster design values, also one can input them from the most recent measurement *via* the boxes above tabbed graphs. Beam sizes sigma x from design model, live machine model, and measurement using BSR flags are plotted in tabbed Graph #2. Similarly, beam sizes sigma y are plotted in tabbed Graph #3, as shown in Fig.3.

Live magnet current and pulse magnet PFN voltage, and their corresponding physics unit are shown in the bottom left tables in Fig.2.

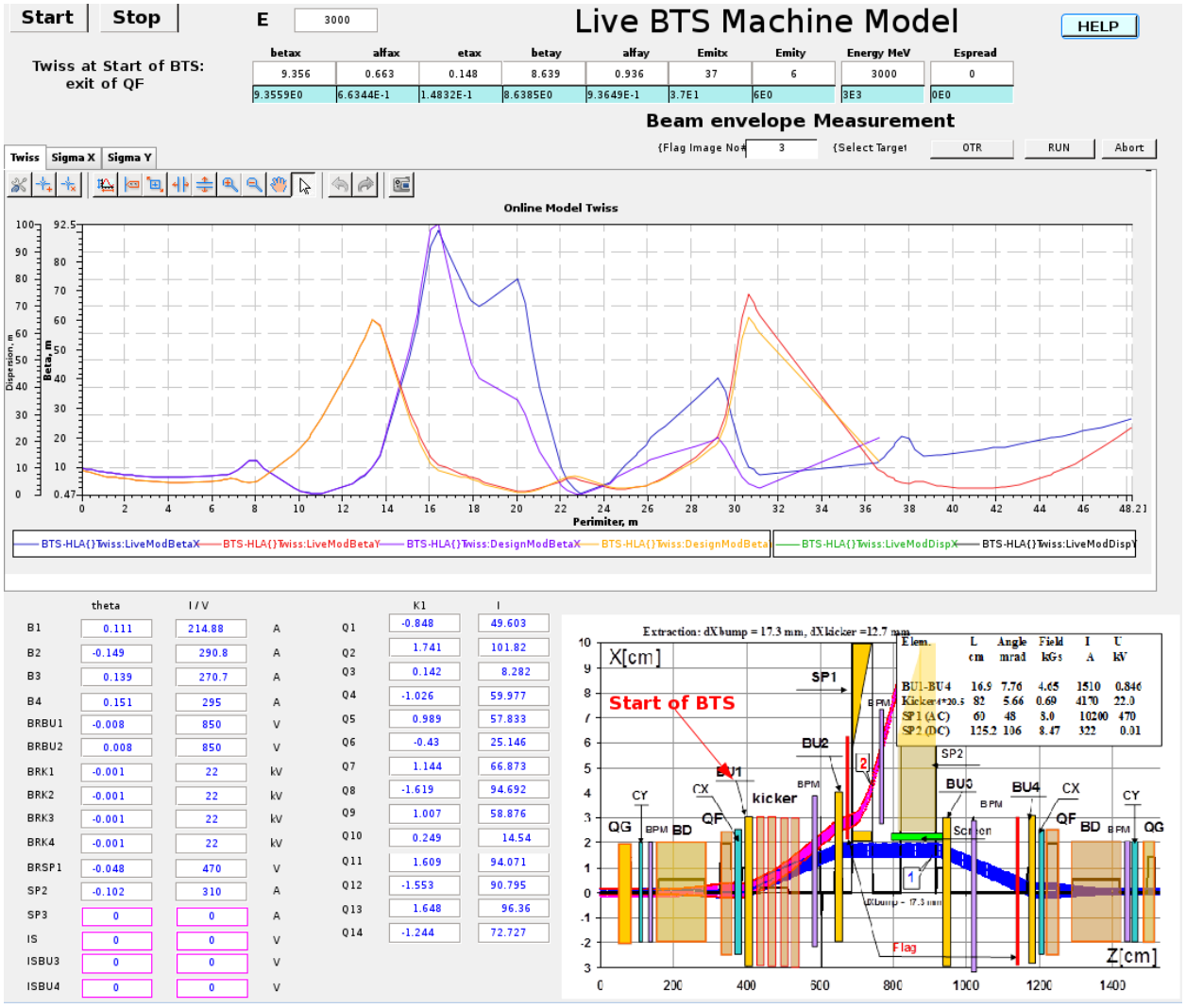

Fig.2 CSS GUI of Live BTS Machine Model.

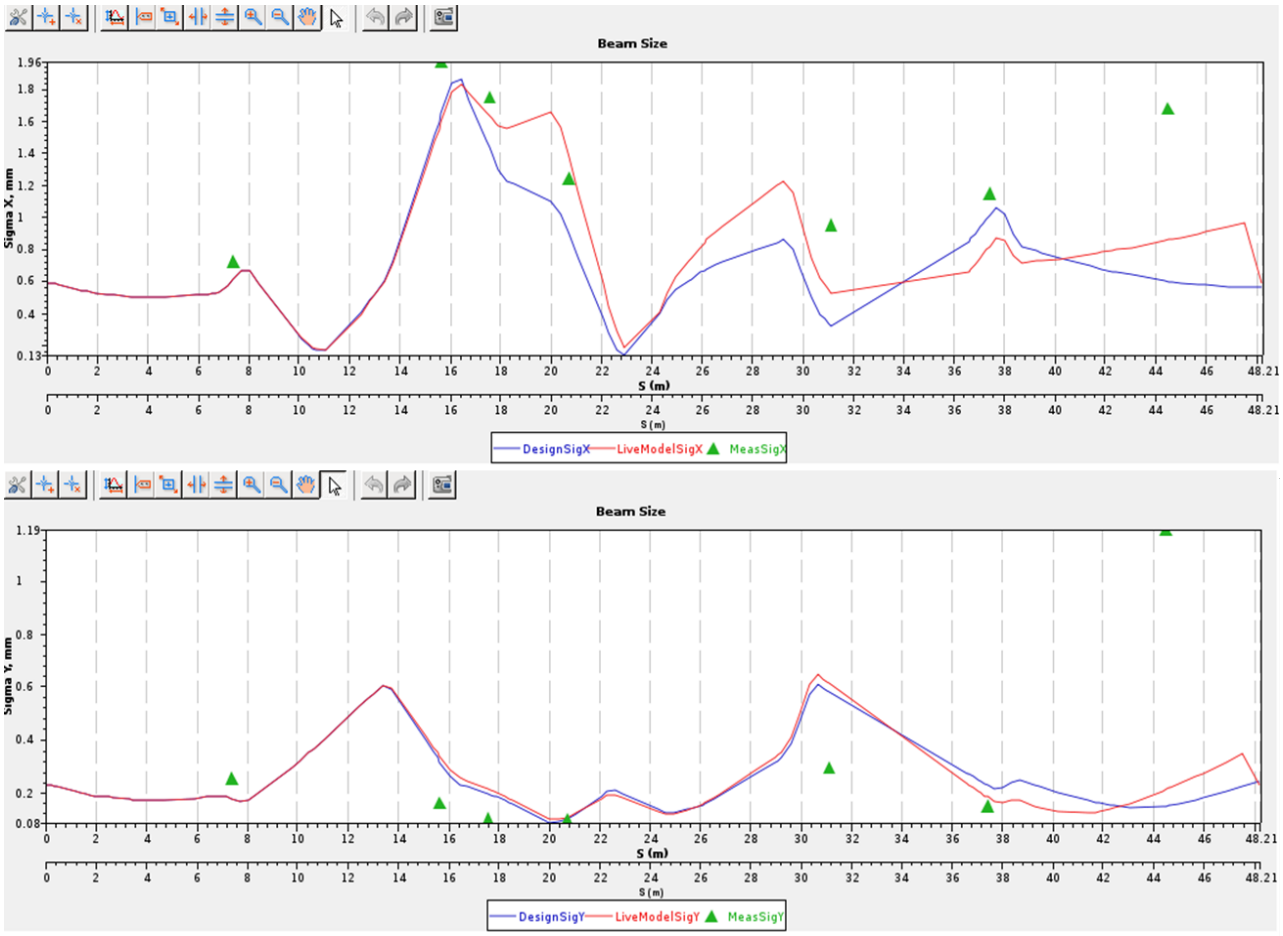

Fig.3 Beam sizes sigma x from design model (blue), live machine model (red), and measurement (green) using BSR flags are plotted at the top. Corresponding beam sizes sigma y at the bottom.

3.3.3 Optics match

Two measurements are needed for the application:

- Check the beam profile in each flag, choose one type of target and adjust the camera gain and filter position without saturation or too low signal. Shot by shot bunch will be different. Averaging several (~10) images is helpful to lower the discrepancy of measurement and model. The beam envelope measurement algorithm is a sequence of inserting flag and acquiring image. Then average the images in each flag and compare with model. As shown in Fig.4. Vertical beam sizes agree poorly between the design (blue) and the measurement (red). Better agreement for the horizontal beam sizes except the last point at the ISVF2 flag. In the measurement, the magnets were set based on the unit conversion and their design values. They were not optimized by the real beam in the live machine case. The beam from Booster was assumed to have the design values.
- Beam twiss and emittance are measured using quad scan in the dispersion free region, Q4 to Q8.

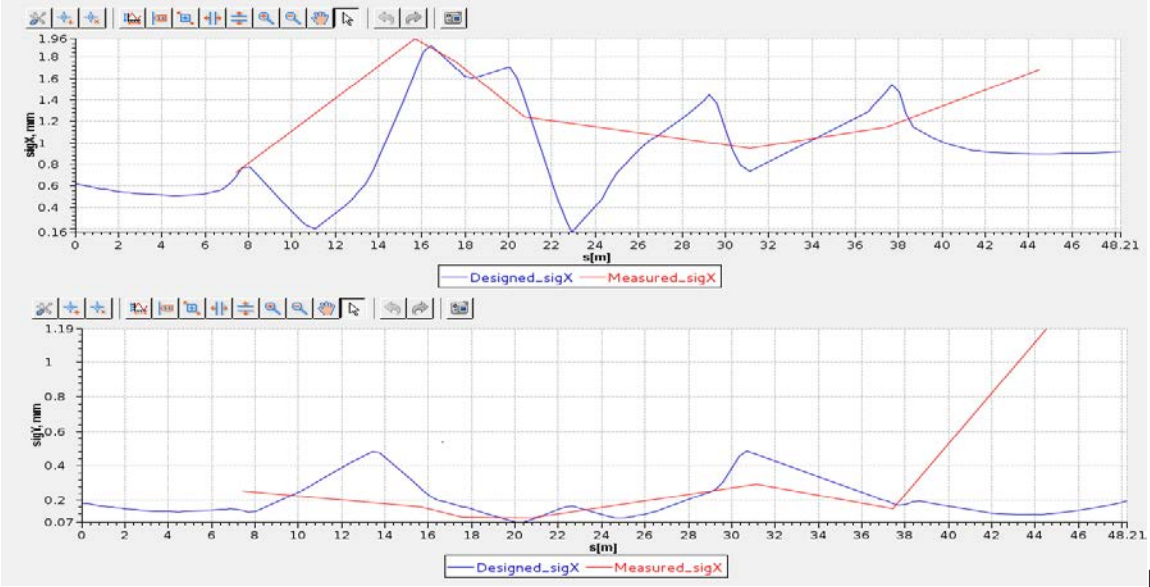

Fig.4

Twiss and beam parameters including energy spread and emittance at the start of BSR can be obtained from Booster turn by turn data and two Booster synchrotron light monitors [1], alternatively, from Booster live machine model. Twiss at the SR injection point is known from the design. Q4 to Q8 are adjusted according to Elegant simulation to have the optimal match from Booster to SR.

3.3.4 SR Injection beam launch angle and position control

It is to measure and control the beam injection angle and position at the SR pulsed septum with correctors in BTS (C6 and C7 for the horizontal; C8 and C9 for the vertical plane). The desired change is based on the SR first turn and BPM reading. User sets the desired position and angle in x and y plane, 'Compute Inj Position' button computes the live injection position and angle and required corrector strength to achieve the desired position and angle. 'Apply Correction' button sets the required corrector strength to correctors. It works well in y plane. But in x plane, due to the off-axis injection, the 10 mm betatron oscillation exceeds the linear region of BPMs, the position and angle control is not as good as the y plane case.

Discover large vertical error:

On April 16, a large error in the BSR vertical twiss functions was measured. Measurements of the beam size at BS-VF2 flag show a beam size of 0.67x0.14mm when 0.69x0.21mm was expected. At this location of the transport line, the only elements prior to the flag are the Booster AC and the DC septa. Measurements on the flags going to the Booster beam dump confirmed the error. On BS-VF2BD1, the 50% error in the vertical beam size remained and a 25% error in the horizontal beam size was measured.

At the time, it was assumed that the error in the beam size was due to an optical mismatch originating in the Booster. The transport line between BS-B2 and BS-B3 is designed to match the Booster optics to the storage ring optics. Therefore we performed quadrupole scans in the BSR line to measure the twiss functions after the BS-B2 magnet.

The vertical twiss functions were measured at BS-Q4, and horizontal at BS-Q5. Table 2 summarizes the results of these scans. The emittance is compared to synchrotron light monitor measurements in the Booster. From the Booster model we expect 38 nm horizontal rms emittance.

Parameter	Expected	Measured
β_x	40 m	32± 1 m
α_x	-7.5	-6.2 ± 0.3
ε_x	33 nm	44 ± 2 nm
β_y	60 m	7.4 ±0.3 m
α_y	-8.2	-0.89±0.04
ε_y	5.8 nm	9.5 ±0.4 nm

Table 2: Summary of Quadrupole Scan Measurements in the BtS.

From these measurements, it is clear that there is a large error in the vertical twiss functions. A beam image was taken at BR-XSVF1, which is the Booster flag that images the beam prior to the Booster extraction septum. The beam size was 0.36x0.13mm. From the Booster model we expect 0.54x0.21mm, and from the twiss function measurements we expect 0.48x0.60mm if there is no focusing between BR-XSVF1 and BS-VF2. These measurements show that there is some discrepancy between the Booster model and the measured beam size. But more importantly they show that there is a vertical focusing error between the two flags. This must come from the Booster extraction AC or DC septa. We will revisit this later.

This focusing error can be and was corrected that evening. The updated lattice input was into the BtS. Beam size measurements were conducted in the remainder of the BtS. The vertical beam size agreed to within 30%. Horizontal beam size agreement was worse. Except for two locations, the error in the beam size is greater than 50%, and is largest in locations where the dispersion is the largest. With the demonstrated error in the extraction septa focusing, the dispersion suppression after BS-B2 may not be perfect and a dispersion wave propagates through the BtS. It was not possible at this time to measure the dispersion.

Injection to the storage ring was attempted with the re-matched lattice. These attempts were not successful. We note that these studies were performed prior to finding the RF spring in the storage ring. The lattice was reverted to the old settings and the re-matched lattice was not used.

Investigations after these studies show that the DC extraction septum has an integrated sextupole component of -288 T/m. Such a field can produce the desired focusing if the beam is not passing through the center of the septum. In fact, a 5mm horizontal offset in the trajectory will produce the exactly the correct focusing to reproduce the BS-VF2 result. The following day a quick test to confirm this result was performed. The beam was imaged on BS-VF2, and the Booster AC extraction septum voltage was varied. An increase of 20V on the AC septum showed a change in the vertical beam size from 0.13mm to 0.15mm. This confirms that the DC septum has some focusing. Time did not permit further investigations.

To do list:

When commissioning restarts, the following studies for the BtS are suggested:

1. Booster extraction AC and DC septa should be tuned so that the beam is passing through the middle of the DC septum.
2. The dispersion should be measured to the Booster beam dump and through BS-B3.
3. Twiss functions should be measured at BS-Q4 and BS-Q5.
4. Rematch the BtS lattice for on axis and off axis injection.
5. When matching injection to the storage ring, attention should be paid that the beam is passing through the center of the storage ring injection DC septum.
6. Measure the beam energy spread from spectrum algorithm at BS-VF6.
   etc.

References:

[1] Booster Acceptance Test Report, by NSLS-II BNL and BINP Commissioning teams

4. SR commissioning

4.1 Lattice verification

NSLS-II storage ring linear lattice parameters have been measured with various methods. Several tools, such as beam optics analysis using Turn-by-Turn (TbT) beam-position monitors, and LOCO, etc., have been debugged and tested during the phase I commissioning. After implementing several iterations of corrections on the orbit, tune and optics, the current linear lattice of the storage ring is quite close to the designed model. These well-developed tools will help us to re-establish the linear lattice in the next phase commissioning stage. The tools for linear lattice characterization are reviewed and some obtained results are showed here, which can be used as the reference for the next stage.

4.1.1 Beta-function measurement and Beta-beat correction

Mainly, two methods are used to measure the linear optics: (1) using BPM TbT data to measure the β-functions at the locations of BPMs; (2) fitting the measured orbit response matrix to re-construct the lattice model. Extracting the Twiss parameters from TbT data can be accomplished within a very short time (<1min). Re-constructing the lattice model with LOCO algorithm is more expensive because both the measurement of ORM and the LOCO fitting are quite time-consuming (~2hrs), but it can provide more lattice information. The LOCO method is described in other section. In this section, we only report the results obtained from the TbT data.

The optics analysis using the TbT data [1] has been implemented with several Python scripts by different accelerator physicists. The correction of optics was implemented by correcting the Betatron oscillation phase advance errors among the BPMs. The needed quadrupole strengths correction are obtained by solving the linear equation,

$$\Delta\vec{\phi} = M\Delta\overrightarrow{K_1}.$$

Where $\Delta\vec{\phi}$ is the vector of phase advance errors at the locations of BPMs, which needs to be corrected. M is the response matrix between the phase advance and quadrupoles' integrated strengths, which is calculated with the design model and the quadrupole unit conversion coefficients.

As illustrated in Figure 1, the storage ring linear optics at the locations of BPMs was measured after the errors of phase advance between BPMs were corrected. Comparing with the designed values, the r.m.s of beta-beats are 5-6%. Several iterations on the top of this configuration actually brought the beta-beat further down to 3%. Since the phase advance between adjacent BPMs was corrected, the tunes were shifted to the designed values automatically.

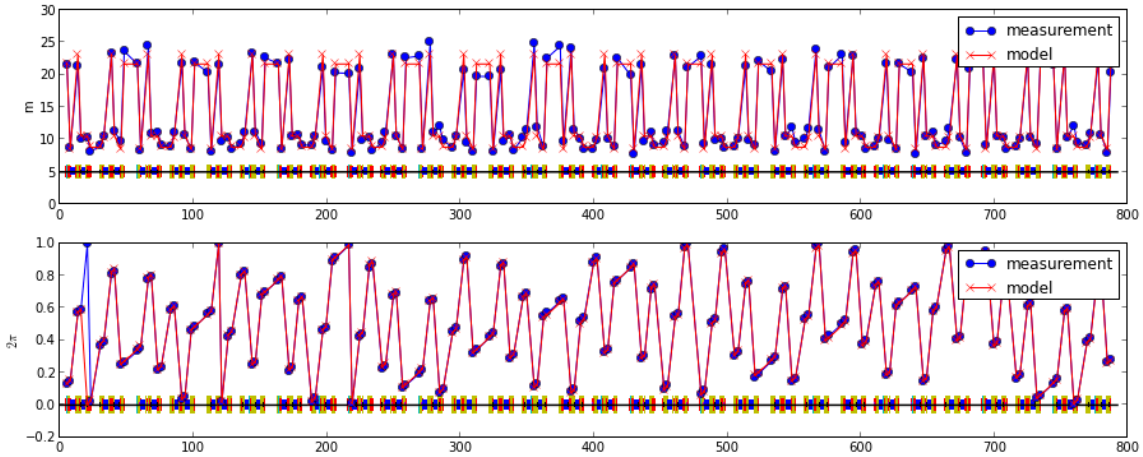

Figure 1a. Corrected horizontal beta-functions at 180 BPMs

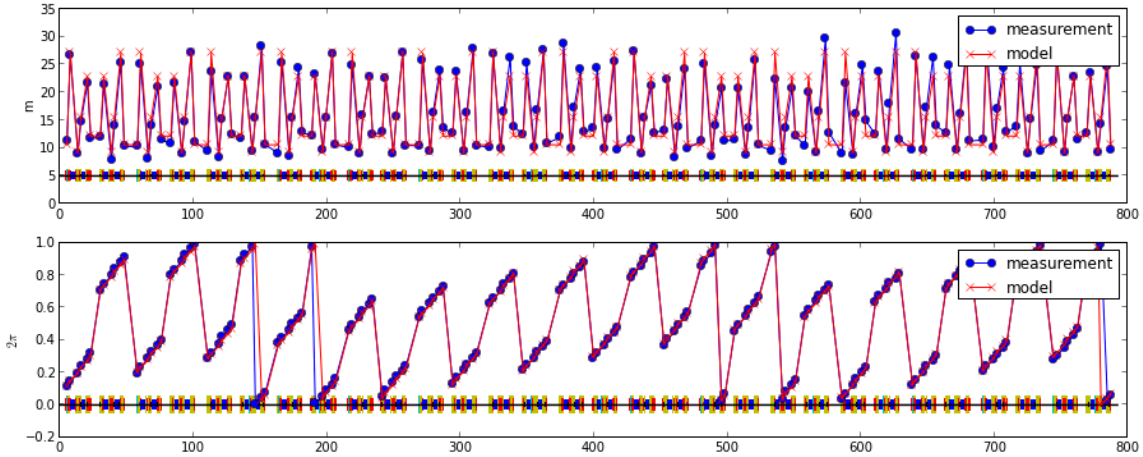

Figure 1b. Corrected vertical beta-functions at 180 BPMs

4.1.2 Quadrupoles errors and model reconstruction

Based on the measured Twiss parameters, a lattice model can be re-constructed by comparing with the designed model. Thus the residual quadrupoles errors can be obtained by solving the same linear equations (after several iterations)

$$\Delta\vec{\phi}_{x,y} = M\Delta\overrightarrow{KL}.$$

Figure 2 gives all 300 quadrupoles errors grouped by families.

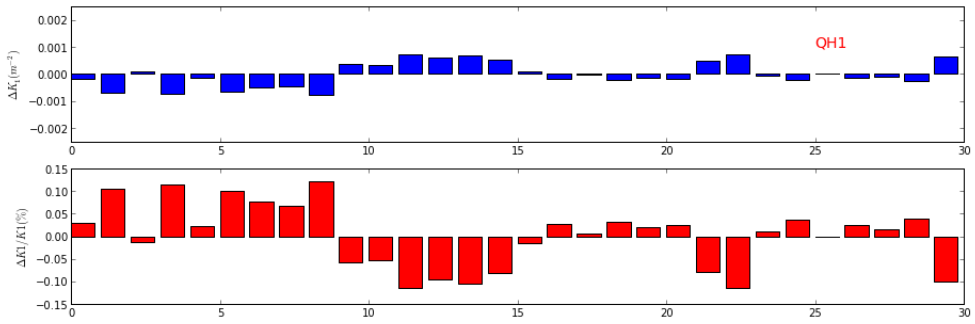

Figure 2a. QH1 family quadrupoles errors.

The top shows the absolute normalized gradient errors; and the bottom shows the relative errors respective to their design values.

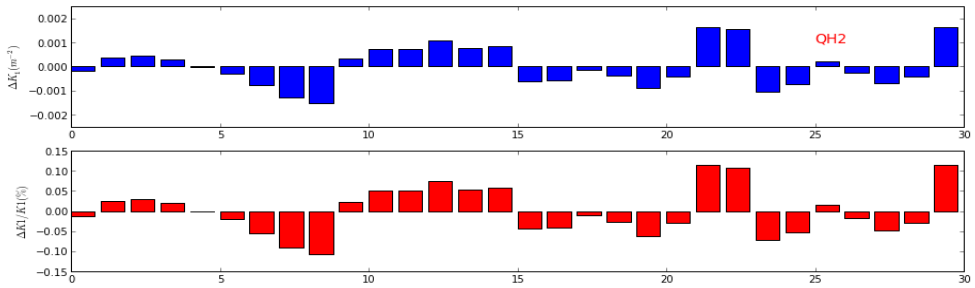

Figure 2b. QH2 family quadrupoles errors.

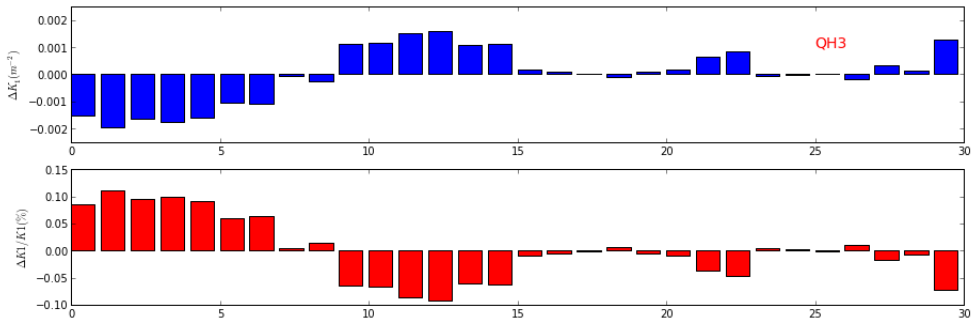

Figure 2c. QH3 family quadrupoles errors.

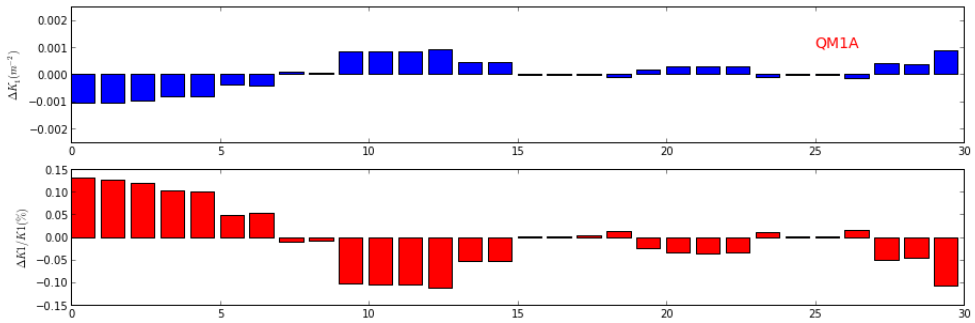

Figure 2d. QM1A family quadrupoles errors.

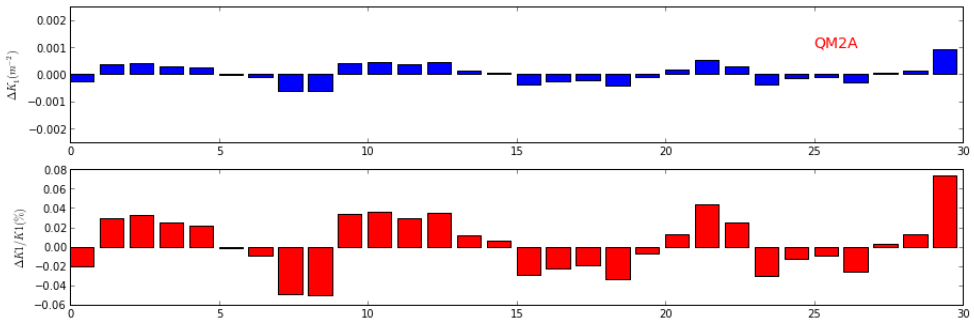

Figure 2e. QM2A family quadrupoles errors.

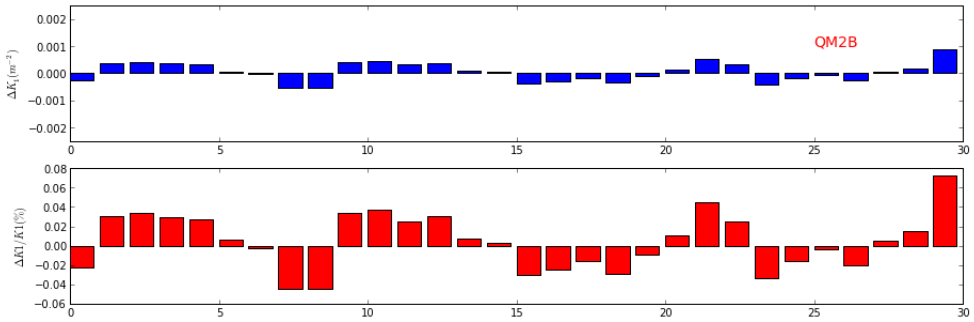

Figure 2f. QM2B family quadrupoles errors.

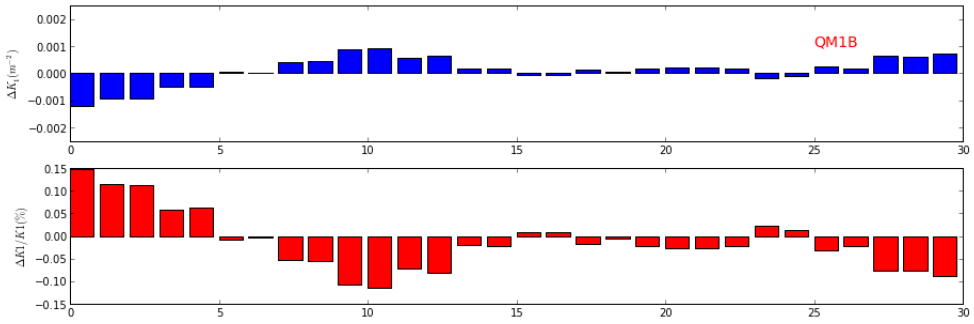

Figure 2g. QM1B family quadrupoles errors.

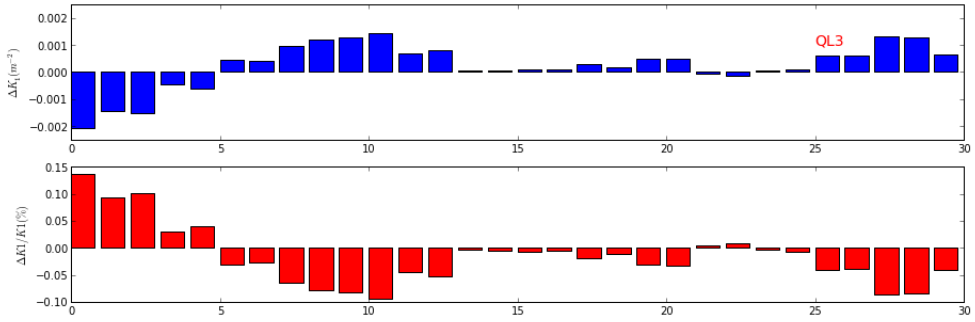

Figure 2h. QL3 family quadrupoles errors.

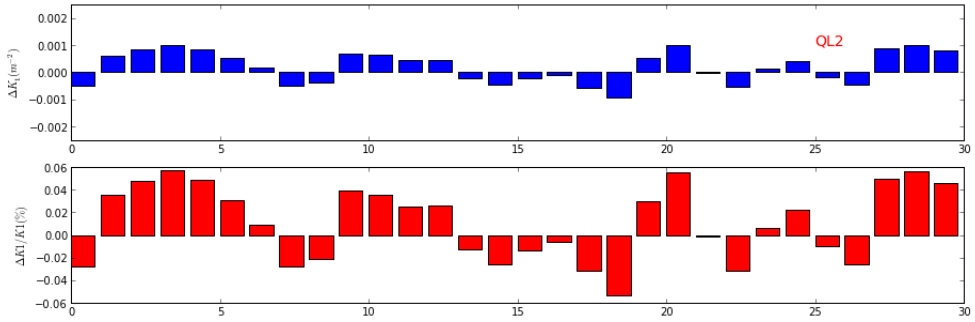

Figure 2i. QL2 family quadrupoles errors.

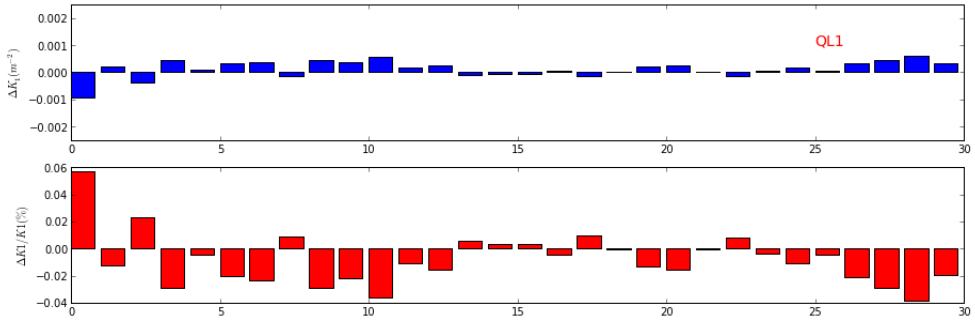

Figure 2j. QL1 family quadrupoles errors.

From Figure 2, no significant quadrupole errors exist after optics distortion correction down to a few percent. All relative errors are less than 0.2%.

The calculated quadrupole errors have been put on the top of the designed model to reconstruct the linear lattice model. The reconstructed model agrees with the measurement quite well, as illustrated in Figure 3.

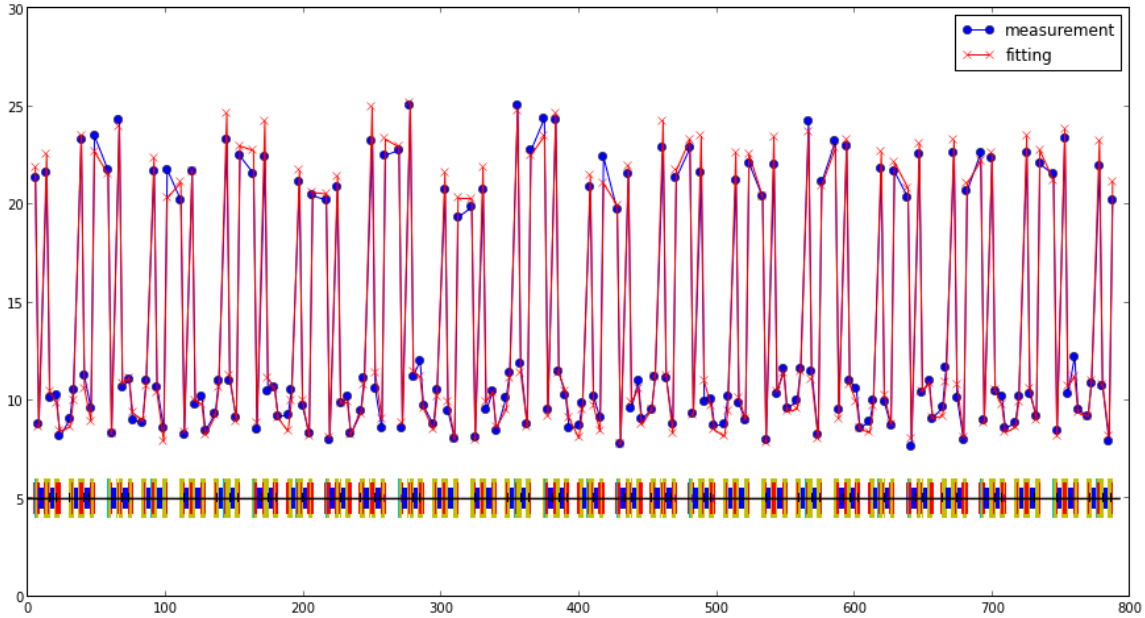

Figure 3a. Re-constructing lattice with quadrupole errors and comparing with the measurement results (the horizontal beta-functions).

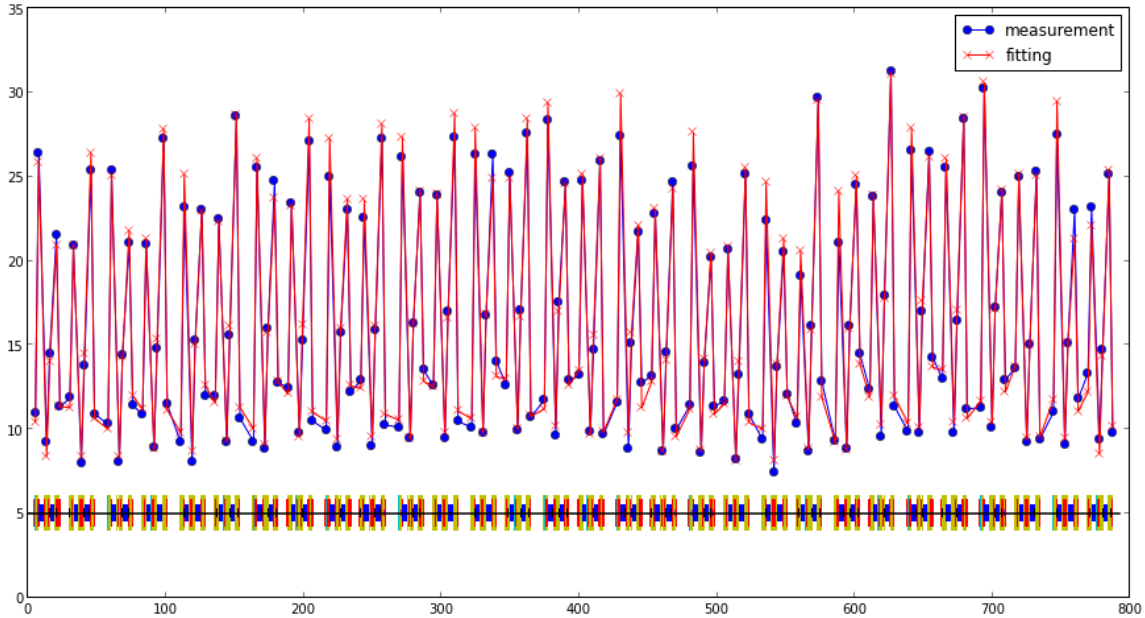

Figure 3a. Re-constructing lattice with quadrupole errors and comparing with the measurement results (the vertical beta-functions).

4.1.3 Tune

Tune was measured with two methods: (1) implementing FFT/NAFF analysis on the TbT data, or (2) sweeping tune with the excited beam. Both methods can give reliable and comparable results. Figure 4 illustrates a FFT spectrum with the Hanning window.

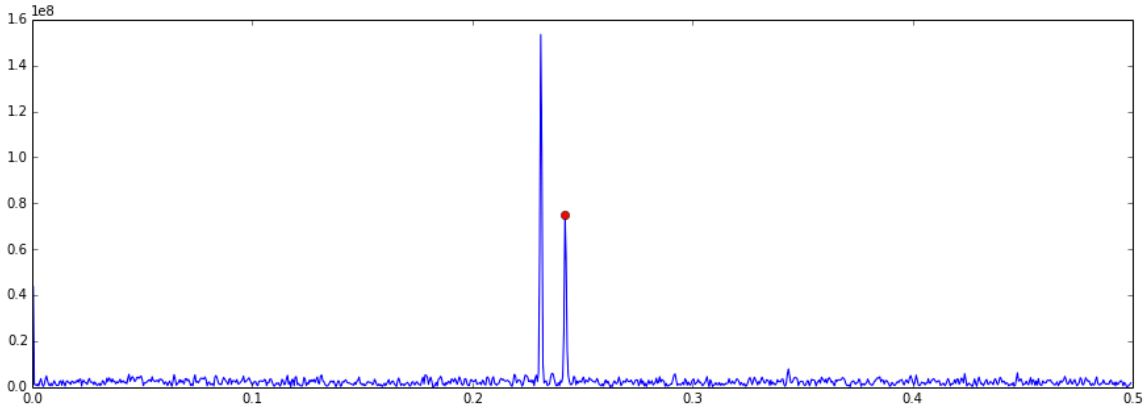

Figure 4. FFT spectrum of the beam TbT data with Hanning window

As mentioned in the previous section, the phase advance errors at the locations of BPMs were corrected, thus the tune (the phase advance of the whole ring) has been corrected automatically to the proximity of the designed value (33.22/16.26). Some tiny residual tune shift can be corrected by using two families of quadrupoles at the non-dispersive sections.

4.1.4 Dispersion

Dispersion was measured by changing RF frequency to change beam energy

$$\delta = -\frac{\Delta f}{\alpha_c f}.$$

Where Δf is the master oscillator frequency change, and α_c is the momentum compaction factor.

The measurements show a good agreement between the design model and direct measured result (see Figure 5a). Some horizontal dispersion leaks from the achromat sections, which should be corrected by the quadrupoles between two dipoles in next phase commissioning. Around 10-15mm vertical dispersion has been observed, and was attempted to be corrected with the 15 skew quadrupoles located in the dispersive region. The r.m.s spurious vertical dispersion reduced from 5.2 mm to 2.9 mm (Figure 5b). The QM families are used for horizontal plane dispersion correction. Two non-dispersion quads family (QH3 and QL2) are optimized together along with dispersion correction to prevent the tune moving away. After 10 iterations performed, horizontal dispersion decreased to 2.45 mm RMS [-16mm ~ +8mm p2p] (Figure 5c) while tune differences were maintained within 0.01.

The correction of vertical dispersion needs to be combined with linear coupling correction in the next stage.

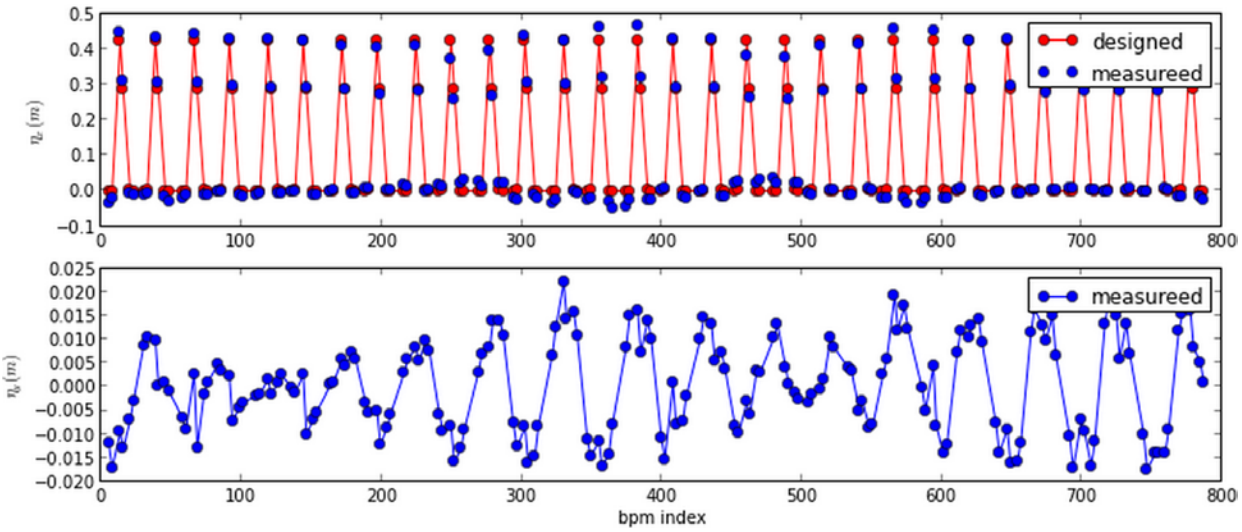

Figure 5a. Measured dispersions at the locations of BPMs

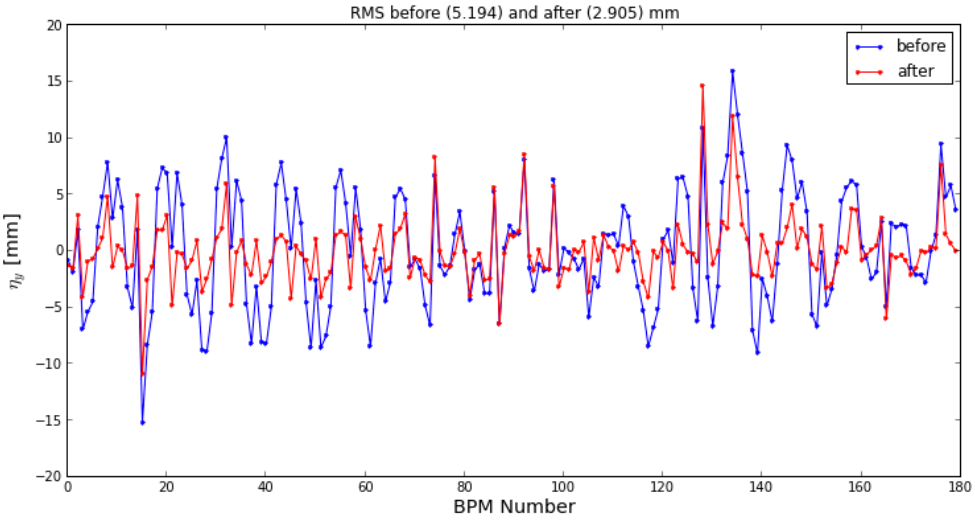

Figure 5b. Comparison of the vertical dispersions before and after correction

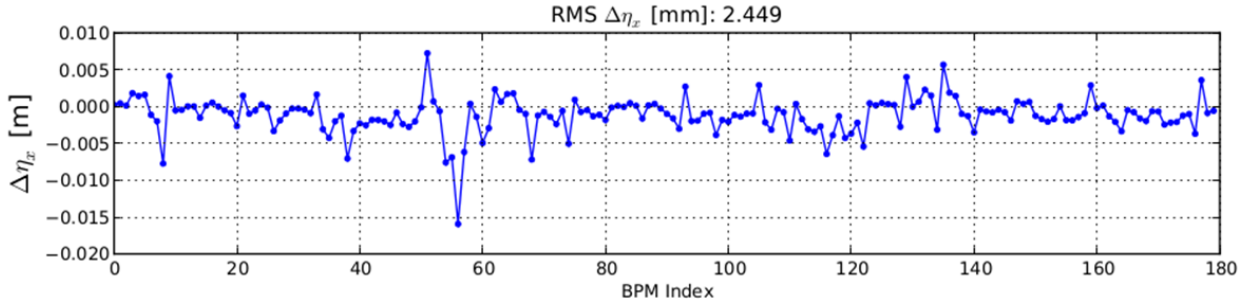

Figure 5c. The horizontal dispersions after correction

4.1.5 Linear chromaticity

Linear chromaticity was measured by fitting the tune into a polynomial while varying beam energy. A typical measurement result is shown in Figure 6. The designed value for the linear chromaticity is +2/+2 for both planes. The measured result was +2.68/+1.94 on May 9, 2014.

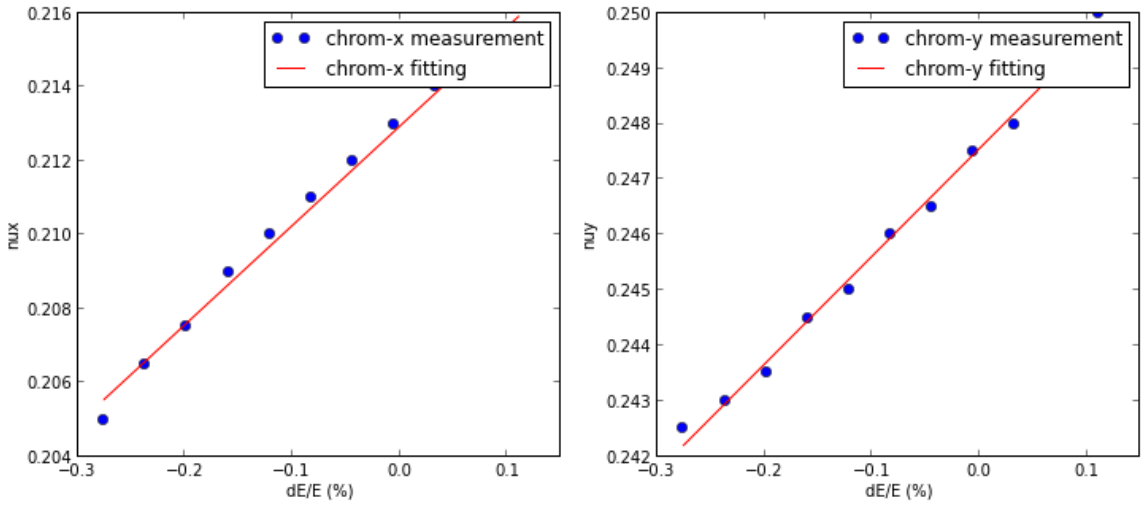

Figure 6. chromaticity measurement and linear fitting

Correction of chromaticity is slightly tricky. Unlike quadrupoles powered independently, one family of sextupoles within the same penton is powered in series. All sextupoles have slightly different transfer functions from power supplies to the field properties. Thus a response matrix between chromaticity and sextupole power suppliers current is calculated at the EPICS PV level. Then chromaticity adjustment is implemented in the same way as tune adjustment to solve the linear equations. Experimentally the chromaticities in both planes have been adjusted within the range [0, 5] units to carry out collective studies.

4.1.6 Linear coupling

The designed tune is quite close to the difference resonance line $\nu_x - \nu_y = 17$. Linear coupling was observed from several aspects: (1) the measured orbit response matrix (ORM) has non-zero elements in the off-diagonal blocks; (2) a relative large residual oscillation in the vertical plane was observed while the beam was excited by horizontal injection kickers; (3) In the meantime, 10-15mm peak-to-peak vertical dispersion was measured around the ring.

The common method to assess the linear coupling is to measure the minimum tune separation between two coupling modes. Experimentally, the minimum tune separation is measured by tuning quadrupoles to bring two coupled mode tunes as close as possible. The minimum distance of two modes is characterized as the coupling coefficient $\left|G_{1,-1,l=17}\right|$ as illustrated in Figure 7a. Beside this traditional method, several alternatives were used to assess and correct the coupling: (1) the non-zero off-diagonal elements in the ORM can be used to calculate the needed corrector strength, or (2) the one-turn matrix can be directly fitted from turn-by-turn data of beam position monitors after a kick is applied. After linear coupling correction the minimum tune separation reduced by a factor of 4-5. In the meantime, after beam

is excited with the same amount of kick strength from one of the injection kickers, the vertical residual oscillation amplitudes before and after correction are found to decrease from 1.1mm (peak-to-peak) to 0.2mm (Figure 7b). The beam lifetime decreased from 9.03hrs to 5.38hrs with the beam current 4.15mA (20 bunches), which indicates vertical beam size was reduced significantly after coupling correction.

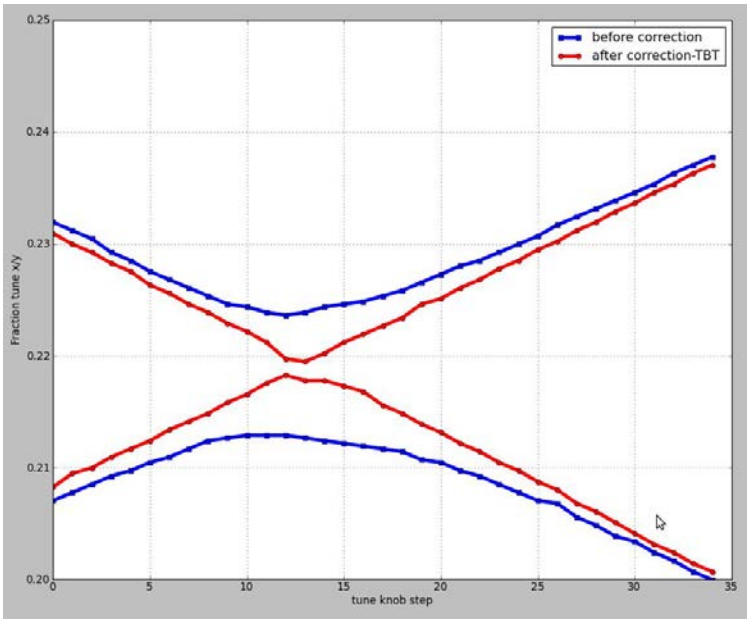

Figure 7a. Tune separation before and after linear coupling correction

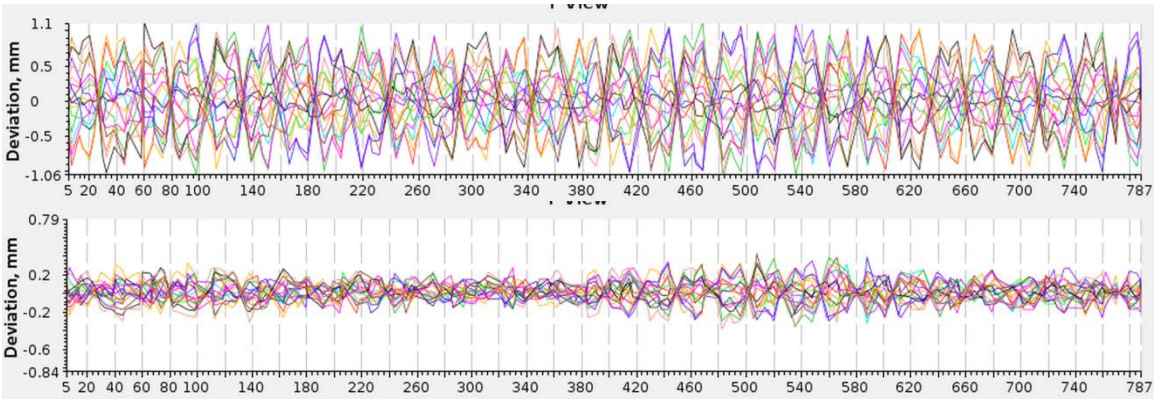

Figure 7b. Residual vertical oscillations after beam are excited by a same kick before (upper) and after (lower) correction.

4.1.7 Summary

The NSLS-II storage ring linear lattice was measured and corrected with various methods. Overall the actual machine is quite close to the design model after the Phase I commissioning. Beta-beat is within 5%; tune and linear chromaticity are in the proximity of the desired values, and can be adjusted effectively with the given knobs; linear coupling and the vertical spurious dispersion were corrected, some preliminary improvement was observed. Further improvements are expected by multiple iterations.

Acknowledgements

The commissioning of the storage ring lattice is a team effort. I would like to thank all my colleagues for providing data, and sharing experience for this documentation.

References:

[1] P. Castro-Garcia, Doctoral Thesis, CERN SL/96-70 (BI)

4.2 Orbit correction

The orbit correction in NSLS-II commissioning is based on orbit response matrix~(ORM). Before the ORM measurement is possible, we used the theoretical matrix and converted the physics unit [m/rad] to machine unit [mm/A]. We also implemented the most-effective-corrector method provided by F.~Willeke. The local bump is implemented based on same ORM, but with non-zero target orbit.

4.2.1 Orbit Response Matrix

The orbit response matrix~(ORM) is defined as

$$M_{ij} \equiv \frac{dx_i}{d\theta_j} = \frac{\sqrt{\beta_i \beta_j}}{2 \sin \pi\nu} \cos(\pi\nu - |\psi_i - \psi_j|)$$

where x_i is the orbit reading at the i-th BPM and theta_j is the j-th corrector strength. β, ψ, ν are twiss parameters.

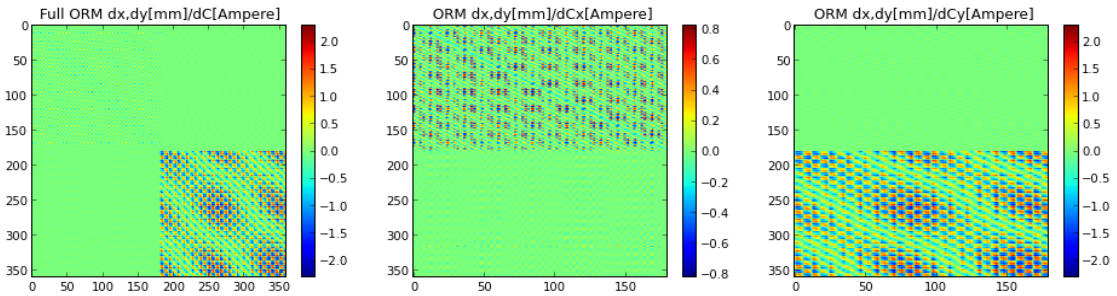

Figure 1 The first ORM measured by python-aphla. Full ORM, all columns due to horizontal kick and all columns due to vertical kick

For the commissioning, we used only 180 BPMs and ignored the insertion device and injection straight BPMs. All 180 slow correctors are used. The strength limit for correctors are [-18.201, 18.201] Ampere and about [-1,1] mrad equivalently (see aphla for exact result).
Before we have stored beam with reliable BPM signal and low noise, we were using the theoretical matrix.

The following example shows how to measure ORM:

```
bpms = ap.getElements('BPM')
cors = ap.getElements('COR')
bpmlst = [(b, 'x') for b in bpms] + [(b, 'y') for b in bpms]
corlst = [(c, 'x') for c in cors] + [(c, 'y') for c in cors]
ap.measOrbitRm(bpmlst, corlst, dxmax=0.5, nx=3)
```

Internally measOrbitRm adjust each corrector for several times and fit the line for each ORM element. The measured and theoretical ORMs are compared for two cells. The measured ORM was also used for LOCO fittings.

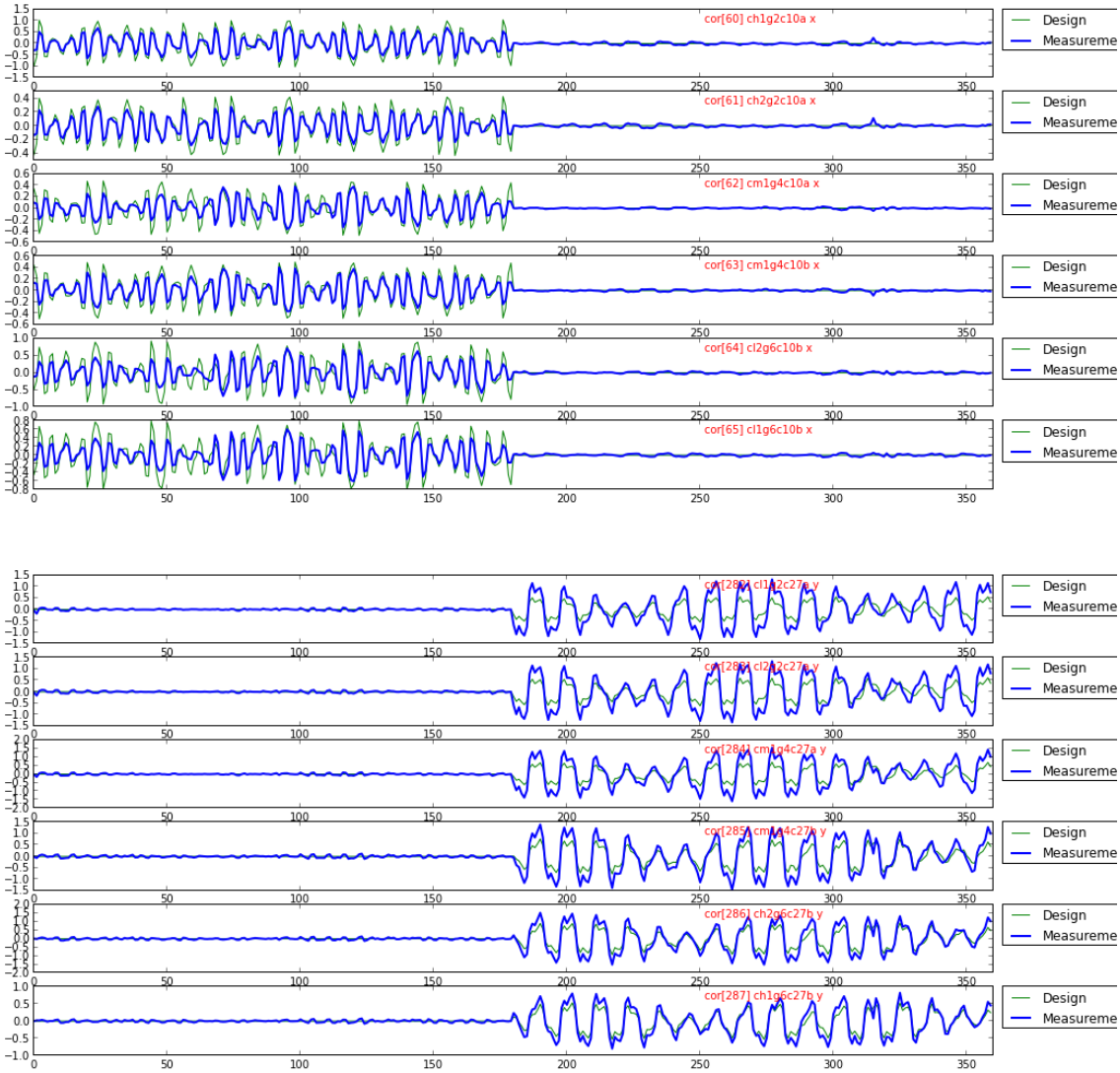

4.2.2 Orbit Correction

The orbit correction uses ORM to solve for dθ

$$M \cdot d\theta = -x,$$

where M is a the matrix with 180x180, dθ is the adjustment for 180 correctors and x is the current static orbit. We used SVD (singular value decomposition) to solve this equation. At the beginning where the orbit was around 2--4~mm, we used about 10 singular values. As the correction iterates, we used up to 40. This scheme was not available before a stable orbit reading, i.e. stable x values in the above equation.

The most-effective-corrector method for orbit correction was successful when we first got the stored beam. It is similar to the situation where only one or a few of singular values are used. This method scans calculated ORM and find the most effective corrector which reduces the RMS of static orbit. Each iteration gets one corrector with new setpoint value.

All the orbit correction scripts are provided as Python notebook with both code, comments and plots included. With carefully measured ORM and asymptotical corrector stepsize, the orbit was corrected to x{rms}=0.1 mm, y{rms}=0.07 mm and peak-peak values x{p-p}=0.7 mm and y{p-p}=0.3 mm (before beam based alignment). Further improvement could be realized by smaller step size of correctors and frequent corrections (as a slow orbit feedback).

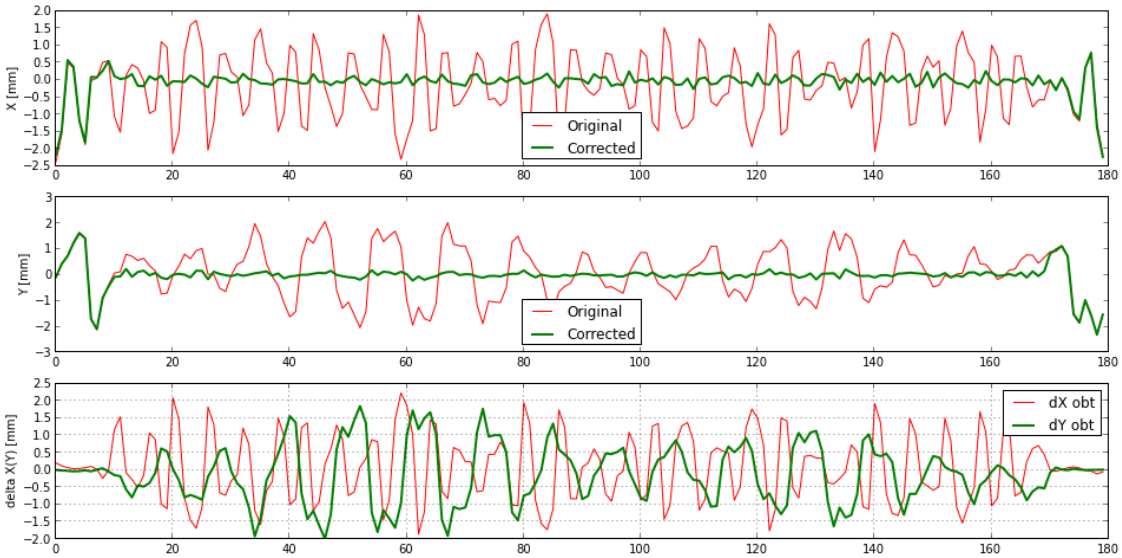

Figure 2 Correct orbit but fix the injection straight. When at on-axis injection, we kept the injection straight to maintain optimized injection efficiency. Both planes are correct separately and no strong coupling were found.

Before the first obstacle spring was found and removed, orbit correction in the vertical plane often dumped the beam. This made us believe that there was unexpected small aperture in the vacuum chamber. The region was identified with BPM turn-by-turn sum signal.

4.2.3 Local Orbit Bump

Orbit correction in python-aphla is indeed a local bump routine with target orbit all zeros. The general version is

$$M \cdot d\theta = dx,$$

where dx is the change of orbit.

Since initially we were off-axis injection, this local bump method is essential for keeping injection offset and angle while correcting the orbit elsewhere.

The 3-bump and 4-bump are also implemented in high level application called mleap. Each local bump can be calculated by either corrector strength or orbit displacement. These calculations are based on theoretical twiss parameters and we have found they are valid when bump amplitude are moderate.

The kick strength ration for 3-bump method can be found in many text books:

$$\frac{\theta_2}{\theta_1} = -\sqrt{\frac{\beta_1}{\beta_2}}\frac{\sin(\psi_3 - \psi_1)}{\sin(\psi_3 - \psi_2)}$$
$$\frac{\theta_3}{\theta_1} = -\sqrt{\frac{\beta_1}{\beta_3}}\frac{\sin(\psi_2 - \psi_1)}{\sin(\psi_2 - \psi_3)}$$

At a target point s between 1 and 2, the position and angle are

$$x_s = \theta_1\sqrt{\beta_1\beta_s}\sin(\psi_s - \psi_1)$$
$$x'_s = \theta_1\sqrt{\frac{\beta_1}{\beta_s}}[\cos(\psi_s - \psi_1) - \alpha_s\sin(\psi_s - \psi_1)]$$

and between 2 and 3

$$x_s = \theta_3\sqrt{\beta_3\beta_s}\sin(\psi_3 - \psi_s)$$
$$x'_s = -\theta_3\sqrt{\frac{\beta_3}{\beta_s}}[\cos(\psi_3 - \psi_s) - \alpha_s\sin(\psi_3 - \psi_s)]$$

Among the five local bump method, ORM based one was used more often. One fruitful application was to identify the small aperture regions.

4.2.4 Beam Based Alignment

We all knew that beam based alignment was critical for better orbit correction, coupling correction, tune correction and beta beat correction. Without aligning BPM with quadrupole, the corrected orbit will not go through the quadrupole center and a tune correction will distort the corrected orbit again.

For each one of the 180 BPMs, there is a quadrupole only about 8~cm away. This makes it possible to use ALS method to align BPMs with the nearby quadrupoles.
The algorithm is easy to understand and more importantly model independently.

It is based on the effect that when beam passes through the center of quadrupole, adjusting the quadrupole strength does not produce orbit kick. When this happens the BPM reading is the ``target orbit'' we are looking for.

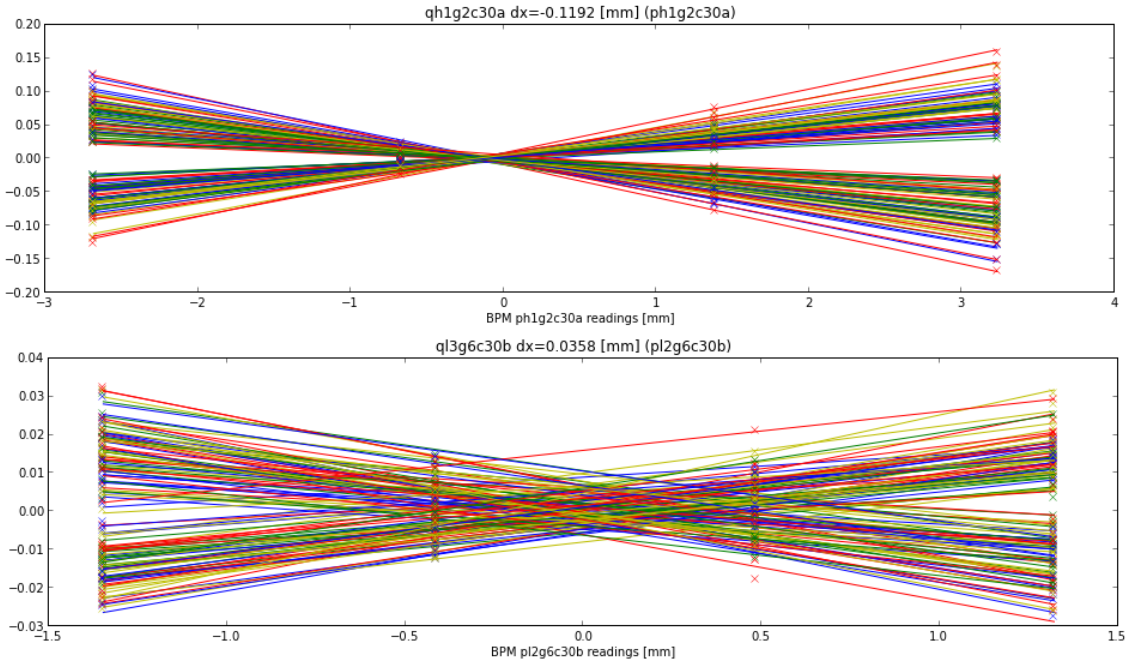

Figure 3 Beam based alignment for two BPMs, the top one has smaller f ootprint at y=0 axis (smaller error bar) and is more reliable.

The orbit change due to the quadrupole kick depends on both the beam offset at the quadrupole and the quadrupole strength. The linear relationship makes this method easier and more reliable. By fitting the orbit change with beam offset, we can find at which offset changing quadrupole strength does not produce any orbit distortion.

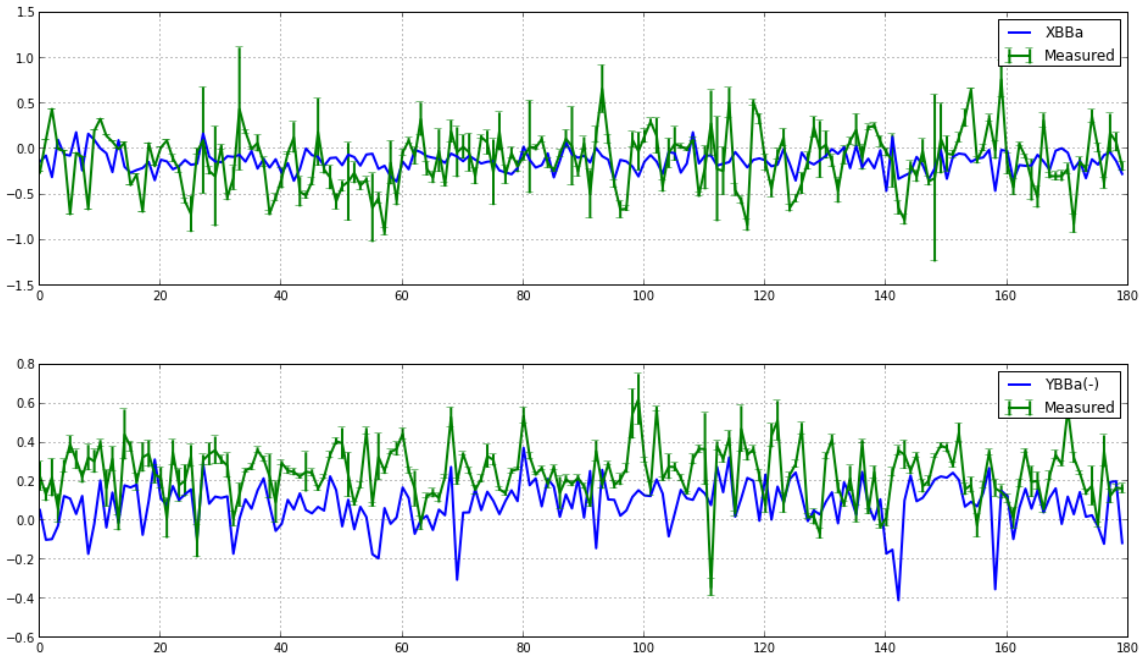

Figure 4 BBA results compared with survey data and BPM electrical offsets

The final numbers are shown in Fig. 4, where a positive number means the quadrupole center is in positive direction with respect to the paired BPM, i.e. The BPM readings indicating beam is passing through the center of quadrupole. The BBA data come from BPM offset and quad survey/alignment. But it is hard to get exact match due to the uncertainty mainly in BPM offset. It is hard for me to believe survey/alignment are off by 0.4—1 mm.

4.3 Slow orbit feedback System

NSLS-II slow orbit feedback (SOFB) system is designed to suppress the beam movement caused by the low frequency noises such as ground motion, temperature drift etc. It includes the BPM for orbit measurement, feedback calculation, and slow correctors for orbit correction.

4.3.1 Principle

In NSLS-II, there are 180 BPM around the storage ring. Each BPM measures both H (horizontal) and V (vertical) beam positions. The total orbit measurement includes 360 H and V position data. The BPM readings have resolution of 200nm.

There are also 180 slow correctors around the storage ring. Each corrector can bend the beam in H and V plane. The corrector has maximum bending angle of 800uRad in H and V planes.

The principle of SOFB includes three steps:

1) Measurement of orbit response matrix

This step can be descripted by the following equation

$$R_{MxN} \bullet \theta_{Nx1} = d_{Mx1}$$

N is the number of correctors, M is the number of BPMs. R is the orbit response matrix. θ is the corrector strength and d is the beam position measured by BPMs. For NSLS-II, M=360 and N=360. During orbit response matrix measurement, each corrector is kicked and the change of orbit is measured. The measurement corresponds to one column of R. After all corrector kick, we can obtain the full matrix R.

2) SVD

3) The pseudo inverse matrix of R can be obtained by singular value decomposition (SVD). From SVD, R can be written as:

$$R_{MxN} = U_{MxN} \Sigma_{NxN} V^{T}{}_{NxN}$$

And the pseudo inverse matrix is

$$R^{-1}{}_{NxM} = V_{NxN} \Sigma^{-1}{}_{NxN} U^{T}{}_{NxM}$$

The SVD calculation is carried out by a python script. The ill-conditioned response matrix will cause numerical instability. The Tikhonov regularization is applied to prevent such instability.

4) Feedback

After obtaining the pseudo inverse matrix, the orbit feedback is applied:

$$\theta_{Nx1} = R^{-1}{}_{NxM} \bullet d_{Mx1}$$

A PID loop is applied to make the feedback system stable.

4.3.2 Implementation

The SOFB design was first simulated on the virtual accelerator. After we designed and tested the SOFB on the virtual accelerator, we moved the design to the NSLS-II storage ring.

The SOFB system for NSLS-II storage ring includes all the 180 BPMs (6 BPMs/cell), and all the 180 slow correctors (6 correctors/cell). The sampling/correction rate is 0.5Hz. This rate is mainly limited by the slow corrector ramp rate (2A/second) and the SOFB data communication between epics softioc. The response matrix consists both horizontal and vertical plane. The response matrix size is 360x360.

4.3.3 SOFB Commissioning

The SOFB commissioning is carried out near the end of commissioning phase 1, when the beam can be injected into the storage ring and had a lifetime over than a few hours. The total dedicated beamtime for SOFB commissioning system was less than 2 hours.

The first step of commissioning of SOFB system is to measure the orbit response matrix. From the CSS page, we used 0.5A step for both horizontal and vertical corrector current change. Each step of horizontal or vertical corrector change will generate a column of the response matrix. The total measurement time in each step includes corrector settle time, BPM settle time, and the corrector reset time (to original value). It is about 6 seconds per step. For 360 corrector planes (180 horizontal and 180 vertical), it takes about 40 minutes to finish the orbit response matrix measurement.

The second step of the SOFB commissioning is the SVD calculation. This step is carried out in the softioc with Python code. The Tikhonov regularization is used to eliminate the small eigenvalues. This steps takes less than one second to finish.

The third step is to turn on the SOFB and to tune the PID parameters. Since Kd is sensitive to the sensor noises, we always set the Kd to zero during the SOFB commissioning. We spent total about 1.5 hours to try different Kp and Ki parameters for different conditions.

The conclusion is: as long as Kp is less than 2.0, the system is stable. This conclusion agrees with the theoretical analysis. The final optimum Kp and Ki parameters are Kp=0.9 and Ki=0.3. Under these conditions, the orbit converges to reference orbit quickly and has a minimum offset at the stable state.

The following picture shows the control panel for the SOFB system. It shows functions and commissioning results of SOFB system.

1) The orbit response measurement shows very little coupling between H and V plane. The response matrix mainly have non-zero data in two regions: the upper-left region which corresponds to H(corrector) – H(BPM) response, and the lower-right region which corresponds to V(corrector) – V(BPM) response. The values in the H-V and V-H region are small.

2) The pseudo inverse response matrix shows that most of the non-zero values are located around the diagonal line. The Tikhonov regularization is used to remove the numerical instability caused by small eigen values. This result agrees with the theoretical calculation and the simulation results from virtual accelerator.

3) When SOFB is turned on, the beam orbit quickly converges to the reference orbit. The orbit different RMS values in H and V plane give quantitative criteria for the effeteness of SOFB system. In the attached picture, it shows that the RMS value drops from 0.7mm to 0.1mm in H plane, and from 1.06mm to 0.08mm in V plane after SOFB is turned on.

4) SOFB system can also be used as a tool for orbit correction: the system can bring the orbit to any of the referent orbit. This is useful for accelerator physicists to “design” any referent orbit (such as local bumps). They can then turn on SOFB system to correct the orbit and stabilize the orbit to the referent orbit. For a large orbit correction, where the difference between the real orbit and the reference orbit is huge, SOFB might give a large asynchronized corrector currents change and kick the beam away to the vacuum chamber. This happened once during the SOFB commissioning. The solution is to first use smaller Kp and Ki to bring the beam closer to the reference orbit. This step is similar to orbit correction procedure. Then, we can change to larger Kp and Ki for normal feedback application.

5) Due to the limit beam time, we don’t have many detailed study for all issues of the SOFB system. After the commissioning, it has been used by accelerator physicists and operators as a generator tool. It will be also helpful for the initial stage of phase 2 storage ring commissioning.

Slow orbit feedback control panel

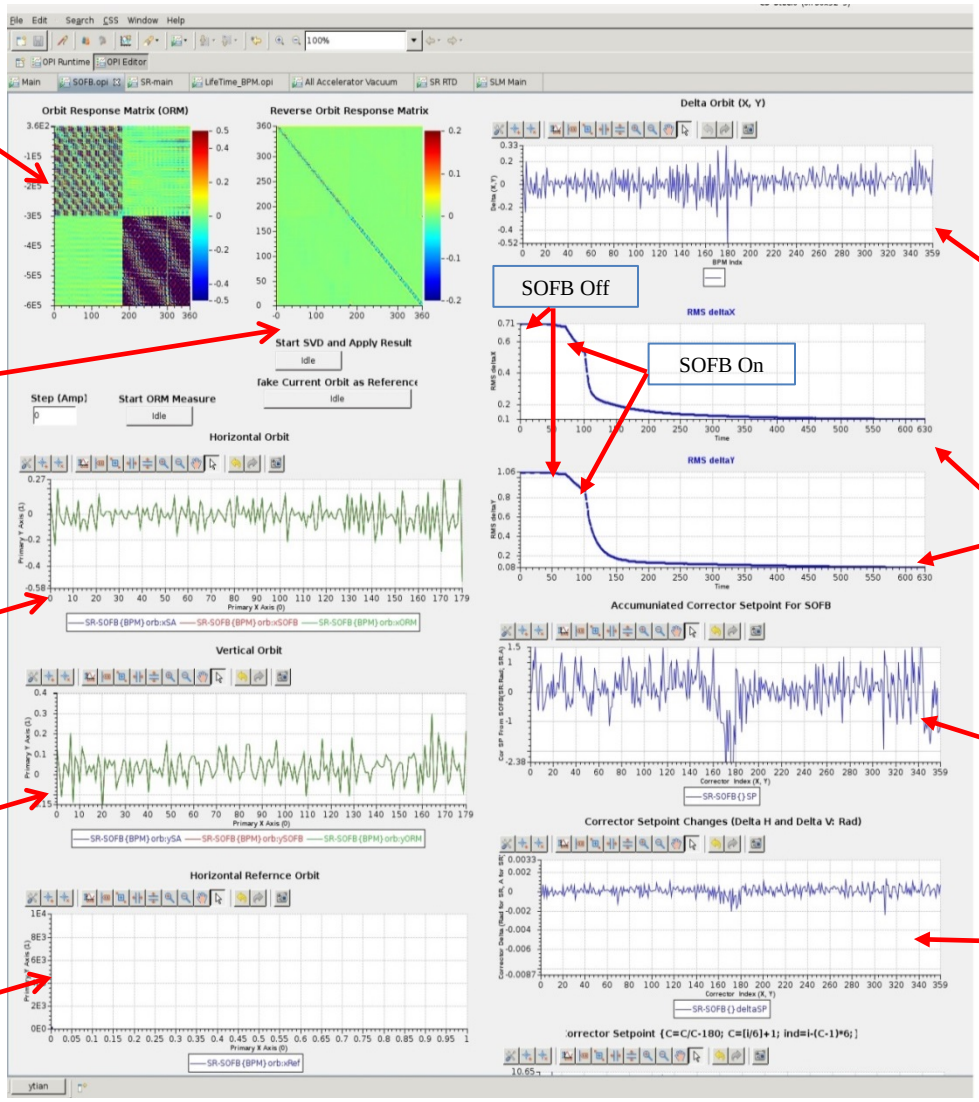

Response matrix (show very little coupling between H and V plane)

Inverse Response matrix

Horizontal Orbit

Vertical Orbit

Horizontal Referent Orbit

SOFB Off

SOFB On

Orbit difference between orbit

RMS values

Total accumulated correctors strength from SOFB

Correctors setpoint in each SOFB cycle

4.4 Tune/Chromaticity Measurement and Control

Different methods have been used to measure the betatron tune. It can be measured by BPM turn-by-turn data Fourier spectrum with fast kickers to excit betatron oscillation. Tune is available from betatron phase advanced method, again using pulse kicked TbT data from all BPMs. Tune can be measured from Bunch-by-bunch feedback system by watching the notch on the spectrum. NSLS II also have a dedicated sweeping tune measurement system to monitor the tune. In the follow section, we describe tune measurement methods and tune adjustment. Along with master oscillator frequency change, the chromaticity is measured and tuned.

4.4.1 Tune measurement system commissioning

A block diagram of sweep tune measurement system is shown in Figure 1. The system uses BPM button delta signal from Hybrid to detect the horizontal and vertical betatron oscillation. Synchrotron oscillation can be detected but the mixer LO phase needs to be adjusted differently to have optimized detection signal for synchrotron oscillation. Mixer IF output baseband signal is sent to network analyzer to measure the transfer function. Beam is excited by 15cm stripline with diagonal kicks. Two 75 W broadband amplifiers are used to feed the stripline.

Network analyzer can be controlled through EPICS CSS panel, sweeping time of the NA is programmable and it's typically takes seconds. This means the sweeping tune measurement system can be worked with stored beam only.

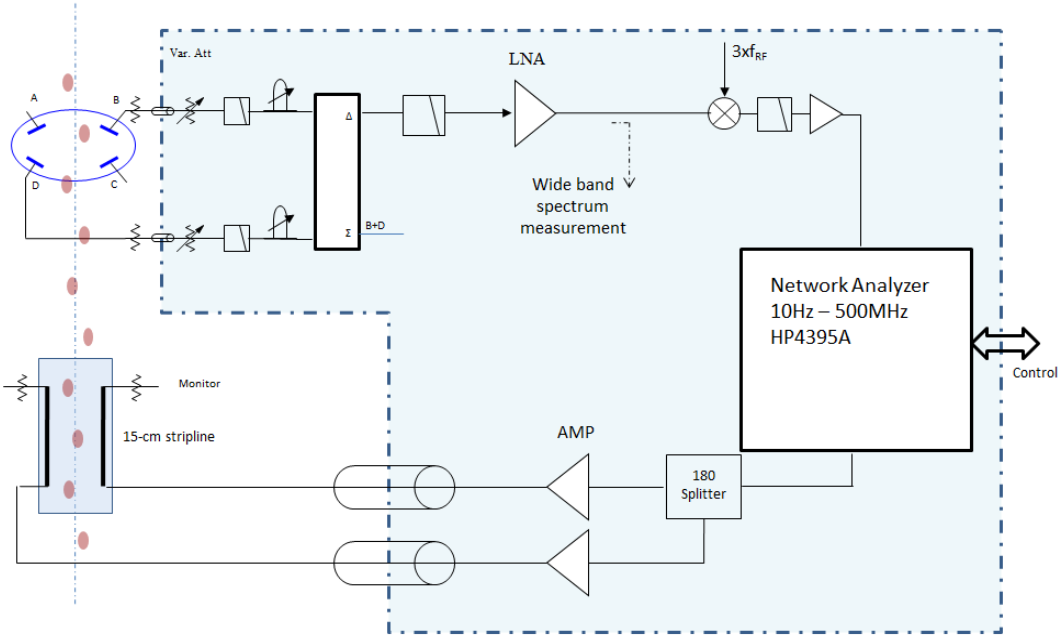

Figure 1, Sweep tune measurement system block diagram

Commissioning of tune measurement system was carried out parasitically. It was found that two jump cables inside the rack was not phase matched, as can be seen on Figure 2. In the screen capture, CH3 (blue) shows the BPM button A signal and CH4 (red) is button C from the same BPM. Two button signals arrived with time difference of more than 500ps. The jump cables were replaced with matched pairs.

Figure 2, raw button signals for TMS, notice the pulses are not arriving at the same time due to cable length difference.

At early stage of the commissioning, when the beam current is too low, we need to use stripline as pickup for the TMS. This gave a much clearer spectrum.

Once the cable timing was corrected, the Hybrid output was connected to mixer down-converter module. Mixer LO phase was adjusted to have optimized detection of betatron motion. There were 126 kHz noise peak observed on the tune spectrum, which might be picked up from environment.

A typical tune measurement spectrum is shown in Figure 3, the spectrum was captured on Apr-12-2014 around 9:30am. CSS panel sets the sweep frequency range for X/Y plane, the program automatically searches the resonant peak and reports fractional tune.

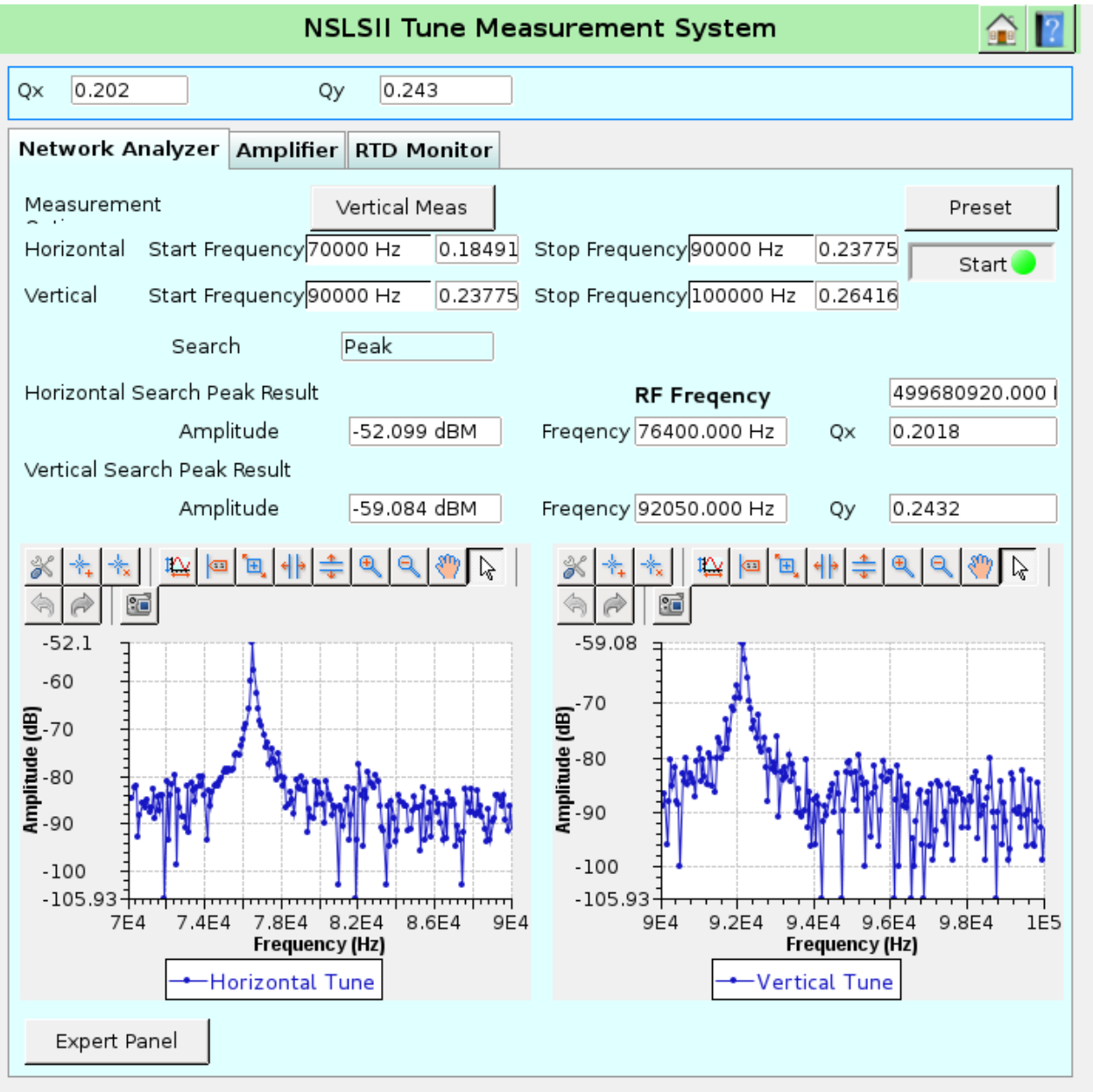

Figure 3: Tune measurement spectrum

4.4.2 Tune measurement with TBT data

To measure the tune from BPMs TBT data, it requires the beam to do betatron oscillation with reasonable strength. In SR, four fast kickers at injection straight are borrowed to excit beam horizontal betatron oscillation. The vertical betatron oscillation parasites to be there due to the coupling from horizontal and kickers tilt. With this method, the vertical plane tune spectrum always includes the horizontal tune.

The fast kicker excitation lasts two turns. After that, the beam betatron decays and damps down due to the synchrotron radiation. It requires that the BPMs timing is locked with fast kickers to catch the betatron oscillation. The tune measurement system from BPM TBT data has

been interfaced with CSS (**Main->SR-OP->Diagnostics->Tbt Tune Measurement)** for monitoring the horizontal and vertical tune. Figure 4 shows an example of the tune measurement from BPMs TBT data. Typically, one of injector kicker voltage is lowered by 0.1 kV to excit the betatron oscillations. The tune is calculated by averaging the FFT of 20 BPM TBT data with FFT length equal to 1024 turns.

A more accurate tune measurement system has been implemented in the CSS page **Main->SR-OP ->Diagnostics->Tbt Tune Measurement new**, where the average FFT (also calculated from 20 BPM TBT data) has length equal to 4096 and up to five peaks of the FFT can be scanned via a Discrete Fourier Transform for accurate tune determination.

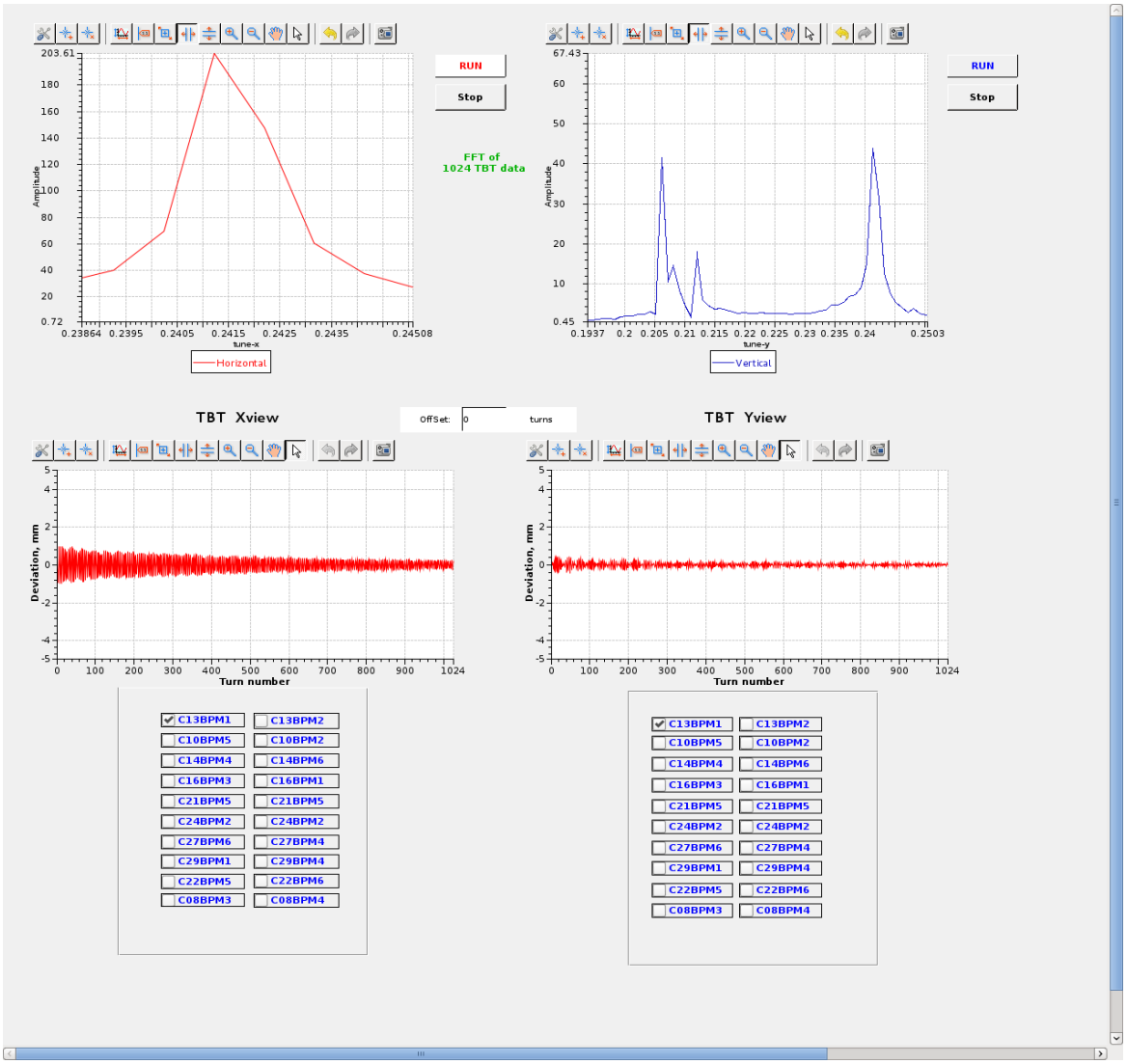

Figure 4: Tune measurement from BPMs TBT data

4.4.3 Tune correction

Tune correction is implemented by adjusting more than two families of quadrupoles symmetrically. The reason of using same family of quadrupoles instead of any individual quadrupole is to keep the optics symmetry. Only the quadrupoles in non-dispersive straights are chosen to adjust tune in order to assure the achromatic condition.

After choosing the quadrupole families, the tunes' responses to quadrupoles strengths/power supplies currents are calculated based on the lattice model, and written as a matrix format

$$M_{x/y,j} = \frac{\Delta\nu_{x/y}}{\Delta I_j},$$

where, $\Delta\nu_{x/y}$ is the tune shift due to the j^{th} quadrupole's power supplier current change ΔI_j. Thus the needed ΔI_j to adjust the amount of tune $\Delta\nu_{x/y}$ are obtained by solving a linear equations

$$\Delta\nu_{x/y} = M_{x/y,j}\Delta I_j.$$

In reality, the achieved tune adjustment is slightly different from theoretical expectation due to: (1) the lattice model is not precise at the early commissioning stage; (2) magnet hysteresis is not negligible. So multiple steps with a small step-size change are needed to shift the tune to the desired values. Overall, this method works very well in the commissioning stage.

4.4.4 Linear chromaticity measurement and control

Linear chromaticity is measured by changing RF frequency slightly (within ±1kHz) to measure the variation of tunes,

$$\xi = \frac{\Delta\nu}{\Delta E/E} = -\alpha_c \frac{\Delta\nu}{\Delta f/f}$$

Beam energy variation with RF frequency change is characterized by the momentum compactor α_c. Thus far, the momentum compactor is not measured yet; its theoretical value from the lattice model has been adopted in this measurement. A typical measurement result is illustrated in Fig. X.

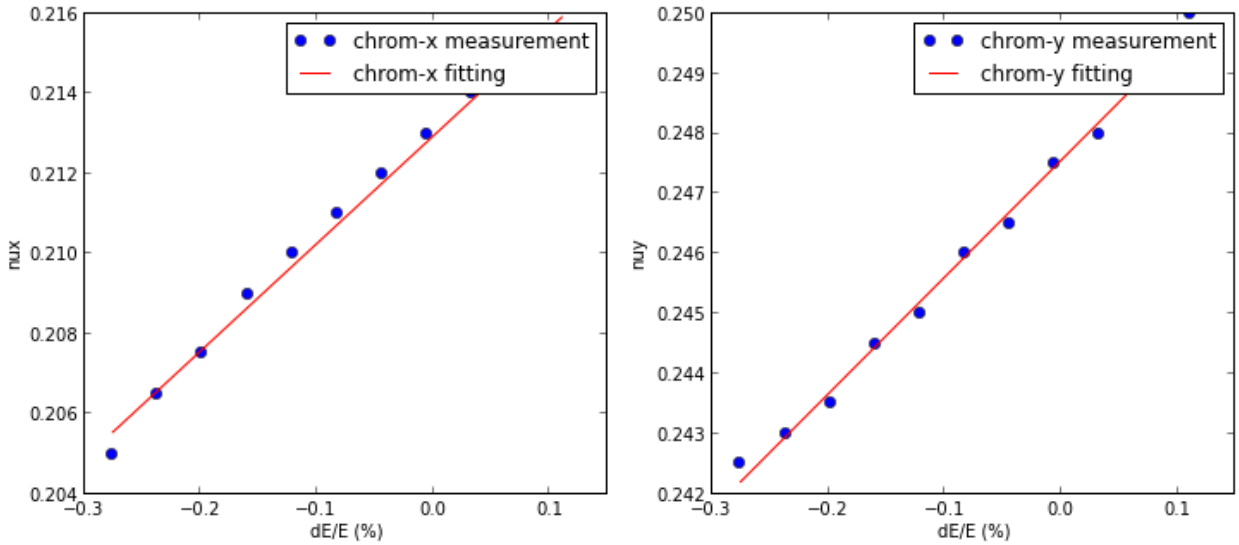

Fig. 5. linear chromaticity measurement result ($\xi_{x/y} = 2.68,1.94$)

Unlike quadrupoles powered independently, the storage ring sextupoles are powered in series. All sextupoles have slightly different transfer functions from power supplies to the field properties. Thus a response matrix between chromaticity and sextupole power suppliers current is calculated at the EPICS PV level. Then chromaticity adjustment is implemented in the same way as tune adjustment to solve the linear equations. Experimentally the chromaticities in both planes have been adjusted within the range 0- 5 units to carry out collective studies.

4.5 Coupling Assessment and Correction

The designed tune of NSLS-II storage ring (SR) is quite close to the difference resonance line $\nu_x - \nu_y = 17$. Linear coupling was observed in the SR from several aspects: (1) the measured orbit response matrix (ORM) has non-zero elements in the off-diagonal blocks; (2) a relative large residual oscillation in the vertical plane was observed while the beam was excited by horizontal injection kickers, which actually was used for tune measurement without vertical excitation. (3) In the meantime, 10-15mm peak-to-peak vertical dispersion was measured around the ring.

The linear coupling comes from the misalignment (rolling) of quadrupoles and the vertical orbit displacement through sextupoles. After beam-base alignment (BBA) was successfully implemented for 180 quadrupole neighboring to BPMs, the achieved standard deviations of closed orbit distortions relative to quadrupole centers are less than 0.1mm. In this case the sextupole contribution to the linear coupling reduces significantly. The rolling of quadrupoles in dispersive region is the main source to create the vertical dispersion.

The common method to assess the linear coupling is to measure the minimum tune separation between two coupling modes. Experimentally, the minimum tune separation is measured by tuning quadrupoles to bring horizontal and vertical tunes as close as possible. The minimum distance of two modes is characterized as the coupling coefficient $\left|G_{1,-1,l=17}\right|$ [1]. Several alternatives are also available to assess the coupling; such as (1) the non-zero off-diagonal elements in the ORM can be used to fit by LOCO algorithm to identify coupling source and the needed corrector strength, or (2) the one-turn matrix can be directly fitted from turn-by-turn data of beam position monitors after a kick is applied.

Several correction algorithms have been tested in the SR to reduce the linear coupling. Their principles and correction results are summarized respectively.

4.5.1 Minimizing non-zero coupling elements in ORM

The coupling elements in the ORM is defined as

$$R_{xy,ij} = \frac{\Delta x_i}{\Delta I_{y,j}} \text{ and } R_{yx,ij} = \frac{\Delta y_i}{\Delta I_{x,j}}$$

where $\Delta x(y)_i$ is the orbit offset observed by the i^{th} BPM, which is created by the current change $\Delta I_{y(x),j}$ of the j^{th} corrector in another plane. If all such elements can be minimized by a set of skew quadrupoles, the two coupling modes are decoupled to some extent. In order to minimize those elements, their responses to all 30 skew quadrupoles are measured and written into a matrix

$$M_{xy,ijk} = \frac{\Delta R_{xy,ij}}{\Delta \mathrm{I}_k}.$$

The ORM without skew quadrupole correction is measured first and used as the object function for correction.

By solving the linear equations

$$R_{xy,ij} = M_{xy,ijk} \mathrm{I}_k,$$

a set of skew quadrupole currents are obtained and applied to minimize these non-zero matrix elements. Usually several iterations are needed to let the solution to converge since the system is not a linear system.

Experimental result

The non-zero off-diagonal blocks of the ORM has been measured (as illustrated in Fig. 1) and used the object function for correction. Since there are numerous elements there, only 3 columns of elements' response matrix (RM) to all 30 skew quadrupoles are measured. For each column, the RM dimension is 360×30, which include both R_{xy} and R_{yx} response to all 30 skew quadrupoles.

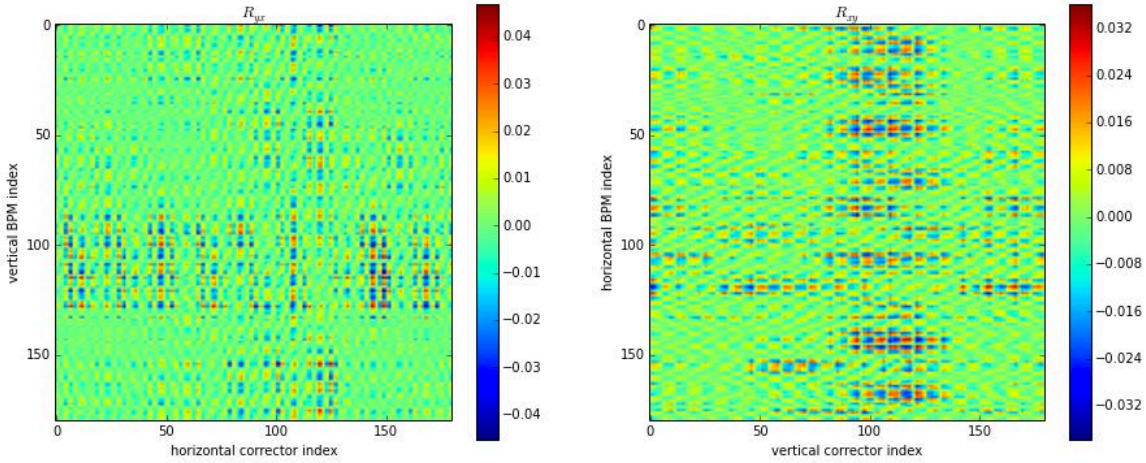

Fig. 1. Two off-diagonal blocks of ORM

By varying three families of quadrupoles in the low-beta function section, the tune separations before and after correction are measured and shown in Fig. 2. The minimum tune separation reduced from ~0.008 unit to ~0.002 unit, which indicates coupling coefficient $\left|G_{1,-1,l=17}\right|$ decreased by a factor of 4.

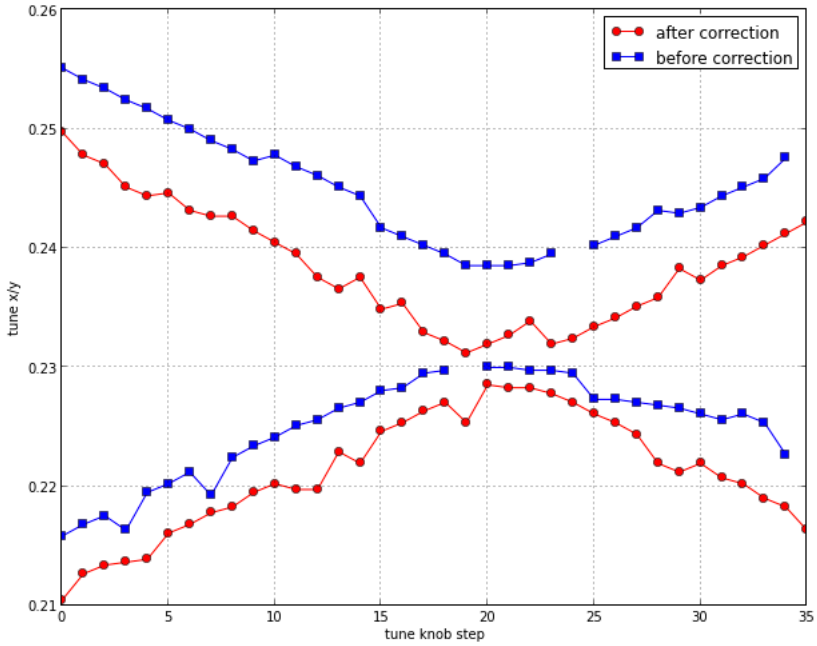

Fig. 2. Tune separation measured before and after correcting linear coupling

In the meantime, after beam is excited with the same amount of kick strength from one of the IS kickers, the vertical residual oscillation amplitudes before and after correction are found to decrease from 1.1mm (peak-to-peak) to 0.2mm (Fig. 3). Actually this is our second method to correct coupling (see algorithm 2 below).

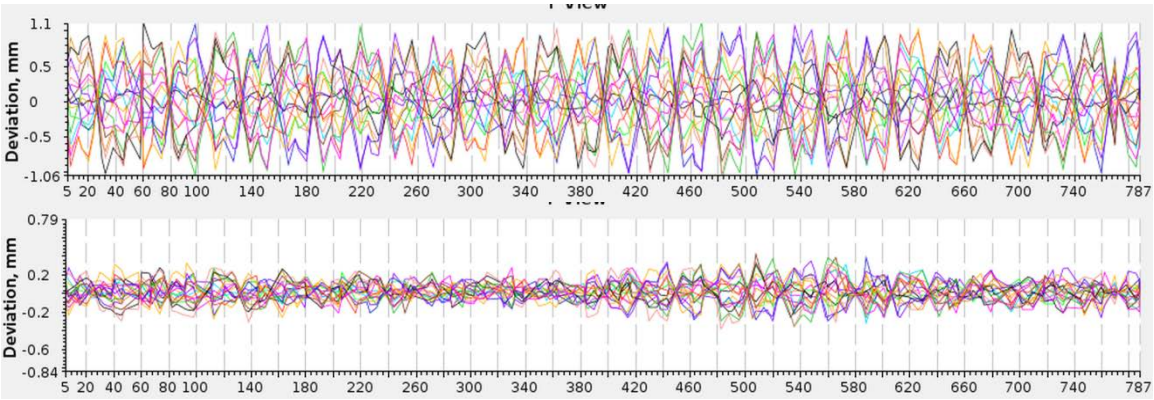

Fig. 3. Residual vertical oscillations after beam are excited by a same kick before (upper) and after (lower) correction.

It is worth to mention here that after coupling correction, beam lifetime decreased from 9.03hrs to 5.38hrs with the beam current 4.15mA (20 bunches), which indicates vertical beam size must reduce significantly after coupling correction.

4.5.2 Minimizing the vertical residual oscillation with the excited beam in horizontal plane

If beam is excited by one injection kicker (horizontal plane only, with negligible vertical component), with initial offset $\vec{x}_0 = [0, \Delta x', 0, 0]^T$ at the location of the kicker, and it will do the betatron oscillation in the following turns. Ignoring the radiation damping, the subsequent BPM readings for next several turns are written as

$$\vec{x}_n = R^n \vec{x}_0,$$

where n is the turn index and R is the storage ring's one-turn transport matrix. $\vec{x}_n = [x, x', y, y']^T$ includes BPMs reading in horizontal and vertical plane. We measure the dependence of the vertical residual oscillation on the skew quadrupoles currents, and write it as a matrix

$$M_{n,ij} = \frac{\Delta y_{i,n}}{\Delta \mathrm{I}_j},$$

where $\Delta \mathrm{I}_j$ is the current change of the j^{th} skew quadrupole, $\Delta y_{i,n}$ is the i^{th} BPM's n^{th} $(n \geq 1)$ turn y readings.

Thus the needed skew quadrupoles strengths for coupling correction can be obtained by solving the following linear equations

$$y_{i,n} = M_{n,ij} \mathrm{I}_j.$$

Since the fractional part of vertical tune is 0.26, at least 4 turns turn-by-turn data are needed to cover a full betatron oscillation. For the same reason as the previous algorithm, several iterations are necessary for the solution to converge.

Experimental result

One IS kicker kicks the beam in horizontal plane at 1/3 Hz to excite the same horizontal betatron oscillation, which couples to vertical plane from coupling. The vertical plane residual oscillation from turn 4 to turn 15 turns were measured and used as the correction object. 12 turns' BPMs response matrix to all skew quads is measured with the dimension $(12 \times 180) \times 30$.

The horizontal oscillation peak is ~4mm with one kicker excitation (Fig.4). The vertical residual oscillation amplitudes before correction and after correction are shown in Fig.5, with the peak suppressed from ~ 1.8 mm to 0.25 mm. Fig. 6 shows the skew quads current for the coupling correction. The peak value is less than 1.5 A.

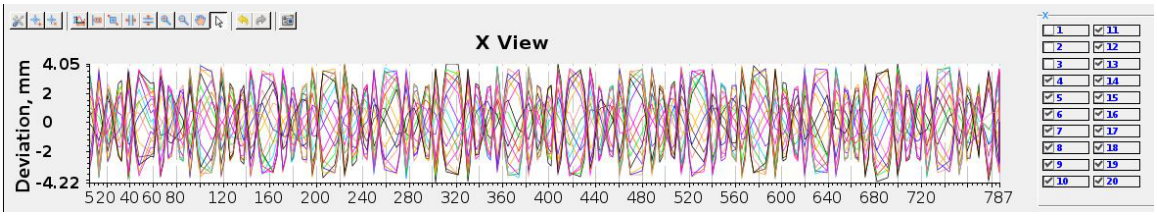

Fig. 4. Horizontal betatron oscillations with one kicker excited

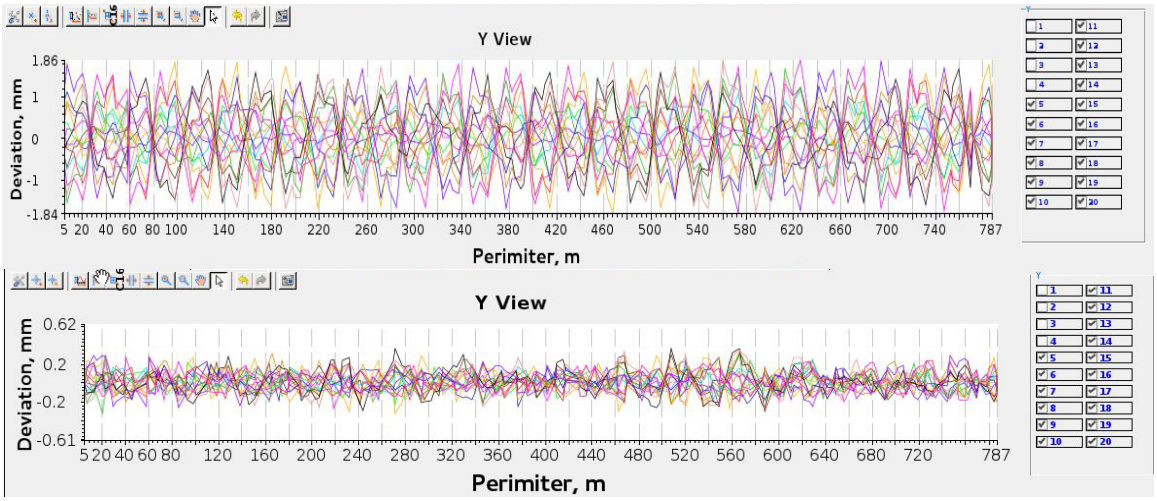

Fig. 5. Residual vertical oscillations before (upper) and after (lower) correction with the same kick strength

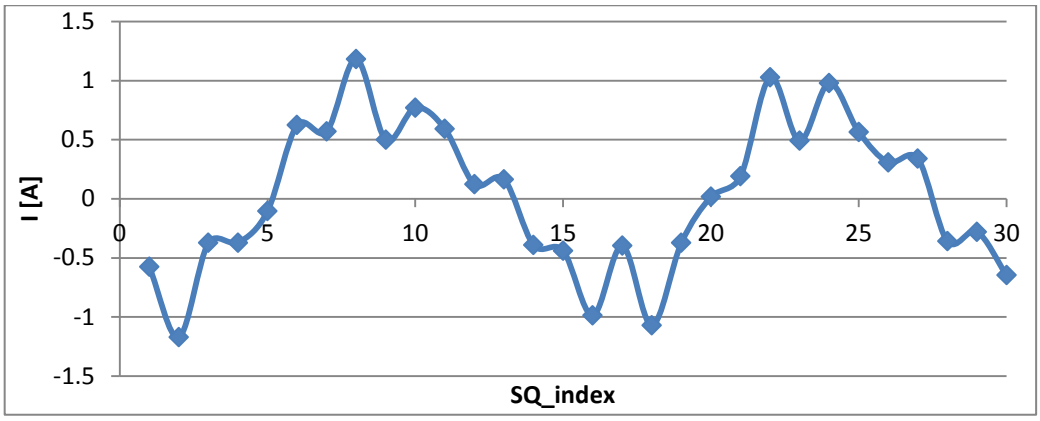

Fig. 6. Skew Quads current to correct coupling

Meanwhile, the tune separation curve is also measured to check the coupling correction by varying three quads families in the low-beta function section, the same method as used in algorithm 1. The tune separations before and after correction are measured and shown in Fig. 7. The minimum tune separation reduced from ~0.011 unit to ~0.0015 unit, which indicates coupling coefficient $\left|G_{1,-1,l=17}\right|$ decreased by a factor of 7.5, similar to the TBT vertical plane amplitude suppression ratio.

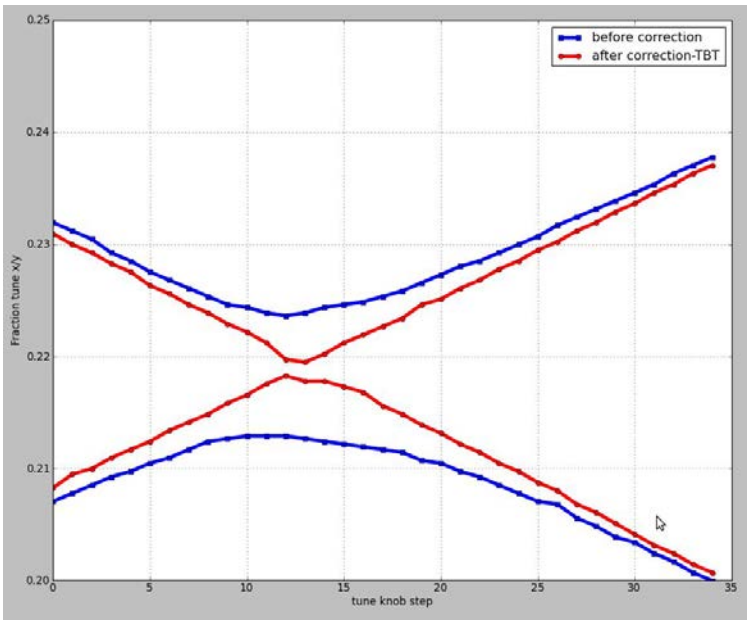

Fig. 7. Tune separation measured before and after correcting linear coupling

The lifetime at 4.2 mA (20 bunches) changes from 9.4 hrs to 7 hrs after coupling correction. The dispersion is measured in Fig. 8.

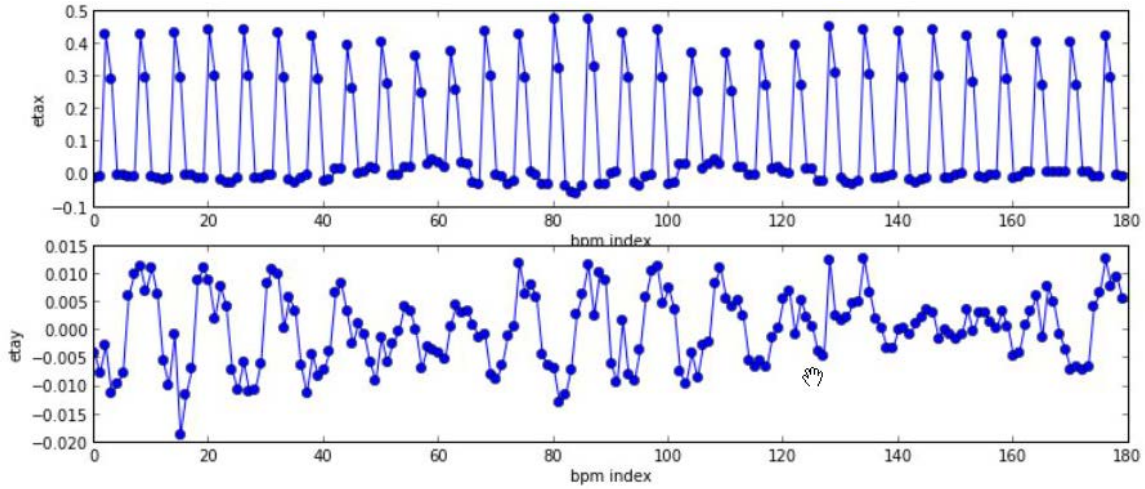

Fig. 8 Dispersion measurement after coupling correction

TBT data is one way, but more obvious and faster to check the coupling, comparing with the tune separation curve measurement. With the kicker excitation itself, the dispersion coupling cannot be reflected. To include this effect, the RF frequency will be changed in the future coupling correction.

References

[1] S. Y. Lee, Accelerator Physics, 3rd Ed. World Scientific, 2012

4.6 Local bumps as a commissioning and diagnostics tool

Local bump was found to be a very useful and powerful tool during the early commissioning of NSLS-II storage ring. Before the stored beam was obtained, the theoretical orbit response matrix (ORM) was used to form a local bump at the injection section for on-axis injection. After the beam was stored, the ORM was measured and compared against the theoretical prediction. Both the theoretical ORM and measurements are very effective to correct the orbit and form local bumps.

4.6.1 Local bump for on–axis injection

When beam was injected into the SR for the first time, the RF system and sextupoles power supplies were switched off. In this case on-axis injection is preferred. Since the injected beam is designed as 24.5 mm away from the SR closed reference orbit (4 mm away from the septum knife) , and the AC bump formed by four injection kickers is 15 mm high, a 9.5 mm high local bump in the horizontal plane is needed. To avoid the heavy beam loss at the septum knife and relief the strict requirement on the injection beam, an 11 mm local bump was set during the initial commissioning. A two-cell wide symmetrical local bump (as illustrated in Fig. 1) is formed using the theoretical ORM.

After RF system was turned on and sextupoles were powered, the injected beam could be captured by the RF buckets and stored. The local bump calculated by the linear ORM can create a relative large residual orbit distortion outside the bump because of the sextupoles' contribution. The residual orbit around the whole ring can introduce a very large optics distortion. Therefore another closed local bump, which includes the sextupoles' contribution, was calculated and applied to the SR to mitigate optics distortion and allow the ring to get efficient injection.

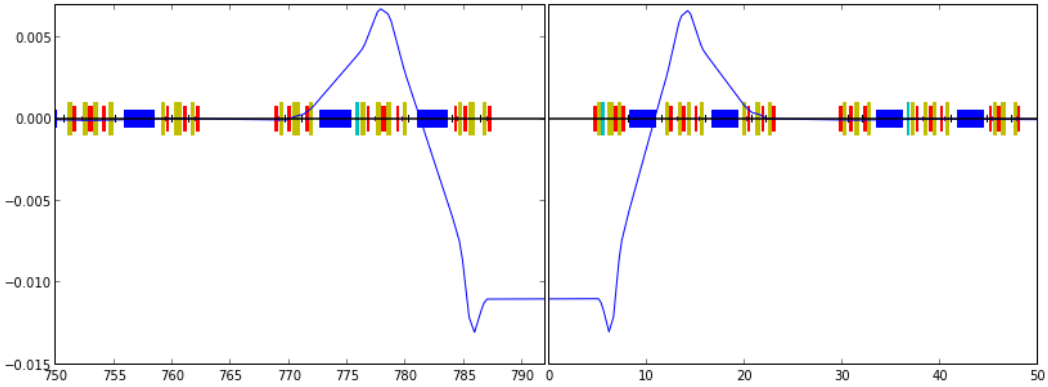

Fig. 1. Local bump for on-axis injection at the injection section

4.6.2 Local bump for physical aperture assessment

During the on-axis injection commissioning, a significant beam loss was found at cell 10 through BPM sum signals. After the beam was stored (after the RF system was turned on), the

beam had to follow an ugly closed orbit to survive. Any attempt to improve the closed orbit distortion killed the beam immediately. Therefore we suspected that some physical aperture inside the vacuum chamber was scratching the beam. A local bump was created in this suspicious region to detect where the physical aperture was.

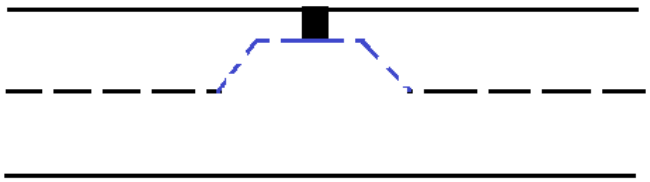

Fig. 2. Local bump to assess physical aperture

By increasing the bump height step by step, the beam orbit gets close to the physical aperture gradually, and a short beam lifetime is expected. Eventually the physical aperture kills beam. The left plot of Fig. 3 shows the experimental result of the beam lifetime versus the local bump height at cell 10. Based on this measurement, we claimed that a physical aperture was located in this area. Actually a hanging RF spring (the right picture in Fig. 3) was found there after the vacuum chamber was opened.

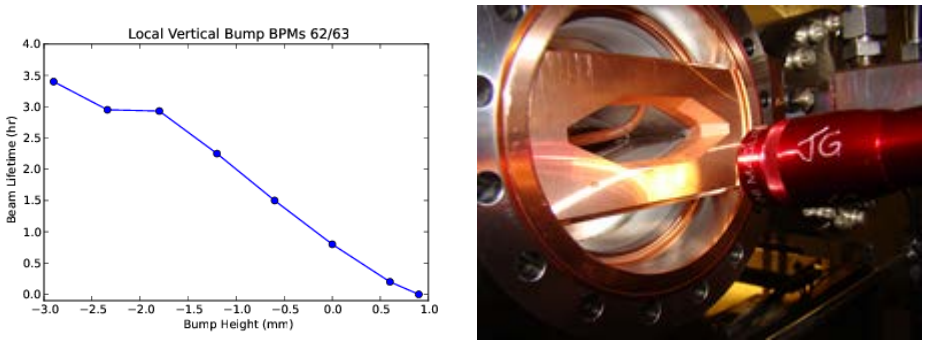

Fig. 3. Beam lifetime's variation with the height of a local bump (left) at cell 10 where a hanging spring (right) was found.

After a hanging spring was found at cell 10, we doubted if there were any other springs hanging somewhere, which wouldn't block the beam in the proximity of the central trajectory, but would induce some local impedance and eventually degrade the ring performance. A moving bump (BPM-by-BPM) was created to scan over the full ring to assess the physical aperture as illustrated in Fig. 4.

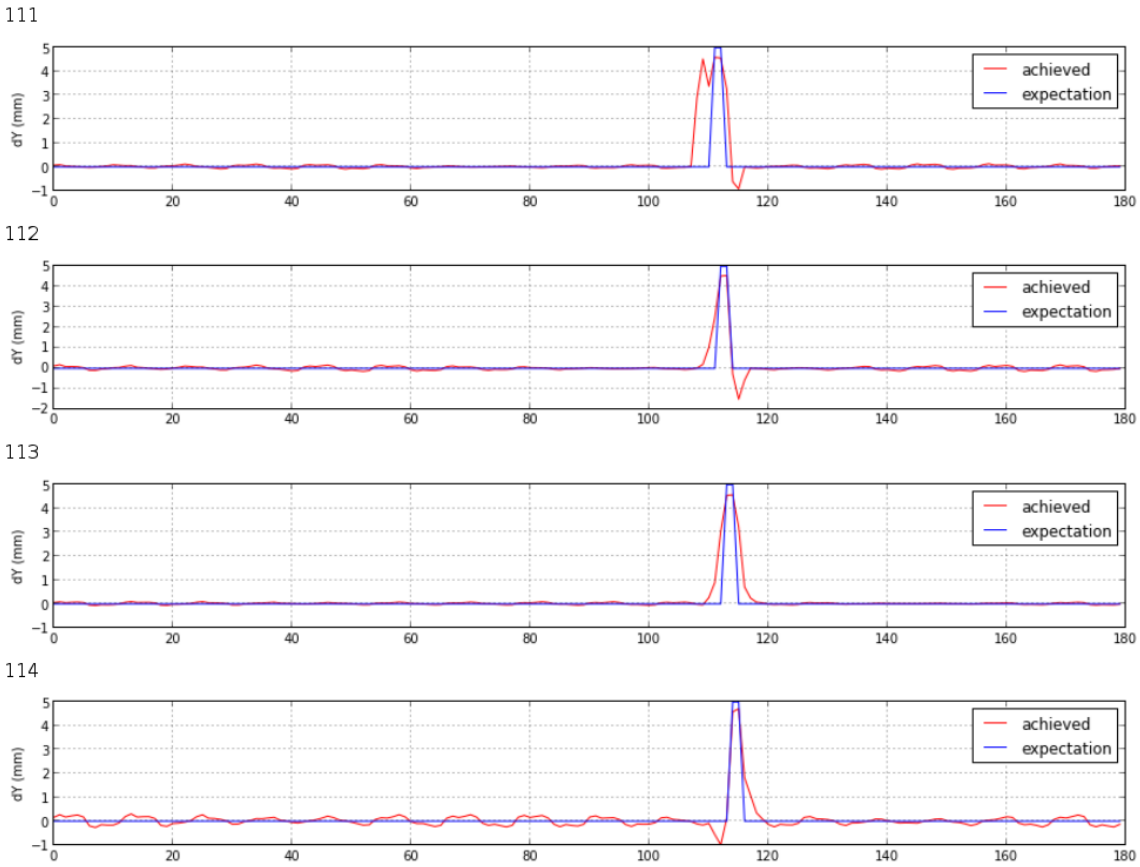

Fig. 3. A moving bump for assessing the physical aperture efficiently

Another suspicious location at the Cell 8's arc was found by the moving bump method. During the shutdown, another hanging spring (see Fig. 4) was confirmed after the vacuum chamber was opened. It has been burned through and melted by the radiation from its upstream dipole.

Thus far, the moving bump has a fixed height all around the ring. A moving bumping scheme, in which the bump height is proportional to the square root beta-function, is being considered for next stage commissioning.

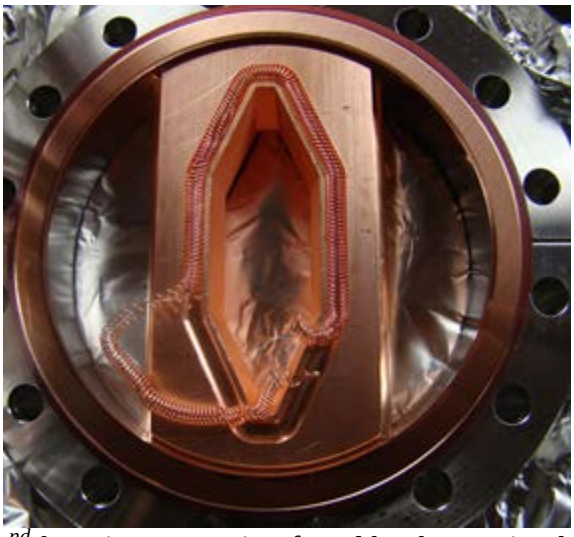

Fig. 4. The 2nd hanging RF spring found by the moving bump method

4.6.3 Local Bump for vertical impedance measurements

First of all we wanted to cross-check how sensitive is the method for local impedance measurements described by V. Kiselev and V. Smaluk in ref. [1] and to improve the applied local bump script, if necessary, for future measurements, when more complex geometries, such as In-Vacuum Undulators (IVU) and Elliptically Polarizing Undulators (EPU) will be installed into the NSLS-II storage ring.

Two Long Straight Sections, Cell 8 and Cell 18, with damping wiggler chambers (fixed gap) have been analyzed in a single bunch mode. The profile of the chamber is changed longitudinally from the octagonal shape (76mm x 25mm) to elliptical shape with 60mm full horizontal and 11.5mm vertical apertures. The collimator type structure with NEG Coating produces reasonable impedance for its measurements and for its further comparison with analytically and numerically calculated data.

Based on the method, we measured four orbit trajectories at low and at high single bunch currents, without and with the local bumps in DW08 straight section (Fig. 5) and in DW18 straight section (Fig. 6) using the prepared script.

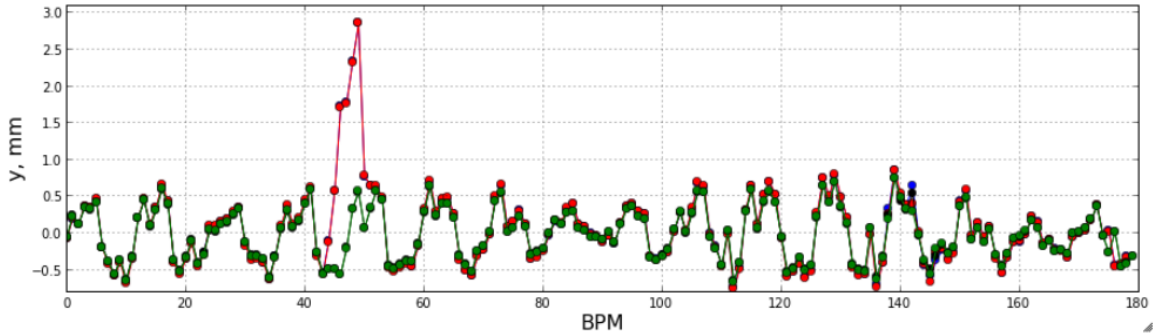

Fig. 5: Four orbit trajectories measured at low and at high single bunch currents without and with a 2mm vertical local bump in the DW8 straight section.

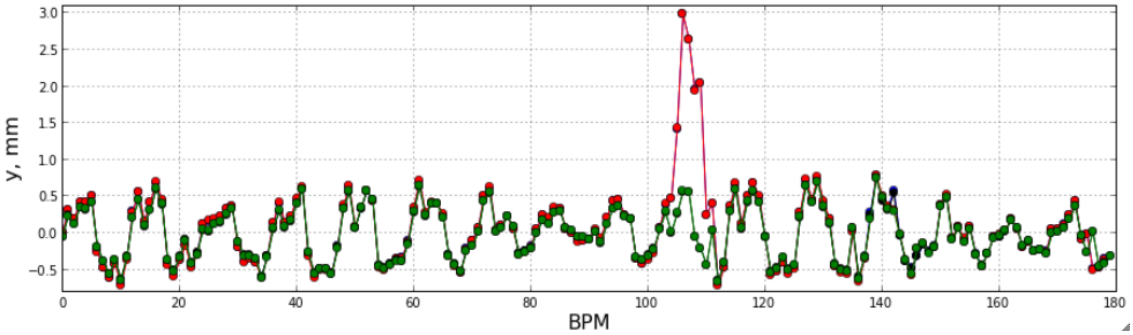

Fig. 6: Four orbit trajectories measured at low and at high single bunch currents without and with a 2mm vertical local bump in the DW18 straight section.

The single bunch currents, 0.15mA and 0.75mA, have been accumulated and four beam trajectories have been measured. The area of interest is the straight section. However the local bump has been spread out into the arc of the storage ring either and it can be seen from BPM P103 and up to BPM P110 of Fig. 6 as an example. The measured local vertical kick factor is $k_y = 235\,V/pC/m$. In the next section we will compare the measured data with the numerically obtained results.

During the next start up we do plan to improve the code and measure the local impedance in different straight sections as well as in the arcs of the storage ring separately. With the modified code we will repeat the vertical local impedance measurements in the same straight sections to be sure the results are the same.

4.6.4 Local for beam diagnostic system calibration

a. Calibration for Synchrotron Light Monitor (SLM) CCD camera

The SLM diagnostic beamline source point is located at the 2nd bend of Cell 30. The CCD camera calibration factor can be calculated from the optics setup, and it can also be calibrated by creating a local bump near the source point. Fig. 7 shows the SLM calibration results with the local bump method. Fitting the slope gives the calibration factor ~ 8um/pixel.

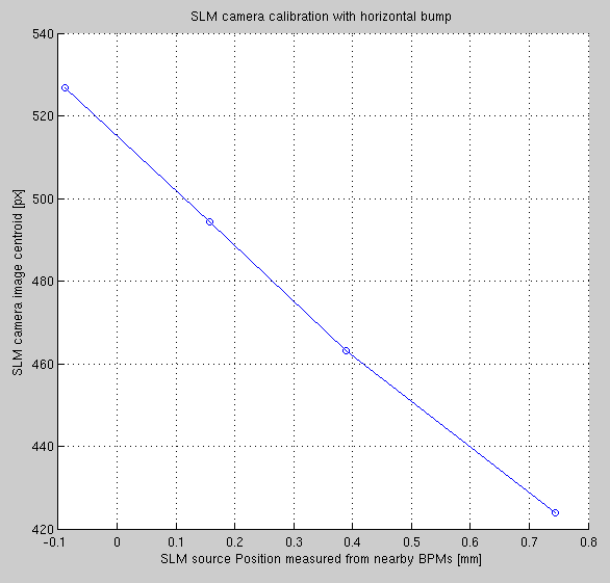

Fig. 7. Calibration the SLM CCD camera with a local bump

b. Calibration of bunch-by-bunch feedback digitizer

Similar to the SLM CCD camera calibration, a parallel local bump was created in between Cell 15 BPM1 and BPM2, where the bunch-by-bunch feedback pickups are located. Moving the local bump height and measuring the digitizer ADC counts, it's possible to calibrate the bunch-by-bunch electronics readings.

Reference

[1] . V. Kiselev and V. Smaluk, “Measurement of local impedance by an orbit bump method”, NIMA 525, (2004), 433-438.

4.7 Injection study

4.7.1 Introduction

By the end of the NSLS-II storage ring (SR) phase I commissioning, routine injection efficiency is better than 90 %. The beam was injected with the designed off-axis injection scheme with accumulated beam up to 25 mA, which is limited by the commissioning goal.

Below we describe the history and results of injection studies, as well as the status of various SR subsystems related to injection.

4.7.2 On-axis injection

Description of on-axis injection

In accordance to the commissioning plan [1-3] the first injection in the SR was performed on axis. The SR PSs were set to the design values. All SR sextupoles were set to zero current for the first turn commissioning. To limit the radiation loss, the beam charge during initial commissioning was kept below 1 nC and injection rate was 1/3 Hz.

The setup of the SR injection straight (IS) section is schematically shown in Fig. 1, including four kickers, producing a closed bump for stored beam, a DC septum and a pulsed septum for beam injection. AC septum and fast injection kickers are used for injection. The injection enabled by 5.2 us (2 SR turns) half-sine, 7.5 mrad kicker pulses. The injected beam and stored beam relative position at the exit of septum is shown in figure 1a. After AC septum, the injected beam is -24.5 mm from the SR closed reference orbit and parallel to the central axis. The four injection kickers (two upstream and two downstream of the AC septum) create the closed bump, which is designed to bump the beam 15 mm towards and parallel to the injected beam. At the end of injection straight, the two fast kickers bring the injected beam to -9.5 mm off and parallel to the SR closed reference orbit. So the injected beam will have natural betatron oscillation due to off-axis injection.

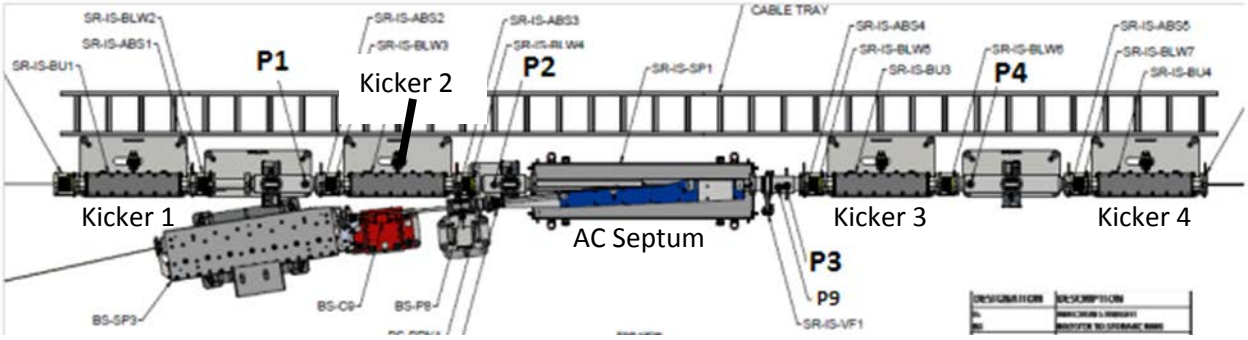

Figure 1: Top view of the SR injection straight section.

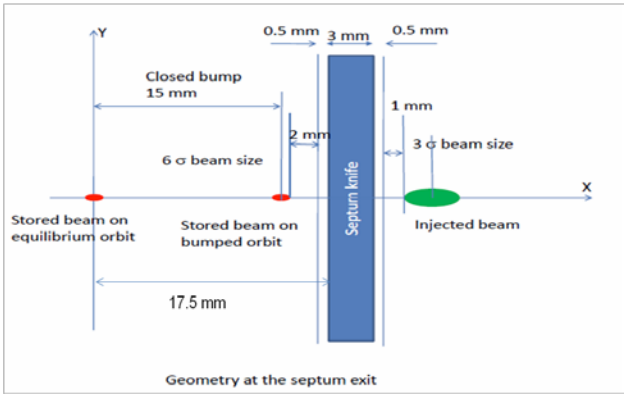

Figure 1a: Injected beam and stored beam relative position at the exit of septum.

During the initial commissioning, -11 mm horizontal local DC bump was applied with the up and down stream cell correctors. This is helpful to minimize the injected beam betatron oscillation and avoid the heavy beam loss at the septum knife to ease the beam strict position tolerance requirement at AC septum. An example of design symmetric DC bump is shown in Fig. 3.

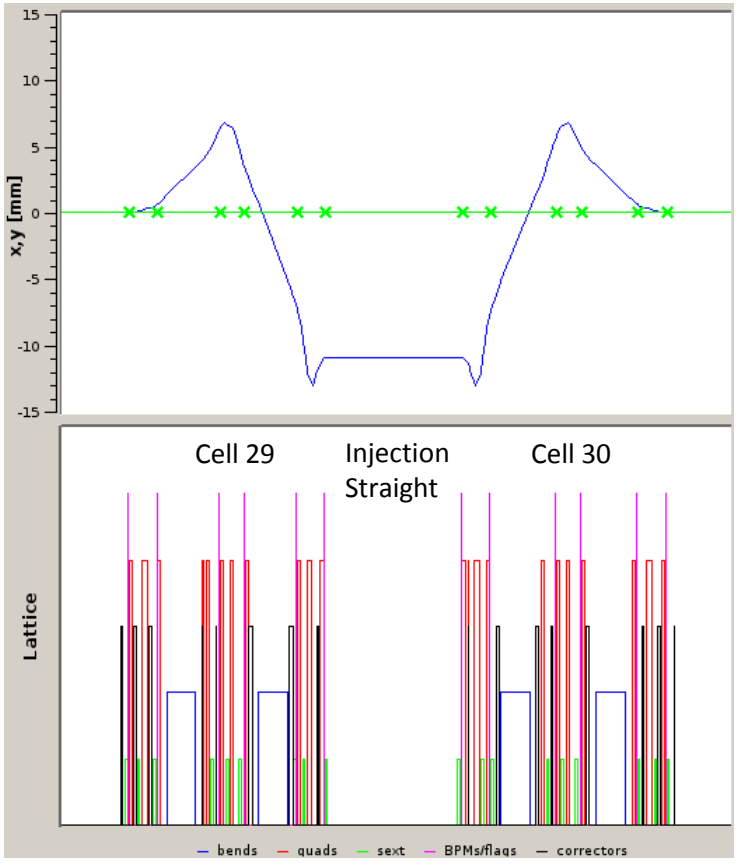

Figure 3: DC bump in injection straight section.

A dedicated first turn analysis software tool (FTA) [4] was created to commission initial injection into SR and to obtain spiraling beam. The FTA provides a convenient graphic user interface, which combines the results of interactive beam trajectory simulations with the BPM measurements. There are several additional FTA modules. One of the additional modules allows

measuring the initial coordinates of the beam from least square root fitting of the readings of BPMs of user's choice. Another useful FTA module provides flexible local correction of beam trajectory as well as creation of various user defined local bumps.

Obtaining first few turns

After commissioning the Booster to SR transfer line (BTS), the beam was successfully transferred through the SR AC septum. However, with the design SR lattice, nominal settings of kickers 3 and 4 and pre-calculated DC bump, the beam was observed only on the first few BPMs in the SR.

After kickers 3 & 4 were adjusted to 7.9 kV and 3.4 kV respectively from nominal 8.4 kV setting, the one complete turn was observed in the ring with significant beam loss and huge horizontal betatron oscillations [5].

As the next step, we used the FTA trajectory correction module to bring injected beam to nominal central trajectory at the end of Cell 1. Then we went through the ring cell by cell utilizing FTA to correct horizontal beam trajectory to few millimeters. Fig. 3 shows intermediate result of this process when horizontal trajectory was corrected down to Cell 4.

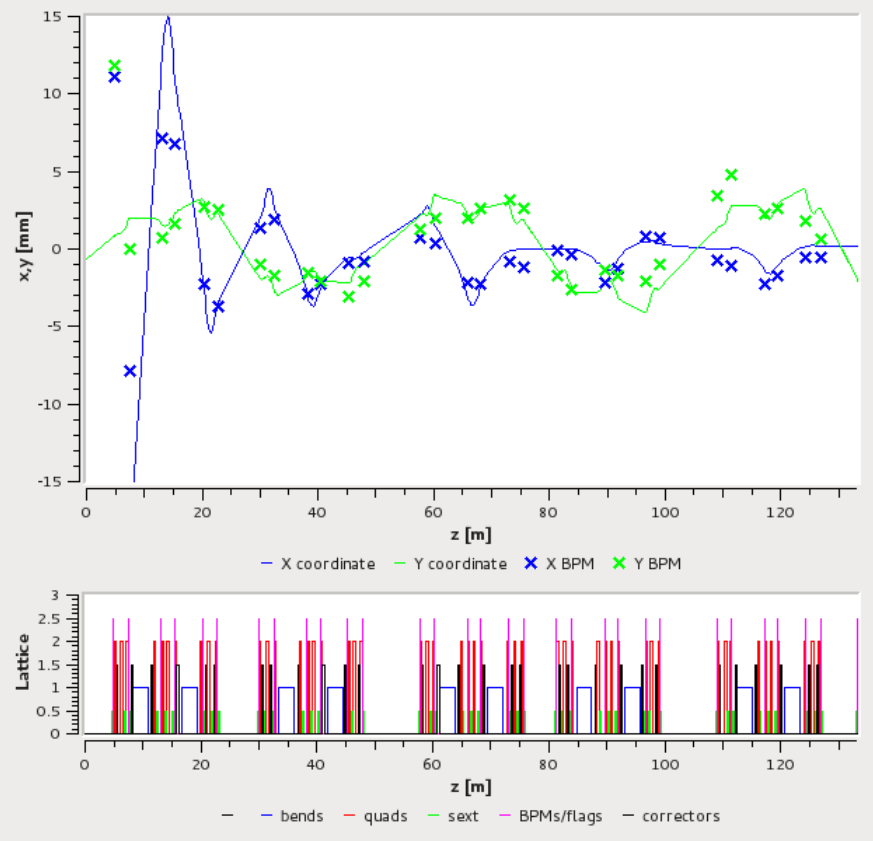

Figure 3: Snapshot of the FTA interactive plot showing live BPM readings and simulated trajectory of injected beam on the first turn down to Cell 4.

The plot corresponds to first iteration of correcting first turn horizontal trajectory.

After two iterations of correcting both horizontal and vertical trajectories we managed to align the first turn trajectory in the SR to +-2 mm horizontally and +-1 mm vertically [6]. While correcting vertical trajectory was trivial, horizontal trajectory could not be corrected to values better than a few mm because of shot to shot oscillations of the beam in X-plane. After trajectory corrections we obtained two turns in the ring.

Although first turn was well corrected we observed large betatron oscillations on the 2nd turn, even though we brought the injected trajectory to 0 angle/displacement in cells 30-01 and implemented the first half of design DC bump in cell 29. This indicated that the beam exited injection straight section with trajectory far from design X=-10 mm, X'=0 mrad.

To reduce the betatron oscillations on the second turn we had to adjust correctors in cell 29 by a lot, completely destroying the designed DC bump. Nonetheless, these new settings gave us clearly visible 3rd turn in the ring [6].

All described observations suggested that there was a problem with injection into SR ring. Therefore, we performed dedicated studies of SR injection.

SR injection studies

We used a dedicated FTA module to measure beam coordinates at the exit of the IS and studied the effects of various settings of kickers 3 and 4 on beam trajectory [7].

First we turned both kickers 3 and 4 off and we still could see the beam on first 4 BPMs in cell 30. Although the readings were not very reliable, we found the beam displacement at IS exit to be ~ -20 mm, and X' ~ 2.5 mrad.

Next, with kicker 3 (and only kicker 3) on and at 4 kV we obtained three complete turns in the ring. The measurement of injected beam coordinates out of the IS shown X=-22.8 mm, X'=0 mrad. This told us that kicker 3 had a negative kick, while by design it had to be positive (kicking beam outside of the ring). We also checked that increasing kicker 3 voltage decreased the trajectory angle and decreasing the voltage increased the angle.

Finally, with kicker 3 on, we turned on kicker 4; we saw that increasing kicker 4 consistently increased the beam trajectory angle, which indicated that kicker 4 had positive angle, again opposite of the design.

Thus, we concluded that the kickers 3 and 4 had wrong polarity. Indeed, changing polarity of injection kickers resolved our problems and allowed us to obtain spiraling beam.

Obtaining spiraling beam

After kickers' polarity was corrected, both kickers 3 and 4 were set to 7.8 kV. We measured that the injected beam had X = -8mm, X' = 1 mrad coordinates at the IS exit, which was rather close to design injection values. Following the algorithm described above, we corrected the first turn trajectory and closed the orbit on the first turn (by creating the proper DC bump). This

dramatically decreased the betatron oscillation on following turns, and allowed us to obtain (with some minor tuning of the DC bump) about 30 turns in the SR [8]. It turns out that even when all the correctors are set to 0 A, beam can still go through many turns.

After beam survives up to 200 turns, the sextupoles were turned on, then the RF system. Finally, as Fig 4 demonstrates, the beam was stored 10k+ turns in the SR [9] (from BPMs TBT sum signal). In fact, the beam was stored with ~3 hr lifetime (from BPMs 1 Hz data). During the process, injection beam launching position and angle, SR close orbit and tune were tuned.

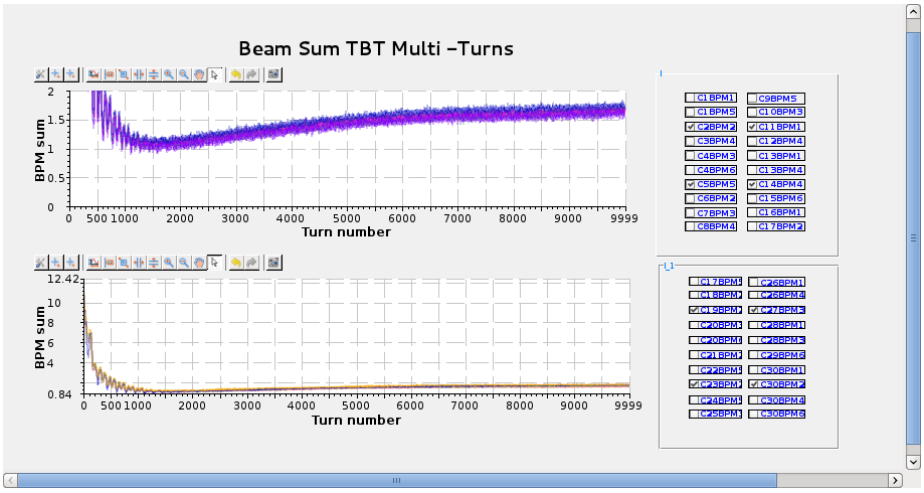

Figure 4: First spiraling beam in the SR.

Reducing betatron oscillations

The betatron oscillation were clearly seen from BPMs TBT data.It was also observed that the capture efficiency could not be further improved by matching the injection angle and position, since the injection angle and position control is limited by the BTS corrector strength and the aperture limit in AC septum.

A method for matching the first and second turn trajectory with two correctors in the last cell before injection was proposed. Two correctors phase advance of ~ 90 degree was chosen for efficient control. By varying each corrector, we measured second turn trajectory change of 180 BPMs and get the response matrix (180*2). Since the method depends on 180 BPMs reading, it is less sensitive to individual BPM accuracy. Figure 5 shows the residual betatron oscillation after several steps iteration. This is proved to be a very quick way to establish the injection beam to the closed orbit and get the beam capture efficiently.

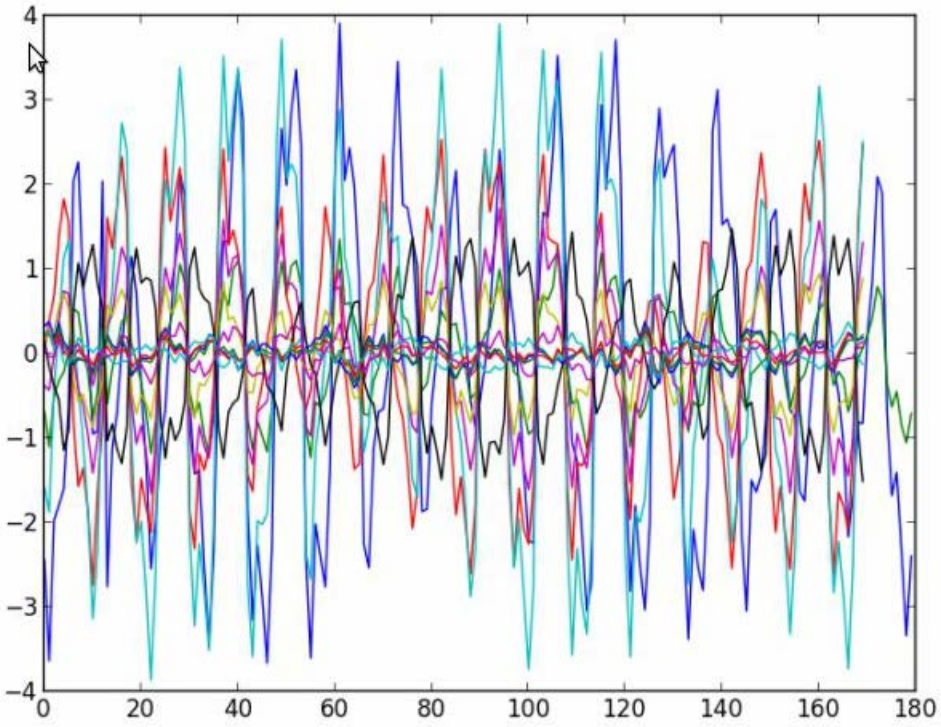

Figure 5: Residual betatron oscillation minimization with two correctors in C29

4.7.3 Off-axis injection

Description of off-axis injection

On-axis injection limits the beam injection to single shot only, as the fast kickers along with the DC bump will bump the stored beam on septum knife. To stack more beams into SR, the nominal off-axis injection is required. So DC bump has to be removed.

To remove the DC bump, the stored beam closed orbit signal was used. First, beam was injected on-axis and stored in SR, then the designed DC bump strength was reduced by several steps. During the process, orbit correction was also applied and the tune was measured and optimized.

First experience with off-axis injection

After removing the DC bump and the lattice correction, the off-axis injected beam could not survive for more than just a few turns in the ring. At that point we performed the first dynamic aperture study, which showed the dynamic aperture of about 4 mm, ~4 times smaller than the design value. The off-axis injection requires the beam dynamics aperture to be larger than 10 mm. With 4 mm dynamics aperture, off-axis injection beam cannot be captured.

The injection fast kickers were used for the dynamic aperture study. The stored beam was excited to do the betatron oscillation, the same way as the injected beam does. The betatron oscillation were started both from angle kick(excite only one kicker) and position kick (excite a pair of kickers, K1 and K2 or K3 and K4). In this way, the whole phase space was covered.

The dynamic aperture studies show [11] that there is a physical obstruction in cell 10, which limits the dynamic aperture. The vertical orbit correction also reflects this section limitation, as the beam close orbit correction from ~-2 mm to predicted center reference always kills the stored beam.

The turn-by-turn (TbT) BPM data taken during dynamic aperture measurements performed over several dates and various lattices and tunes showed that when viewed vs. turn number, beam losses occur in sharp steps (Fig. 6). When these sharp steps occur, the beam loss consistently happens at the same location in the ring, between BPMs 4 and 5 in cell 10 (Fig. 7).

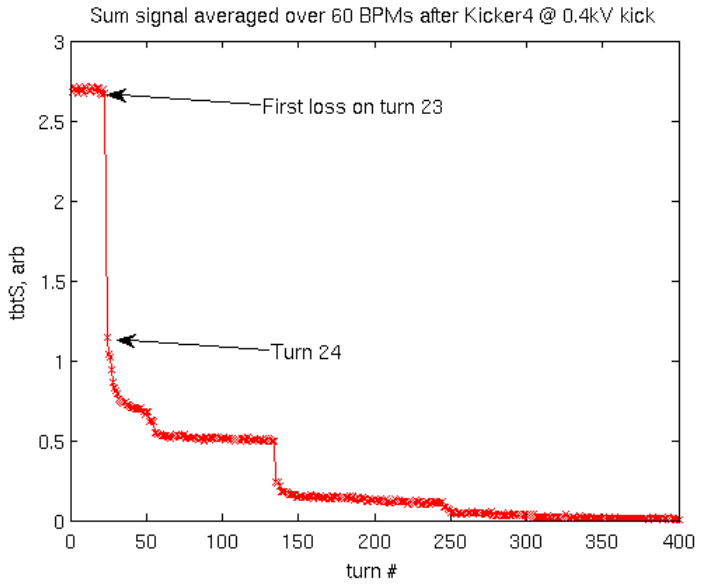

Figure 6: The beam loss as observed from one BPM sum signal

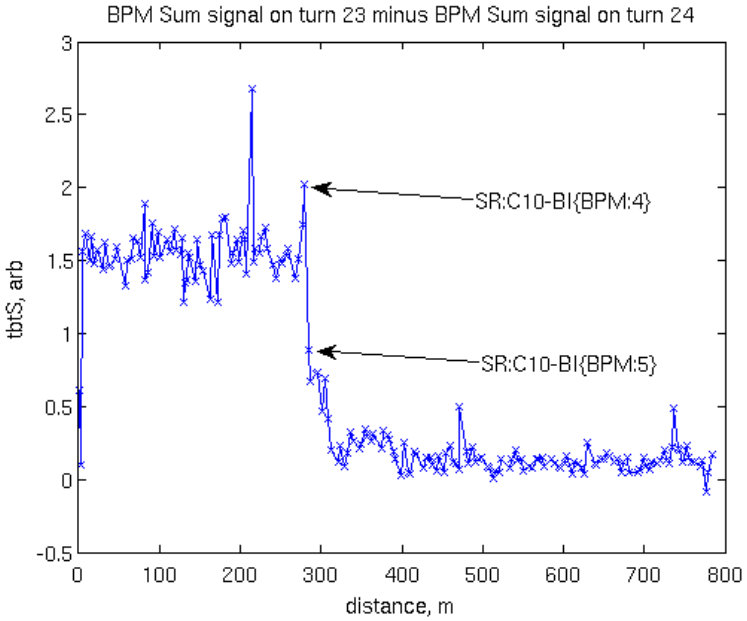

Figure 7: 180 BPMs sum signals along the ring in turn 24

Since such behavior suggested the presence of abnormal physical aperture in cell 10, this cell was investigated more with the aid of local bumps.

Local bump method confirms the physical aperture limitation in cell 10 (refer the local bump). Figure 8 shows the beam lifetime change with the vertical local bump height. When the bump changes from negative side to positive side, the beam was lost. Actually a hanging RF spring (the right picture in Fig. 8) was found [12] there after the vacuum chamber was opened. The spring location is not exactly between P4 and P5, but more upstream between P2 and P3, after the C10 first dipole.

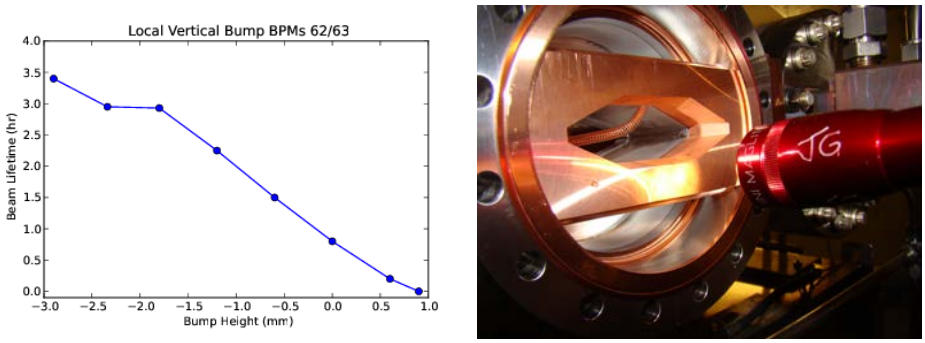

Fig. 8. Beam lifetime's variation with the height of a local bump (left) at cell 10 where a hanging spring (right) was found.

Obtaining off-axis injection

After replacing and properly installing the RF spring in cell 10, the off-axis injection was quickly obtained by following the procedure outlined in the previous section. Established off-axis injection immediately allowed for beam accumulation in the SR [13]. The very first beam accumulation to above 1 mA is shown in Fig. 9.

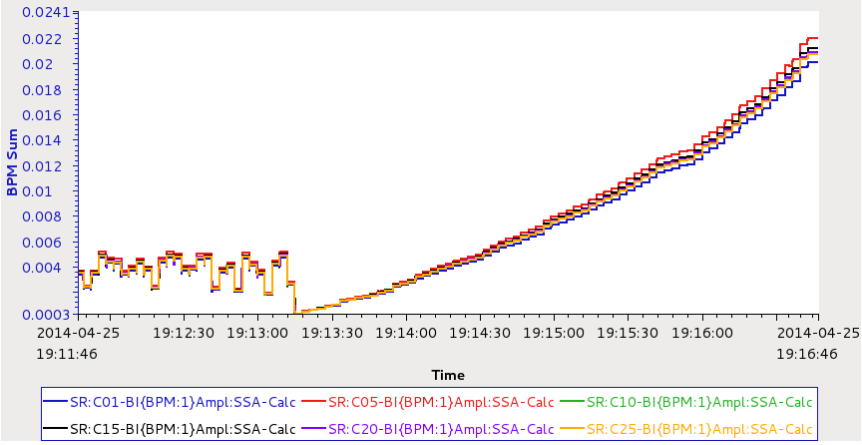

Figure 9: Sum signals of SR BPMs show first beam accumulation in SR ring with established off-axis injection.

After the vacuum conditioning and fast kickers timing alignment (next part), the beam current in the SR was accumulated to the goal value of 25 mA [14] as Fig 10 shows.

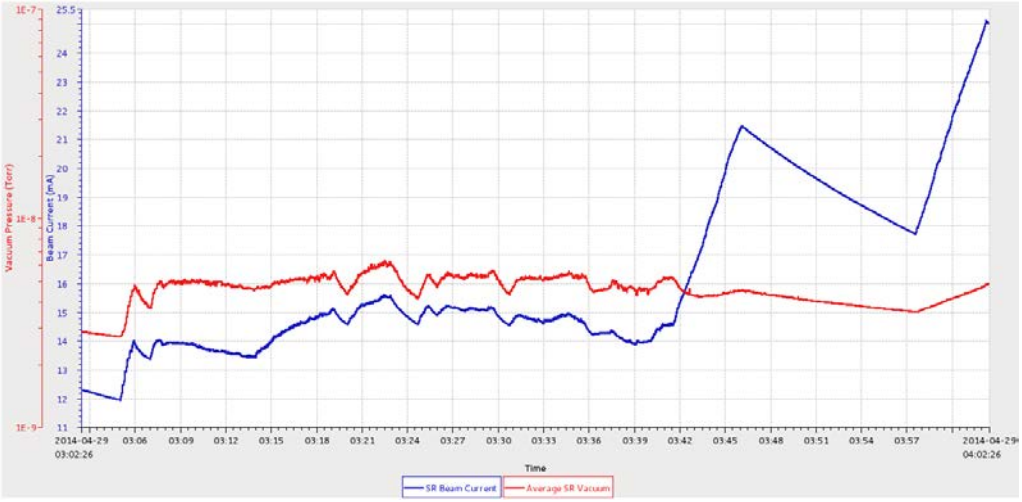

Figure 10: First 25 mA SR fill. Red line is ring vacuum pressure, blue line is the current.

4.7.4 Fast kickers study

The pulsed local bump is created by four pulsed kickers in the injection straight section. The diagnostics, BPMs P1, P2, P3 and P4, in this section is schematically shown in Fig. 1. BPMs P1 and P4 are centered on the SR stored beam trajectory, P2 is shifted by X = -5.8 mm off center and P3 is shifted by X = -15 mm from SR center. These four BPMs are inside the local fast bump and can be used for the bump amplitude study. The 180 BPMs along the ring will be used for the bump leakage study.

Since design pulsed bump displaces stored beam to X = -15 mm in injection septum region, the resulting displacements in BPMs P1, P2 and P4 are in non-linear region and the readback is not so reliable. Therefore, the bump scaled down by a factor of 3 as well as the nominal bump shall be used for pulsed bump studies.

Each kicker has independent voltage and timing control. The kicker voltage to the kick strength conversion is not very precise from the lab measurement. The timing delay is separated into two control parts. One is for four kickers' common delay relative to the injection time, and the other is for each kicker precise delay to compensate the cable length or beam arrival time difference. The initial timing trigger for all kickers is aligned with the beam signal from BPMs raw data and monitored with scope, as shown in figure 11.

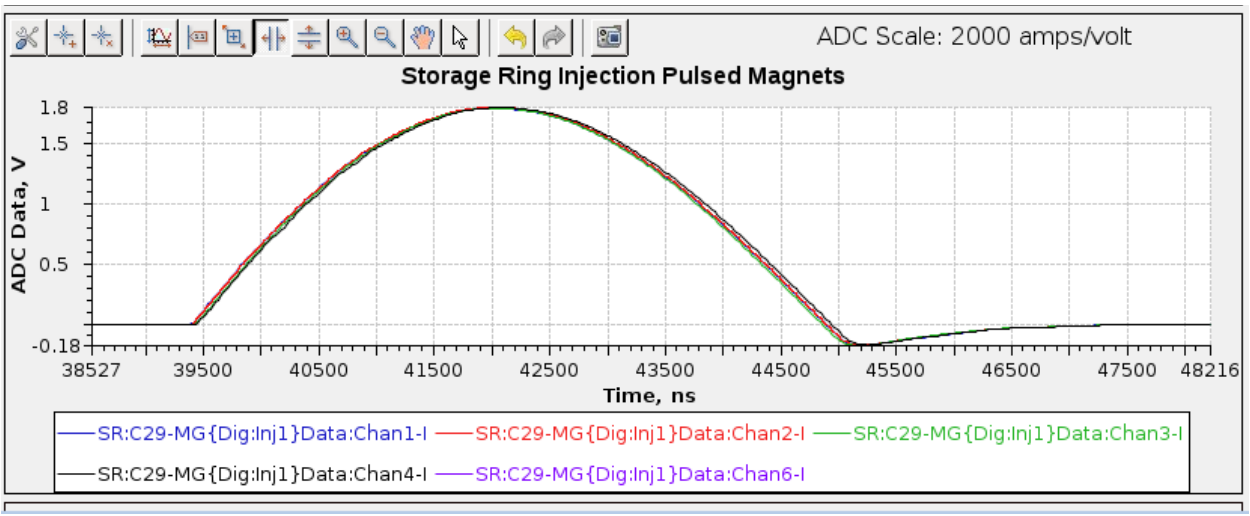

Figure 11: Fast kickers waveform

The initial kicker strength is set based on the measurement calibration. After the off-axis injection was obtained, different filling pattern was required to achieve high current due to bucket current limit. At that time, it was found that when the injection bucket was changed, the capture efficiency was different, so that some buckets could not be captured. The kicker timing and amplitude were studied and optimized.

The timing and amplitude are related, as the kick strength on beam is A*sin(wt). The common timing delay is optimized by moving the bucket number and comparing the capture efficiency (in fact, the capture efficiency for fresh injection does not change, but the stored beam is scratched at septum.) This process moves the beam relative to the pulse peak. It was found that the beam arrival timing was 520 ns away from the pulse peak and the kick voltage was ~5 % higher, which made the local fast bump too high and resulted in the stored beam loss in the septum knife. After fixing the common timing delay and kick amplitude, the beam could be captured well at every bucket.

TBT data also show the local fast bump leakage when all four kickers are set to the same nominal amplitude. Figure 12 shows the amplitude of remaining betatron oscillations was about 1 mm (upper). To minimize the leakage, four kickers' response matrix to 180 BPMs TBT data was used. The kicker voltage changes by 0.05 kV around its working point, so that the kicker calibration is in the working region and the BPMs reading is in linear region. After optimization, the leakage amplitude is lowered by half. Further studies, such as the precise timing alignment, kicker tilt correction, etc. should be conducted.

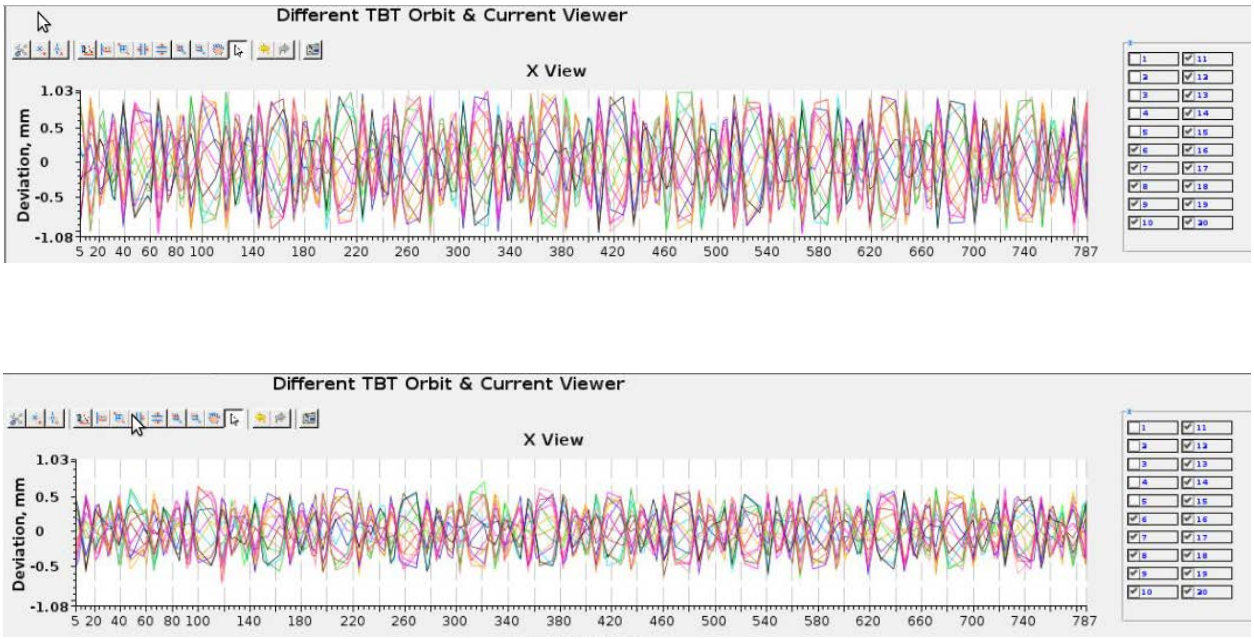

Figure 12: The local fast bump leakage before (upper) and after (lower) kicker strength optimization

4.7.5 Injection 6-D phase space match

If the injection beam transverse phase space (x, xp, y, yp) is mismatch with the SR close orbit at the injection point, the beam will do the betatron oscillation. If the injection beam longitudinal (phase and energy) is mismatch with the SR synchrotron phase and energy, the beam will do the synchrotron oscillation. These oscillations have different behavior as the betatron oscillation fraction tune for is ~0.2 range (a few turns) and the synchrotron tune is ~0.007 (~100 turns). So it is easy to differentiate from the BPMs TBT data. The synchrotron oscillation is only viewed from dispersion region BPMs.

The transverse phase space control knob is from the BTS correctors. The longitudinal control knob is the injection energy and SR RF phase.

For the x plane, the beam is off-axis injection, which naturally introduces the betatron oscillation. Theoretically, this mismatch can be extracted from TBT data with designed oscillation value, but the oscillation is ~10 mm range, which is the BPMs nonlinear region. The data does not show good result.

For the y plane, the beam is on-axis injection. The injection mismatch is fitted 180 BPMs TBT data. The response matrix is from the model, which gives very good fitting. The knob in BTS is C8 and C9. Along with the injection control application (refer BTS section), the y plane phase space was match very well.

For the longitudinal phase space, the dispersion region BPMs were used. Figure 11 shows one dispersion region BPM TBT data. From the TBT x plot, it is clearly that the beam has ~100 turns oscillation period, which due to phase or energy mismatch. The phase mismatch and energy mismatch involve to each other. The equivalent energy mismatch can be estimated from

oscillation amplitude over the designed dispersion value (~0.4 m). The oscillation due to energy mismatch starts from large amplitude, such as Figure 13. The oscillation due to phase mismatch starts from middle and moves to large amplitude, positive or negative depending on the offset. Figure 14 shows the energy percentage equivalent to the phase change at different voltage. With the injection energy control tool and RF phase, the longitudinal phase space could be quickly matched by minimization the dispersion BPMs residual synchrotron oscillation.

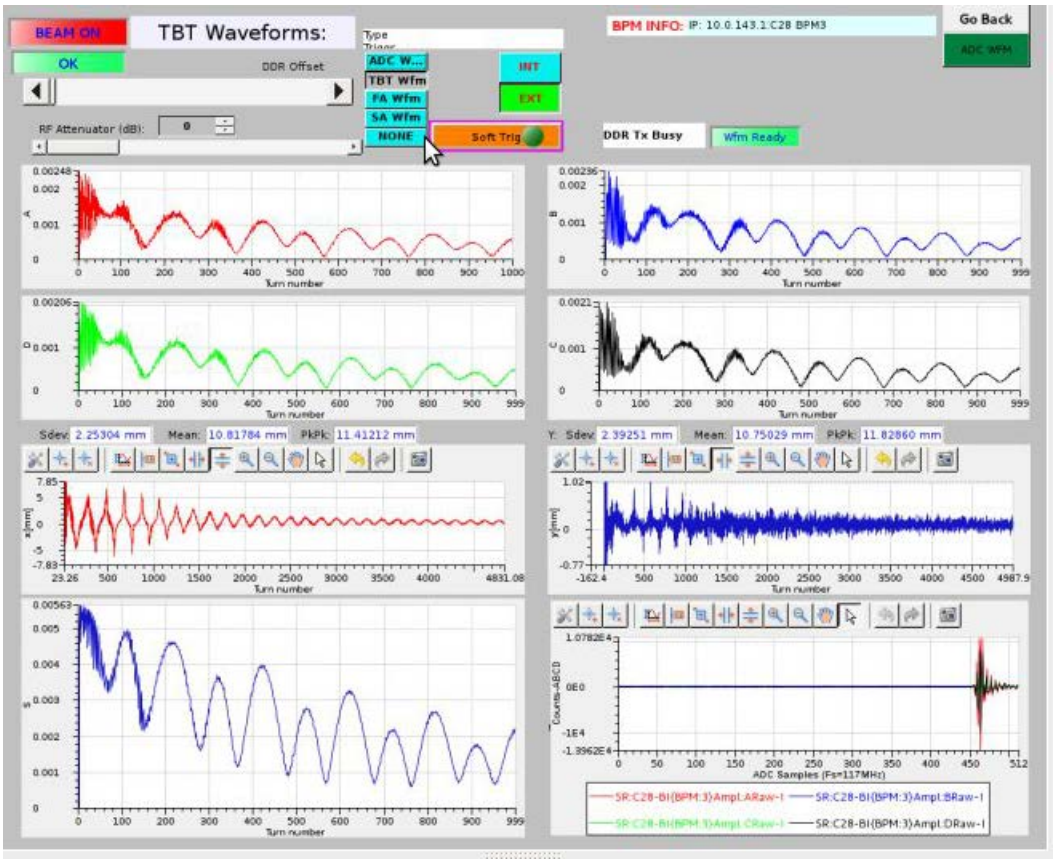

Figure 13: The injection beam energy mismatch monitor from dispersion BPM

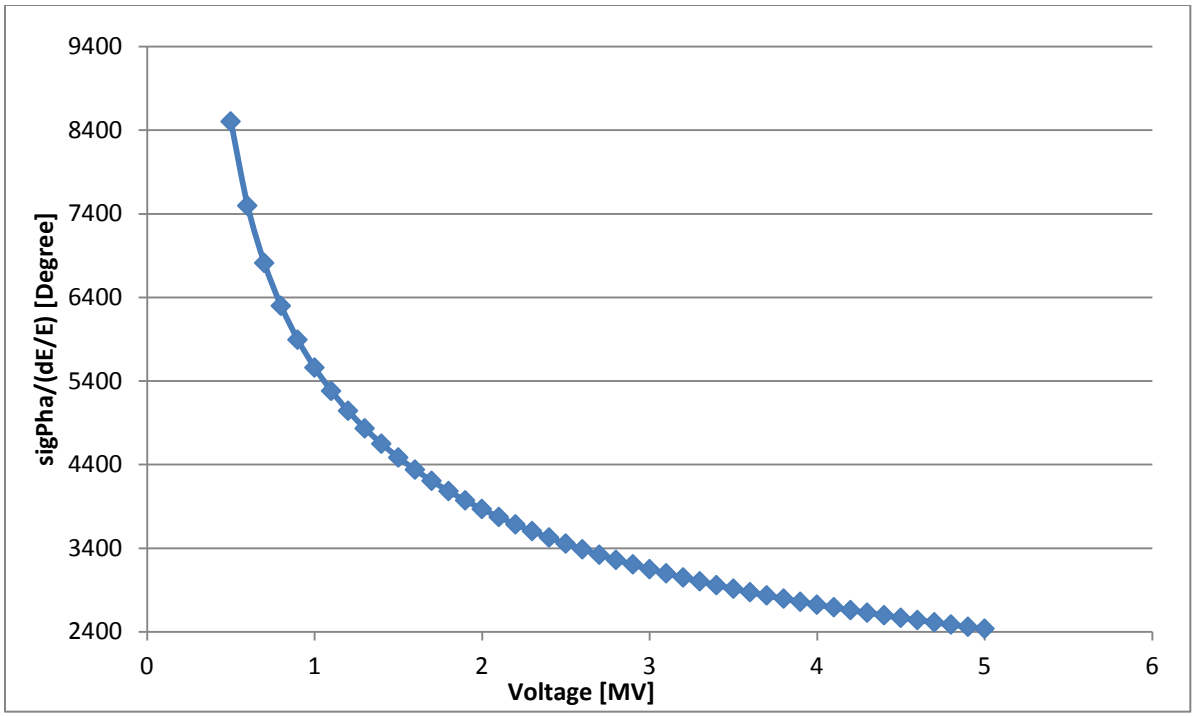

Figure 14: Ratio of bunch length and energy spread VS the RF voltage

4.7.6 Injection efficiency

The injection efficiency is calculated from the SR DCCT current change (dI*Trev) and BTS ICT2 charge. So it includes the loss at the injection region and the loss due to SR capture efficiency.

At the end of commissioning, the injection efficiency is better than 95% steadily.

References

[1] S. Seletskiy, Y. Li "NSLS-II Storage Ring Commissioning Module: First Turn Steering of the Storage Ring Trajectory"
[2] E. Blum, S. Seletskiy "NSLS-II Storage Ring Commissioning Module: Develop a Dogleg With Kickers 3 and 4"
[3] S. Seletskiy, G. Wang "NSLS-II Storage Ring Commissioning Module: Launching through the AC SR septum"
[4] S. Seletskiy "First Turn Analysis Software for NSLS-II Storage Ring", BNL-XXXXXX-XXXX-XX, w.i.p.
[5] NSLS-II online log book entry: https://logbook.nsls2.bnl.gov/logbook/#9376_2
[6] NSLS-II online log book entry: https://logbook.nsls2.bnl.gov/logbook/#9466_2
[7] NSLS-II online log book entry: https://logbook.nsls2.bnl.gov/logbook/#9640_2
[8] NSLS-II online log book entry: https://logbook.nsls2.bnl.gov/logbook/#9709_2
[9] NSLS-II online log book entry: https://logbook.nsls2.bnl.gov/logbook/#9851_1
[10] S. Seletskiy, E. Blum "NSLS-II Storage Ring Commissioning Module: Commission beam accumulation into the same RF bucket"

[11] NSLS-II online log book entry: https://logbook.nsls2.bnl.gov/logbook/#11113_1
[12] NSLS-II online log book entry: https://logbook.nsls2.bnl.gov/logbook/#11362_3
[13] NSLS-II online log book entry: https://logbook.nsls2.bnl.gov/logbook/#11380_2
[14] NSLS-II online log book entry: https://logbook.nsls2.bnl.gov/logbook/#11769_2

4.8 Vacuum performance and beam life time

The beam loss in storage ring depends on the quantum excitation (radiation damping), intra-beam scattering (Touschek effect), and residual gas molecules scattering (elastic: Coulomb scattering and inelastic: Bremsstrahlung scattering).

These four mechanisms have different signatures based on physical machine and dynamical beam parameters, such as residual gas pressure, rf voltage, vacuum chamber aperture, beam size, momentum acceptance, etc. The quantum lifetime contribution becomes visible only when the acceptance is smaller than about seven times of the beam dimension [1]. For normal operation conditions, mostly the quantum lifetime is negligible. For electron beam with very small sizes, the Touschek lifetime (estimated in other section) may dominate, as it is inversely proportional to beam size and the loss rate depends strongly on the momentum acceptance. Both Coulomb and Bremsstrahlung loss rates are proportional to the residual gas pressure, but are independent of beam size. Coulomb scattering alters the beam transverse motion, and excites the betatron oscillations. The particle will be lost when the oscillation amplitude exceeds physical acceptance aperture. So it is limited by the ring transverse acceptance. Bremsstrahlung scatting causes particles to loss energy. The particle will be lost if the energy loss exceeds the ring momentum acceptance. The Bremsstrahlung loss rate is only weakly dependent on the momentum acceptance.

The total beam lifetime is

$$\frac{1}{\tau} = \frac{1}{\tau_{\text{quantum}}} + \frac{1}{\tau_{\text{Touchek}}} + \frac{1}{\tau_{\text{elastic}}} + \frac{1}{\tau_{\text{inelastic}}} \quad (1)$$

The goal of vacuum design is to achieve a pressure level as such that beam lifetime due to residual gas scattering is significantly longer than the Touschek lifetime. The average pressure in NSLS II with beam is designed to be less than 1×10-9 Torr, so that the beam lifetime due to the gas scattering is longer than 40 hours. However, during the initial commissioning, due to the large desorption induced by the synchrotron radiation (SR), the dynamic pressure in the electron storage ring vacuum system is high even the static ultrahigh vacuum has been achieved. The interactions between the electron beam and the gas molecules desorbed from the chamber surface and absorber result in beam loss and emittance growth.

In the follow section, it describes the vacuum performance, its effect on SR beam lifetime and the measured beam lifetime.

4.8.1 Vacuum system and its performance

The majority of the SR vacuum chambers [2] are made of extruded aluminum. To achieve fast conditioning after intervention, sufficient pumping capacity is provided. Table 1 lists all the vacuum pumps for SR. After rough pumping and in-situ bakeout (130°C for 40 hrs to remove adsorbents, such as water, and contaminants on the inner surface), the vacuum cell chambers are pumped by sputter ion pumps (SIP), non-evaporable getters (NEGs), and titanium sublimation pumps (TSP) as the main UHV pumping. The vacuum level and the residual gas composition are closely monitored with the vacuum gauges, ion pump currents and residual gas analyzers (RGA), and to ensure that the chambers remain leak-tight and are free of contaminants.

Table1 List of vacuum pumps for SR

	SIP	TSP	NEG Lump	NEG strips	Gate Valve
SR cell	180	180	6	150	60
Straight	50	10	10	~40	

The gas density inside the vacuum chamber is determined by the installed pumping and by the surface condition of the vacuum chambers and the absorbers, which are bombarded by photons generated by the circulating electron beam. Two NEG strips are installed in the ante chamber and have a combined pumping speed of ~200 l/s/m for chemically active gases. SIPs are employed to pump the inert gases not pumped by the NEGs. The SIPs are located under the photon absorbers where the majority of photon stimulated desorption occurs. The SIPs provide < 100 l/s pumping speed and are part of a combination SIP/TSP. The TSP provides an additional 500 l/s of pumping for active gases.

An average beam channel pressure of less than 1e-9 Torr is needed for stored beam life, and to minimize the amount of radiation produced from bremsstrahlung scattering. Without beam, the vacuum in the storage ring is lower than the design goal with the main residue gas being hydrogen. Figure 1 shows the pressure level without stored beam over the commissioning period, at ~1e-10 Torr.

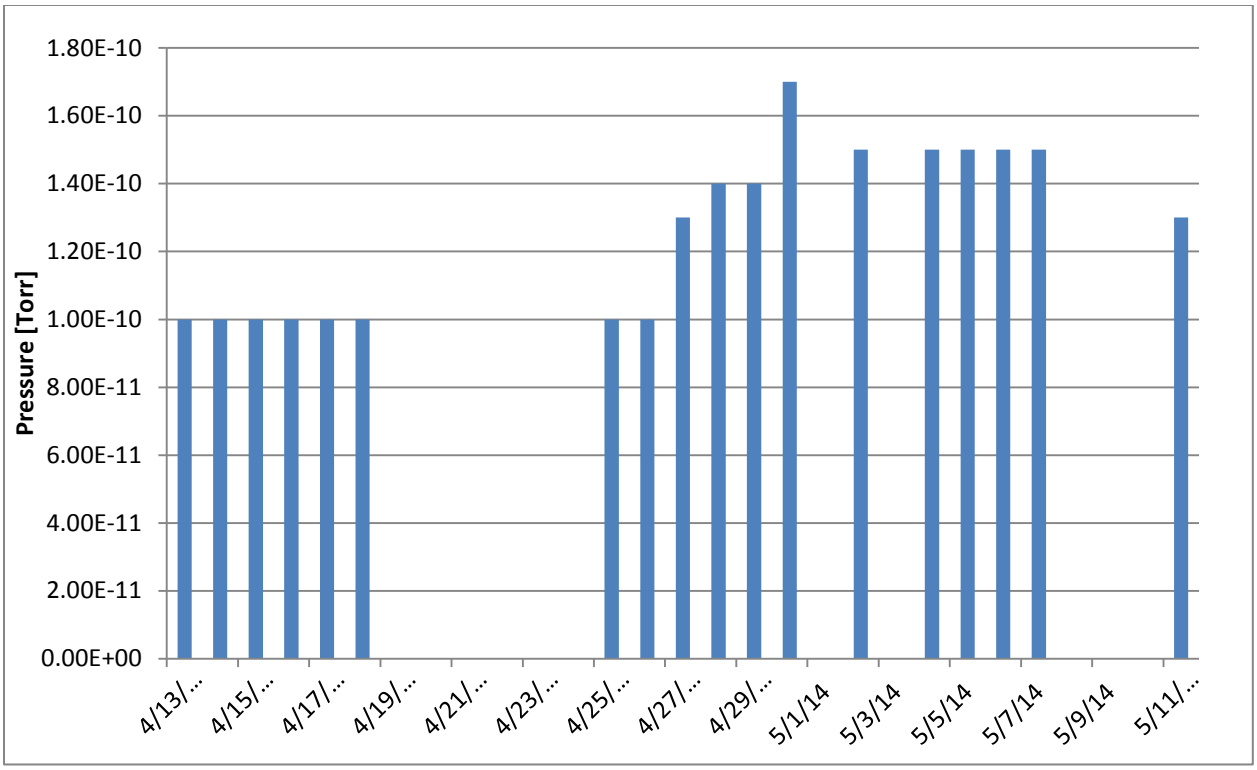

Figure 1: SR average pressures without circulating beam

Figure 2 shows a typical RGA spectrum of the partial pressures vs. the residual gas species without stored beam. The hydrogen (at m/e = 2) is dominating. However, the residual gas (mostly, H_2, CO/N_2, CO_2, CH_4) ratio would change depending on the stored beam current and accumulated beam dosage, $\int I \cdot dt$. The gas scatting loss will depend largely on the interaction of the beam with heavier residual gas.

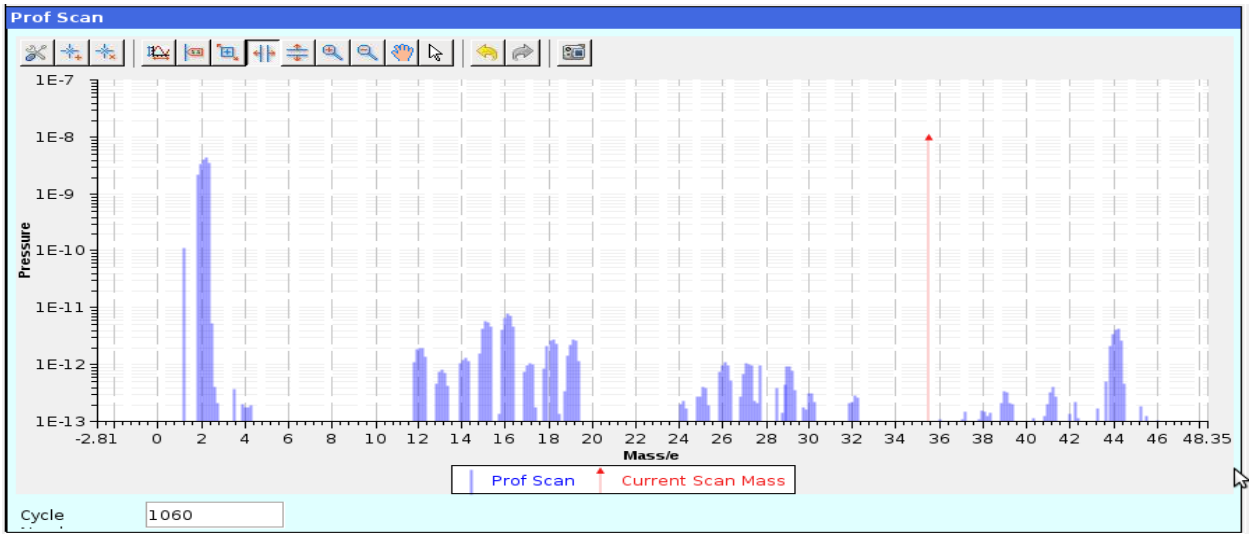

Figure 2: SR partial pressures of residual gas species without circulating beam

Figure 3 shows the typical vacuum pressure history without and with beam. The average vacuum without beam was 1e-10 Torr. At 25 mA, the vacuum pressure increased to 4e-9 Torr due to PSD. Figure 4 shows an example of the SR dynamic gas pressure and stored beam total current with linear correlation. The slope dP/dI decrease exponential with the integrated beam dosage ∫ I.dt, as shown in Figure 5, from the initial 8e-10 Torr/mA decreasing to 8e-11 Torr/mA at the end the phase I commissioning. The slope of this conditioning (on log-log plot) is ~ 0.5 which is less than the slopes of 0.55 – 0.6 observed in other recent SR facilities. Therefore it may require ~ 200 A-hr accumulated dosage to achieve ΔP/I of 1e-11 Torr/mA, a desirable level to maintain low 10-9 Torr pressure with > 100 mA stored beam current.

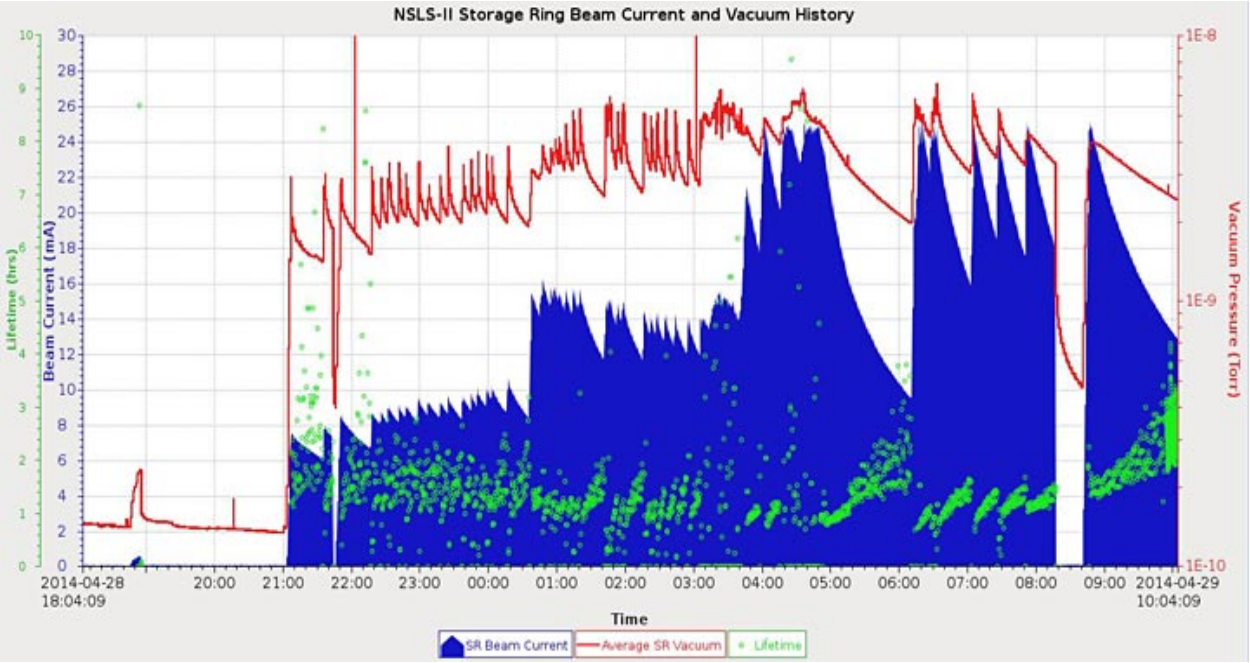

Figure 3: SR Beam current and vacuum history

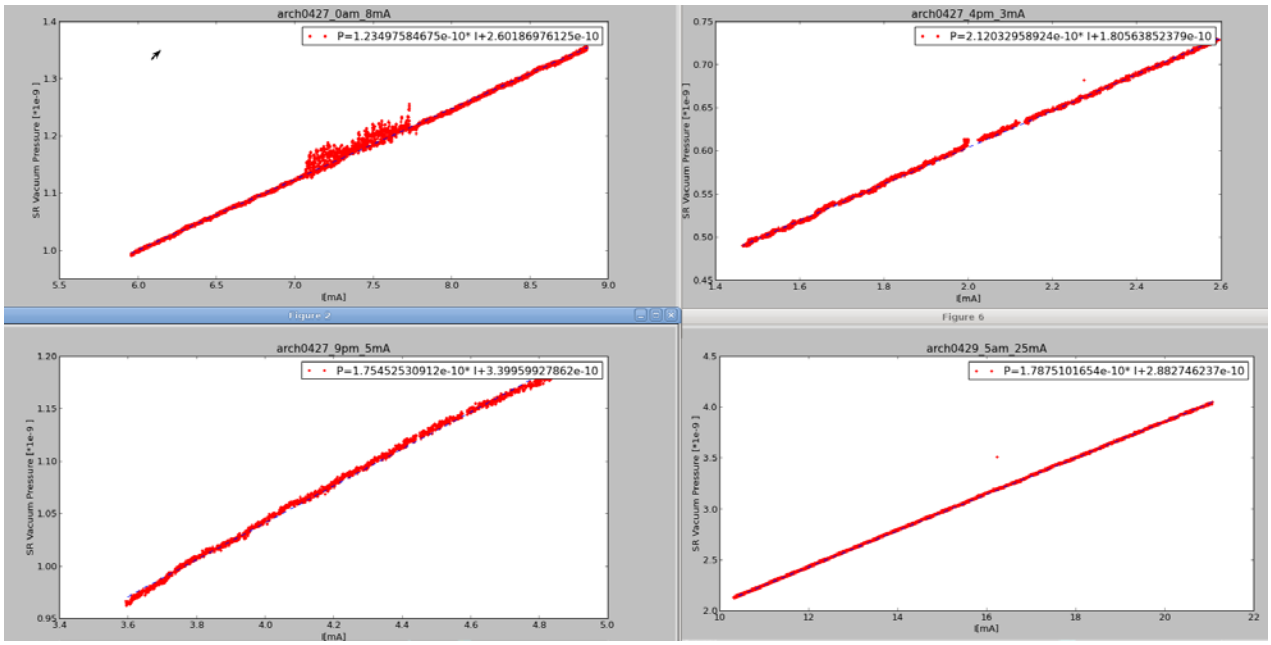

Figure 4: SR dynamic gas pressure increase with beam current at different day

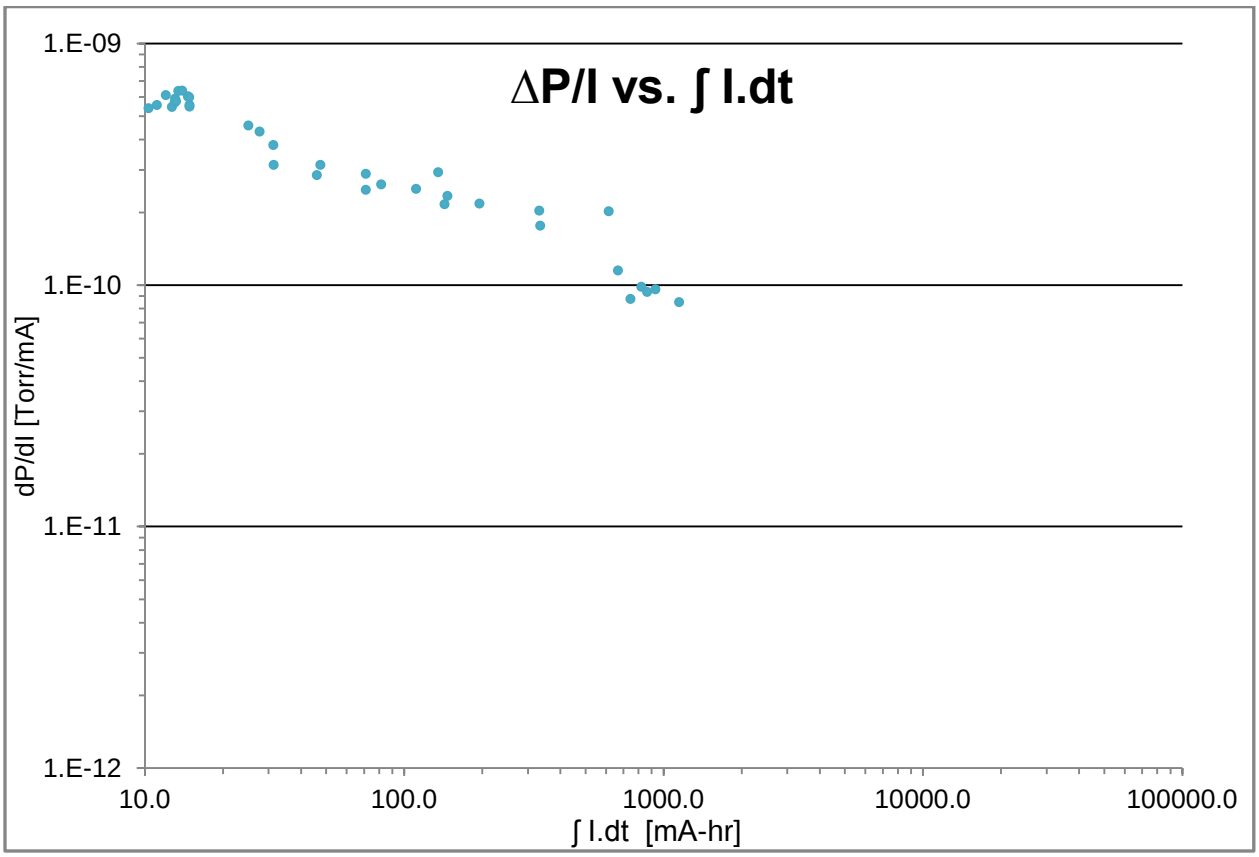

Figure 5: Pressure decrease slope vs. the integrated beam dosage

The Booster and transport line vacuum systems have also performed well, maintaining ultrahigh vacuum throughout the beam commissioning. Figure 6 shows an example of the

Booster average pressure. The average Booster pressure without beam was less than 1e-9Torr. The pressure increased to as high as 4e-7 Torr initially with only 1 mA beam, due to photon stimulated desorption (PSD) at the end of ramp cycle. After two months of beam conditioning, the pressure increase was down to ~1e-8 Torr with similar amount of beam, more than a decade improvement in PSD yield. From the pressure curve right after turning beam off, the contribution from dipole chamber eddy current heating and outgassing is estimated to be less than 1/3. A rough estimate of PSD yield of stainless steel dipole chamber gives ~10^{-3} molecules/photon, after ~ 10 mA-hr beam dosage, only counting photon flux during the 20-msec flat top.

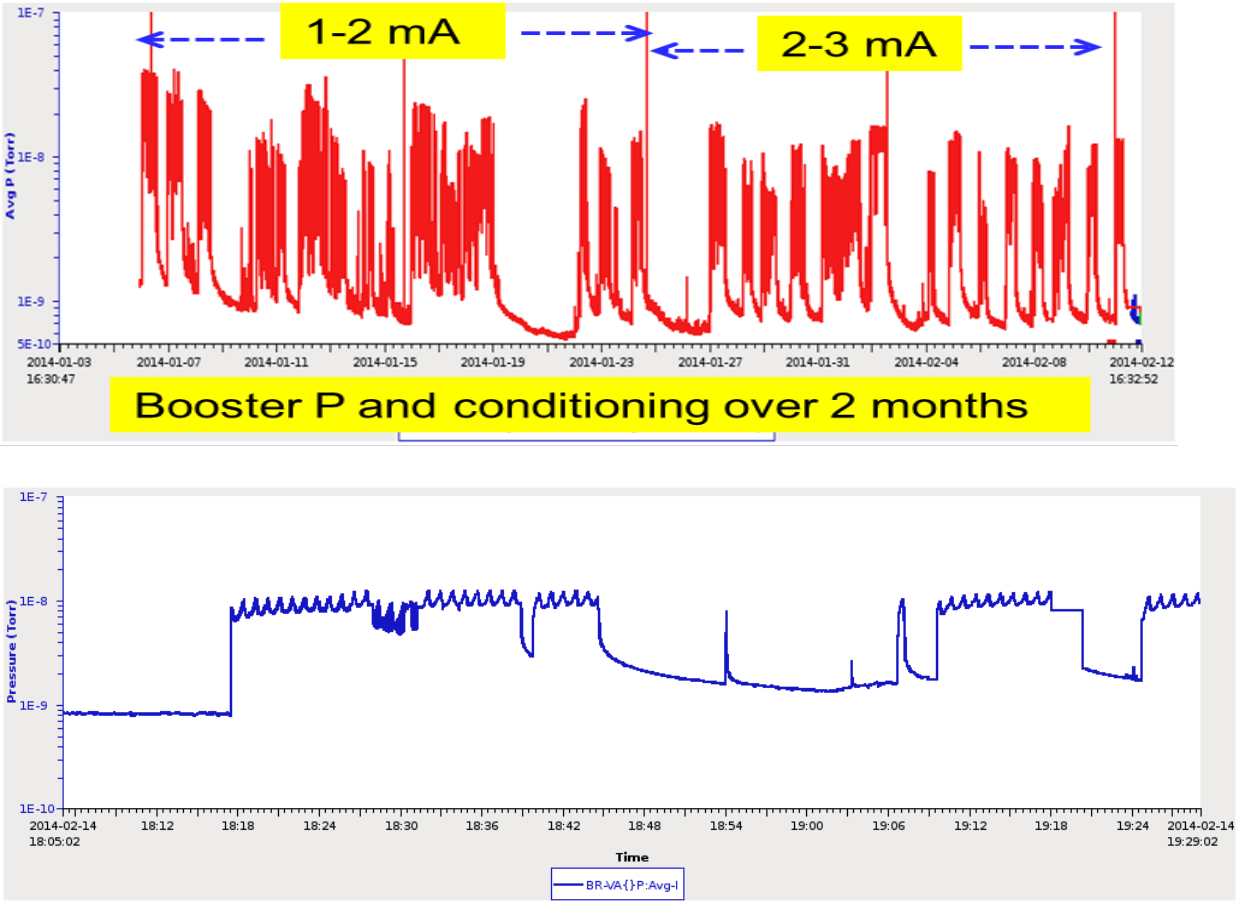

Figure 6: Booster average pressure with 3 mA beam. The gradual decrease of pressure after turning off beam is mainly due to eddy current heating and outgassing of dipole chambers

In summary, the vacuum systems, covering over 1 km of beam channels, have been very reliable and have maintained ultrahigh vacuum throughout the commissioning period. There were 19 recordable fault events caused by vacuum systems during beam commissioning, with 13 events interrupted beam operation. Most events were attributed to failure of ion pump controllers, which either interlocked the gate valves or turned off Linac klystron power. A reset of AC power was usually sufficient to restore IPC operation. However, in three occasions, the IPC had to be replaced with spare units, thus causing down time longer than 1 hour. Through

improved firmware and replacement of an eProm, these IPC will be upgraded in the coming shutdowns.

In SR, aperture restriction and obstruction in the beam channel were identified at several locations in the storage ring using aperture scans with fast kickers to excite betatron oscillations in X plane and correctors to create local bump(refer section 'Physical aperture assessment'). Four cells were subsequently opened for visual inspection, and RF contact springs were found protruding into beam channel at two locations, and were corrected. There are approximately 700 contact springs in storage ring. Among them, ~ 100 are of three-flange combination type (Figure 7), rather difficult to assembly and verify the integrity. In the future, we expect to identify and replace a few more springs with small protrusion into beam channel.

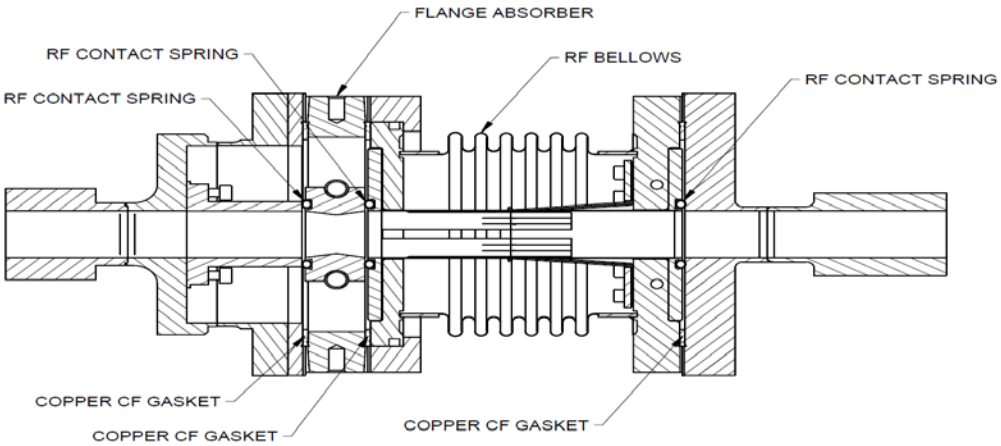

Figure 7: 3-flange assembly (left) with two springs and two Cu gaskets; and the two flange assembly (right)

4.8.2 Gas load and gas scatting effect on beam lifetime

The amount of desorbed molecules produced depends on photon flux [3]. The photon flux is

$$\phi_\gamma = \frac{15}{8}\cdot\sqrt{3}\cdot\frac{P_{ins}}{u_c}\cdot\frac{N_e\cdot N_B}{2\cdot\pi\cdot\rho_B} = \frac{15}{8}\cdot\sqrt{3}\cdot\frac{P_{ins}}{u_c}\cdot\frac{I_0\cdot\tau_{rev}/e}{2\cdot\pi\cdot\rho_B} \quad (2)$$

Where P_{ins} is the instantaneous power radiated by a single electron, u_c is the critical energy, N_e is the number of electrons per bunch, N_B is the number of bunches and ρ_B is the bending radius. It is proportional to the total beam current.

$$P_{ins} = \frac{cC_g}{2\cdot\pi}\cdot\frac{E^4}{(\rho_B)^2}$$

$$u_c = \frac{3/2\cdot h_q\cdot c\cdot\gamma^3}{\rho_B}$$

Here, c is the speed of light, $C_g = \frac{4\pi}{3}\frac{r_e}{(m_e c^2)^3} = 8.846\times10^{-5}\frac{m}{GeV^3}$ for electrons, h_q is the Planck constant 1.05e-34 J-s, E is the electron beam energy, γ is the Lorentz factor, τ_{rev} is the SR revolution period.

For NSLS II, the electron beam energy is 3 GeV and bending radius is 25 m. The critical energy is 2.311 keV and P_{ins} is 525.46 GeV/s.

The flux of desorbed molecules is

$$\phi_{mol} = \phi_{\gamma} \cdot \eta$$

The ratio η between the number of desorbed molecules and incident photons depends on the incident angle, the photon spectrum, the power deposition, the radiation dose, the type of metal surface and more. The ratio value 1.5e-5 molecule per photon is used based on the vacuum data, after ~ 100 A-hr accumulated dosage.

Under room temperature conditions, the gas load from desorption is

$$Q_{gas} = \phi_{mol} \cdot k_B \cdot T$$

where k_B is the Boltzmann constant, $1.38e-23\ J/K$. T is the room temperature. With pumping speed S, the vacuum pressure is given as

$$P_{gas} = Q_{gas}/S$$

For the beam lifetime an important parameter is the specific pressure increase

$$\alpha_p = \frac{P_{gas}}{I_0}$$

The pressure is given as a certain basic pressure P_0 and a contribution from the gas desorption

$$P(I) = P_0 + \alpha_p \cdot I$$

It depends on the total beam current, not the filling pattern.

With the atomic weight G_A, the gas density is then given by

$$\rho_{gas}(I) = \frac{P(I) \cdot G_A}{k_B \cdot T} \tag{3}$$

Bremsstrahlung scattering:

The beam lifetime due to bremsstrahlung scattering is

$$\tau_{bs}(I) = \frac{\chi_0}{\frac{4}{3} \cdot \ln\left(\frac{E}{\Delta E}\right) \cdot c \cdot \rho_{gas}(I)} = \frac{\tau_0}{1 + \frac{\alpha_p}{P_0} \cdot I} \tag{4}$$

Where ΔE is the energy acceptance, $\chi_0 = 716.4 \cdot \frac{A}{Z(Z+1) \cdot \ln\left(\frac{287}{\sqrt{Z}}\right)}$, Z is the atomic number and A

is the atomic weight. $\tau_0 = \frac{\chi_0}{\frac{4}{3}\cdot\ln\left(\frac{E}{\Delta E}\right)\cdot c\cdot\frac{P_0\cdot G_A}{k_B\cdot T}}$ is the beam lifetime due to the static vacuum pressure.

The bremsstrahlung scattering beam lifetime mostly depends on heavier residual gas, but weak dependence of SR energy acceptance. $1/\tau_{bs}$ is linear proportional to beam current.

Figure 6 shows the bremsstrahlung scattering lifetime (upper) and vacuum pressure (lower) change with stored beam current. The basic pressure P_0 is set 2.4e-10 Torr and α_p is set 1.5e-10 Torr/mA from Figure 5. As the residual gas component, it is hard to measure the residual gas ratio exactly, as the RGA only monitors local gas away from the beam channel. The desorbed gas only includes CO, which underestimates the beam lifetime. With the above data, τ_0 is 325 hr. At 25 mA, the bremsstrahlung scattering lifetime is ~20 hr. If the residual gas is replaced as H2, the lifetime will increase by a factor of 49.

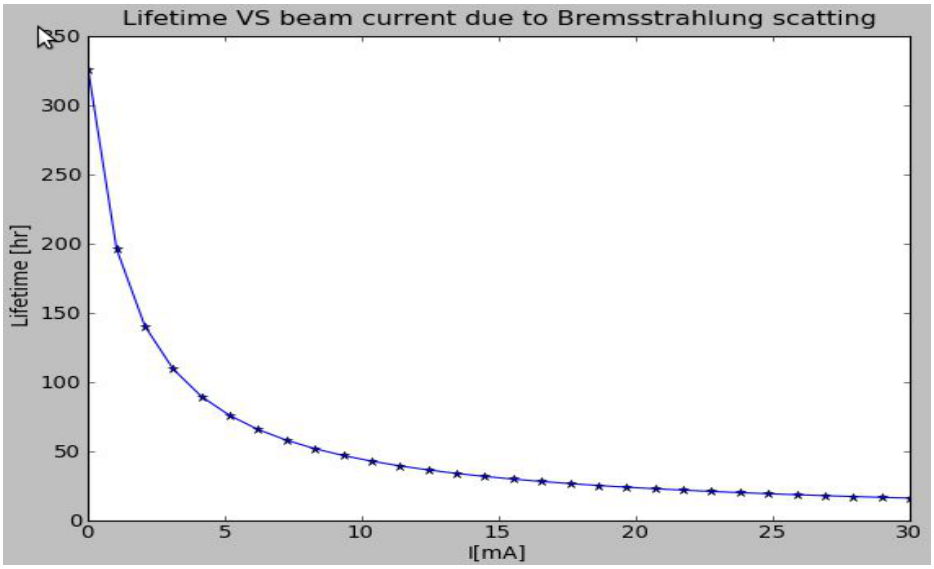

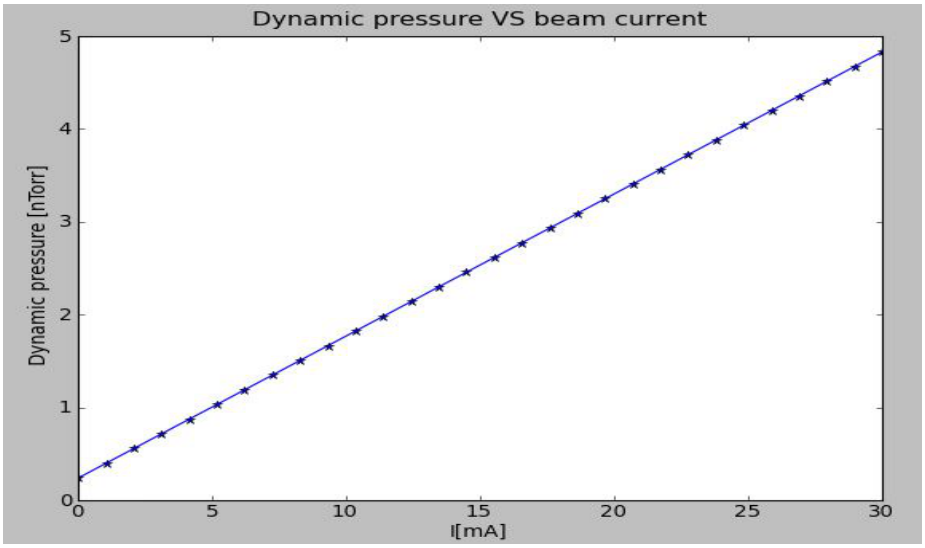

Figure 6: The bremsstrahlung scattering lifetime (upper) and vacuum Pressure (lower) change with stored beam current

Coulomb scattering:

The beam lifetime due to Coulomb scattering [1] is

$$\tau_{cs}(I) = \frac{E^2[GeV^2]\cdot A_y^{min}[mm-mrad]\cdot T[K]}{0.272\cdot\langle\beta_y\rangle[m]\cdot(P_0+\alpha_p\cdot I)[nTorr]\cdot Z^2\cdot N} \quad (5)$$

Where $\langle\beta_y\rangle$ is the average vertical beta function, $A_y^{min} = (g/2)^2/\beta_y$ is the y plane minimum acceptance and g is the minimum gap, N is the number of atoms per molecule. $1/\tau_{cs}$ is linear proportional to beam current.

Figure 7 shows the Coulomb scattering lifetime change with stored beam current. The g is 10 mm with $\beta_y = 3.36m$ for damping wiggler location. The average vertical beta function is 13.8m. The rest parameters are the same as bremsstrahlung scattering lifetime estimation. At 25 mA, the Coulomb scattering lifetime is ~13 hr. Similarly, it underestimates the beam lifetime with heavy residual gas.

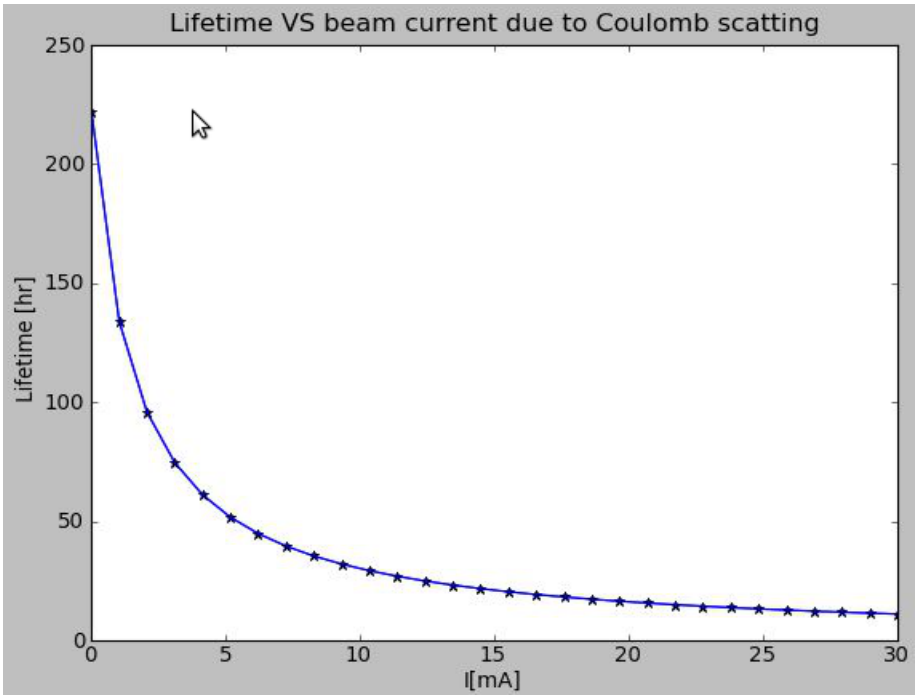

Figure 7: The Coulomb scattering lifetime with stored beam current

4.8.3 Touschek Lifetime

Beam lifetime in the NSLS-II ring is expected to be Touschek-dominated due to the small emittance. Toushchek scattering process leads to non-exponential decay of (single-bunch) intensity

$$N_b(t) = \frac{N_b(0)}{1 + t/\tau_{tous\_1/2}}$$

where $\tau_{tous\_1/2}$ is the so-called Touschek half-life (but also called Touschek lifetime below), given by

$$\frac{1}{\tau_{tous\_1/2}} = \frac{\sqrt{\pi} r_e^2 c N_b}{\gamma^3} \left\langle \frac{C(\zeta)}{\sigma'_x V \varepsilon_{acc}^2} \right\rangle \tag{6}$$

where $\zeta = \left[\varepsilon_{acc} / \gamma\sigma'_x\right]^2$, $C(\zeta) = -\frac{3}{2}e^{-\zeta} + \frac{\zeta}{2}\int_\zeta^\infty \ln(u)\frac{e^{-u}}{u}du + \frac{1}{2}(3\zeta - \zeta\ln\zeta + 2)\int_\zeta^\infty \frac{e^{-u}}{u}du$,

$V = 8\pi^{3/2}\sigma_x\sigma_y\sigma_z$ is the beam volume, ε_{acc} is the momentum acceptance and the brackets denote averaging over the ring circumference.

4.8.4 Measurement

Beam lifetime measurements are achieved by fitting either the dc current transformer (DCCT) data or 180 BPMs sum signal as a linear function of time over short time intervals. As the DCCT noise is big, at low current, the lifetime fitting from DCCT is not good, but at high current, it is very close to the BPMs data fitting.

It is hard to measure the lifetime from each mechanism, as the combined lifetime due to all of the effects is always measured. Contributions due to gas scattering, however, can generally be separated from the Touschek as they generally do not depend on beam dimensions (ignoring ion trapping) and only depend on the total beam current through current-dependent outgassing rates, which could be ignored in simplified models or in the limit of low beam intensity. Touschek lifetime, on the other hand, has a strong dependence on beam dimensions as well as single-bunch current.

A very limited number of dedicated lifetime measurements were performed during the last week of the commissioning. Below we present and analyze a subset of them that allows one to estimate the Touschek lifetime.

For the Touschek lifetime, we studied single bunch measurements on 05/08/14, with bunch-by-bunch feedback (BBF) turned on, as well as 20 bunch fill data from 05/11/14 (both data sets are with emittance coupling corrected to estimated value of □=0.32%). F
the maximum total beam current was ~8mA. The measured lifetime vs. single bunch current (circles) is plotted in the figure 8. Note that the trends for both datasets are reasonably close, however scaling the 05/08/14 data to 18 bunches (shown in crosses, but not used in the fits below) makes them even closer. There could be a reasonable justification for this, since our bunch trains are not very uniform, so the first and the last bunch(es) usually have lower intensity.

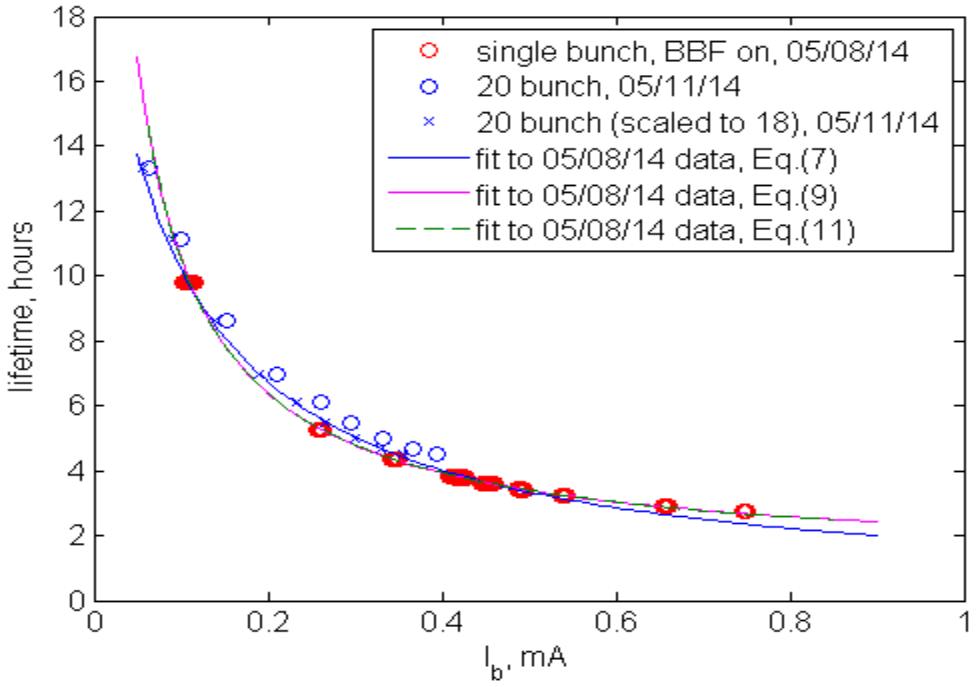

Figure 8: Measured lifetime vs. single bunch current (circles)

Two different 2-parameter fits were performed to the single bunch data from 05/08, and they are plotted in solid lines. Obviously they both well approximate the 20 bunch data as well. Both fits ignore current-dependent outgassing, thus assuming that the total lifetime consists of current-independent gas scattering contribution, as well as the Touschek contribution, inversely proportional to beam current.

The first fit, shown in blue, is given by

$$\tau_{\text{total}}(I_b) = \frac{\beta\,\alpha / I_b}{\alpha / I_b + \beta}, \tag{7}$$

where β and α are the fit parameters, and I_b is the single bunch current. The fit obviously well describes the data we have available. However, we know that the Touschek modeling it includes is somewhat simplistic, as, at these intensities, a significant bunch-lengthening with current has been measured with the streak camera (see the results in "Diagnostics Commissioning with Beam" section).

To accommodate this effect we approximated the streak camera data with a simple linear dependence,

$$\sigma(I_b) \approx 12 + 11.43 \times I_b, \tag{8}$$

where the bunch length is given in ps, and beam current in mA. In the second fit, shown in magenta, we incorporated the bunch-lengthening effect into the Touschek lifetime by

$$\tau_{\text{total}}(I_b) = \frac{\beta\,\alpha\sigma(I_b)/I_b}{\alpha\sigma(I_b)/I_b + \beta}, \tag{9}$$

One could argue that the fit is probably somewhat better when describing the higher current points, although one has to perform multiple, more detailed measurements, to confirm this.

The values of α, obtained from these two fits result in the Touschek lifetime values (taken at 0.5 mA single bunch current) of 4.0 and 3.7 hours respectively, while fitted β give 21 and 47 hour values for the gas lifetime.

Finally, we attempted to account for current-dependent outgassing, approximating the data available from the vacuum history as $P(I_b) = (1.5 + I_b[\text{mA}]) \times 10^{-10}\,\text{Torr}$. This expresses the average gas pressure (around 05/08) at the location of the vacuum gauges, rather than the average pressure along the beam orbit when the measurements were taken. The two could be different. In addition, the residual gas composition is not continuously available, and there is some uncertainty about other parameters that define the gas scattering lifetimes. Thus we still kept the overall scale-factor fit parameter β, for the gas lifetime and fitted the total lifetime as follows (I_b in mA),

$$\tau_{\text{total}}(I_b) = \frac{\beta\,(1.5 + I_b)^{-1}\alpha\sigma(I_b)/I_b}{\alpha\sigma(I_b)/I_b + \beta\,(1.5 + I_b)^{-1}} \tag{10}$$

This fit is plotted in dashed green, and, to the resolution of the figure, it is identical to the previous fit (to Eq. (9)). With the fit parameters obtained, the above equation results in 3.8 hours Touschek and 34 hours gas lifetimes at 0.5 mA single bunch current.

Note that for all three fits the fitted values for the Touschek lifetime are reasonably consistent. At this point it is impossible to estimate the systematic error, while the statistical error from the data we presented comes out to about 10% level.

What value for the Touschek lifetime should we expect at this point? At 0.5 mA/bunch and taking the best measured or inferred values available today, specifically 2.5% momentum acceptance, ε_x=2.1 nm horizontal emittance, K=0.32% coupling and τ=18 ps, we obtain, f $\tau_{\text{tous\_1/2}} \approx 4.3\,\text{hours}$, which is not too far away from the fitted values quoted above.

For the gas scattering effect on the beam lifetime, it is also estimated for multi-bunch filling pattern with different high beam current. Figure 9 shows the measured beam lifetime up to 8 mA with bunches distributed in 20 buckets. As expected, it decreases with beam current.

Figure 10 shows the inversed lifetime change with beam current. Coulomb and Bremsstrahlung scattering have similar contribution to the electron beam losses in storage ring. From the above formula, the gas scattering lifetime contribution is proportional to the beam current. The measured beam lifetime inverse also linearly fits well beam current. With the overestimated residual gas, the gas scatting lifetime contribution is about 1/5 of measured beam lifetime. So the beam lifetime main contribution is not from the residual gas scattering.

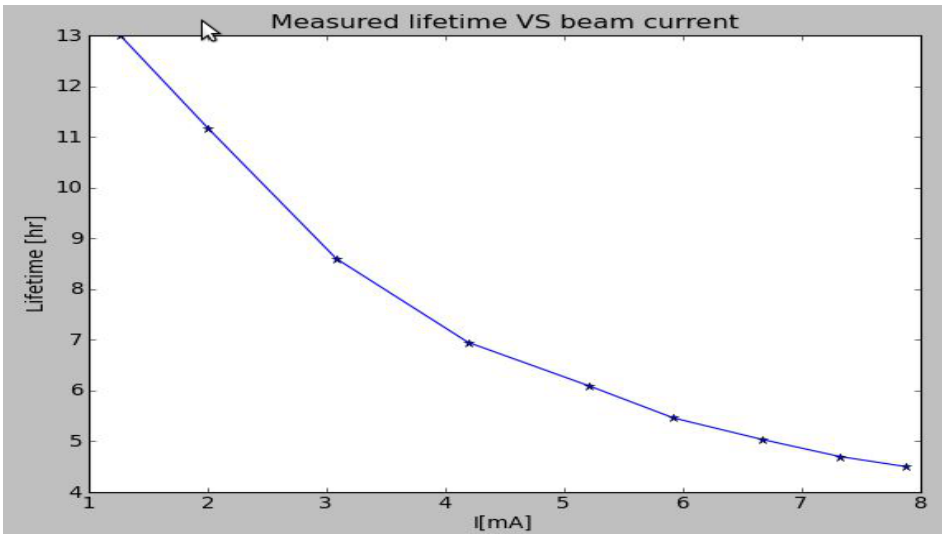

Figure 9: Beam lifetime measurement

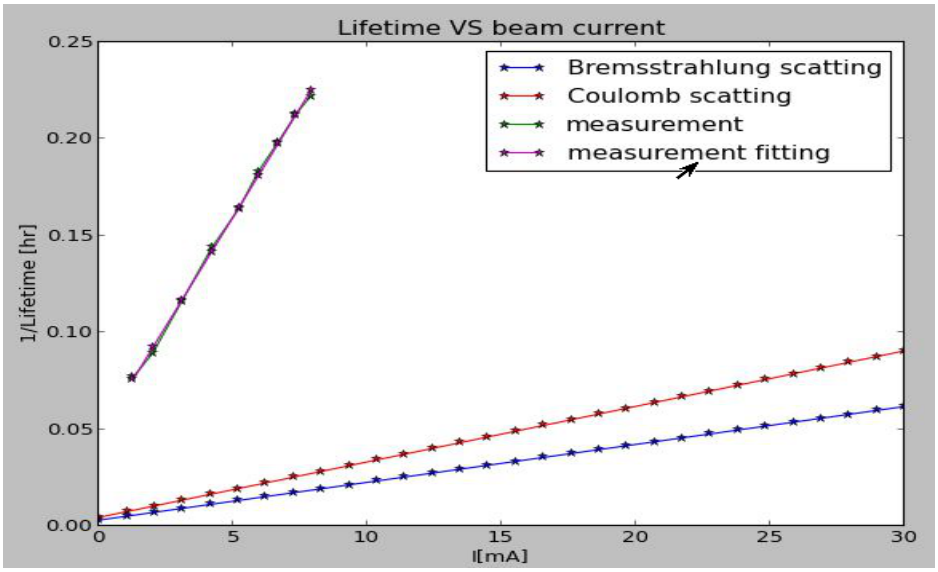

Figure 10: Beam lifetime comparison

4.8.5 Summary

During phase I commissioning, NSLS II static vacuum pressure achieved to 1e-10 Torr and dynamic vacuum pressure linearly increase with current up to 4e-9 Torr at 25 mA. The dP/dI decreases with increasing beam dosage, which desorbs the chamber gas. By the end of the commissioning, the dP/dI decreased by a factor of 10, down to 1e-10 Torr/mA.

With a rather limited number of dedicated measurements we believe we can estimate the Touschek lifetime (taken at 0.5 mA / bunch) to be around 3.8±0.4 hours which is reasonably consistent with our expectations. Based on this analysis, and provided NSLS-II can achieve the design momentum aperture (with IDs installed), we should expect the design value of Touschek

lifetime of > 3hours to be easily achievable. The gas scattering (elastic and inelastic) contribution to the beam lifetime is estimated from vacuum conditions. Even with heavy atomics, it is about 5 times longer than the measured beam lifetime. The beam lifetime is dominated by Touschek lifetime, but not the residual gas scattering lifetime.

Future studies should include more detailed measurements at a larger number of fill patterns, preferably when the outgassing rates have stabilized. Care has to be taken to improve the uniformity of the desired fill patterns by either improving the bucket selection tool in CSS or by kicking out the extra charge in selected bunches using the presently available feature in the bunch-by-bunch feedback system. An alternative technique to clearly separate the contributions of gas scattering and Touschek effects to the total lifetime would be to simultaneously measure the lifetime of individual bunches for a few bunch fill that has significantly different single bunch intensities. This could be accomplished i.e. by specialized processing of BPM ADC signals. Separately, scraper measurements would allow one to better model the elastic scattering lifetime and understand the ring acceptances, while pinger measurements should provide better understanding of the momentum acceptance. Finally, the better we can characterize the bunch dimensions in 6D (by measuring/inferring the emittances, energy spread and bunch length) the better we can model the Touschek lifetime in the NSLS-II ring.

4.9 Experience with Software Tools

The softwares used in our commissioning are mainly in four categories:

1. CS-Studio (Control System Studio) or CSS panels. They were able to support almost all equipment controls and displays in the commissioning. Some IOCs (Input/Output Controller) were also setup to do pre/post-processing to expand the data processing capabilities.
2. Python scripts and notebooks. This is a good candidate for controls with physics logics, e.g. orbit correction, tune adjustment, local bump and various measurements. It is also used for setting up IOCs to process data and feed to CS-Studio.
3. Matlab based middle layer toolkit and LOCO (Linear Optics from Closed Orbits). They are used widely across the light source facilities and have many advanced features. Some lattice fitting results are done with LOCO.
4. Specific tools, such as MASAR~(machine snapshot and restore), Ramping manager, Archiver, ...

4.9.1 CS-Studio Panels

CS-Studio is a powerful tool to monitor and control hard-wares. In EPICS, each PV (process variable) represents an indicator of hardware (or software). It can be scalar or vector. We can build panels (BOY screen) in CS-Studio with various widgets. This is like the Graphical User Interface (GUI) applications but easier to develop. CS-Studio has provided enough widgets for our commissioning.

We were complaining about the stability and hardware resource consumption of CS-Studio at the beginning, but it was then significantly improved as the commissioning moved on. Users from both operators group and physics group helped the developer to find the problem and improve CS-Studio.

CS-Studio is a frontend mainly for data display and simple direct controls, the data manipulation capabilities are limited. A middle layer, e.g. softIOC, or even lower level software can process the data and feed to CS-Studio via network to display. Not like developing a GUI applications with high level programming languages (Python, MATLAB, TCL/TK) where any logic and display are handled on same host without extra network traffic. Some softIOCs developed by physicists were very helpful in the commissioning. E.g. To display the orbit of each turn from BPM turn-by-turn data, a softIOCs was setup to take 180 waveforms (each with size upto 10k) and takes one number from each waveform and send 180 numbers back to CS-Studio as the orbit. Some of these developments can be pushed to either lower level or transferred to dedicated IOC server to obtain better performance and reliability for user operations.

4.9.2 Python

A python library was developed for the commissioning. It has wrapped the lower level controls, collected design lattice properties and hardware unit conversions. Some basic physics routines such as orbit response measurement, orbit correction are implemented. This helps to write a high level script on the fly. Some Python notebooks are transferred between scientific

operators from shift to shift. It has a good feature of containing both controls scripts and results. E.g. the tune correction, orbit correction, local bump, etc.

4.9.3 Special tools: MASAR, Channel finder, Channel Archiver

MASAR

The MASAR (MAchine Snapshot, Archiving, and Retrieve) is an important tool used during the commissioning, which is developed by the NSLS-II Controls group for machine save/compare/restore function. MASAR is an EPICS V4 service, and it is a server-client based tool-set. The server and client are implemented in C++ and Python. The server takes machine snapshots, archives data in a relational database, and retrieves data from the database. The client provides a GUI that retrieves snapshot data, compares the data with the live machine, compare multiple snapshots, and restores the machine with given snapshot data.

The user creates a list of channels, which can be any record data type, such as scalar values, arrays or strings, that are important for the system in a configuration file and, then, MASAR saves the current configuration. To take a snapshot, the client specifies the name of the snapshot configuration and a name for this snapshot event. When the server receives a command to take a machine snapshot, the server retrieves the list of channel names in the configuration from the database. It then gets the current value of all the channels from IOC, and saves the data as a snapshot event into the database.

Channel finder service and applications

The High level applications tend to prefer a hierarchical view of the control system where they can group channels by type (such as BPM, horizontal corrector) or location. These applications require retrieving a large set of channels' value or alarm state. Channel finder applications have simplified user interaction by requiring the user to providing only the channels' criteria that they are interested in, such as element type BPM or element Name ICT1, instead of the complete set of channels name.

User provides a list of channel names (PVs) with given properties and tags and channel finder service (CFS) stores these information for different applications. The Properties are keyword-value pair data, where the keywords are predefined, such as element name with value P1, element type with value BPM, s Position with value P1 0.5 et. al, whereas the tags are plain strings, such as aphla.sys.LTB, aphla.sys.SR. The channel finder applications use CFS plugin, to query the service for a group of channels based on the set of criteria, which is based on one or any combination of channel name, properties and tags. The channel finder applications client are supported by CSS (such as channel viewer to show a group of PVs with their name, properties and tags, Channel line plot viewer to plot a group of PVs live data, waterfall plot to show time plot of all queried channels) or python (APHLA: accelerator physics high level application).

Channel Archiver

An EPICS Channel Archiver is installed to record the values of many interesting PVs over time (such as ICT charge, power supply readback, vacuum pressure, which are predefined by PVs' owner). This data is then available for online queries, for plotting with the CSS Data browser, and may be exported in several formats (such as spreadsheet, Matlab, h5) for analysis.

4.10 Experience with Timing System

The Timing system for the NSLS-II delivers clocks, triggers and time stamp information to all technology subsystems and experimental areas in the light source. The basis for the timing system is an event link with machine event information transmitted synchronously with respect to the 500MHz RF system clock. This link is distributed throughout the complex with a constant delay with respect to a central distribution point. The distribution media is multi-mode fiber. The fibers fan out from a single location near the RF clock source.

System events are generated under software control in the EVent Generator (EVG) and are decoded into local electrical trigger pulses and clocks by the EVent Receivers (EVRs). In addition to receiving system events these devices generate time stamp information for the subsystems. The accelerator clock is shown in Figure 1.

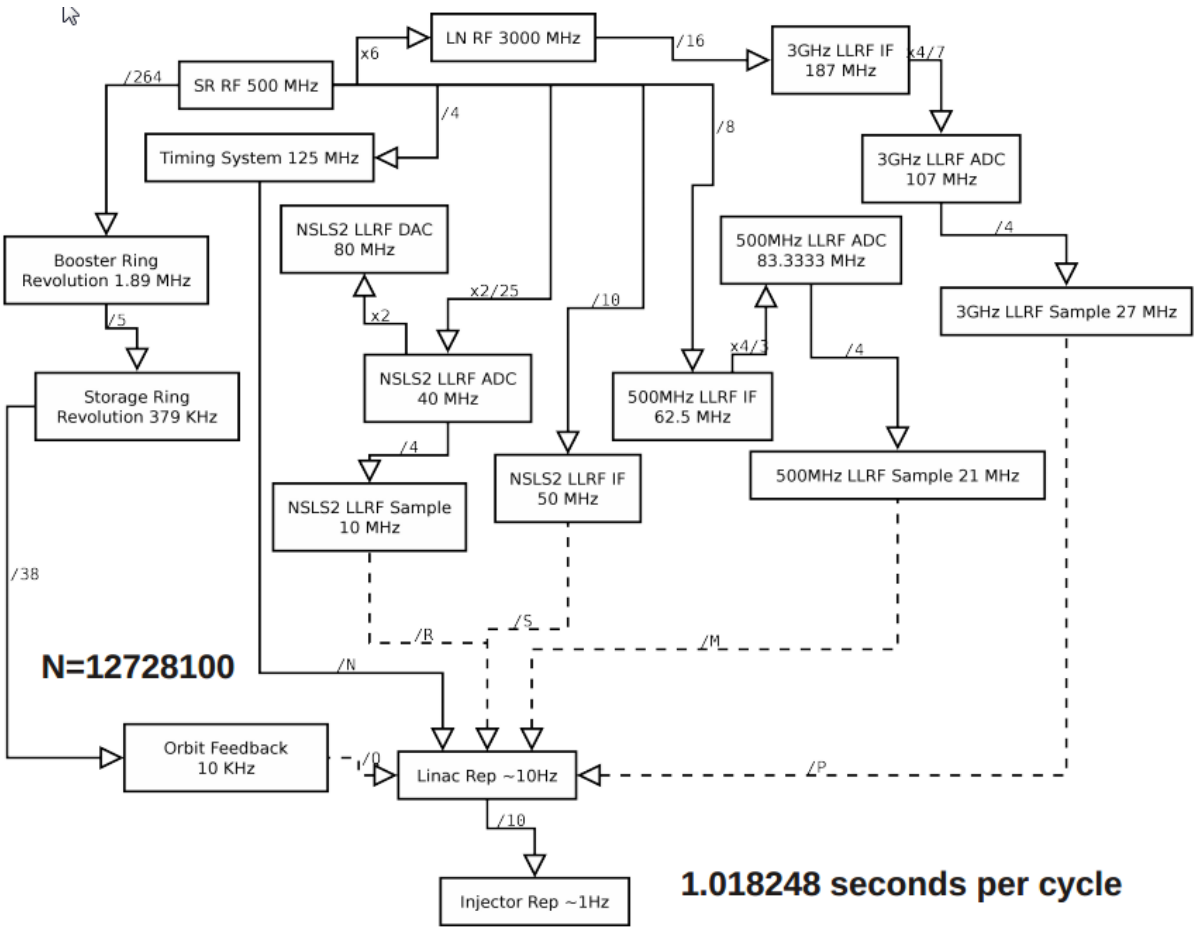

Figure 1: Accelerator clock

The primary consumers of timing signals are the magnet power supply controllers (PSCs) and electron beam position monitors (eBPMs), as well as the fast beam orbit feedback system which connects them. These devices accept a common ~10kHz clock to ensure synchronous operation. Triggers are also provided to the RF acceleration systems, the Electron Source, other diagnostics (ICT, FCT, Flag…) and fast pulsed magnets for beam injection and extraction.

The timing jitter tests were made from the NSLS2 BPM receiver's ADC clock. This clock is derived from the RF master clock and distributed by the Micro Research Timing hardware in the form of the revolution clock (Frev=Frf/4/330). Frev is then used to lock a PLL giving Fadc = 330*Frev. The stability of this clock is critical to the performance of a BPM receiver. A Rohde & Schwarz FSUP signal source analyzer was used to acquire spectrum and jitter measurements of the BPM ADC clock. Several tests show the jitter error is about 1 ps, which is within the specification 5 ps.

Prior to the commissioning, all timing signal cables were connected from the EVRs to each triggered device. These cables, as well as the signals they carry, were then validated as part of device testing. An initial rough calibration of individual trigger delays was done using calculations of electron beam time of flight, and approximations of cable delays. Precise delay calibration was done with the electron beam signal during commissioning.

An important control function of the timing system is the triggering of the Electron Source, to determine the precise time at which electrons enter the storage ring. By varying this time it shifts the whole injector timing relative to SR timing and place injection beam in SR different bucket. This is the process by which the ring is "filled" with electrons. On top of this, the SR filling pattern application is developed for daily operation. The interface is shown in Figure 2. The user should set the desired current and pattern. Once the SR DCCT current reaches the desired current, this application will stop the injection. User can also stop the injection any time manually. There are three patterns to choose, Fill one, uniform fill and pattern file. 'Fill One' is for single bucket injection, setting with the bucket number. 'Uniform fill' is for the fill pattern that can be described with the number of gaps and fill percentage. 'Pattern File' is for any general pattern fill, which user defines the filled bucket start number. It covers the above two pattern, but needs HLA to set the waveform into a PV. Figure 2 shows the example of uniform fill with 10 gap, 50% fill and current limit at 24.5 mA. Figure 3 shows the filling pattern monitor measurement during the filling process.

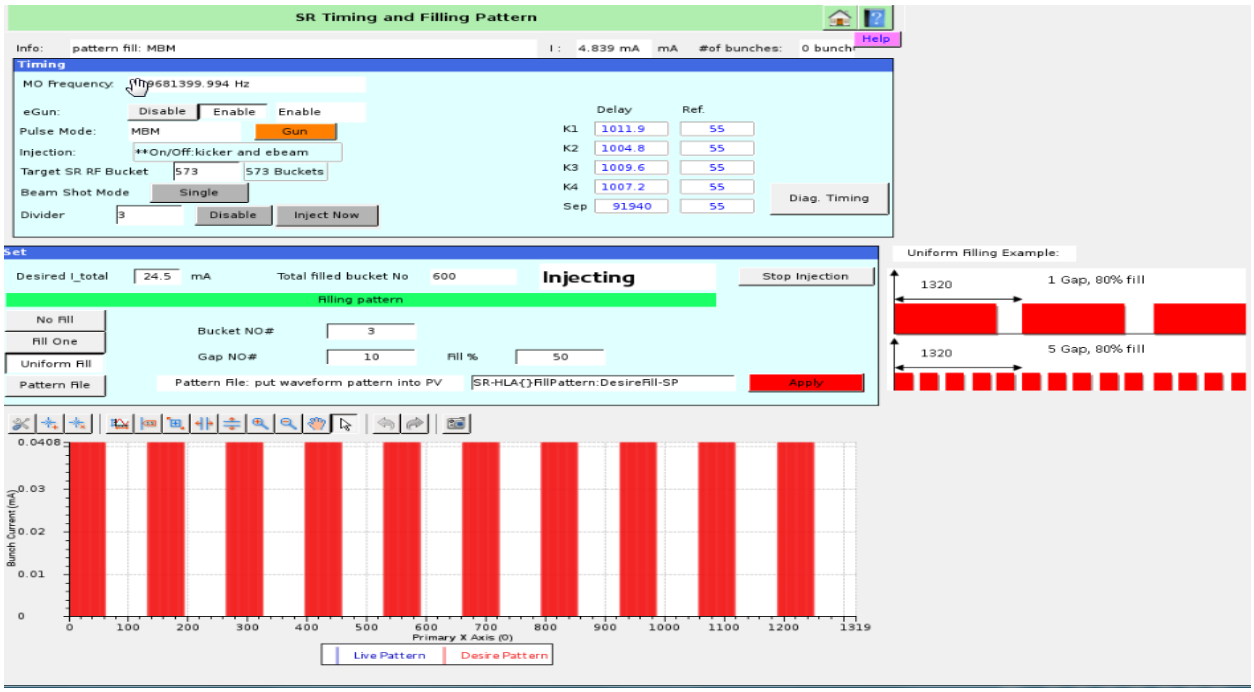

Figure 2: SR filling pattern control panel

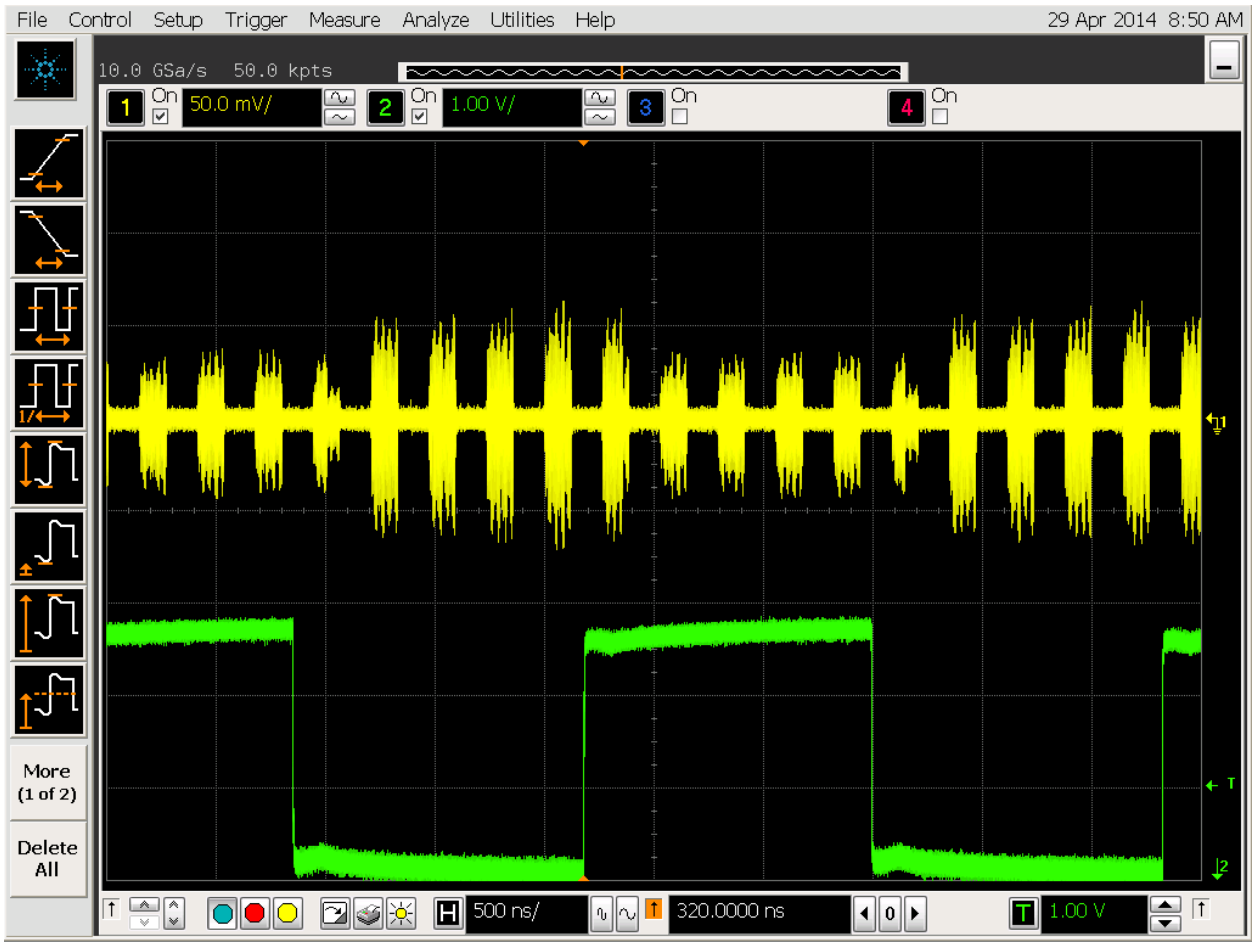

Figure 3: SR Filling pattern monitor

In summary, the timing system for NSLS-II met all requirements necessary for the successful commissioning of the accelerator systems.

4.11 Applying Matlab LOCO to the NSLSII Storage Ring Commissioning

4.11.1 Introduction

Linear Optics from Closed Orbits (LOCO) has been a powerful beam-based diagnostics and optics control method for storage rings and synchrotrons worldwide ever since it was established at NSLS by J. Safranek [1]. This method measures the orbit response matrix and optionally the dispersion function of the machine. The data are then fitted to a lattice model by adjusting parameters such as quadrupole and skew quadrupole strengths in the model, BPM gains and rolls, corrector gains and rolls of the measurement system. Any abnormality of the machine that affects the machine optics can then be identified. The resulting lattice model is equivalent to the real machine lattice as seen by the BPMs. Since there are usually two or more BPMs per betatron period in modern circular accelerators, the model is often a very accurate representation of the real machine. According to the fitting result, one can correct the machine lattice to the design lattice by changing the quadrupole and skew quadrupole strengths. LOCO is so important that it is routinely performed at many electron storage rings to guarantee machine performance, especially after the Matlab-based LOCO code [2] became available. The Matlab version includes a user-friendly interface, with many useful fitting and analysis options.

4.11.2 Basic LOCO Algorithm

If the linear optics in a storage ring is known, then the closed orbit response matrix can be easily calculated. The LOCO algorithm reverses this process. Given the measured orbit response matrix, the code determines the actual linear optics of the ring, including the errors in the optics. The quadrupole strengths can then be adjusted to correct the errors.

The closed orbit response matrix is defined as

$$\begin{bmatrix} \vec{x} \\ \vec{y} \end{bmatrix} = \begin{bmatrix} M_{xx} & M_{xy} \\ M_{yx} & M_{yy} \end{bmatrix} \begin{bmatrix} \vec{\theta}_x \\ \vec{\theta}_y \end{bmatrix}, \quad (1)$$

where (x, y) is the horizontal and vertical shift in closed orbit at all the BPMs for a change in strength of the steering magnets of (θ_x, θ_y). The size of the orbit response matrix is the number of BPMs times the number of steering magnets, so the measured orbit response matrix typically contains thousands or tens of thousands of data points. The measurement accuracy of the closed orbit is usually in the order of a micron, so the orbit response matrix contains a huge number of data points reflecting the optics of the ring.

The way to find the optics model that best fits the data is to minimize the chi-squared difference between the measured data and the model,

$$\chi^2 = \sum_{i,j} \frac{(M_{ij}^{\text{meas}} - M_{ij}^{\text{model}})^2}{\sigma_i^2} \equiv \sum_{k=i,j} E_k^2 \qquad E_k = \frac{M_{ij}^{\text{meas}} - M_{ij}^{\text{model}}}{\sigma_i}, \quad (2)$$

where σ_i is the measured noise level on the i^{th} BPM, and E_k is the error vector. Minimizing the length of the vector E is equivalent to minimizing chi-squared.

Finding the best fit optics model simply requires minimizing a single function, χ^2. The algorithm used in LOCO is Gauss-Newton minimization. Model parameters are adjusted to generate a ΔE such that

$$E_k^{new} = E_k + \frac{\partial E_k}{\partial K_l}\Delta K_l \quad , (3)$$

where K_l are the parameters varied to fit the response matrix, and each column of the matrix $\partial E_k/\partial K_l$ corresponds to the change in the orbit response matrix error vector with some fit parameter K_l.

Depending on the fit parameter, the LOCO code uses an analytical calculation of $\partial E_k / \partial K_l$ or uses AT [3] to numerically calculate the derivative. The model fitting is now a linear algebra problem,

$$-E_k = \frac{\partial E_k}{\partial K_l}\Delta K_l \quad , (4)$$

where the matrix $\partial E_k / \partial K_l$ is inverted to find the ΔK_l that best cancels the difference between the measured and model response matrices. There are far more data points in the response matrix than there are fit parameters, so the equation is over-constrained. LOCO uses singular value decomposition (SVD) [4] to invert the response matrix.

The change in the response matrix with quadrupole gradients is not entirely linear, so the fitting must be iterated a few times to converge to the best solution. If the initial model is far from the actual ring optics, the problem may be sufficiently nonlinear that the iterations do not converge. In the past, such problems were addressed (with varying results) by reducing the number of singular values used in SVD and/or reducing the number of fit parameters in initial iterations. More recently, Levenberg-Marquadt minimization has been added as a fitting option in LOCO when the problem is too nonlinear for Gauss-Newton minimization [5].

4.11.3 LOCO Fit Parameters

The standard parameters fitting from the orbit response matrix are quadrupole gradients, BPM gains, steering magnet calibrations, skew quadrupole gradients, BPMs' rolls and deformation parameters, steering magnet rolls.

The parameters in blue are primarily associated with the uncoupled quadrants of the response matrix, M, in equation 1 (i.e. the diagonal quadrants giving the horizontal shift at BPMs from changing horizontal steering magnets and the vertical shift when changing vertical steerers). The parameters in red are associated with the coupled, off-diagonal, quadrants of M. The red parameters only need to be included when the coupled parts of the response matrix are included in the fit.

Depending on the desired results or error sources, other parameters that are sometimes fit include: normal and skew gradients in sextupoles or insertion devices, steering magnet or BPM longitudinal positions, and steering magnet energy shifts.

4.11.4 LOCO with Constraints and Improved Fitting Technique

Two ways to improve the LOCO technique have been implemented – the constrained fitting method and the Levenberg-Marquadt algorithm [5-8].

- **LOCO Fitting with Constraints**

The constrained fitting is introduced to cure the degeneracy problem caused by the coupling between fitting parameters (mainly the neighboring quadrupoles). This is a common problem that occurs to many machines in different severity. The constraints are implemented by putting penalties for the step sizes between the solutions of successive iterations. It has been shown to be an efficient way to remove the less restrictive patterns from the solution and it results in fitted lattices with small changes from the starting point. This enables precise control over the machine optics, even for machines where the degeneracy problem has made the original form of LOCO not useful.

- **Levenberg-Marquadt Fitting Algorithm**

The Levenberg-Marquadt algorithm is a robust solver for general nonlinear least square problems. It is useful for LOCO in cases when the initial guessed solution is not close enough to the minimum. In such cases the Gauss-Newton solver may fail because the solution it finds could lie outside of the region where linearization of the model is valid. The Levenberg-Marquadt algorithm is based on the trust-region strategy – the solution it finds is confined in a region where the linear model is valid. The size of the trust region is controlled implicitly or explicitly and is adjusted after every iteration.

4.11.5 LOCO Applications

There are a variety of results that can be achieved with LOCO:

1. Finding actual gradient errors.
2. Finding changes in gradients to correct betas.
3. Finding changes in gradients to correct betas and dispersion.
4. Finding changes in local gradients to correct ID focusing.
5. Finding changes in skew gradients to correct coupling and vertical dispersion η_y.
6. Finding transverse impedance.

These are some of the most common LOCO applications. LOCO can also be used for various other applications, such as beam-based alignment of sextupoles (fitting normal and skew gradients in sextupoles), local chromaticity calibration (fitting response matrices measured at varying RF frequencies), and local transverse impedance measurements.

4.11.6 LOCO Applications to the NSLSII Storage Ring Commissioning

- **Application List**
  1. Calibrate/control optics using orbit response matrix and dispersion(x)
  2. Determine quadrupole gradients (x)
  3. Correct coupling and vertical dispersion (x)
  4. Calibrate BPM gains, steering magnets (to do)
  5. Measure local chromaticity and transverse impedance (to do)

1). Degeneracy Problem and Solution: A general nonlinear least-square problem is to minimize the merit function $f(\mathbf{p}) = \chi^2 = \sum[y_i - y(x_i;\mathbf{p})]^2$where p is a vector of the fitting parameters, (x_i, y_i) are the measured data, and $y(x;p)$ is a nonlinear model function. The error vector is a column vector r whose components are $r_i = y_i - y(x_i;\mathbf{p})$. Jacobian matrix J is defined as, $J_{ij} = \frac{\partial r_i}{\partial p_j}$. Each column of J is the derivative of the error vector with respect to a fitting parameter. In a fitting, two parameters can be deeply coupled, therefore, their contributions to the merit function are indistinguishable. The coupling is characterized by$\rho_{12} = \frac{\mathbf{J_1^T J_2}}{\|\mathbf{J_1}\|\|\mathbf{J_2}\|}$, $\|\cdot\|$ stands for the 2-norm of its argument. In an extreme case, it is impossible to determine the two fitting parameters. Their corresponding columns of J differ by only a scaling (ρ=1). More generally, phase advance between two quads ($\Delta\phi$) determines their coupling strength. Strong coupling occurs when $\Delta\phi \approx n\pi$, here n=0, 1, 2, etc., no matter the two quadrupoles are physically next to each other or separated.

The correlation of QH1 quad (#1) in the lattice with all the quads, including itself, is plotted in Fig. 1. Quad number 1-30, 31-60, 61-90, 91-150, 151-210, 211-240, 241-270, and 271-300 are for QH1, QH2, QH3, QM1, QM2, QL1, QL2, and QL3 quadrupoles respectively.

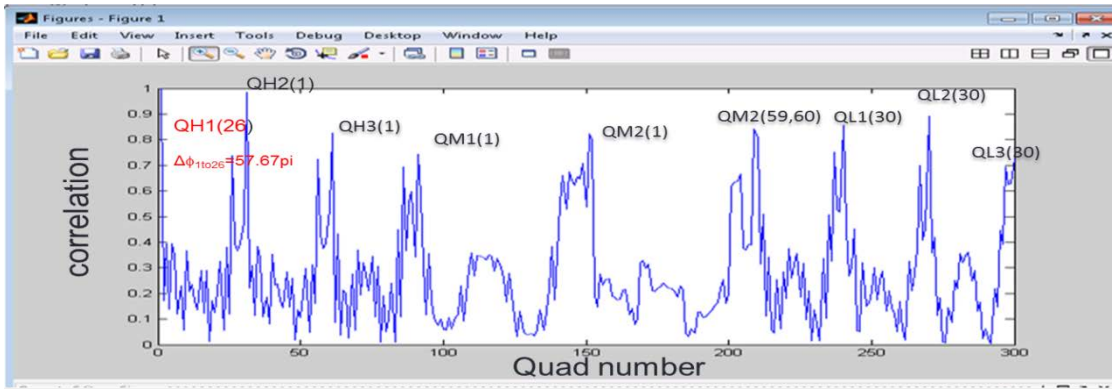

Fig. 1 The correlation of QH1 (#1) quad in the lattice with all the quads including itself.

The correlation peaks appear at the neighboring quadrupoles. LOCO is able to accurately fit the combined integrated gradient of the two magnets but it would not be able to distinguish the individual contributions when ($\Delta\phi \approx n\pi$). No single "best solution". Any solution differs from the global minimum by less than a certain value determined by the noise level is a valid and equivalent solution. Therefore, LOCO is not easy to carry out in NSLSII Storage Ring.

In some cases, LOCO fitting converges to an unrealistic solution with large changes to the quadrupole strengths ΔK. The quadrupole gradient changes can be so large that the resulting lattice model fails to find a closed orbit and subsequent iterations become impossible. It happens in the Storage Ring (SR) commissioning at the shift on April 30th 2014. Scaled Levenberg-Marquardt method was chosen in the LOCO fitting. The solution has ΔK larger than realistic and along with a spurious zigzag pattern between adjacent quadrupoles. Chi-square was reduced by a factor of 400 at the 3rd iteration, the ratio of quadrupole strengths $K(4)$ and the design values $k(1)$ is plotted in Fig.2.

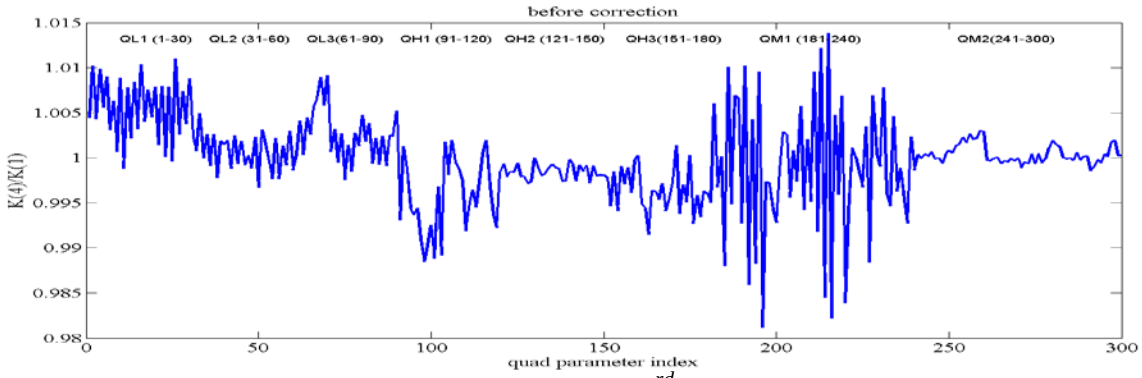

Fig.2 The ratio of quadrupole strengths K(4) at the 3rd iteration and the design values k(1).

The fitting scheme is less restrictive over certain patterns of changes to these quadrupoles with which the correlated quadrupoles fight each other and the net effect is very inefficient $\chi 2$ reduction, i.e., small $\chi 2$ reduction with large changes of ΔK. Such a solution is often not very useful in optics correction because after the solution is dialed in, the quadrupoles do not respond as predicted by the lattice model due to magnet hysteresis.

We will show that adding constraints to the fitting parameters is an effective way to combat this problem of LOCO [6-8]. Optimizing the weights of less constrained fit parameters and applying them for the SR commissioning *via* the following numerical study: In the error lattice, the amplitude of random quad strength errors +/- 0.3% is applied to all the quadrupoles. Quad gradient fit errors, as shown in Fig.3, imply more weights should be given to QL1, QL3, QH1, and QM1 families. We chose ten times larger weight, 0.1, for them.

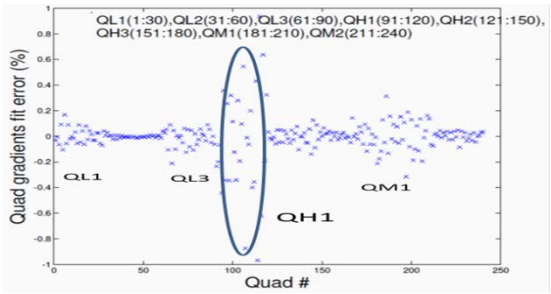

Fig.3 Quad gradient fit error, which is defined as the difference between the quadruple gradient found by LOCO and the gradient in the initial error lattice divided by the gradient in the ideal lattice.

Apply constrains to the LOCO fitting: At the 3rd iteration, chi-square is reduced by a similar amount; however, the ratio of the quadrupole strengths $K(4)$ and the design values $k(1)$ is reduced by a factor three in rms, as shown in Fig.4.

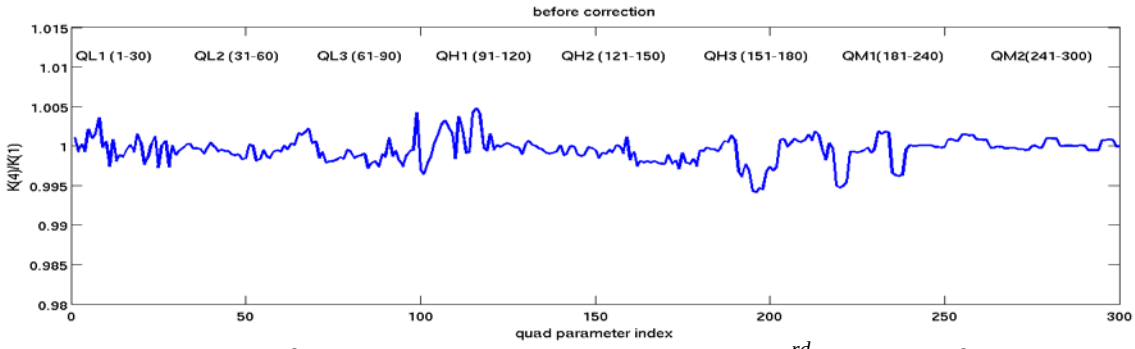

Fig.4 The ratio of the quadrupole strengths K(4) at the 3rd iteration of LOCO fitting with constraints and the design values k(1).

Besides, we have checked the degeneracy of all other fit parameters. There are no correlations between different BPM calibrations and different corrector calibrations. There exist some correlations between quad gradient and BPM calibration, quad gradient and corrector calibration, and corrector and BPM calibrations. They are often small, except the one between corrector and BPM calibrations. However, including the dispersion in the fit can provide an absolute calibration of the BPMs and correctors. Without dispersion there is always degeneracy between the scaling of BPMs and corrector magnets. This will create a small singular value per plane which needs to be removed. If dispersion is included and the RF frequency is not fit (which is often the case since the accuracy of RF changes is usually very good) then the horizontal degeneracy should disappear. If there is substantial vertical dispersion then the vertical degeneracy will also disappear. To force this, the coupling is sometimes increased just to obtain a good vertical BPM calibration. [5].

2). LOCO Improvements

Problems:

- It takes 80min for a complete orbit response matrix (ORM) measurement (360x360). The size of a Jacobian matrix J is (360x360) by n_{fit}. n_{fit} is the number of fit parameters, ~(4x360+300+30).
- SVD(J) is slow, several minutes.

Solutions:

- Implement SVD($J^T \bullet J$) successfully in the routine 'loco.m' before the commissioning. SVD($J^T \bullet J$) takes seconds. Here, the size of ($J^T \bullet J$) is $n_{fit} x n_{fit}$.
- Reduce the number of correctors used in the ORM measurement from 180 per plane to 60 while keeping all the BPMs for maximizing the information in the shift of April, 17th, 2014, no significant degradation appears in the LOCO fitting result since there are still two correctors per betatron period. The time for a LOCO measurement is ~27min, a factor of three less.

It is realistic to apply LOCO for the beta beating and coupling correction since it takes only 30min for an iteration.

3). Beta Beating Correction

Fix twiss using normal quads. Iterate several times!

Apply the LOCO fitting result in Fig. 4 to correct the linear optics. Tunes measured using the turn-by-turn (TBT) data are 33.21 in x and 16.24 in y, and LOCO fitted tunes are 33.207 and 16.243. They agree reasonably well. Beta beat was reduced down to 2.5% (rms) in x, and 4.1% in y. Beta x (top) and beta y (bottom) are shown in Fig.5. Here, red and blue curves are the LOCO fitted result and the design model respectively. Injecting to the SR using this lattice, the injection efficiency improves to ~95 to 96%. Beta beat x (top) and beta beat y (bottom) are shown in Fig.6.

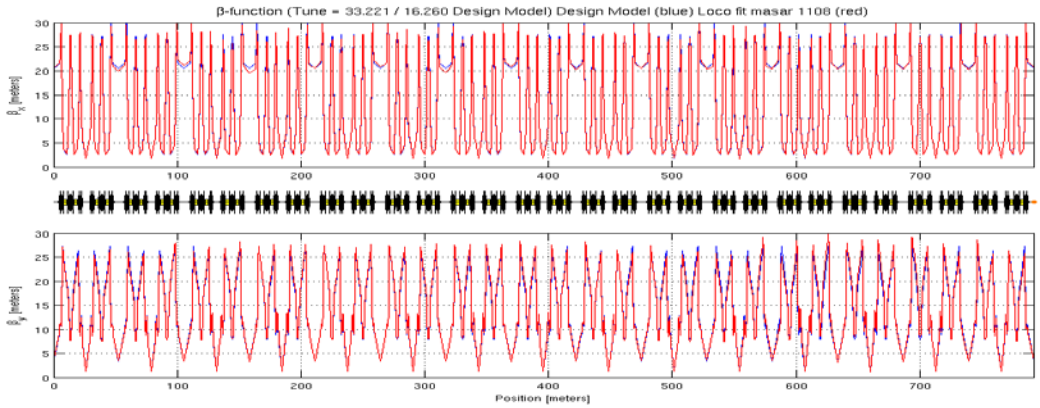

Fig.5 Beta x (top) and beta y (bottom). Here, red and blue curves are the LOCO fitted result and the design model respectively.

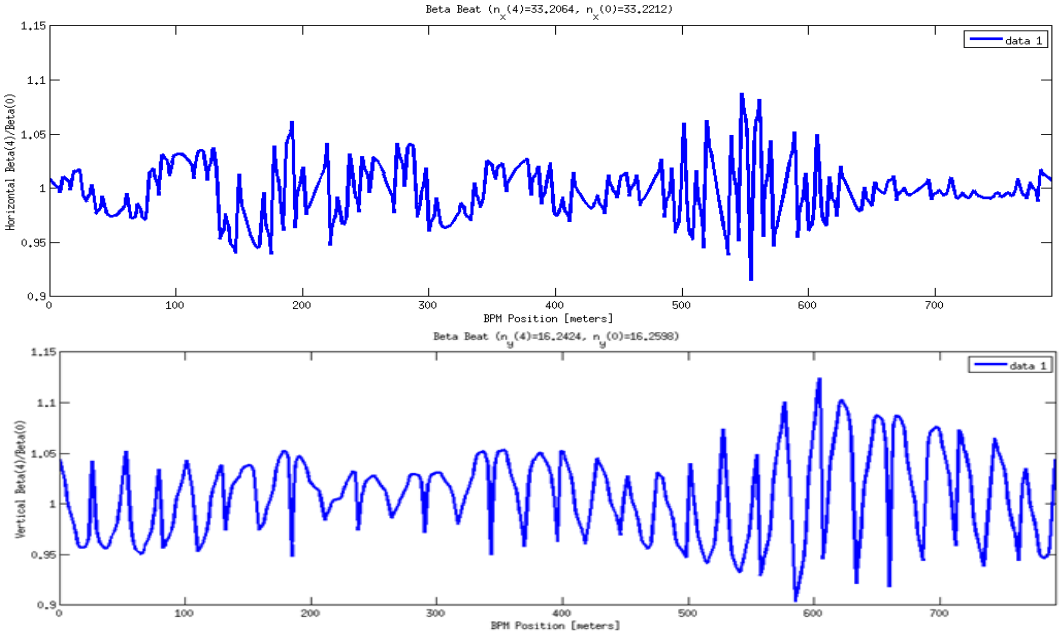

Fig.6 Beta beat x (top) and beta beat y (bottom). Beta beat is defined as the ratio of the beta at the 3rd iteration of the LOCO fitting and the design beta.

Apply the LOCO correction again for the purpose of bringing the tunes closer to the design values. The TBT measured tunes are 33.22 and 16.25. The LOCO fitted tunes are 33.217 and 16.252. They agree well. Beta beat is corrected down to 2.7% (rms) in x, and 3.1% in y. Beta x (top) and beta y (bottom), as shown in Fig 7, red and blue curves are the LOCO fitted beta and design model beta respectively.

Injecting using this lattice, the injection efficiency further improves to ~99%.

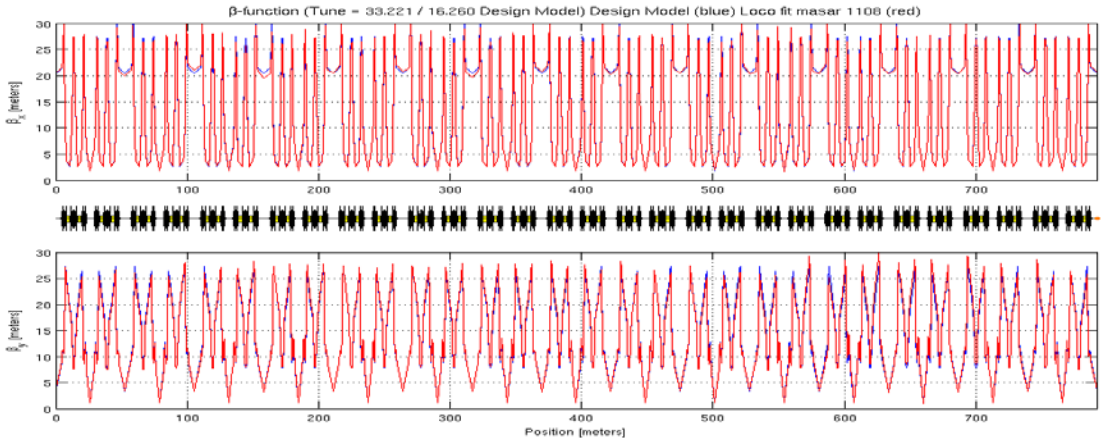

Fig.7 Beta x (top) and beta y (bottom). Red and blue curves are the LOCO fitted beta and ideal model beta respectively.

After the beta beating correction, the changes of all the quad strengths relative to their design values are plotted in Fig.8, each quadrupole family per plot.

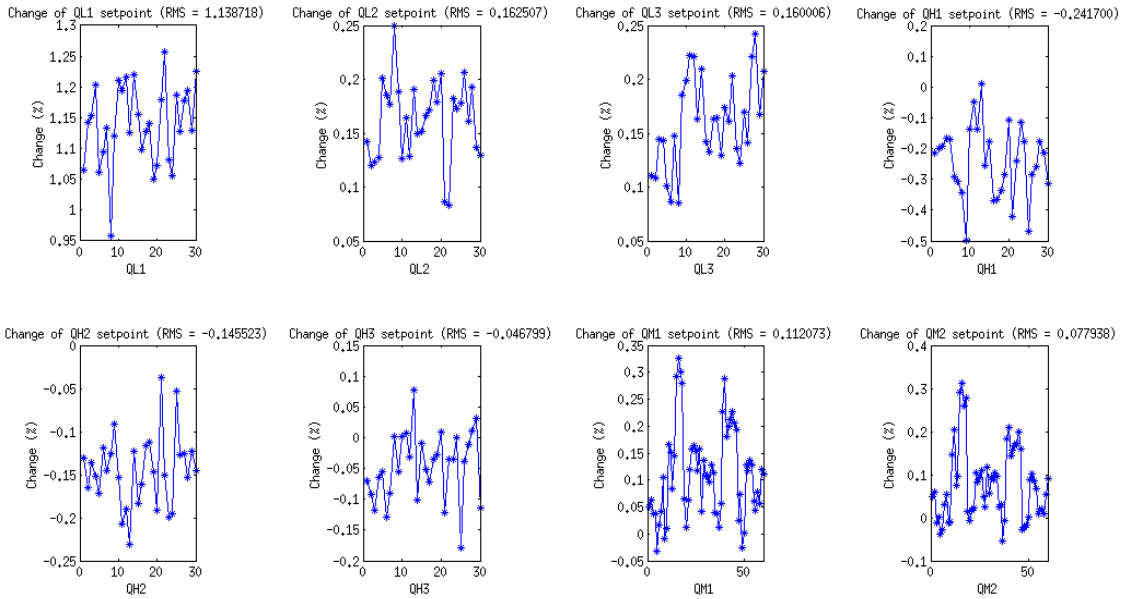

Fig.8 The change of quad strengths relative to their design values in %, each quad family per plot.

4). Coupling and vertical dispersion correction:

Sources of dispersion:

There are two main terms that can create vertical dispersion:

$$\eta_y'' + K\eta_y = \frac{1}{\rho_y} - K_s\eta_x$$

– Dipole errors (steering magnets, misalignments, …) or intentional vertical bending magnets
– Skew quadrupole fields at the location of horizontal dispersion (due to quadrupole tilts, or vertical offsets in sextupoles)[9]

$$\kappa_{\eta_y} = \int ds\, K_s \eta_x \sqrt{\beta_y}\, e^{i\phi_{\eta_y}}$$

$$\frac{\phi_{\eta_y}}{2\pi} = \mu_y(s) - \frac{s}{C}(\nu_y - 5)$$

Vertical dispersion directly causes the increase of the vertical emittance by quantum excitation.

Dispersion correction scales like product of horizontal dispersion times the square root of vertical beta function time skew quadrupole strength. Dispersion from steering magnets scales like the bending angle.

Use accelerator toolbox (Andrei Terebilo) and Matlab LOCO for the simulations.
Response Matrix fitting -'deterministic', small number of iterations.

Optimize weight of dispersion in LOCO fit

- The relative contribution of vertical dispersion and coupling to the vertical emittance depends on the particular lattice (and the particular error distribution).
- Therefore the optimum weight for the dispersion in the LOCO fit has to be determined (experimentally or in simulations).
- The larger the weight factor, the better the vertical dispersion gets corrected, but eventually the coupling 'explodes'.

Set weight to optimum somewhat below that point.
In the SR commission, we set comparably large weight ~60 (5 times higher than the LOCO default value) on the vertical dispersion in order to correct vertical dispersion effectively. As shown in Fig.9, the vertical dispersion was significantly reduced from the blue curve (before the correction) to the red curve (after the correction). Further increasing the weight doesn't reduce the vertical dispersion and made the x-y coupling worse.

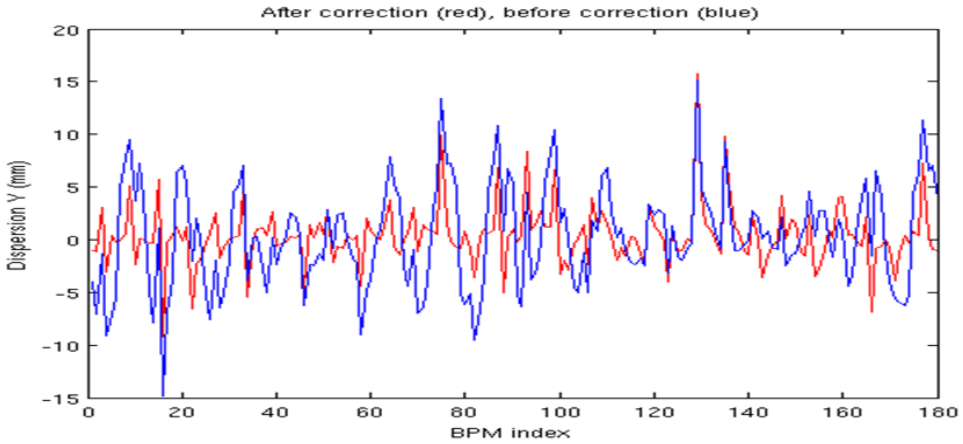

Fig.9. The vertical dispersion before the correction (blue) and after the correction (red).

The coupling calculated using the LOCO fitted machine model is ~0.3% after the beta beating and vertical dispersion correction. The equilibrium beam envelope is calculated using Ohmi's beam envelope formalism [10]. The coupling is defined as the ratio of the mean vertical and horizontal beam emittance.

Radiation-Diffusion matrix is calculated only for the elements with radiation, including dipoles, quadrupoles, and sextupoles, and set to zero for the rest elements. The cumulative radiation-diffusion matrix at the ring entrance is needed for the envelope matrix calculation. The equilibrium beam envelope, including 6-by-6 equilibrium envelope matrix, tilt angle of the XY ellipse, and rms size along the principal axis of a tilted ellipse, is obtained for each ring element. The tilt in degree (top left), emittance x in nm·rad (top right), emittance y (bottom right), and horizontal and vertical beam sizes in μm (bottom left) are shown in Fig.10.

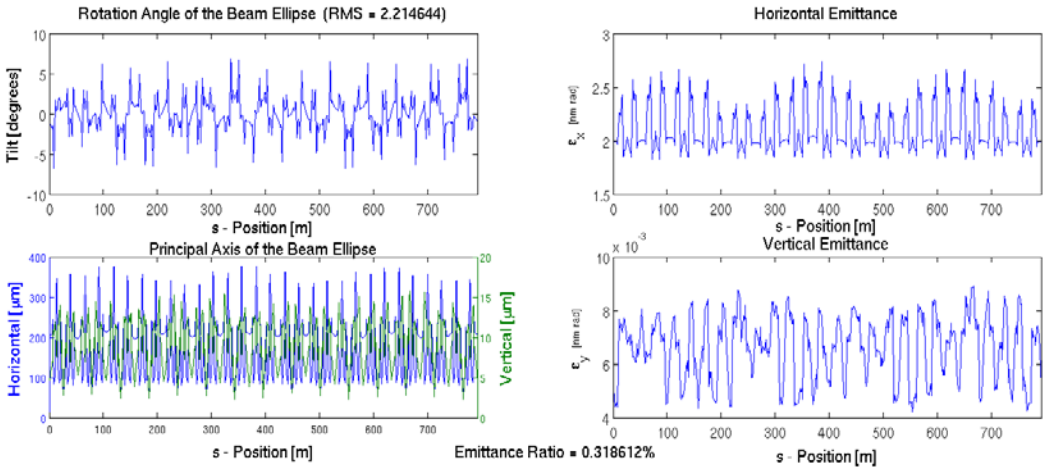

Fig.10 The tilt in degree (top left), emittance x in nm·rad (top right), emittance y (bottom right), and horizontal and vertical beam sizes in μm (bottom left).

4.11.7 TBT twiss measurement

NSLSII SR is equipped with multiple TBT BPMs. The TBT beam position signal is a combination of various source signals. $\mathbf{x}(t) = \mathbf{A}\mathbf{s}(t) + \mathbf{n}(t)$. $\mathbf{A}$ is the mixing matrix. There are only a few meaningful source signals, such as betatron oscillation and synchrotron oscillation. Form a matrix of the BPM data

$$\mathbf{X} = \begin{pmatrix} x_1(1) & x_1(2) & \cdots & x_1(T) \\ x_2(1) & x_2(2) & \cdots & x_2(T) \\ \vdots & \vdots & \ddots & \vdots \\ x_m(1) & x_m(2) & \cdots & x_m(T) \end{pmatrix}$$

, m BPMs and T turns [11,12].

It has been proven [13] that when the BPM reading contains only one betatron mode, i.e.

$$x_m(t) = \sqrt{2J(t)\beta_m}\cos(\phi(t) + \psi_m) .$$

Then there are only two non-trivial SVD eigen-modes because each BPM sees different phase.

$$\mathbf{x} = \mathbf{U}\mathbf{S}\mathbf{V}^{\mathrm{T}} = s_+\mathbf{u}_+\mathbf{v}_+^{\mathrm{T}} + s_-\mathbf{u}_-\mathbf{v}_-^{\mathrm{T}}$$

$$u_{+,m} = \frac{1}{s_+}\sqrt{<J>\beta_m}\cos(\phi_0 + \psi_m), \qquad v_+(t) = \sqrt{\frac{2J(t)}{T<J>}}\cos(\phi(t) - \phi_0),$$

$$u_{-,m} = \frac{1}{s_-}\sqrt{<J>\beta_m}\sin(\phi_0 + \psi_m) \qquad v_-(t) = -\sqrt{\frac{2J(t)}{T<J>}}\sin(\phi(t) - \phi_0)$$

u: spatial vector **v**: temporal vector

Beta function and betatron phase advance can be calculated from the spatial vector.

$$\psi_m = \tan^{-1}\left(\frac{s_-u_{-,m}}{s_+u_{+,m}}\right) \qquad \beta_m = \frac{1}{<J>}[(s_+u_{+,m})^2 + (s_-u_{-,m})^2]$$

Independent Component Analysis (ICA) for TBT Data Analysis

What SVD essentially does is to de-correlate the sample data to find an orthogonal basis to reinterpret the sample data. Although there are numerous transformations that de-correlate the sample data, the result is unique because SVD makes sure the first component has the largest variance and the second component has the second largest variance and so on. However, SVD does not guarantee separation of the source signals, especially when the singular values (SVs)

approach each other, SVD always produces modes with mixing. On the other hand, ICA does not show any dependence on the relative magnitudes of the SVs. ICA makes use of the fact that the power spectra of source signals are distinct and the autocorrelation covariance matrices are diagonal to find the source signals [11].

ICA method can de-couple the normal modes in the presence of linear coupling. It finds the paired betatron modes automatically, as shown in Fig.11, beta x mode (left) and beta y mode (right); therefore, the phase and beta at all the BPM positions are obtained.

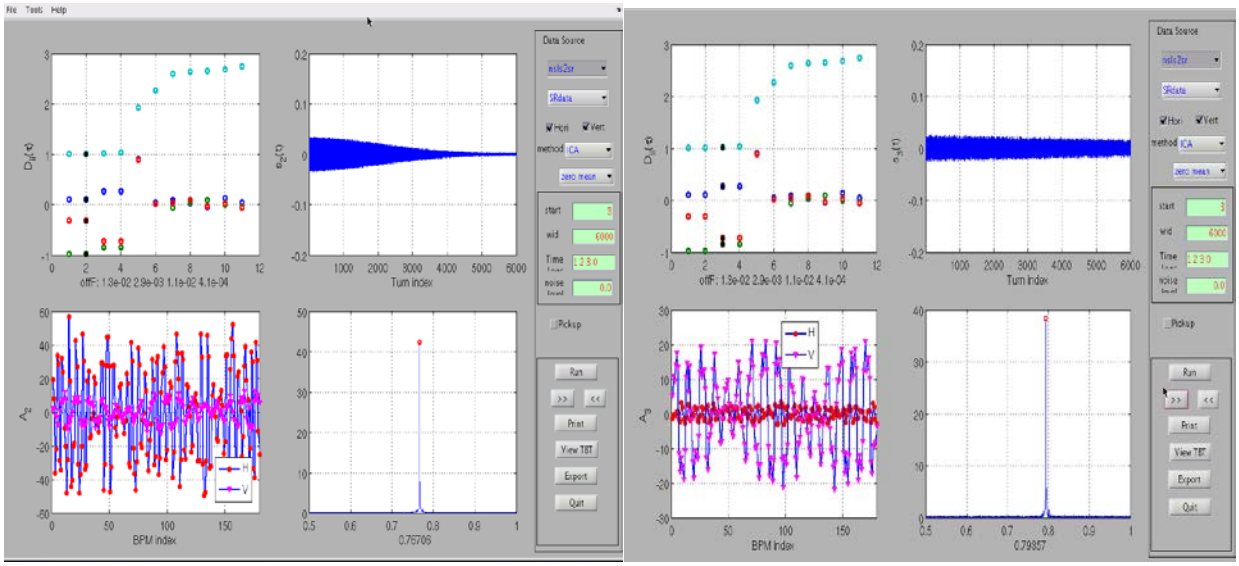

Fig.11 Beta x mode (left) and beta y mode (right). There are four figures for each of them. We label the top left figure as Figure 1 and other figures Figure 2, 3, 4, clockwise.

Figure 1 shows the diagonal elements after joint approximate diagonalization for each mode. Different colors are used for the time-lags. The current mode is marked with '*'. Two modes are paired if their diagonal elements are the same. Figure 2 shows the temporal pattern, which is normalized so that ||s||=1. Figure 3 shows the FFT of the temporal pattern. A red circle is used to mark the peak frequency, which is shown in x-label, too. Figure 4 shows the spatial pattern. If both horizontal and vertical data are used, there will be two curves with different colors, red for H, magenta for V.

The TBT and ORM data were taken at the shift on April 18th 2014. Beta beats fitted by LOCO (blue) and measured by TBT data (red) are shown in Fig. 12, beta beat in x (left) and beta beat in y (right). They are in a reasonably good agreement. The LOCO fitted tunes are 0.2263/0.1997, and the TBT measured tunes are 0.2329/0.2064. The agreement on the tunes is not as good as the measurements, which were done after the beta beating correction and are described in ‘Beta Beat Correction’.

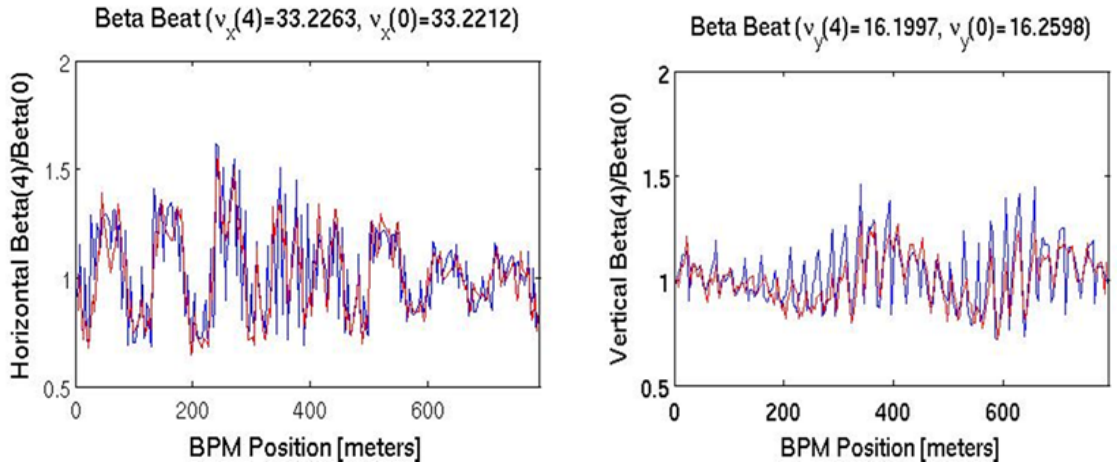

Fig.12 Beta beats fitted by LOCO (blue) and measured by TBT data (red). Beta beat x (left) and beta beat y (right).

For the two different approaches of the beta beating correction: LOCO and TBT method, the strategy is to apply the TBT method to correct beta beating down to a several-percentage level since it is faster; afterwards, apply LOCO to correct beta beating further down to a sub-percentage level. This two-step approach has been approved successfully in the SR commissioning.

Acknowledges:
Special thanks to Xiaobiao Huang for many productive discussions and share his tool kit with me, and James A. Safranek for getting me started on LOCO, also many useful discussions.

References:

1. J. Safranek, "Experimental determination of storage ring optics using closed orbit response measurements", Nucl. Inst. and Meth. A388, (1997), pg. 27.
2. J. Safranek, G. Portmann, A. Terebilo, C. Steier, "MATLAB-based LOCO", proceedings of the 2002 European Particle Accelerator Conference, Paris, France (2002).
3. A. Terebilo, "Accelerator Toolbox (AT)", http://www.slac.stanford.edu/~terebilo/at/.
4. Numerical Recipes, Cambridge University Press.
5. X. Huang, et al., "LOCO with constraints and improved fitting technique", Beam Dynamics Newsletter No. 44.
6. X. Huang, Indiana University PhD thesis (unpublished), 2005
7. X. Huang, et al, "Fitting the fully coupled ORM for the Fermilab Booster", Proceedings of PAC05, Knoxville, TN
8. X. Huang, et al, "Low alpha mode for SPEAR3", Proceedings of PAC07, Albuquerque, NM
9.Christoph Steier, "Linear Lattice Correction: Coupling", USPAS 2012 Summer – Beam based diagnostics
10. K. Ohmi et al, Phys. Rev. E, Vol.49,1994.
11. X. Huang, PRSTAB, 8, 064001, 2005.
12. X. Huang, "Model independent analysis and independent component analysis for BPM data analysis", USPAS 2012 Summer – Beam based diagnostics
13. Chun-xi Wang, et al. PR-STAB 6, 104001 (2003).

4.12 RF System Commissioning with Beam

The RF system configured for storage ring commissioning mainly consists of a 500MHz PETRA type normal conducting 7-cell cavity, a 310kW CW transmitter equipped with a klystron tube, and a FPGA based cavity field controller (CFC) for the low level RF (LLRF) control. The 7-cell cavity took the position of the upstream CESR-B type superconducting cavity which was being assembled and tested separately at that time. The 7-cell cavity has two tuners used for controlling the resonant frequency and field balance. Transmitter D, the one close to the NSLS-II clean room and the computer room, is used to power the 7-cell cavity, while transmitter C is reserved for blockhouse tests. A high power circulator with a reject load was installed between the transmitter and the cavity so that full reflection from cavity will not cause any damage to the transmitter. The CFC generates the LLRF drive signal and can run in both feed forward mode and feedback modes. In the feedback mode the cavity field amplitude and phase can be regulated to specified values.

4.12.1 The 7 cell PETRA type cavity

Figure 1 shows the PETRA type 7-cell cavity just removed from the beam line. It consists of 7 water cooled cells, where the two plunger tuners are located on cell #2 and cell #6, and the three cavity field pickups located on cell #2, cell #4 and cell #6. The input port has a coaxial coupler so that an adapter piece is used to convert from a waveguide to the coax. The fundamental mode is pi-mode based on TM010 pattern. Higher order modes (HOMs) have also been studied.

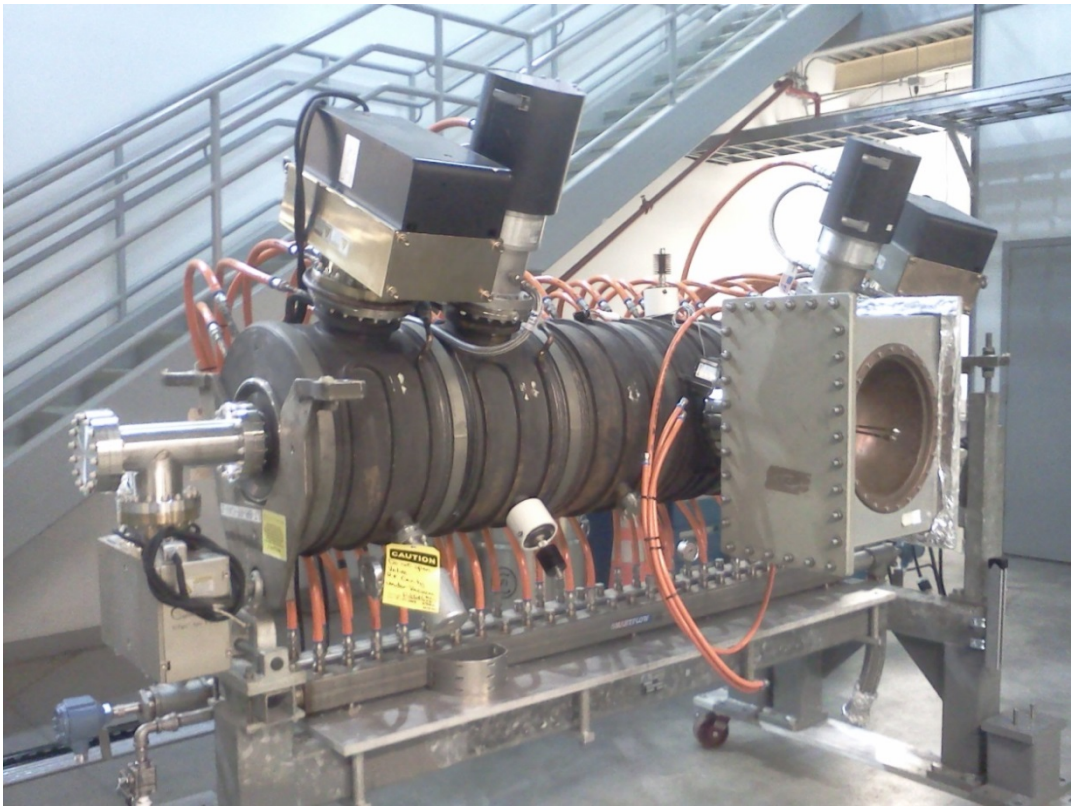

Figure 1. The PETRA type 7-cell cavity

The fundamental mode

The 7-cell cavity fundamental mode properties are listed in Table 1. It needs to be pointed out that the coupling strength of the input port to the cavity has changed from 1.65 at atmosphere to 1.52 when the cavity is under vacuum. Figure 2 shows the fundamental mode field balance tuned by adjusting the tuners and monitored with bead pull. Figure 3 shows the Smith chart of Q0 measurement.

Frequency (MHz)	499.68 nominal
r/Q (Ω)	798
Q0	29700
Rsh (MΩ)	23.7
Voltage for commissioning Vc (MV)	2.0
Input port coupling strength β	1.53 under vacuum
QL	11700
Cavity power (kW)	84.4
Beam energy (GeV)	3.0
Beam energy loss per turn Va (kV)	288
Beam current (mA)	25
Momentum compaction	3.7e-4
Synchronous phase $\cos^{-1}$(Va/Vc)	81.72°
Beam power (kW)	7.2
Forward power (kW)	94.3
Reverse power (kW)	2.7
Detuning angle	-13.05°
Detuning frequency (kHz)	-4.93
Synchrotron frequency (Hz)	2711
Synchrotron tune	7.16e-3

Table 1. The 7-cell cavity properties for storage ring commissioning

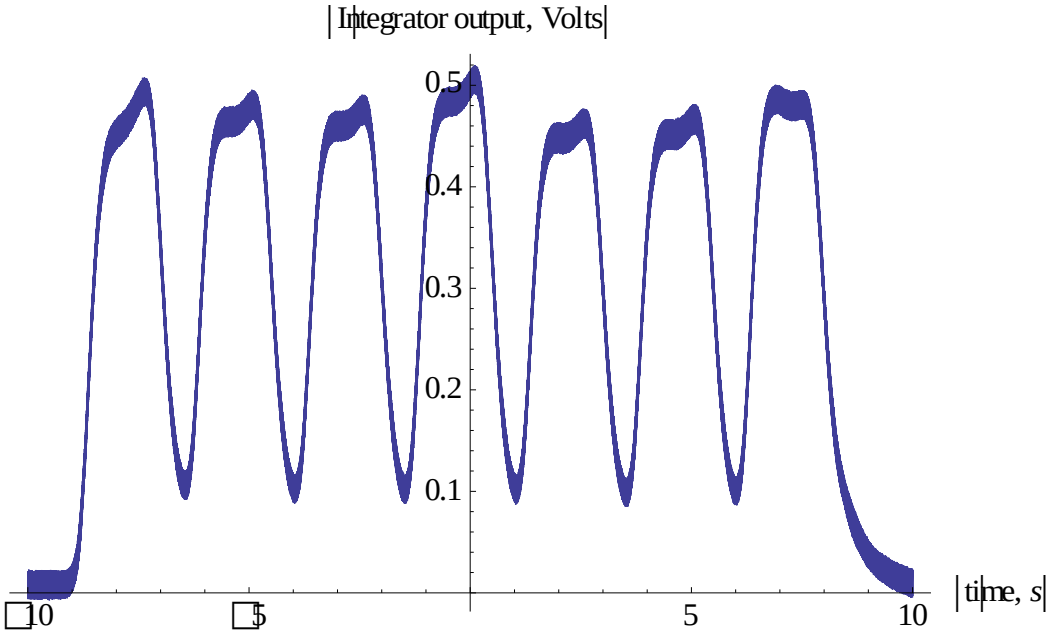

Figure 2. Field balance of the 7-cell cavity

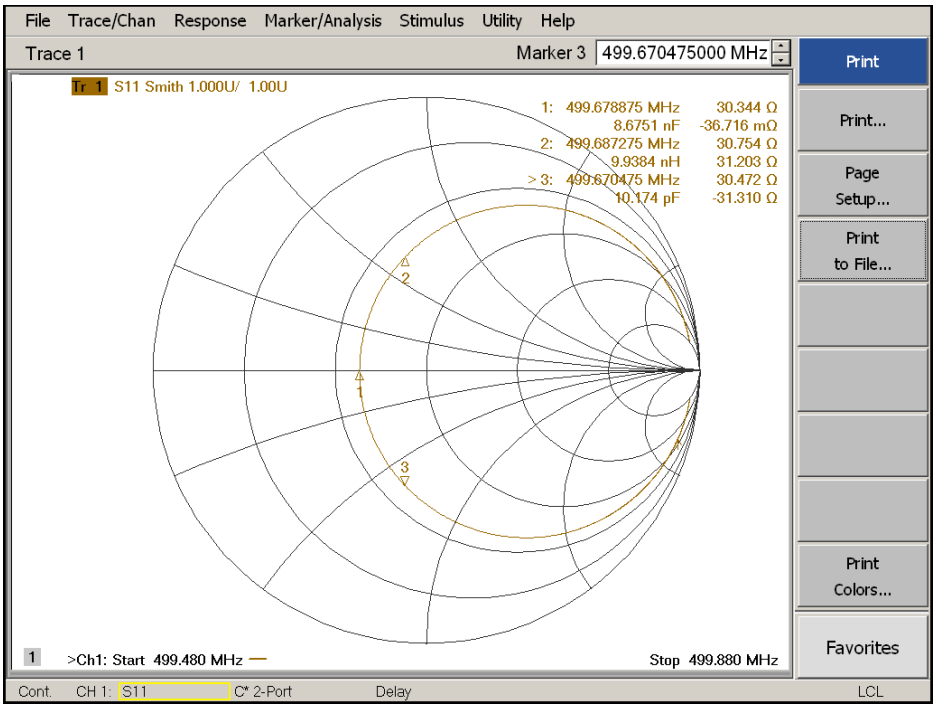

Figure 3. Q0 measurement of the 7-cell cavity

Higher order modes

The 7-cell cavity was not originally designed for storage ring operation, therefore in design its HOMs was not specifically optimized for high current cases. For NSLS-II storage ring commissioning, these HOMs have been extensively studied with both simulations and experiments, and the effects of the HOMs on the beam have been minimized by manipulating cavity water cooling temperature as well as both plunger tuners.

Figures 4-6 shows the three main HOM bands of the cavity at 85°F. These HOM peaks need to be tuned away from the revolution lines, the synchrotron side bands and betatron side bands to avoid undesired instabilities on the beam. Figure 7 shows an example of identifying a HOM with both simulation and beadpull.

Prior to the cavity being installed into the tunnel, the two tuners were adjusted independently to optimize the HOM spectra. Then the two tuners are locked to each other and move together for frequency compensation. The cavity cooling water inlet temperature was adjusted in situ during ring commissioning to further optimize the performance.

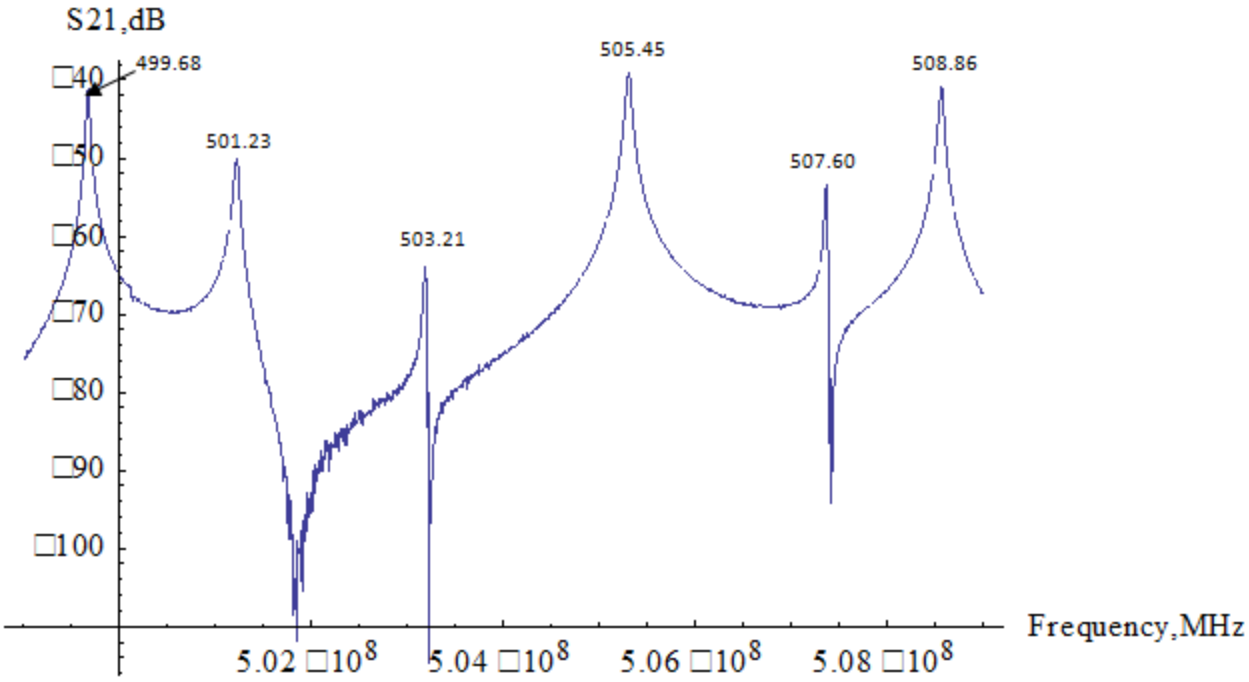

Figure 4. Frequency spectrum at cavity temperature of 85^0F. Range 499MHz to 509MHz

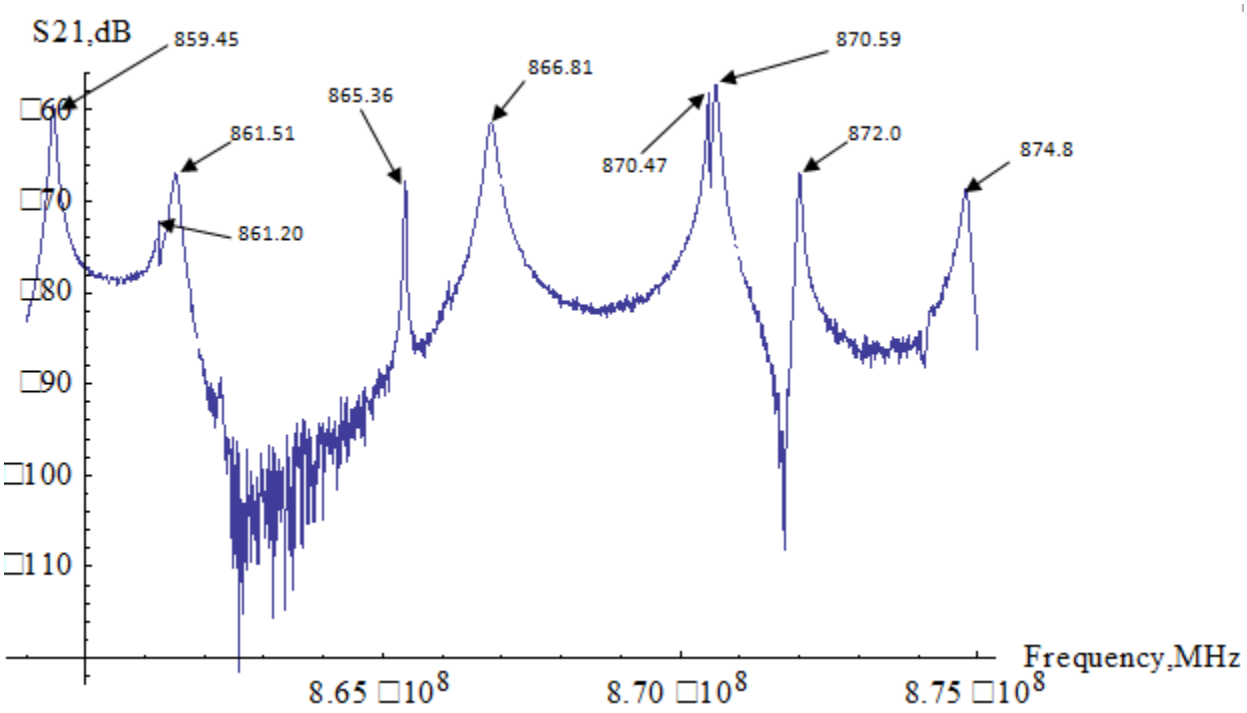

Figure 5. Frequency spectrum at cavity temperature of 85^0F. Range 859MHz to 875MHz

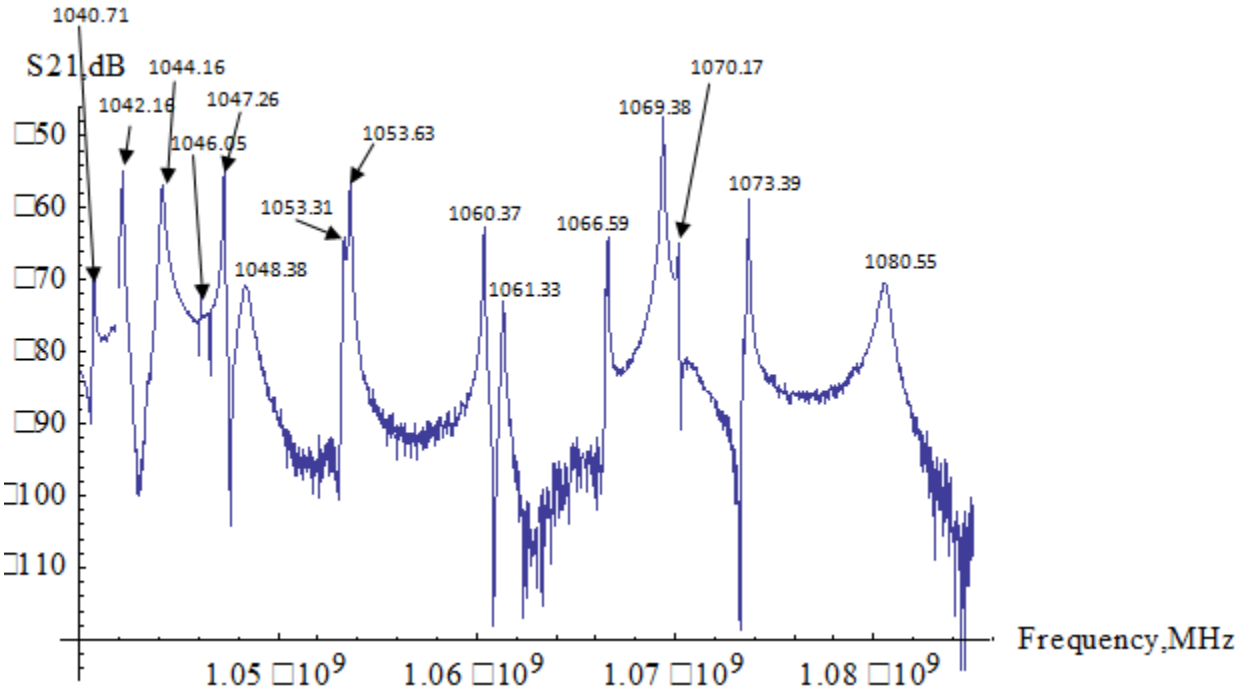

Figure 6. Frequency spectrum at cavity temperature of 85^{0}F. Range 1040MHz to 1085MHz

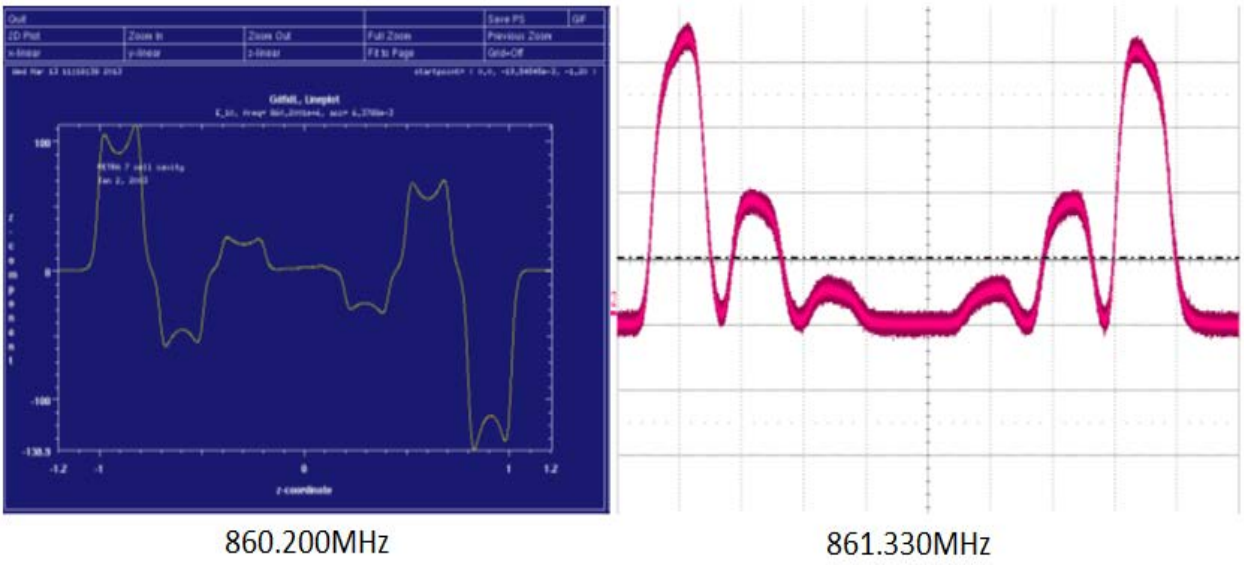

Figure 7. An example showing a HOM was identified with both simulation (left) and beadpull (right)

4.12.2 The 310kW transmitter

The 310kW transmitter works very well without much surprise. There are some alarms whose descriptions need to be made visible at the EPICS GUI. Also accurate timers between

stages of the transmitter state and machine would help the control room to determine time elapsed. One thing we have noticed is that when one of the klystron power supply switching frequency harmonics and the synchrotron frequency are close to each other, the stronger horizontal beam synchrotron oscillation is observed at high current. This is explained below.

Interference between the power supply switching harmonics and the beam synchrotron frequency

The transmitter's power supply switching unit has a switching frequency of 1.325kHz. The harmonics of 1.325 kHz are visible on the cavity power spectrum. In particular, the 2nd harmonic frequency 2.65 kHz, is very close to the beam nominal synchrotron oscillation frequency 2.7 kHz at 2 MV cavity voltage. As the cavity voltage is being adjusted, the synchrotron frequency moves to the 2nd harmonic. Figure 8 shows when the synchrotron frequency is 2.715 kHz which is away from the 2nd switching harmonic, it is clean and little horizontal beam oscillation is observed. Figure 9 shows when the synchrotron frequency is 2.67 kHz which is very close to the 2nd switching harmonic, the peak is significantly widened and the beam horizontal oscillation became significantly stronger (Figure 10 and 11). It is most likely that this beam oscillation has a different cause than the switching harmonic which is over -80 dB below the carrier. However, it would be good to avoid the overlap between the synchrotron frequency and the 2nd switching harmonic. One solution is to adjust the switching frequency for various operation scenarios. The switching frequency is designed to be adjustable and the approach is being investigated.

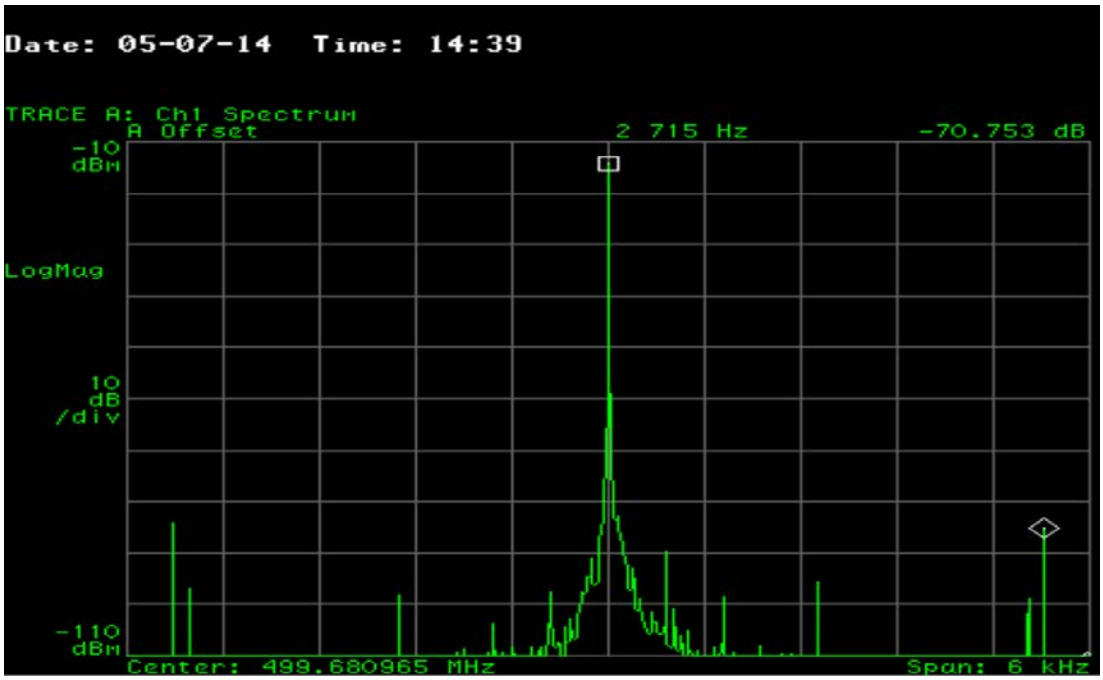

Figure 8. The synchrotron oscillation peak 2.715kHz is clean when away from the 2nd switching harmonic 2.65kHz.

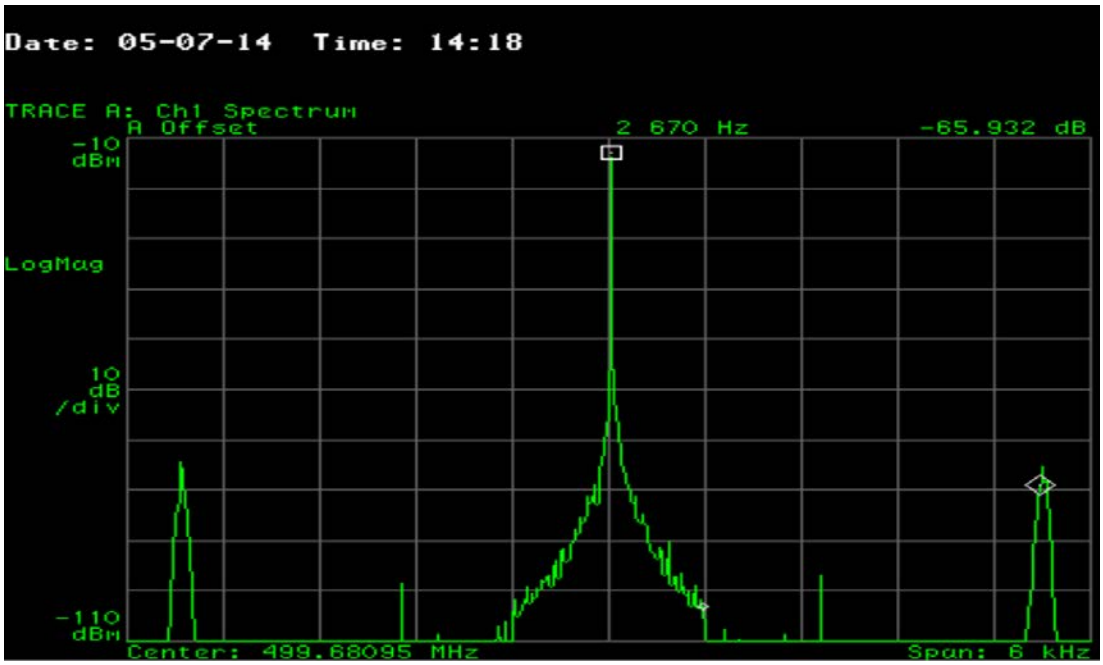

Figure 9. The synchrotron oscillation peak 2.67kHz is widened due to beam instability. Large beam horizontal oscillation is observed with a BPM.

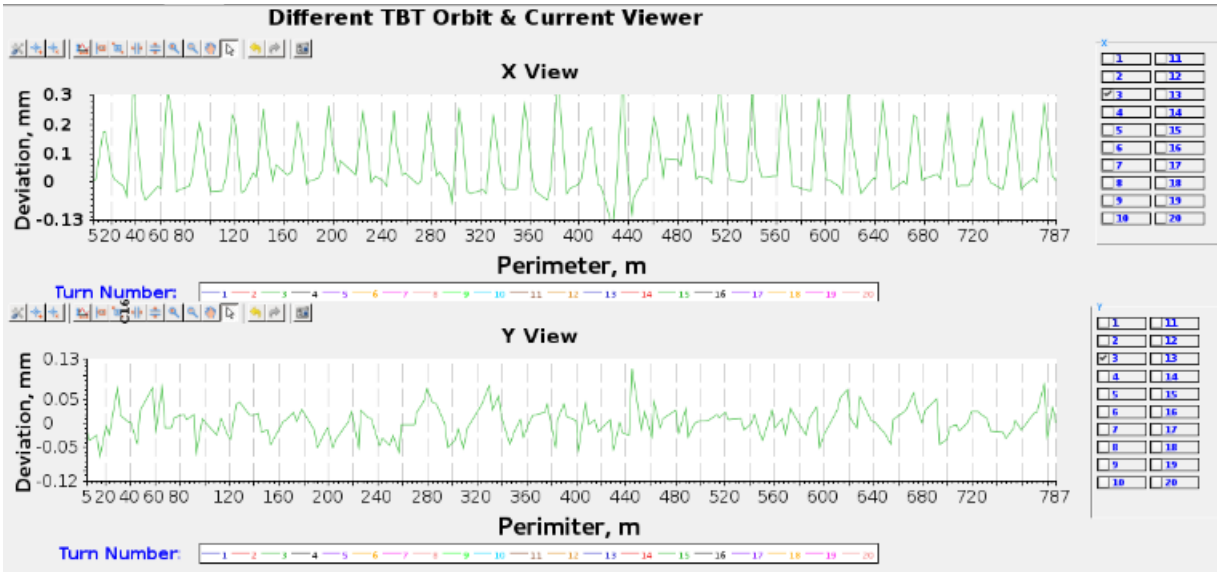

Figure 10: SR BPMs' transverse oscillation shows the energy modulation at high beam current

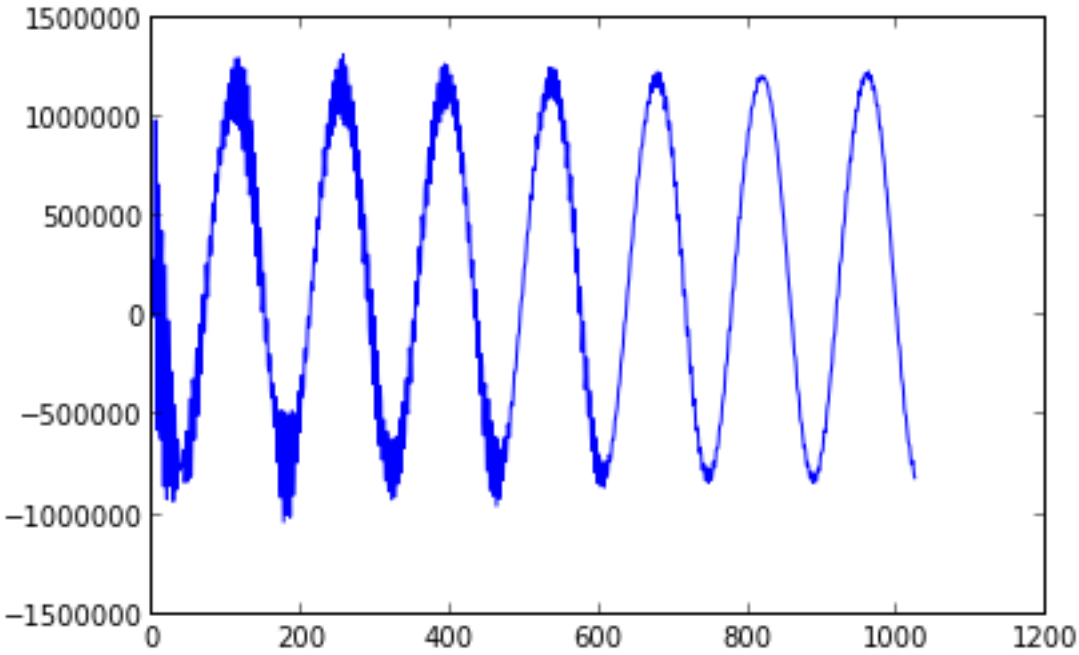

Figure 11: Dispersion region BPM shows synchrotron oscillation at high current

4.12.3 The cavity field controller

The cavity field controller (CFC) is a FPGA based LLRF control module specifically tuned for storage ring operation. Figure 10 shows the EPICS GUI of the CFC. It has both feed forward and feedback modes. In the feedback mode, the cavity field amplitude and phase are maintained to pre-specified values via a proportional-integral control loop (PI loop). The CFC has pre-built functions in the feed forward control, which are very helpful for both cavity conditioning and PI loop optimization. It can also use a data array as feed forward excitation, where the residual not removed by the PI loop can be used to manipulate beam. Furthermore, it has scope functions to monitor various RF channels, and a circular buffer to store pre- and postmortem data of a system trip for diagnostics and troubleshooting.

Figure 11 gives an example of using the CFC to shake the beam. In this configuration both the feed forward and feedback switches are at “enable” position. This means the feed forward input tries to disturb the cavity field while the feedback loop tries to keep the field steady. Here the feed forward excitation has fixed amplitude and a phase profile modulated at 5.49kHz, approximately twice the synchrotron frequency. With properly chosen proportional-integral coefficients, kp and ki, there will be some residuals of the phase modulation excitation left in the cavity field, and quad pumping of the beam could be performed. Furthermore, both the amplitude and phase of the feed forward excitation can be programed to implement certain functions. In principle, the amplitude and phase of the cavity field can also be shaped in the feedback mode, just like that for the boosting RF. However this path has not been fully explored for the storage version CFC yet.

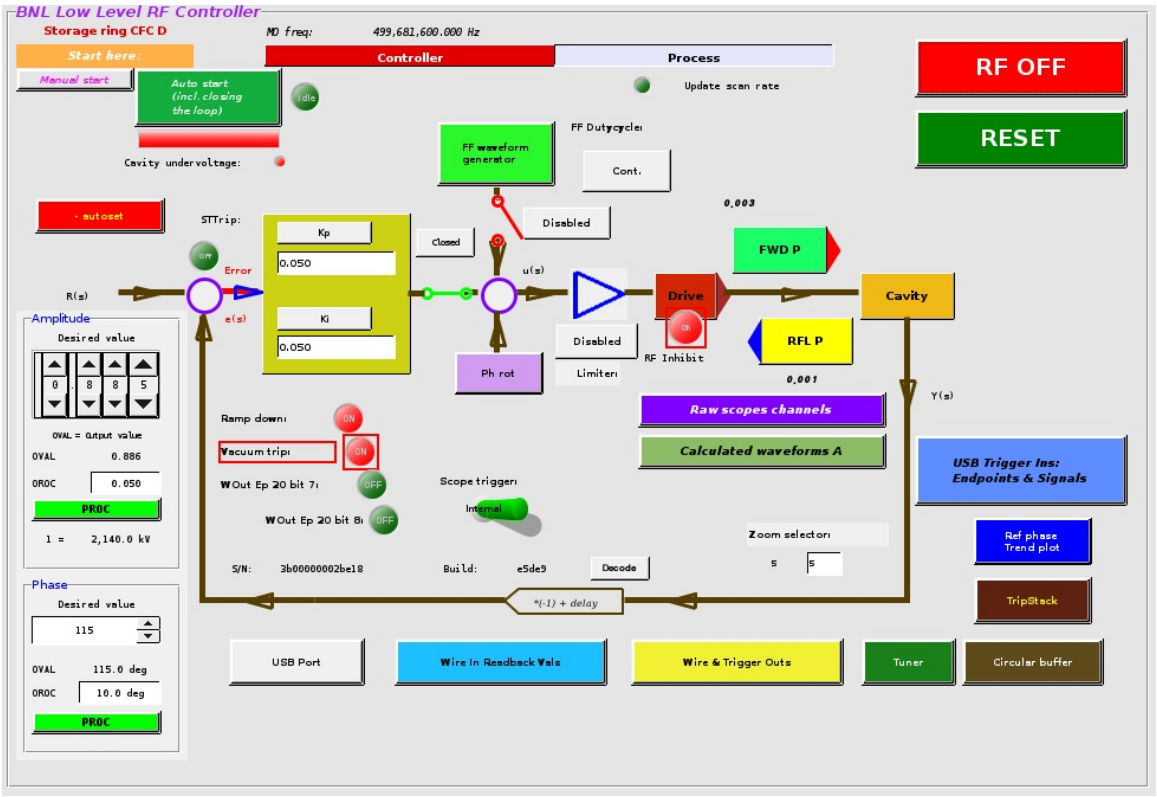

Figure 10. The cavity field controller GUI

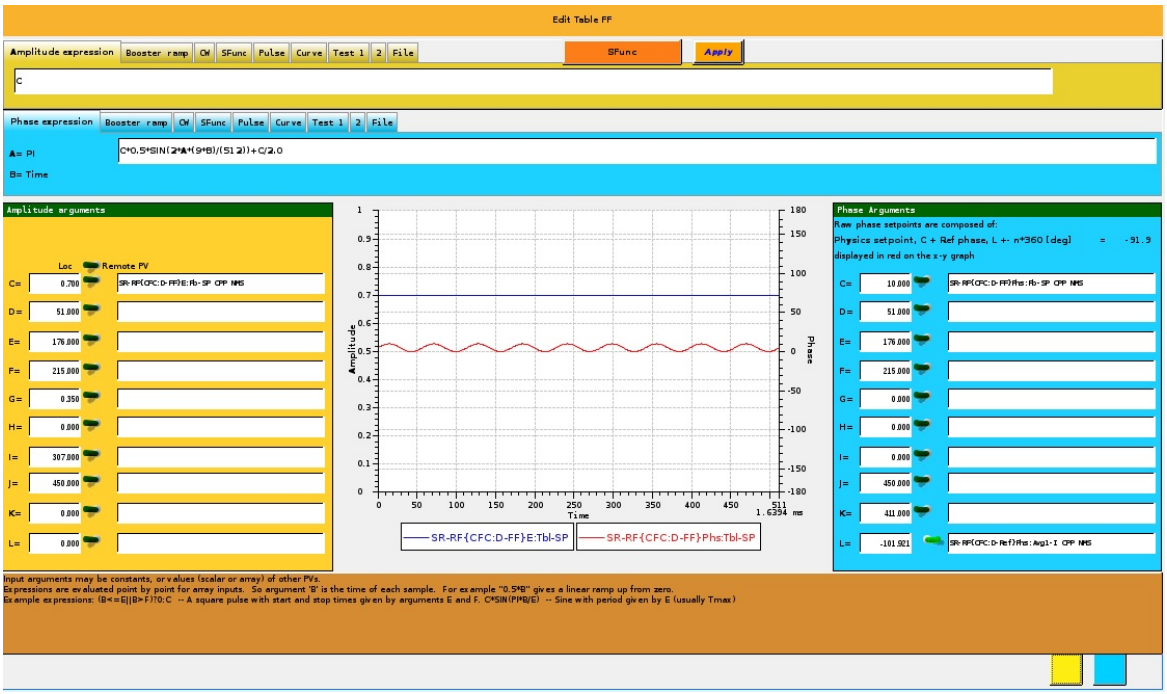

Figure 11. Cavity field phase modulation at twice the synchrotron frequency, via feed forward phase excitation. The phase modulation strength is exaggerated to show the variation.

4.13 Diagnostics Commissioning with Beam

This chapter summarizes the storage ring diagnostic systems commissioning results. The following diagnostic systems are available in NSLS2 storage ring:

1. IS flag, multi-position flag to see injection beam and/or one turn beam;
2. DCCT, measure the total stored beam current and lifetime;
3. FPM, measure the bunch to bunch filling pattern;
4. LCM, loss control monitor, including scrapers and Cherenkov beam loss monitors;
5. TMS, tune measurement using sweeping method;
6. BxB feedback, to suppress the transverse beam instabilities;
7. SLM, visible synchrotron light monitor;
8. BPM, measure beam orbit and trajectory
9. XDB, x-ray diagnostic beamline;

TMS, BxB feedback and BPM commissioning results are discussed in other chapters. As a completion of this chapter, we present some of the commissioning results of these systems here as well. X-ray diagnostic beamline was not ready for phase I commissioning, it will not be discussed in this report.

4.13.1 IS Flag

Figure 1-1 shows the installed diagnostic components in the storage ring injection straight (C30). There are four special BPMs in the injection straight to measure the bumped store beam. Fifth BPM called BtS P9 is centered with the injecting beam. Multi-position flag is available to monitor the beam profile/centroid, for the injecting beam and one turn beam. Injection straight flag, BtS P9, IS P3 and P4 will see the beam at very early stage of commissioning.

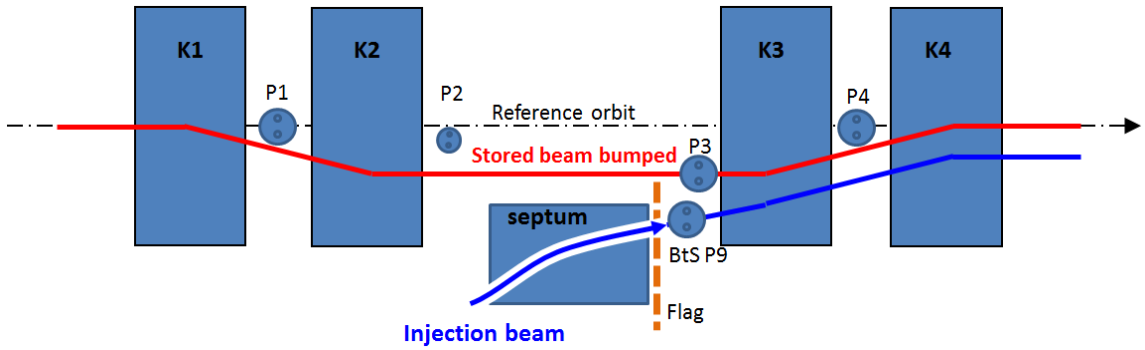

Figure 1-1, Overview of diagnostics in storage ring injection straight

YAG screen is used for the IS flag, the screen is installed at 45 deg so that electron beam generated florescent light can be easily visualized. The light passes through the vacuum window and reflected down towards the CCD camera. f = 75mm lens is used in front of the camera. YAG screen assembly and CCD camera are mounted on linear stages and movable by linear motor. The screen has full travel range of 75mm and the camera can be traveled by 100mm. This way the screen can be positioned to see injection/one-turn beam and the image is always focused.

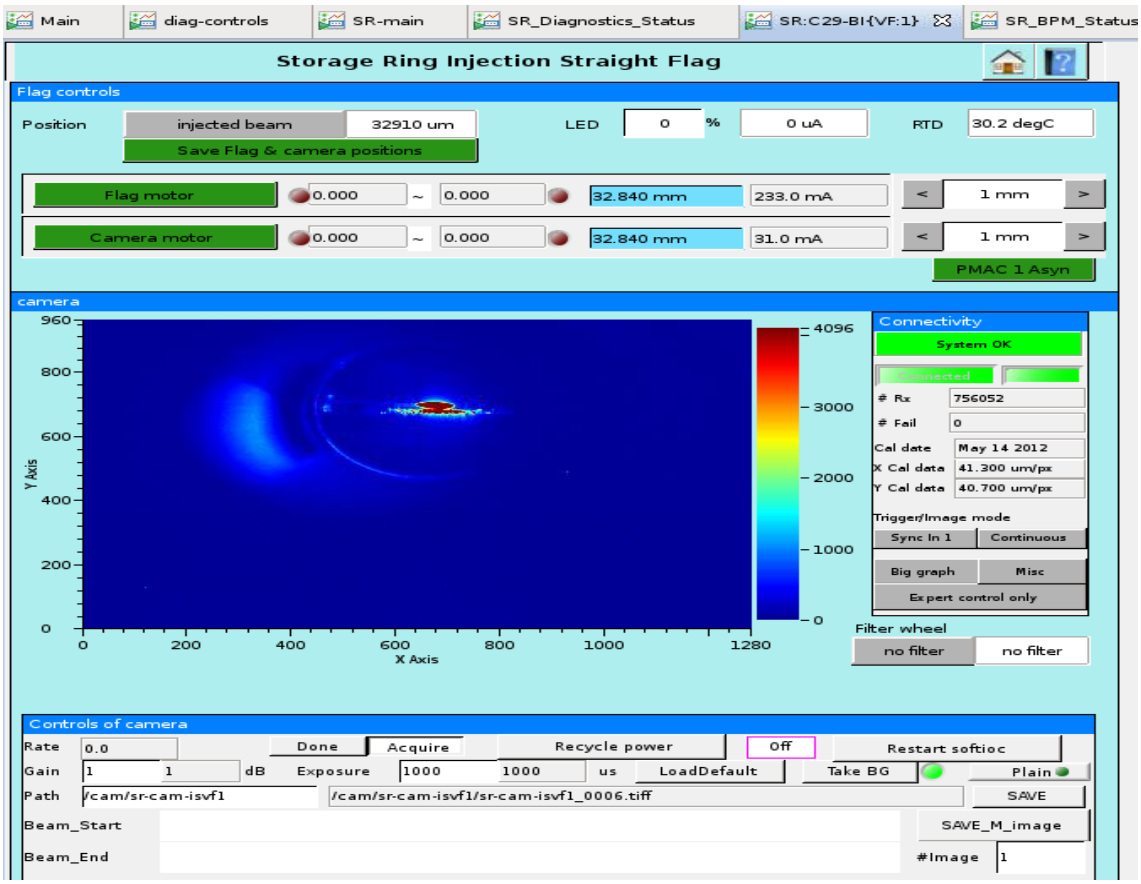

Figure 1-2, first image on IS flag

At ~21:40 Mar-27-2014, beam passed through pulse septum and observed on IS flag, see screen capture in Figure 1-2. On the image, one can see the 10 x 10 mm calibration square; the beam image and some reflection probably due to pellicle splitter. The circle shape should be vacuum window and left side spot probably came from ambient light. Beam charge was about 0.5nC on BtS ICT2, the YAG screen was saturate even at such a low current. Add OD filter and probably with less exposure time might help. Figure 1-3 shows the beam profile after one turn.

It's worth to point out that YAG screen cannot stop the 3GeV beam. Beam can still circulate the ring multi-turn even with flag inserted in the beam path.

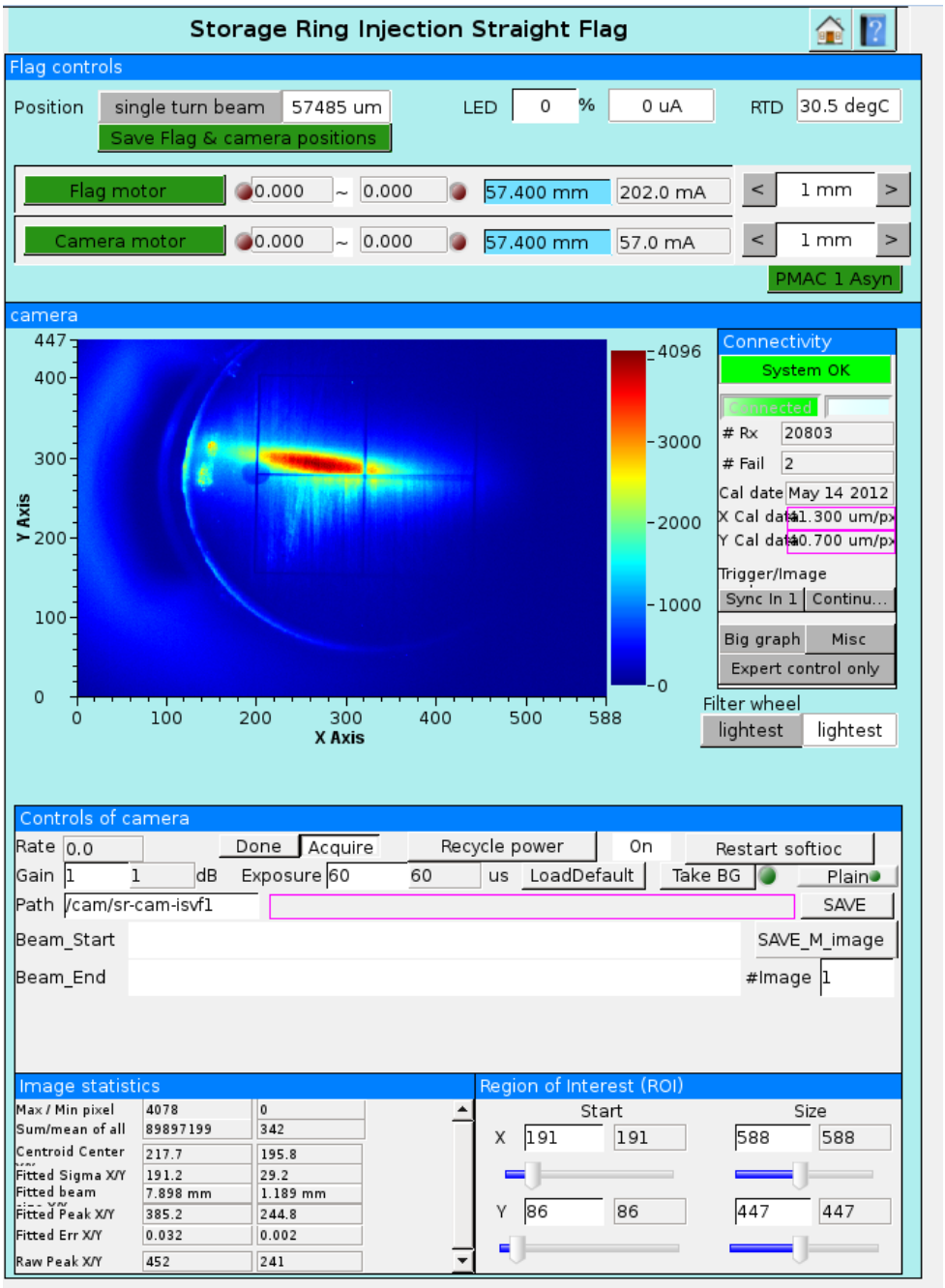

Figure 1-3, one turn beam profile on IS flag

Possible future studies for IS flag may include:

- Systematic measurements of YAG screen saturation effect.
- Understand where the reflection comes from
- Verify the CCD image orientation

4.13.2 DCCT and lifetime

One Bergoz in-flange type DCCT is installed at C03 injection straight. The DCCT sensor has octave chamber profile which is same to nearby sections. DCCT related electronics locate in the rack on the mezzanine, including a calibration current source. DCCT output signal goes to digitizer after 1->4 buffer, one channel of buffer output is used for EPS interlock PLC. 24-bit digitizer is used to sample the DCCT output signal. The digitizer can be programmed to have different anti-alias low pass filter. Maximum sampling rate of the digitizer is 216 kHz.

With stored beam in the ring, beam lifetime can be calculated from DCCT measured total current. Beam current decays due to following reason:

- Elastic scattering with residual gas (Columb scattering)
  => leading to transverse deflection and subsequent loss at transverse aperture limitations
- Inelastic scattering with residual gas (Bremsstrahlung)
  => leading to energy losses exceeding the acceptance
- Collisions between electrons (Touschek scattering)
  => leading to energy losses exceeding the machine's energy acceptance
- Photon emission (quantum lifetime)
- Trapped ion or macro dust in beam potential

Since the probability of collisions increases with electron density in the bunch, high brightness synchrotron light sources operating at low emittances and large beam current are usually lifetime limited from Touschek scattering.Beam lifetime can be expressed as:

$$I(t) \cong I_0 e^{-\frac{t}{\tau}} \qquad (1)$$

Where τ is overall beamlife of above mentioned effects, it can be considered as constant at short period of time. While $t << \tau$, first order of Taylor expansion gives:

$$I(t) \cong I_0\left(1-\frac{t}{\tau}\right) \qquad (2)$$

Lifetime can be found from a linear fit of I(t) vs. t, the slope (-1/ τ) gives the beam lifetime.

During SR phase-1 commissioning, large noise signals were pickup by DCCT electronics. A programmable low pass filter is added before the digitizer to eliminate the noises.

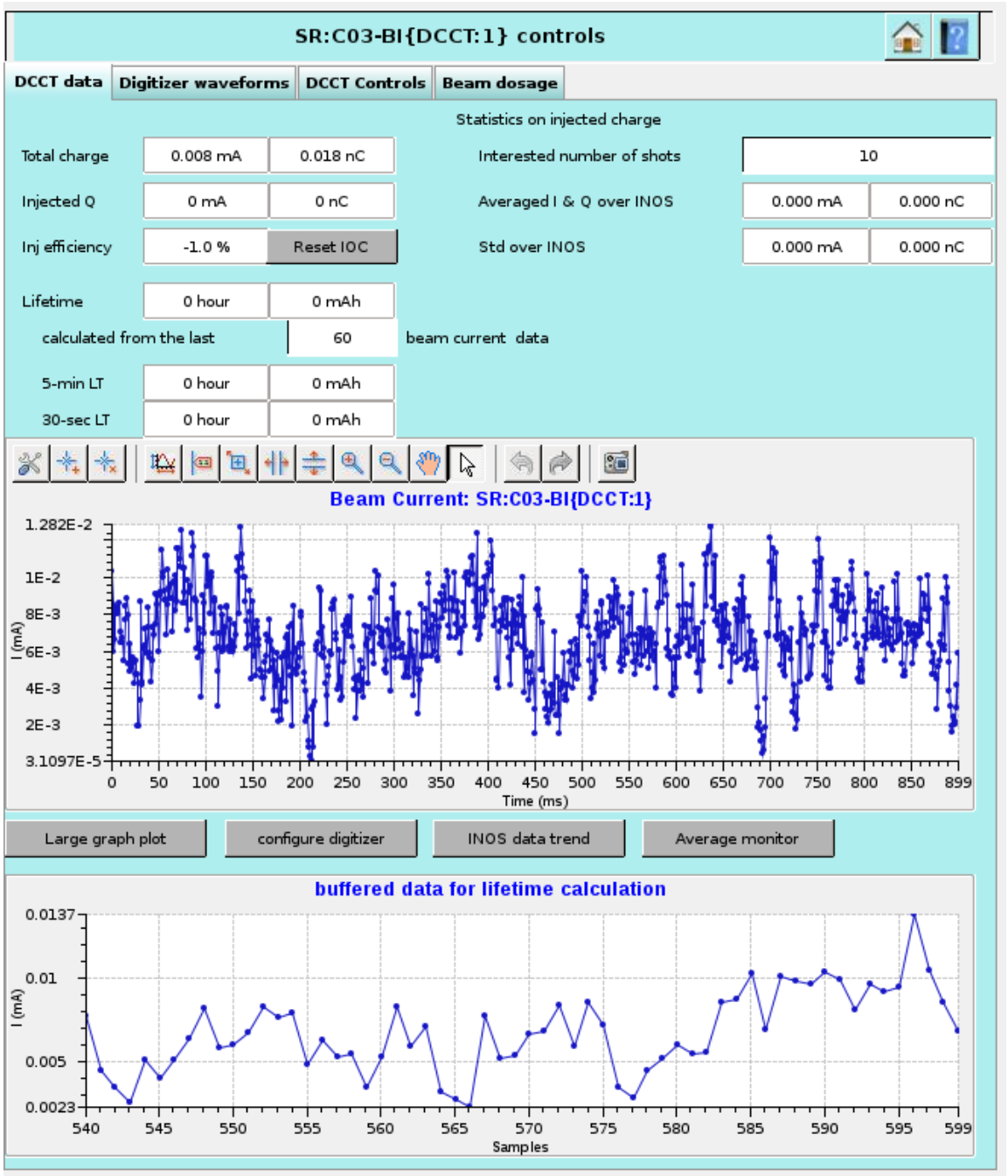

Figure 2-1, DCCT CSS panel

DCCT CSS main page is shown in Figure 2-1, digitizer waveform data and DCCT control/calibration are available from corresponding CSS pages as well.

DCCT digitizer is external triggered at 1Hz rate, sampling rate and number of samples can be adjusted. Average beam current from 1Hz trigger is reported as the total current. Beam lifetime can be calculated from history buffer of past 600 triggers. Three lifetime calculations are available, one is fitted from past 5-min history data; second lifetime is fitted from the past

30-seconds history data and third lifetime can be calculated from user defined number of history points.

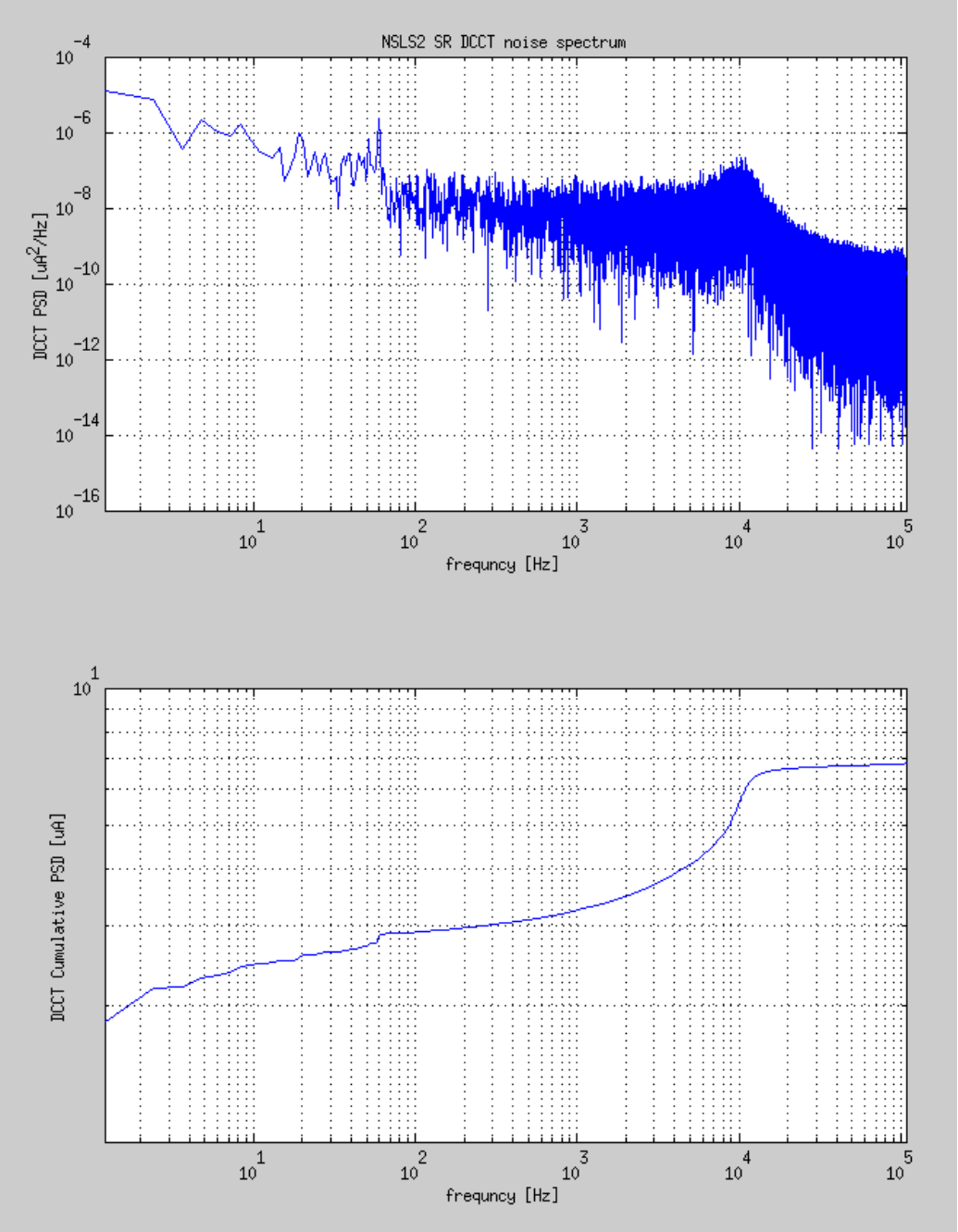

Figure 2-2, DCCT noise spectrum, 200mA range.

Figure 2-2 shows the typical SR DCCT noise spectrum. With average 1Hz data, the noise level is ~ 2uA. With maximum digitizer sampling rate of 216 kHz, the noise level is ~ 7uA. This noise spectrum is with 50Hz low pass filter before the digitizer, there is a small noise peak at 60Hz probably coming from digitizer itself.

During the phase-1 commissioning, DCCT reported current was noisy. Typical noise level was ~ 40uA. This introduced us difficulty to fit the lifetime in short period of time. Figure 2-3 gives the offline lifetime calculation from archived history data. A history buffer of 100 points were used to get a reasonable good lifetime fitting.

Figure 2-3, DCCT current and lifetime

BPM SUM signal was used to calculate the beam lifetime during the commissioning, especially when the total current was low. There are limitations by BPM SUM signal: the SUM signal strength depends on the beam position; and the BPM attenuation settings affect the SUM signal readout. In principle these effects can be calibrate out and BPM SUM signal could be a useful diagnostic tool. In fact, from all 180 BPMs SUM signal, beam lost was able to be localized.

Following tests needs to be accomplished for the next phase commissioning:

- Check the DCCT noises at various conditions when the beam is back in the ring. DCCT output is fanned out to EPS interlock. If possible, a dedicated DCCT (or BPM SUM signal) could be used for interlock.
- Check the beam lifetime calculated from 1Hz rate DCCT values. Adjust the number of DCCT history points to calculate the lifetime to find optimized settings.
- DCCT noise was decreased from 40uA to 3uA, with external low pass filter. Will check the noise level with beam.

4.13.3 FPM

Filling pattern monitor system measures the bunch to bunch filling pattern in the storage ring. All 1320 bucket charges will be sampled and displayed on the CSS panel. The bunch by bunch charge/current will be calibrated with the storage ring DCCT total current. Update rate of the filling pattern could be 1 Hz or longer, depends on the control network traffic. The digitizer can sample up to 47 turns of bunch by bunch current, average of bunch current in these many turns help to improve the resolution. Sampling rate of the digitizer is 8GHz. With 8GHz sampling rate of the digitizer, there are 16 samples between every 2ns bucket. Sometimes this sampling rate is not sufficient to get a reliable filling pattern monitor. Mixer down-converter circuit will be added to condition the signal more suitable for 8GHz digitizer. A 20GHz sampling rate scope is available to monitor the same filling pattern signal. EPICS communication to the scope is somehow slow and not reliable. The scope was very helpful for directly observation.

Dedicated button BPM signals are used to measure the bunch filling pattern in NSLS2 storage ring. Raw button SUM signal from Hybrid network is send to fast oscilloscope (digitizer), digitized data is processed to get the filling pattern.

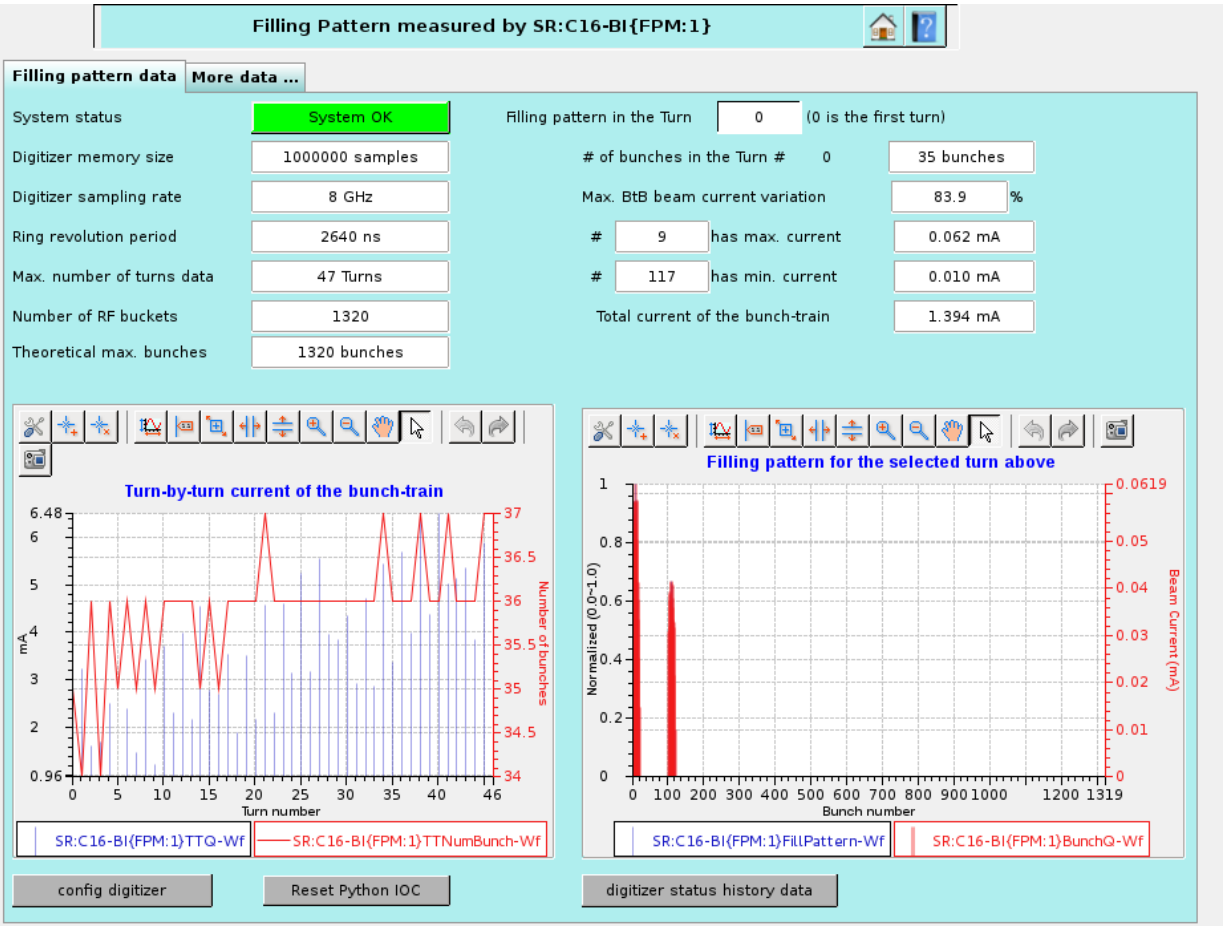

Figure 3-1, SR filling pattern monitor

Figure 3-1 shows an example of measured filling pattern. With total current of 5mA on DCCT, about 60% of the charge was filling in the first bunch train start from bucket #0, the rest 40% charge is in the second bunch train started from bucket #100. There are ~ 18 bunches in each train. Bunch to bunch current variation was inherited from the e-Gun.

Figure 3-2 is a typical filling pattern scope waveform at early stage of commissioning. Beam survived for more than 150 us at that injection shot. Zoom in the waveform one can see there are 20 bunches in the train which was determined by e-Gun pulse width.

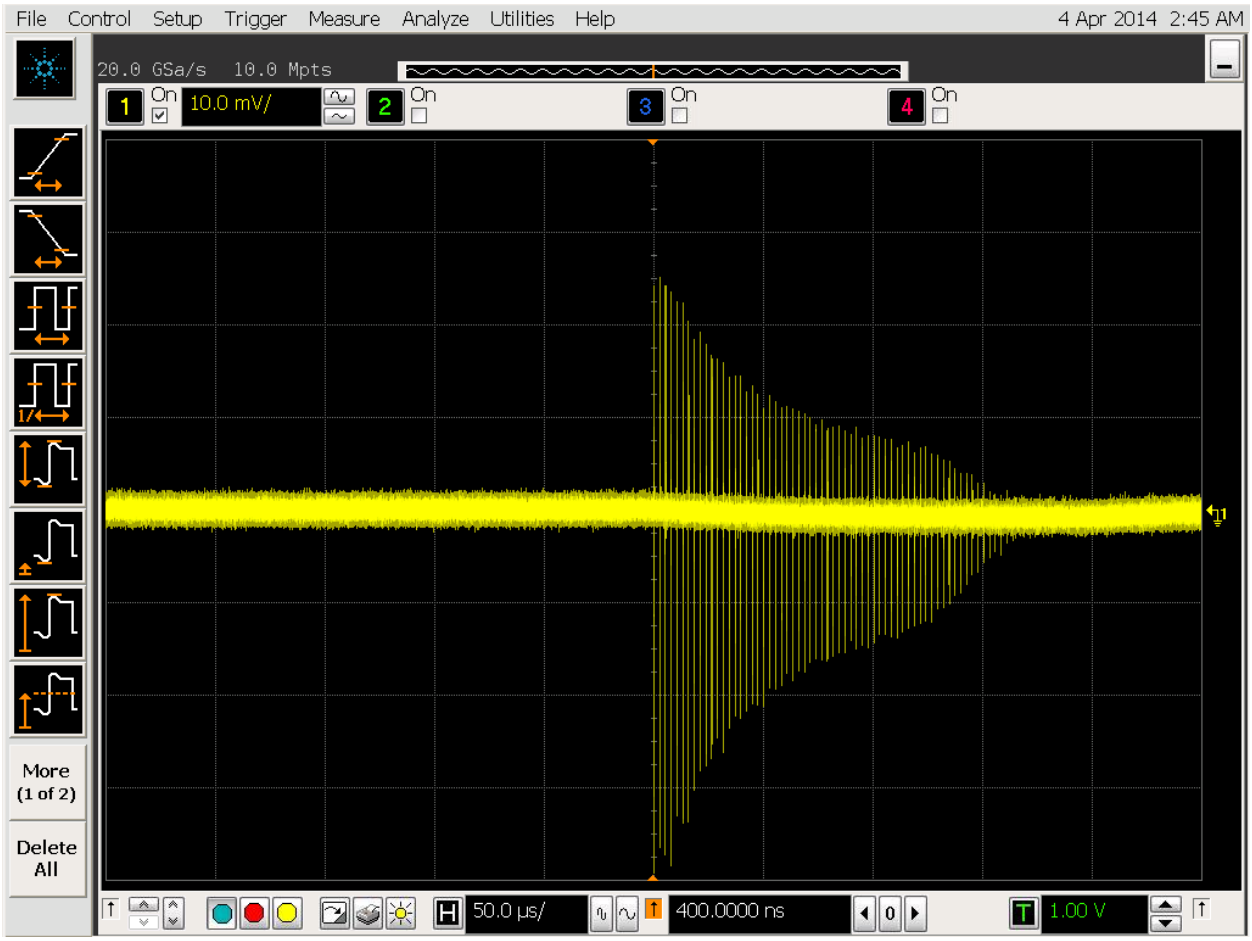

Figure 3-2, 20GHz scope waveform shows beam survived for more than 150 us.

Future commissioning of FPM system, we will investigate the following:

- Mixer down-converter may be needed to expand the Hybrid output signal so that it's more suitable for 8GHz digitizer. Settings of the mixer down-converter circuit need to be optimized with beam.
- Adjust the digitizer timing if necessary
- Calibrate the FPM bunch to bunch current with DCCT
- Check the FPM nonlinearity depends on beam position
- Check the FPM dynamic range
- Test with arbitrary bucket filling

4.13.4 LCM

There are fiver scrapers and five Cherenkov beam loss monitors (CBLM) installed in C30 and C01, where high density concrete is used for better shielding. The purpose of this configuration is to have beam losses in a controllable manner near injection area so that beam loss at other part of the ring is minimized.

Scraper blades are controlled with linear motors with 1um resolution and 3um repeatability. Horizontal blade has 40mm travel range, it is 38mm from the chamber center when fully retracted and can be inserted 2mm cross the chamber center. Vertical blade has 11.5mm travel range. When electron particle hits the scraper, it losses energy hence will be bend inward towards the chamber wall. Glass rods are installed at selected locations to detect the lost electrons outside the vacuum. When electron passes through the Glass rod, it generates Cherenkov light which will be reflected towards the end of glass rod. Optics setups in the end boxes include photo diode and PMT and related signal condition electronics. Cherenkov light converted into electrical pulse signal to be detectable with digitizers. CBLM #2 and #4 have two types of sensors, while CBLM #1,3,5 have photo diode channel only.

Location of NSLS2 storage ring scrapers and CBLMs in C30 and C01 is shown in the following drawing:

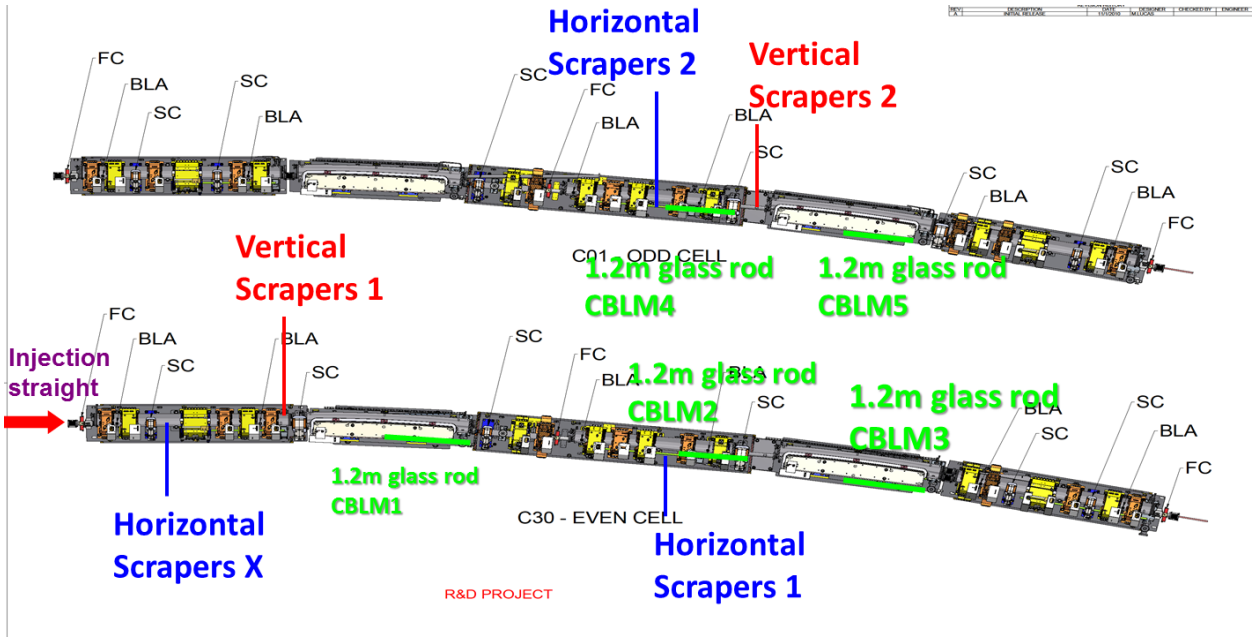

Figure 4-1, locations of scrapers and Cherenkov beam loss monitors

There are also 2 neutron detectors which are part of the beam loss monitoring system. These devices are not yet installed because they are located in a difficult position (atop the rolling shield above the storage ring kickers) and the cabling details are still being worked out.

Other diagnostic systems can be used to get beam loss information, for example use 4-button Sum signal from all the BPMs around the ring, beam loss locations can be identified. ICTs and DCCTs in the complex can be used to measure the beam transfer efficiency, so that how much beam losses can be measured in-between any of these current monitors.

During SR phase-1 commissioning, scrapers were used for fault studies. They were used for some shift to limit the beam lifetime. Functional tests had been done for CBLM with beam. Figure 4-2 shows a screen capture when beam first arrived at C30 around 22:00, Mar-28-2014. First three CBLMs saw injection beam lost signal. When beam started circulating for multi-turns, CBLMs detected signals were much smaller since beam lost was not in the area.

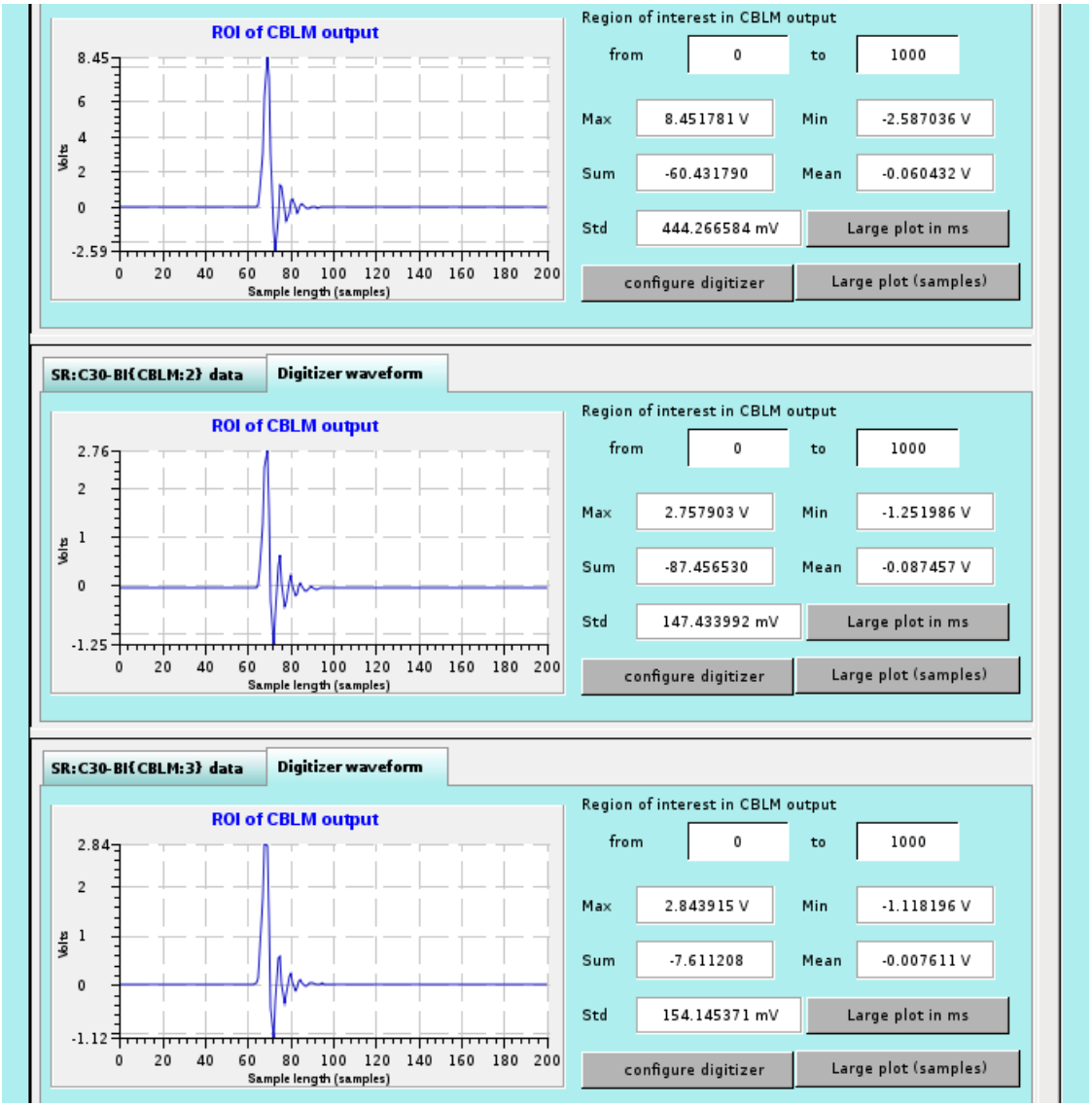

Figure 4-2, CBLM saw beam loss signals.

For the future studies related the LCM, the following tests can be carried out:

- CBLMs calibration by intentional dump injecting beam at CBLM area
- Turn to turn beam loss pattern using PMT, which has fast response time
- Using horizontal scraper to control the off energy particle lost in area
- Using scrapers to control beam lifetime and to calibrate CBNL with stored beam
- Using scrapers to measure dynamic aperture

4.13.5 BxB feedback system

Transverse bunch by bunch feedback system is installed at C16, block diagram of the system is shown in Figure 5-1. Dedicated button BPMs are used as pickup for the feedback system. Raw button signals are feed to mezzanine racks through 3/8'' Heliax cables. X/Y position signal is available after the broadband Hybrid box. The signal is then detected by a low noise RF front end before send to high speed digitizer. Correction signals processed from the digitizer are amplified by 500MHz broadband amplifiers. Transverse kick is realized by feeding the opposite stripline kicker plates. Figure 5-2 shows the installed stripline kickers in the ring tunnel.

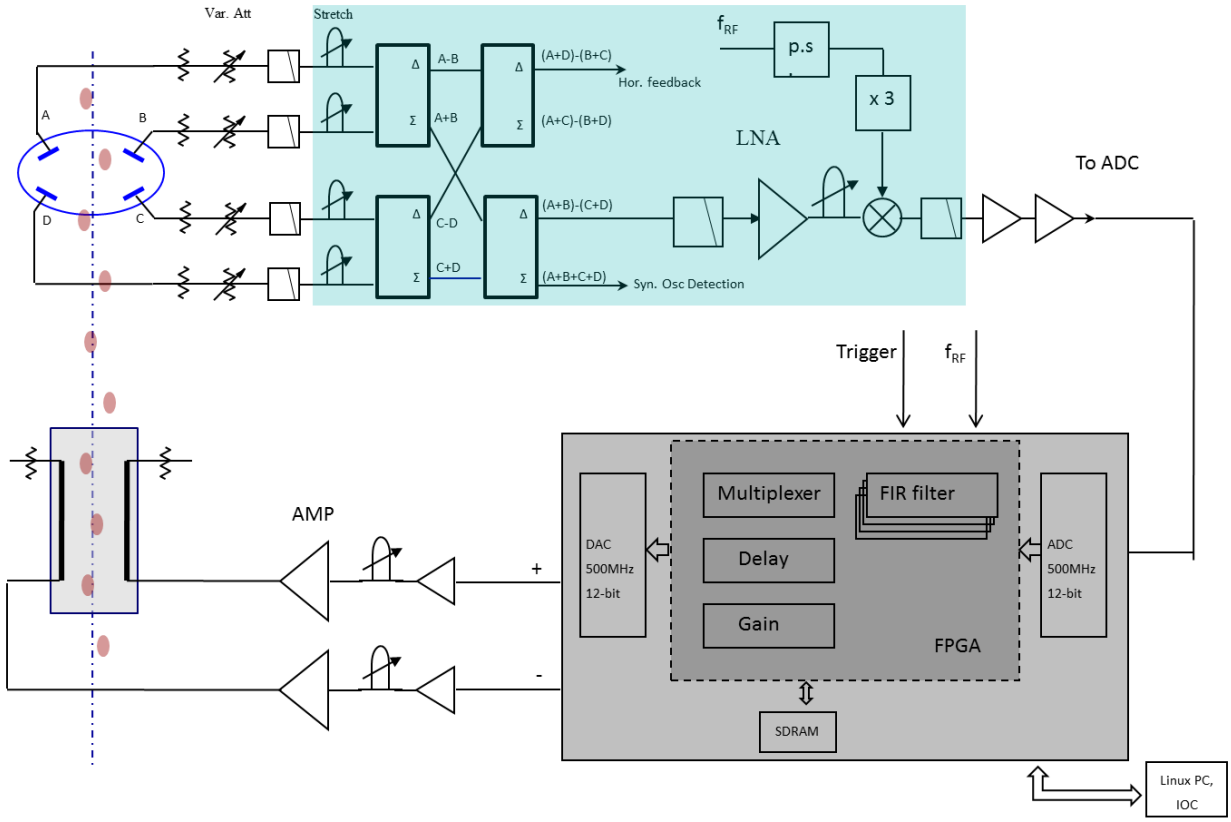

Figure 5-1, Block diagram of NSLS2 SR transverse bunch by bunch feedback system.

Figure 5-2, Stripline kickers in the storage ring tunnel.

Bunch-by-bunch feedback system was commissioning on May 07-09, 2014. During the SR phase-1 commissioning, single bunch current was found to be limited around 0.8 - 0.9mA. Beam was getting unstable vertically and single bunch current was not able to increase above this threshold. Although the reason of this instability is not quite understood, transverse bunch-by-bunch feedback system is able to stabilize the beam so that single bunch current can increase up to 6.5mA, limited by vacuum pressure.

While fill the ring with multi-bunches, depends on the filling pattern, longitudinal instabilities were observed at around 10mA. Typically the instability got so strong that partial beam loss happened at around 13mA. Longitudinal beam motion was so huge that beam could be moved horizontally to several mm range at dispersion area. It was also monitored on the filling pattern scope that button BPM SUM signal was jumping. This indicated the longitudinal motion was not only dipole mode. Bunch length (hence the BPM SUM signal) was not constant. Huge longitudinal motion could lead the transverse feedback to a positive loop, so that beam was kicked out. Third digitizer unit was used to monitor the longitudinal bunch motions.

Preliminary studies show there are fast ion effects. Figure 5-3 gives vertical transient measurement results. With a total current of 9mA distributed in 500 buckets, turning the feedback loop off for ~20ms, tail part bunches started oscillating more. Mode analysis reveals

the unstable motion has frequency ~ 3MHz and 28MHz. This agrees with the ion induced frequency. Likely the unstable modes around 1300-1314 were from CO+ and CH4+, and modes around 1246 were induced from H2+.

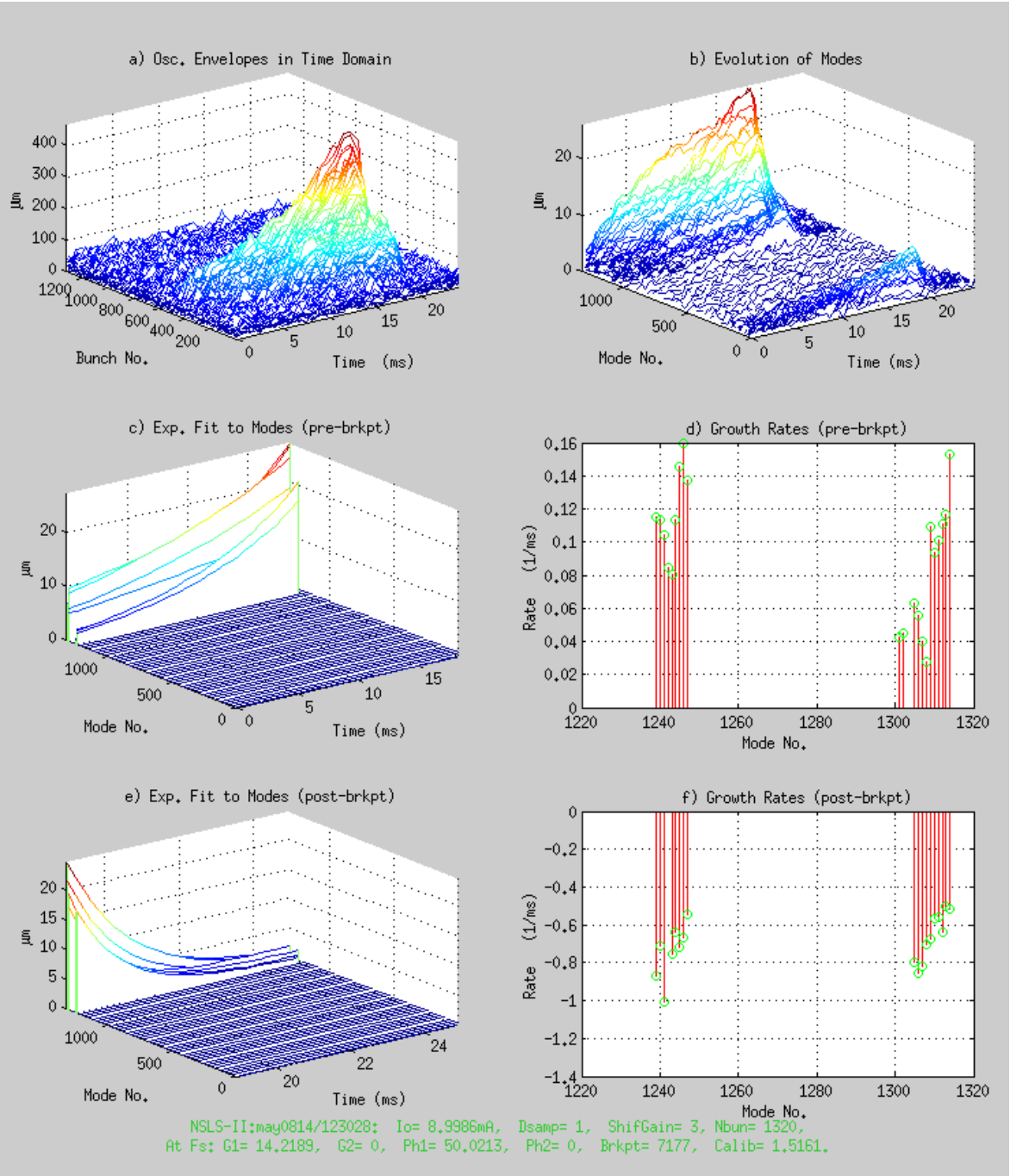

Figure 5-3, vertical bunch by bunch feedback transient measurement shows fast ion effect

Similarly, longitudinal unstable modes can be analyzed. Preliminary analysis shows longitudinal HOM induced unstable mode #919 (348MHz + n*frf). Most likely this mode was coming from 7-cell PETRA cavity. Changing the cavity temperature (from 38.4 to 39.2 degC),

the longitudinal unstable mode moved to #603 (228MHz + n*Frf). As the super-conducting moves in for the next phase commissioning, this cavity induced HOM instability are expected to disappear. Beside its major function of feedback, bunch-by-bunch feedback system commissioning has demonstrated other useful features. It can be used to clean out any buckets. The system can excite one single bunch to measure the bunch transfer function. Betatron tune can be measured automatically from the notch when the feedback loop is closed. Figure 5-4 gives the vertical plane transfer function measurement results at various single bunch current. As the current increase, vertical betatron peak moves toward a nearby peak. When two peaks merge, beam was getting very unstable vertically and single bunch current was limited. This looks like TMCI instability, the thing is that small peak didn't move as the current increased which doesn't agree with TMCI theory. The small peak could be driven by external noises.

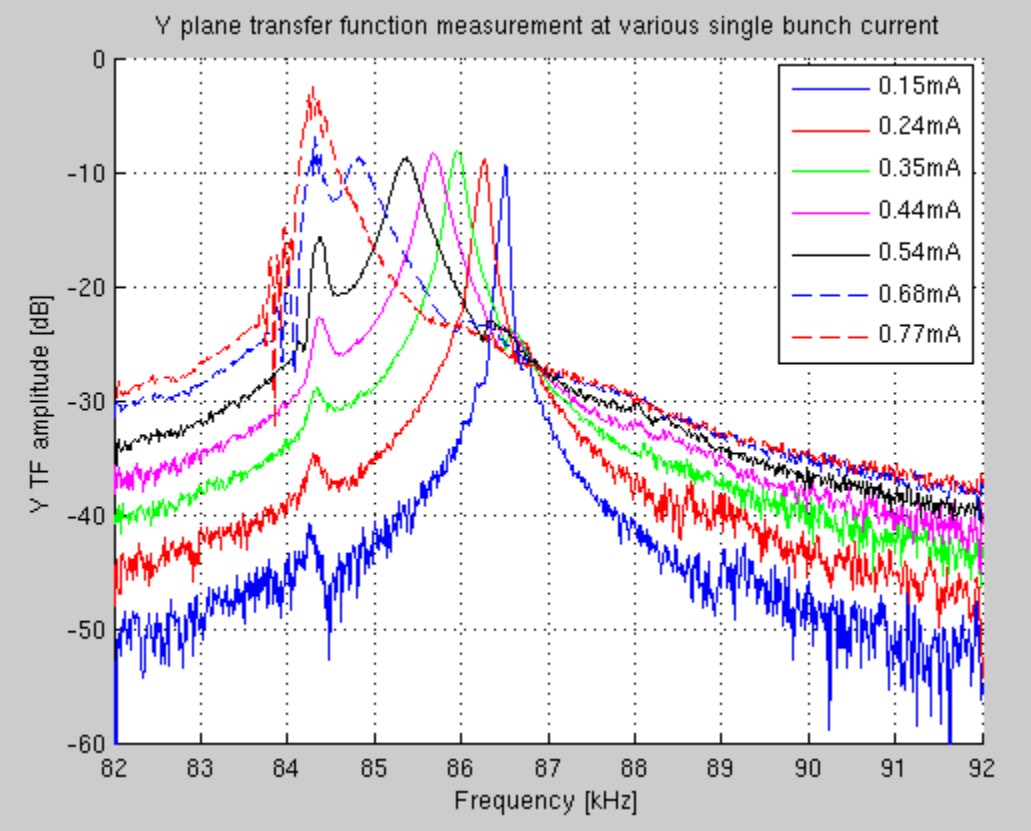

Figure 5-4, transfer function measurement using bunch-by-bunch feedback system.

For the next stage of ring commissioning, we plan to carry out various studies related to bunch by bunch feedback system:

- Transverse impedance characterization
- Beam excitation and purification
- Fast-ion related studies (measure oscillating amplitude, tune shift along bunch train. Bunch current information may be needed)
- Resistive wall related studies (with w/o ID)
- Measurements with different chromaticities

4.13.6 SLM

Visible synchrotron light monitor (SLM) diagnostic beamline utilizes the radiation from C30 BM-B. Nominal source point is ~2.75mrad into the dipole. The beamline has acceptance of +/-1.5mrad horizontal and +/-3.5mrad vertical. Visible light from the dipole synchrotron radiation will be reflected by in-vacuum mirror. The visible light is guided into SLM hutch locates on the C30 experimental floor. There are various optics setups on the 4'x10' optical table, currently there are three branches setup: CCD camera branch; fast gated camera branch and streak camera branch. Visible light can be guided to different cameras.

Following drawings show the SLM layout, see Figure 6-1. Figure 6-2 shows the optical table setup.

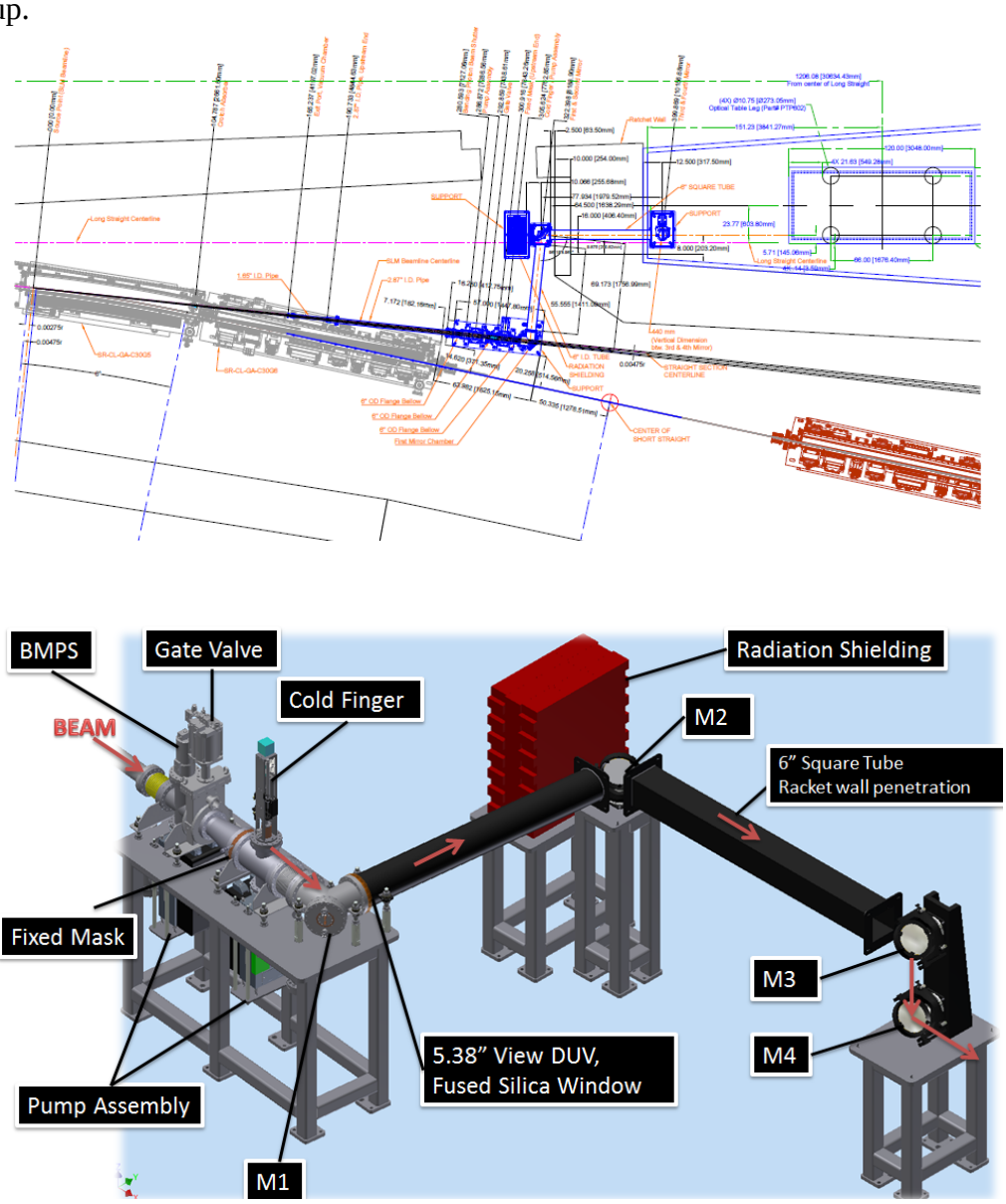

Figure 6-1, SLM beamline layout (top) and major components illustration (bottom)

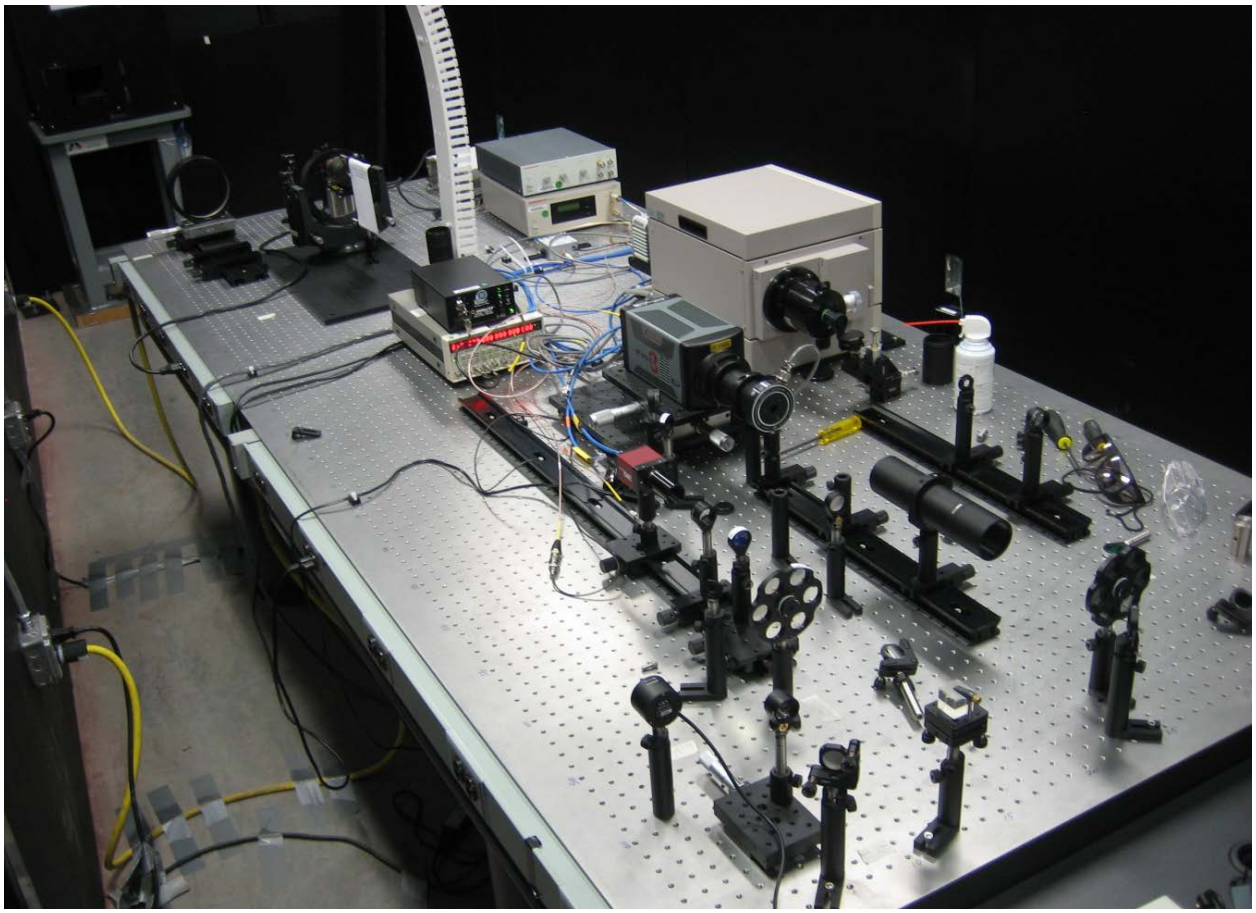

Figure 6-2, optics setup in the SLM hutch. Visible synchrotron light comes down from the top-left corner, focused by 2m lens.

The light is wrapped around to three camera branches. First light was observed in the SLM hutch, before the beam circulating the ring. Figure 6-3 shows the first turn image captured on Apr-02. Electron beam was going around for 1-2 turns. CCD the camera was able to see synchrotron light. BtS ICT2 read about 1nC charge.

The image was not focused. That's why two bright spots appears on the image, dark band in the middle is the cold finger shadow. Fine optics adjustment was carried out once the hutch was granted safe to access.

Lack of remote control/monitoring of BMPS brought us headaches. The shutter was closed by mistake after one maintenance day. It was able to be opened locally through the EPS PLC panel at C30 mezzanine. Hope this problem can be solved for the next period of commissioning.

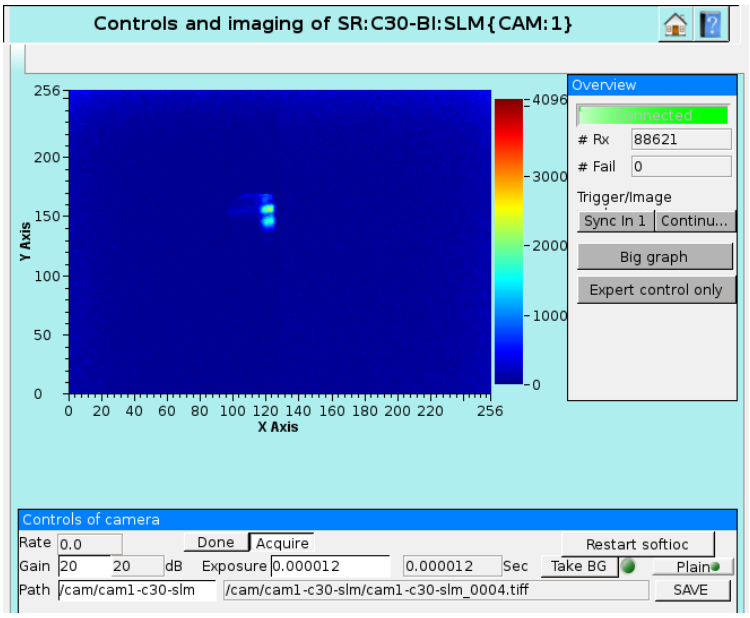

Figure 6-3, First light observed in the SLM hutch, Apr-02-2014

No dedicated shifts were available for the SLM beam commissioning, most of the tests and measurements were carried out parasitically. Figure 6-4 shows the first three turns profile captured using gated camera. Beam was injected on axis and survived for several turns. Left one is turn #1, middle one is turn #2, right side is turn #3. When taking the image, there is no stored beam, beam survived for turns. Note beam was moving in vertical direction as well, due to mis-matched injection vertical angle. One turn #2, vertical beam size was enlarged, probably due to lattice mis-match so that beam was doing some Quadrupole motion in vertical plane.

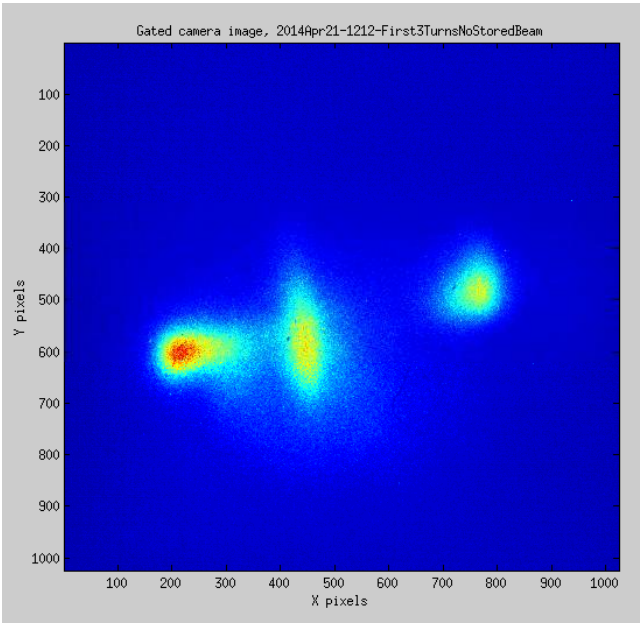

Figure 6-4, first three turns profile with on-axis injection

Using streak camera, bunch length at different single bunch current was measured. Figure 6-5 shows the results at three different RF gap voltages. Notice that bunch length is shorter around 0.6-0.7mA, where the threshold current is to see vertical instability. Bunch lengthening looks a lot even from 0.1mA to 0.5mA, which indicate big longitudinal broadband impedance. Further studies are needed to understand the longitudinal broadband impedances.

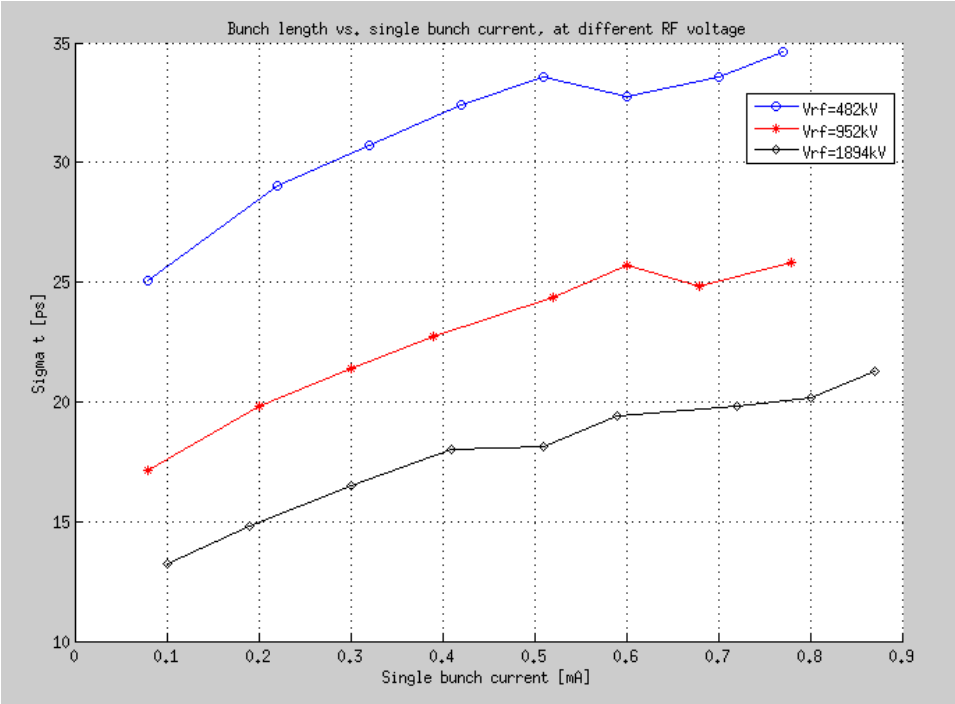

Figure 6-5, bunch length vs. single bunch current, at three different RF gap voltages.

For the upcoming commissioning and future machine studies, we can follow the lists:

- Make sure BMPS are remotely controllable. Logic of the BMPS should be straightened.
- Fine adjust of optics setups.
- CCD camera can be used to study the microwave instability threshold. SLM source point is selected with dispersion.
- Future application of CCD camera includes double slit interferometer beam size measurement, pi-mode beam size measurement etc.
- Streak camera can be used to measure:
    - Bunch length vs. single bunch current Ib; => Im{Z//}, imaginary part of ring broadband impedance
    - Synchronous phase vs. single bunch current Ib; => Re{Z//}, real part of ring broadband impedance
    - Microwave instability threshold (together with CCD measure sigma_x at dispersion);
    - Bunch length and synchronous phase with harmonic cavities;
    - Longitudinal instability measurement; (coupled bunch instabilities)

    - Synchronous phase transient in the bunch train due to transient beam loading; (with external GATE or dual sweep)
    - Injection transient measurement, help to optimize the injecting beam phase and energy => important for top-off; (to see the injecting beam only with no stored beam, need to kick the beam out after ~50ms after injection using bunch purification system)
    - Transverse motion using cylindrical lens setup
    - Fast-ion caused transverse motion studies
    - Other measurement during machine study, especially RF cavity related.
- Gated camera can be used to measure:
    - Measure the single bunch, single turn profile
    - Injection damping for injecting beam and stored beam (combine with purification system to kick out the beam after damping down)
    - Filamentation of injecting beam, which has large oscillation amplitude
    - Filamentation of stored beam while excited at betatron frequency => nolinear dynamics
    - Help for injection tuning etc.

4.13.7 BPM

There are six BPMs in the each cell, total 180 BPM in multipole chambers. All BPMs in NSLS2 have capability to measure 117MHz ADC raw data, 378kHz TbT data, 10kHz fast acquisition and 10Hz slow acquisition data. ID straight sections and injection straight have BPMs installed and see the beam. FA data is streaming out the fibre port to cell controller and used for fast orbit feedback. SA data is always available for orbit monitor and correction. ADC, TbT and FA waveform data are available from BPM IOCs. The waveform data can be retrieved on Internal/External triggers. External trigger to all BPMs around the ring guarantee sampling beam position/trajectory synchronized.

Three external trigger event codes have been used for SR BPM commissioning. They are event code 32, 66 and 47. Event code 66 and 47 trigger when the e-Gun gets beam, differences are 47 is locked to the storage ring 378kHz fiducial, no matter which bucket is filled in. Event code 32 is continuous 1Hz trigger, this code is used when there are stored beam and users want to acquire waveform data continuously. BPMs can be triggered synchronously with on-demand mode. For more information of these event codes, refer to timing sections.

Due to BPM pickup physical location and cable length difference, BPM electronics need to be timed well to get real turn-by-turn data. At the early stage of commissioning, before BPMs timed well, raw ADC waveform supplied powerful diagnostic information. Figure 8-1 shows an example of BPMs ADC waveform data. The data was acquired at 5:47:49, Apr-03-2014, when beam survived for 5-6 turns. One can see BPMs were roughly timed but not perfect aligned.

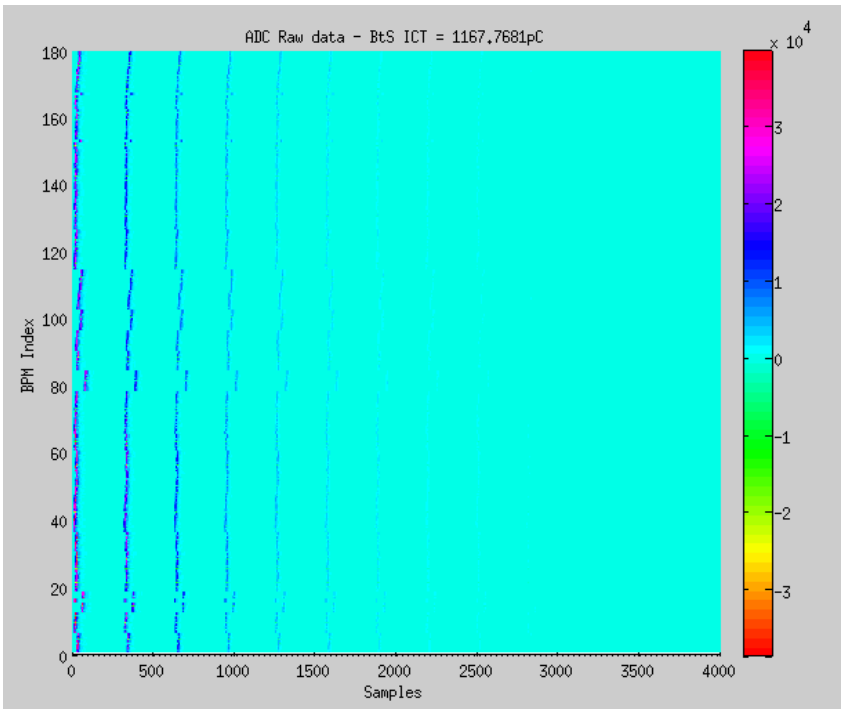

Figure 7-1, ADC waveform data from 180 SR BPMs, beam survived for 8-9 turns.

From ADC data, first turns beam position and SUM signal can be retrieved. Shown in Figure 7-2, are button A,B,C,D signals, x/y position and SUM signal from ADC waveform data.

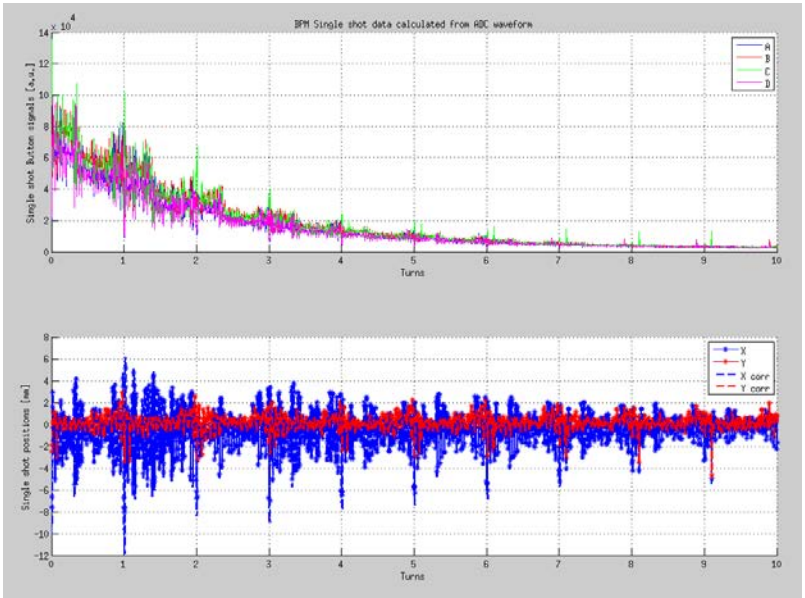

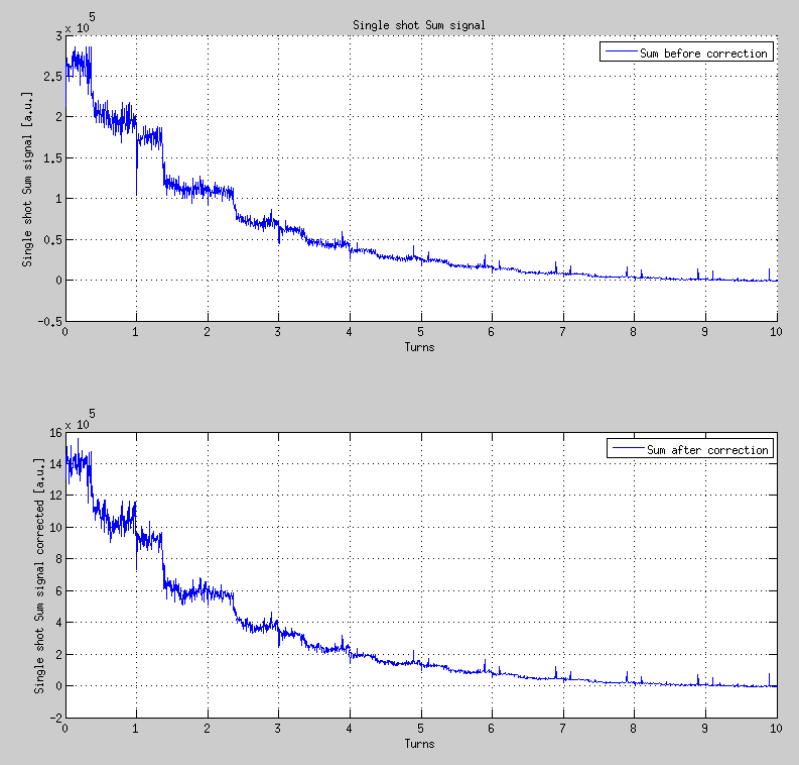

Figure 7-2, (top) first turn button A,B,C,D signal and x/y positions, 5th order nonlinear correction was applied for beam positions; (bottom) Button SUM signal, correction was applied to SUM signal taking in to account of position dependency, cable length, electronics attenuation etc.

Due to large beam offset on the trajectory, nonlinear correction was applied to the positions and button SUM signal. It was found that beam was partially lost near C10 BPM4 at every turn around. Turned out that's the location where a RF spring obstacle was found.

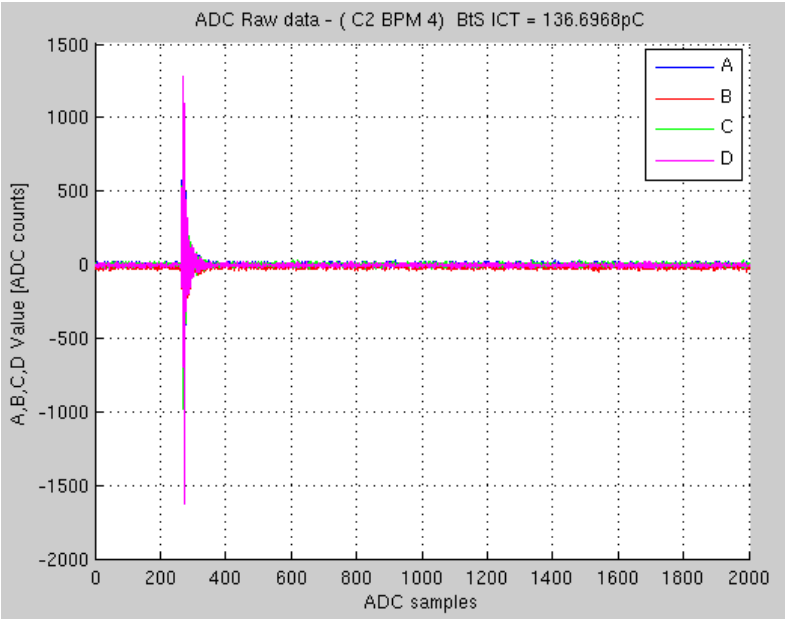

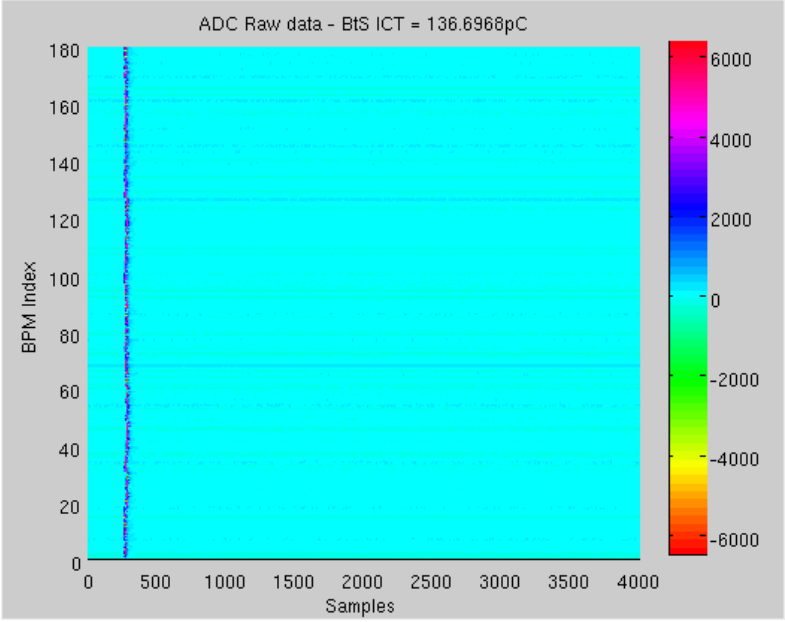

Figure 7-3, BPM timed well. (top) four-button signals from one of the BPM C2-BPM4; (bottom), mesh plot of all 180 BPMs ADC waveform. Beam survived one-turn in the ring and all BPMs timing are aligned.

When injecting to different buckets in the ring, BPM timing was re-adjusted using event code 47. Figure 7-3 shows the ADC waveform image. Note single bunch beam was injecting to SR bucket #0, one can see all BPMs see the beam signal arrive at same ADC count. This guarantees all BPMs report the data in the same turn. To check the signal leakage to nearby turns, beam was kicked out right after one turn. One BPM TbT waveform data, beam arrived at sample #4. There were little leakage to nearby turns with SR target bucket 0 to 1000.

Once the BPM timed well, various physics measurements have been carried out use TbT data and FA data. We will not discuss the physics measurements in this chapter, please refer to related chapters in the report. These measurements include but not limited to:

- Injection optimization using BPM TbT data
- Beam spectrum from BPM TbT data and FA data
- Lattice measurement (phase advance, beta-function) using BPM TbT data
- Beam based alignement
- LOCO
- Beam dynamics studies
- Beam instability studies

With stored beam, besides various physics measurement using BPM data, one can study the BPMs performance on the following topics. Only preliminary test was done and we would like to continue the test in the future commissioning/studies.

- BPM resolution at various current
- BPM position dependency on current and filling pattern
- BPM long term stability

- BPM mechanical stability and beam stability
- Linear and nonlinear gain calibration with beam

4.14 BPM Commissioning with Beam

4.14.1 Introduction

The NSLS-II RF BPMs incorporate the latest technology available in the RF, Digital, and Software domains. A single design has been achieved that meets all NSLS-II operational requirements for all the injection components as well as the storage ring. During the linac and then booster commissioning BPMs performed very well and met the specifications. However, it is the storage ring performance specs, especially the resolution and long term drift, which impose the strictest requirements. The goal of this write-up is to describe the key specifications that were achieved during the initial stage of Storage Ring beam commissioning, as well as to document the key BPM commissioning experiences.

NSLS-II storage ring is equipped with 180 RF BPMs (2 per each multipole girder, 3 multipole girders per ring cell) plus a number of "specialized" BPMs, 4 in injection straight, and (eventually) two or more per every ID straight. Storage ring BPM data can be provided to the user in 4 switchable modes, ADC, TbT (Turn-by-Turn, up to 100 kSamples per on-demand buffer), FA (Fast Acquisition, 10 kHz, up to 100 kSamples/bufer) , and SA (Slow Acquisition, 10 Hz, continuous). Specifications for storage ring BPM resolution (stored beam) requirements are summarized in the table:

Parameters/ Subsystems				Conditions	*Multipole chamber RF BPM Resolution Requirement	
					Vertical	Horizontal
50 mA to 500 mA Stored beam resolution – 20% to 100 % duty cycle	BPM Receiver Electronics	Turn by Turn (80% fill)		Data rate = 378 kHz	3 μm rms	5 μm rms
		Assuming no contribution from bunch/ fill pattern effects		0.017 Hz to 200 Hz	0.2 μm rms	0.3 μm rms
				200 Hz to 2000 Hz	0.4 μm rms	0.6 μm rms
				1 min to 8 hr drift	0.2 μm peak	0.5 μm peak
		Bunch charge/ fill pattern effects only		DC to 2000 Hz	0.2 μm rms	0.3 μm rms
	Mechanical motion limit at Pick-up electrodes assembly (ground & support combined)		Vibrations	50 Hz to 2000 Hz	10 nm rms	10 nm rms
				4 Hz to 50 Hz	25 nm rms	25 nm rms
				0.5 Hz to 4 Hz	200 nm rms	200 nm rms
			Thermal	1 min to 8 hr	200 nm peak	500 nm peak

Due to administrative limits (25 mA total beam current towards the end of this commissioning period) the specs could not be fully tested simply because of insufficient beam intensity. However, a significant progress in verifying the resolution performance of BPMs was achieved at lower currents. Extrapolating these results (described below) to higher beam currents we should easily meet the resolution specs listed in the table. Separately, due to lack of time, no long term drift studies have been performed and these will be scheduled later.

4.14.2 BPM Resolution Measurements

BPM resolution measurements were performed using a dedicated BPM button assembly located on girder 2 in cell 28. This assembly is not used in normal operations but was rather instrumented with electronics module specifically for this test. The module was connected to the 4 BPM buttons using a combiner/splitter assembly to make the measurements independent of transverse beam motion. The connection scheme sums the 4 button signals with a 4:1 combiner and then splits the summed signal using a 1:4 splitter, which are then connected to the 4 input channels of the electronics. With this connection scheme each of the 4 channels of the electronics will see the same signal and electronics performance can be measured independent of beam motion.

The resolution measurements were performed using three different fill patterns; single bunch, 50 bunches, and approximately a 60% fill (~800 bunches). For each of these fill patterns beam was injected into the storage ring and then allowed to naturally decay. To help speed up the decay process, scrapers were inserted to a position which limited the beam life-time to approximately 15-30 minutes. Data was then collected from the BPM approximately every 5 seconds along with the beam current from the DCCT. The data collected from the BPM was; raw ADC data (1Mpts), TbT data (10Kpts), and FA data (18Kpts). Over 100 data files were collected for each fill pattern as the beam decayed. Figure 1 shows the raw ADC data for the 3 different fill patterns.

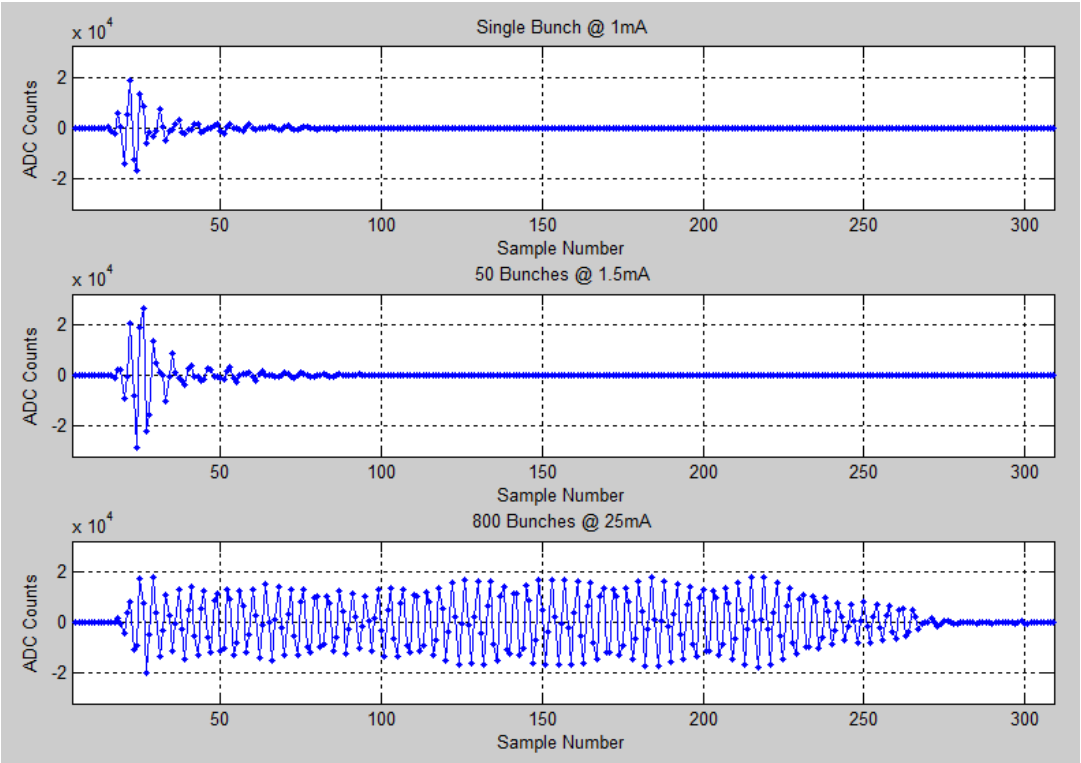

Figure 1. Raw ADC data for different fill patterns

The single bunch resolution performance of the electronics is shown in Figure 2 for TbT data and in Figure 3 for FA data. The digitizer on the BPM has 16 bits of resolution so the maximum value is 3.2767 x 104. The maximum ADC value of each of the four channels was found and the mean value of these maximums is plotted on the ordinate of the resolution plots. At the time of these tests the maximum single bunch beam current that could be stored in the ring was about 1mA, which was not enough to bring the ADC's of the electronics to full scale, so the full scale resolution could not be measured. At around ½ full scale the resolution is about 12um for TbT data and 2um for FA data. A resolution gain of a factor of six is expected from TbT positions to FA positions, since the bandwidth reduction is a factor of 38.

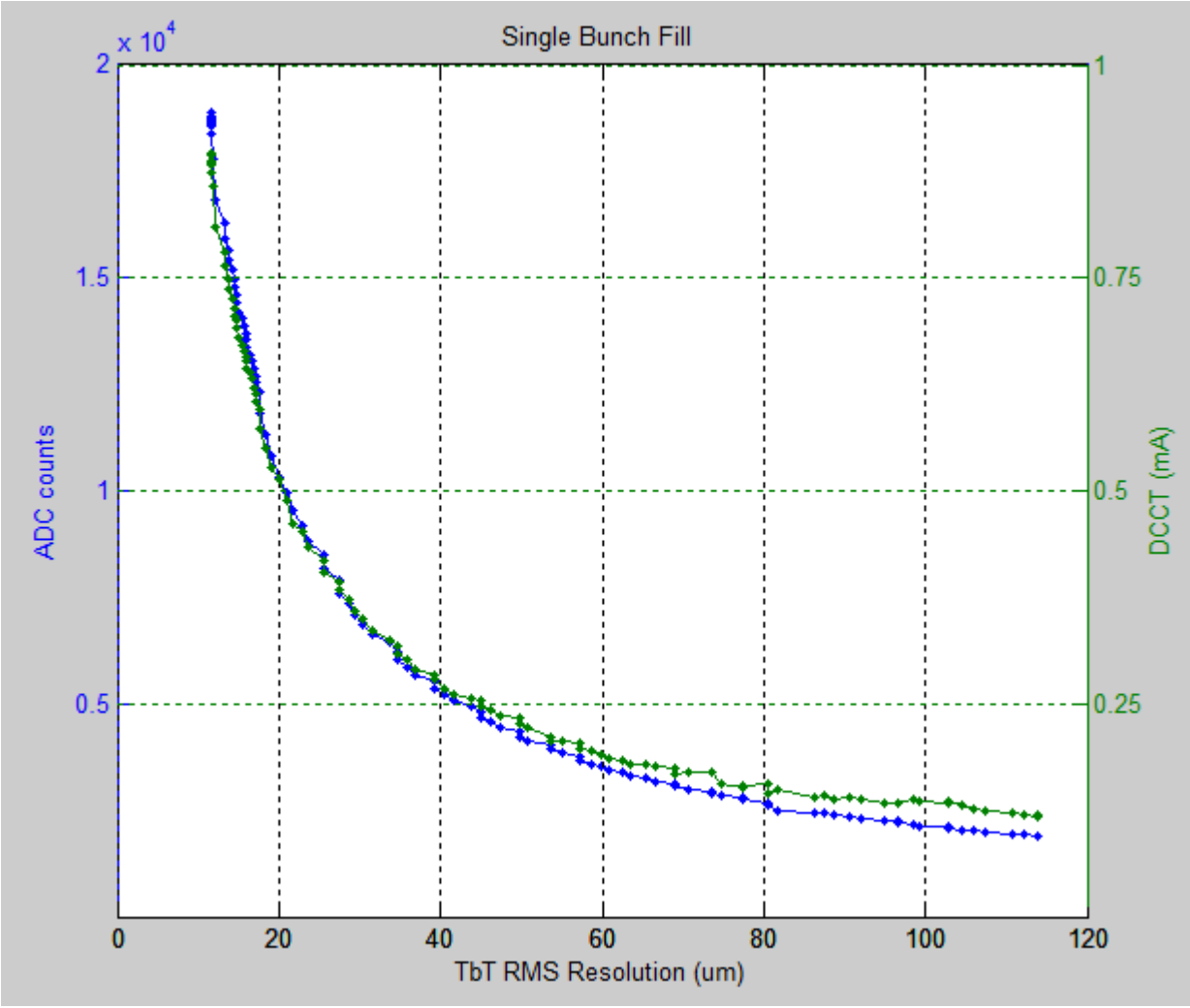

Figure 2. TbT Single Bunch resolution

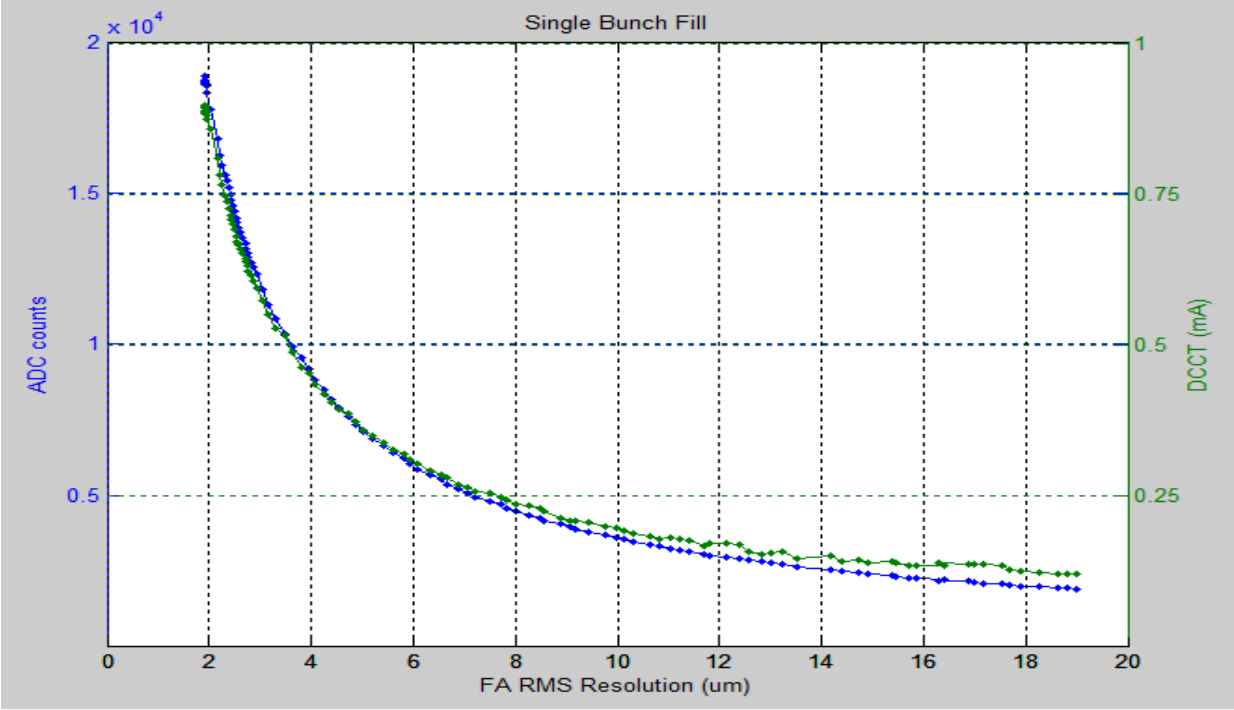

Figure 3. FA Single Bunch resolution

For a 50 bunch fill pattern the results are shown in Figure 4 for TbT data and in Figure 5 for FA data. With this fill pattern the BPM's reached saturation at about 1.6mA of beam current. At full scale the resolution was measured at 7um for TbT data and just over 1um for FA data.

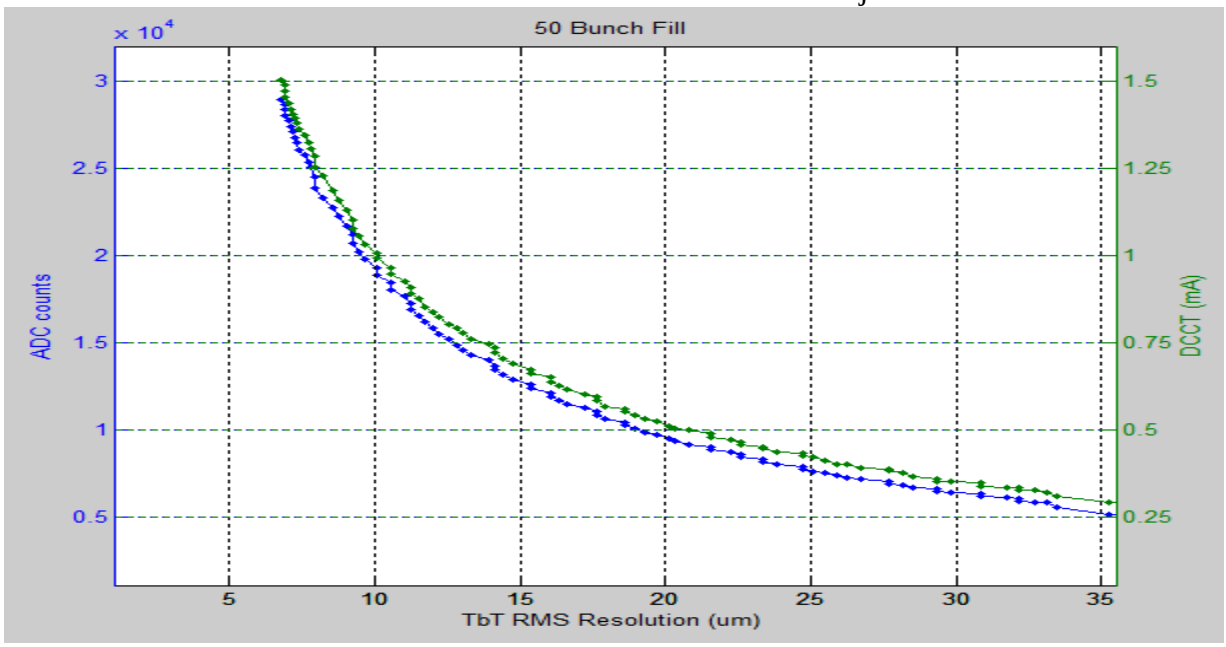

Figure 4. TbT 50 Bunch resolution

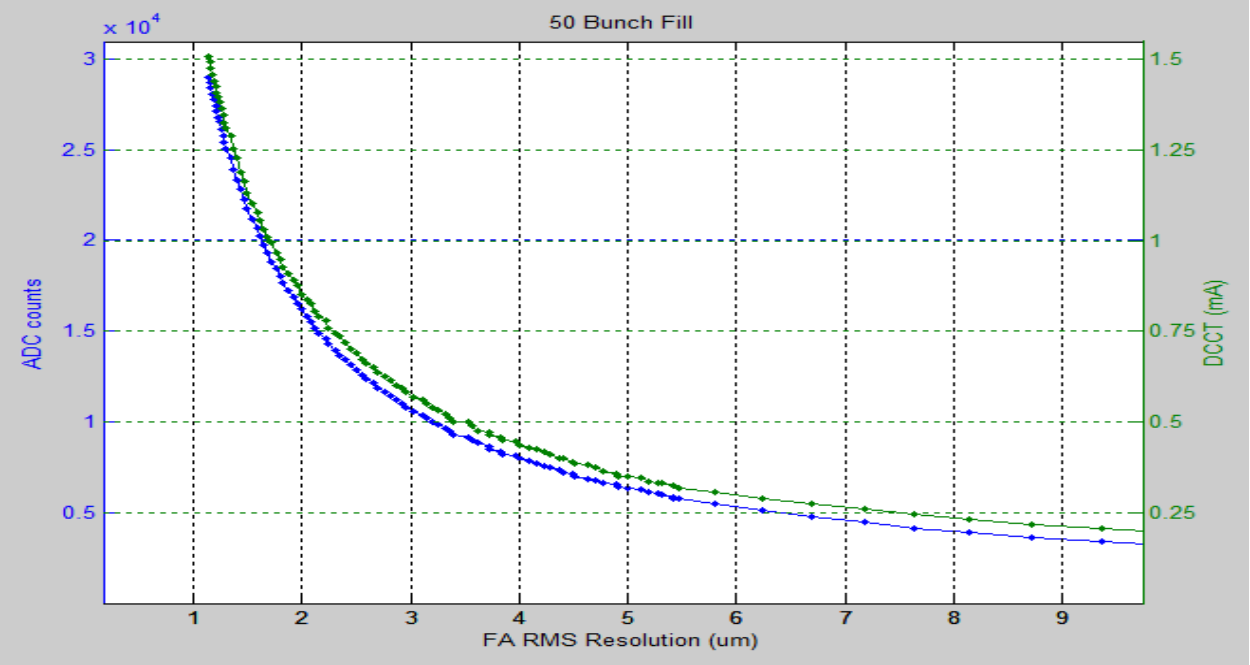

Figure 5. FA 50 Bunch resolution

The final measurement was done with a fill pattern of about 800 bunches, or 60% fill. The limiting factor for this test was the administrative limit of 25mA maximum beam current, so the BPM's didn't quite reach their full scale range. At beam currents above 15mA the results became irregular as the maximum ADC count values fluctuated greatly between data sets and stopped monotonically increasing as beam current increased. This can be seen in Figures 6 and 7 below. Above 15mA of beam current the maximum ADC values smear out, which could be an indication of longitudinal instabilities at these higher beam currents.

Figure 6. TbT 60%

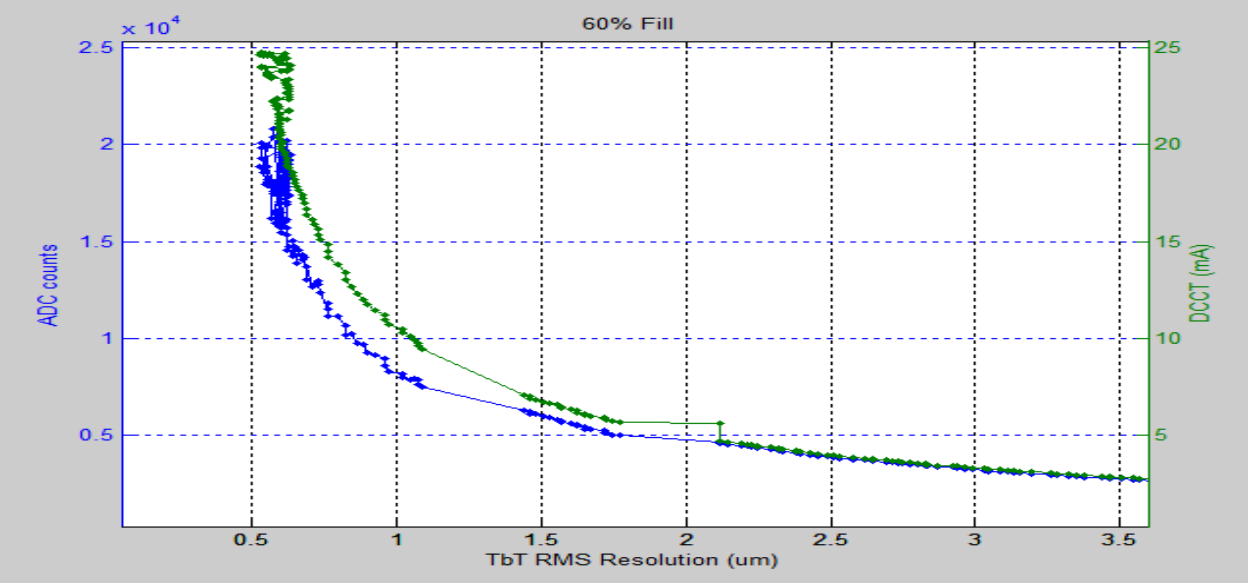

Fill Bunch resolution

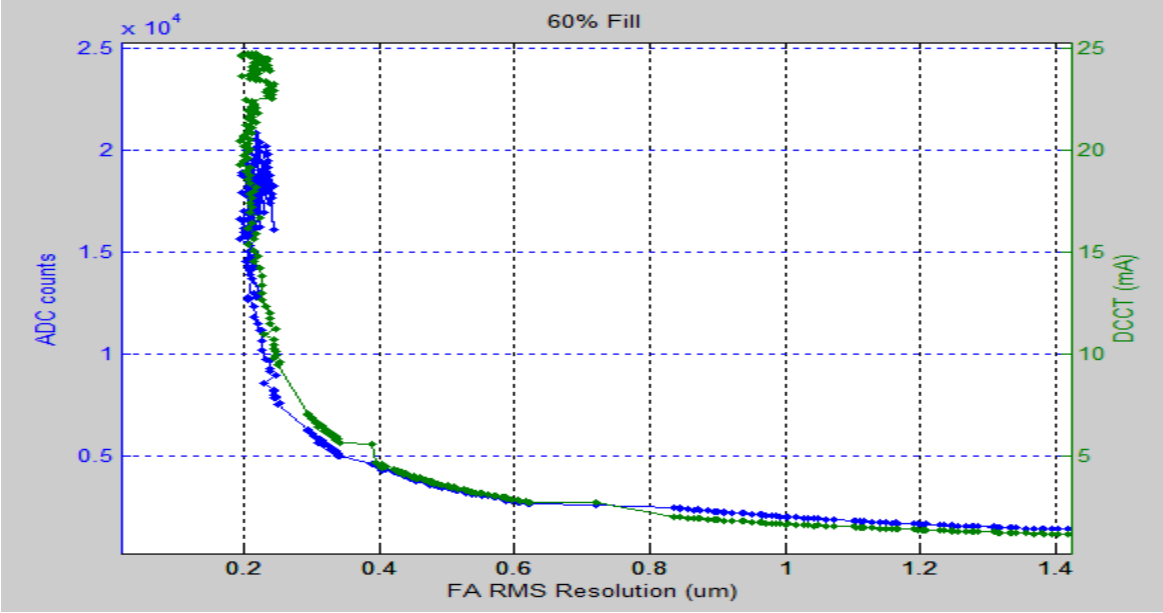

Figure 7. FA 60% Fill Bunch resolution

4.14.3 BPM FA Data and First Look at Orbit Noise

BPM FA data, sampled at 10 kHz, is available on demand in buffers of up to 100 kSamples, which could include horizontal, vertical, and sum signals. Separately these data is streaming to the Fast Orbit Feedback System yet to be commissioned. Monitoring and analysis of the FA data is essential for assessing beam orbit stability, as well as for troubleshooting the ring and locating problem components, which could be for instance oscillating power supplies, vibrating

quads, low frequency RF system noise, to name a few. In this section we present and example data to show that BPM FA data acquisition worked as expected.

These data was taken on 05/04/14 with single bunch at about 1 mA. The data is plotted in frequency domain, where we plot the power spectral density (PSD) up to the Nyquist frequency of 5 kHz. For simplicity we average the PSDs from all 180 BPMs. Higher frequency parts of the vertical FA signals show very few features, except for the peak at 2685 Hz, discussed below, i.e. the orbit is largely undisturbed, see Figure 8.

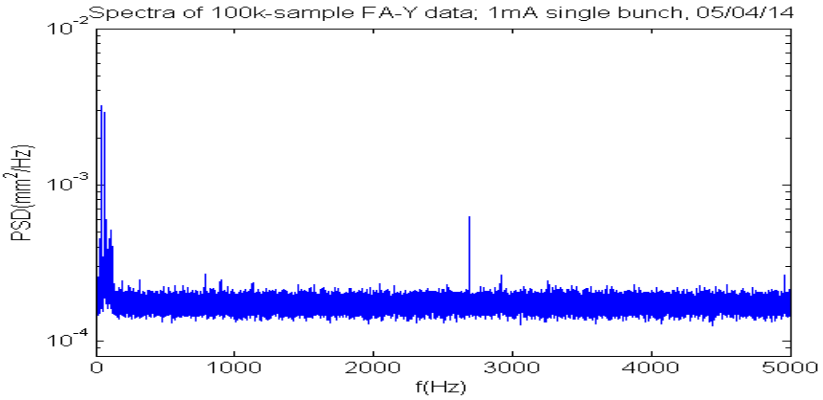

Figure 8. Average PSD for 180 vertical BPM FA signals

Low frequency part of this plot, shown also in Figure 9 on a log-log scale, does show 1 Hz booster cycle frequency and its 2nd harmonic, as well as some peaks at ~39Hz and ~62 Hz possibly induced by component vibration. We emphasize that the amplitudes are quite low.

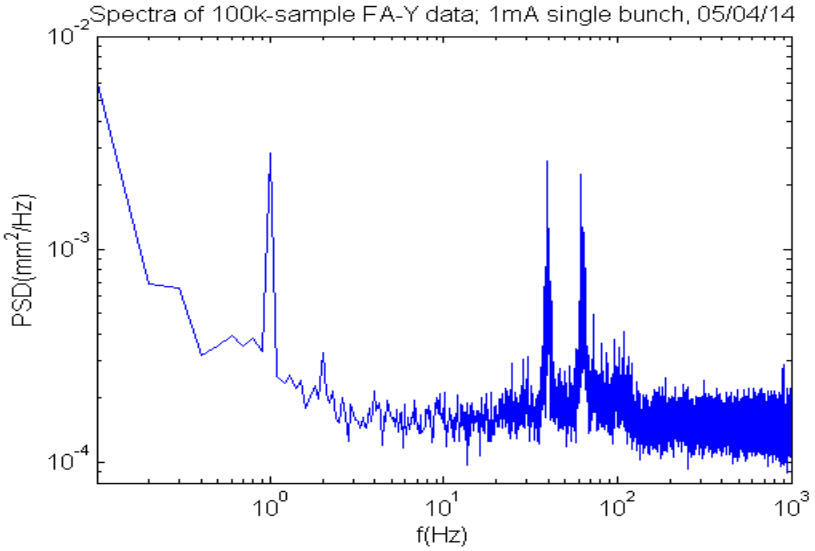

Figure 9. Low frequency average PSD for 180 vertical BPM FA signals

Similarly plotted data for the horizontal plane (taken on the same trigger as the vertical data above) shows a lot more features, see Figure 10. Unlike the vertical, here we separately plot the average PSD for 60 BPMs located in areas with non-zero dispersion, and then the average for

120 non-dispersive BPMs. Clearly, dispersive BPMs exhibit a very large and broad peak at the synchrotron frequency of ~2.8 kHz. When these data was taken we believe the beam was longitudinally unstable, so BPM FA data analysis provides a good diagnostics for this effect. An even stronger and a very narrow peak shows up at f_0=2685 Hz. Harmonically related peaks at $f_0/2$ and $3f_0/2$, as well as a number of narrowband peaks at low frequency are also clearly visible. At the moment the exact origin of these peaks is unconfirmed except we believe they correspond to real beam motion, and, since they prominently show up only on the dispersive BPMs, they originate in the RF system. We suspect that these lines are harmonically related to the switching frequency of the HVPS (Ampegon, formerly Thomson). There is an option to adjust this frequency and it will be explored in the future.

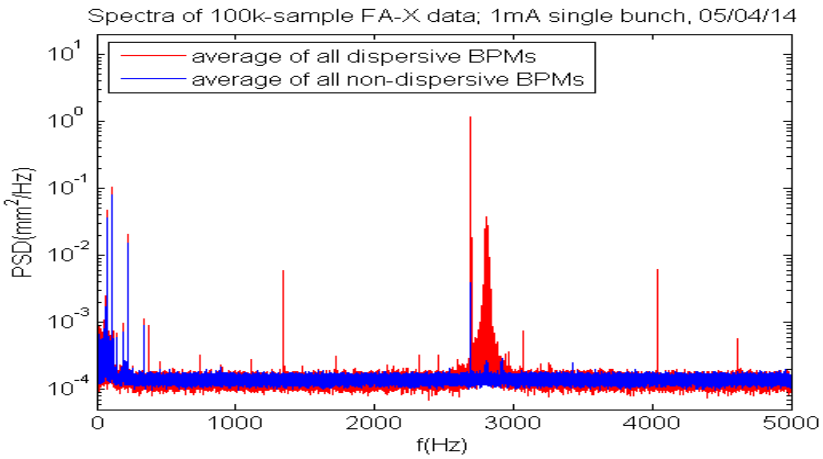

Figure 10. Average PSDs for horizontal BPM FA signals

Low frequency portion of this plot, Figure 11, shows significantly stronger booster noise than in the vertical, with booster harmonics up to 5 Hz clearly visible.

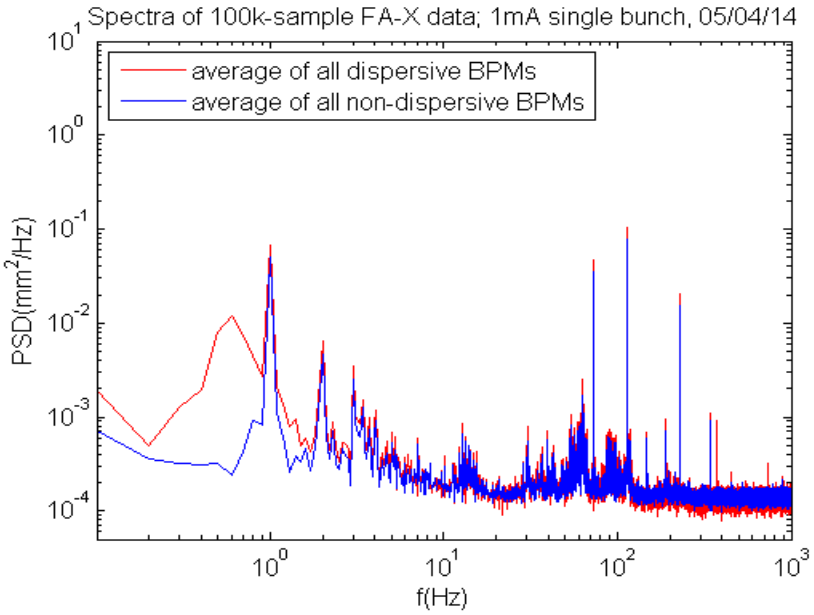

Figure 11. Low frequency average PSDs for horizontal BPM FA signals

More detailed investigations of orbit noise, and localizing its sources will be performed in the future.

4.14.4 BPM Timing Adjustment Experience

The Beam Position Monitor Electronics calculates a single horizontal and vertical position for every revolution. To function correctly the electronics needs to have its timing signals properly adjusted. This involves the adjustment of two different delay values, one being a fine adjustment and one a coarse adjustment. The fine adjustment, called the geographic delay, provides a delay of the machine clock (Frev) signal which is received from the timing system. The delay resolution is approximately 8.5ns, which is the ADC sampling clock period, and the range of the delay is a single revolution, which is 2.6us. The machine clock signal provides the critical signal to instruct the DSP engine to begin a new position calculation. For every machine clock signal received a new position calculation is performed. The function of this delay is to provide a knob to the user to permit compensation for various cabling delays and beam transit delays between BPM's, thus allowing all BPM's in the ring to perform their position calculation on the same bunches. The BPM calculates a new position for every revolution, but unless a trigger signal is received via the timing system, the results are not saved to memory. This is where the coarse adjustment, called the trigger delay, comes into play. This value delays the trigger signal so that the desired revolutions of the beam are saved to memory. Once a trigger is received the next N ADC samples and position calculations are saved to memory. For the storage ring BPM's this value was found to be a value of 10,795,750 which corresponds to an actual delay of about 92ms to properly align to the first injected revolution. The timing was done experimentally, one BPM at a time, using the CSS panel shown below in Figure12 which was developed by Tony Caracappa. This CSS panel helped streamline the operation by allowing changes and showing the results for an entire cell. In theory, all trigger delays should be equal, and only the geographic delays should change as a function of its location in the ring. For most cases this was found to be true, but some anomalies were discovered. The reason we believe is from timing cables with inverted polarity, plus perhaps cell to cell timing discrepancies. We are currently investigating these issues. Regardless, the flexibility of the BPM timing architecture permitted us to overcome these issues and still properly align the timing. All 180 storage ring BPM's were successfully timed in and operational in under 2 hours by Joe Mead and Marshall Maggipinto.

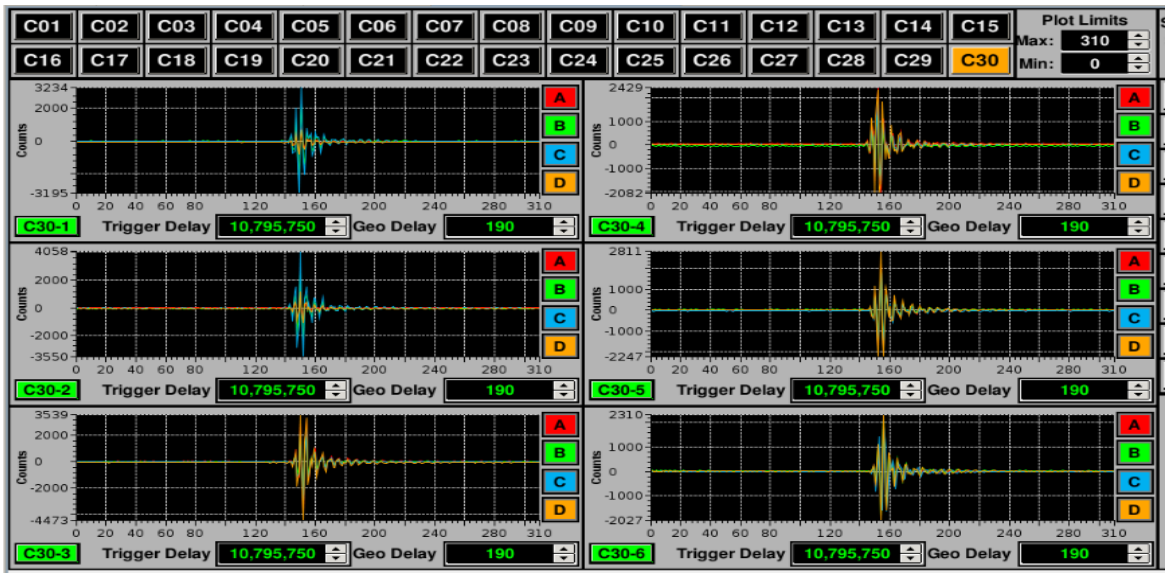

Figure 12. BPM Timing CSS panel

4.14.5 BPM Triggering Modes

The flexibility of the BPM architecture permits it to be triggered in various modes and configurations. The raw ADC data, turn-by-turn (TbT) data, and Fast Acquisition (FA) data are all on-demand data streams and are only available to the user if a trigger signal is received by the BPM. After the trigger signal is received, up to millions of data points from each data stream is stored to the large DDR memory on the BPM. Depending on beam conditions, the trigger scenarios may vary. During the initial operation when first turn was being attempted, the BPM's were set to trigger on the booster extraction event (Event 66). In that scenario, the BPM's could reliable capture the data for the first few million turns. After stored beam was achieved the BPM's were set to trigger on the 1 Hz event (Event 32), so that BPM data would be constantly refreshed to users. In this mode limited record lengths are available do to the communication of long waveforms through the control system. If a user wanted to capture a single shot, long data record, the BPM's can be placed into internal trigger mode and then issued a global single shot event. In this mode the BPM's will trigger only once, to allow time for large records to be offloaded from the local DDR memory through the control system and to the high level applications. These were the main triggering modes of operation used during commissioning. About halfway through commissioning it was observed that if the targeted injection bucket was greater than 200, the BPM's would start reporting positions on incorrect turns. After discussions with Michael Davidsaver, it was learned that the timing of this event (66) was relative to targeted bucket and therefore moved with respect to the machine clock. Since different BPM's need different geographic delays, this timing shift could cause inconsistent results between BPM's. The problem was solved by Michael adding another event (47) to the timing system which always has a fixed timing relationship to the machine clock.

4.14.6 Conclusion and Outlook for BPM Studies

BPMs were by far the most heavily used diagnostics during the commissioning. A great number of high level applications, described elsewhere in this report, make use of BPM data. These include, to name just a few, stored beam orbit measurement, correction, and (slow) feedback (typically using SA data); various linear lattice diagnostics tools (LOCO from SA, tune measurement from TbT, etc.); dynamic aperture and other non-linear lattice diagnostics tools relying on kicked TbT beam response and many others.

It is also worth emphasizing, that even without running any sophisticated tools, the ability to quickly check BPM ADC signals at any ring location or glance through minimally processed TbT data around the ring was absolutely crucial for the ring commissioning. For instance, the very first turn around the ring was closed and confirmed simply by looking at ADC-sum BPM signals all around the ring. Similarly, an aperture in cell 10 (which later turned out to be a hanging RF seal) was first suspected from the fractional drops of kicked beam TbT BPM sum signal which persistently showed up on BPMs at that particular location (see the discussion and figures in sub-section 12.3, “Off-axis Injection”, of “Injection” chapter of this report).

So far the overall experience with BPMs was very positive, especially after additional triggering modes were added. Of course, as is typical for any commissioning, we did encounter and fixed some of the newly discovered issues with the BPM system. We emphasize that several important hardware issues (i.e. kHz noise due to data link oscillator coupling) were identified at the early stages of the injector commissioning, and they were fixed before the SR commissioning commenced. During the SR commissioning proper, the hardware issues with BPMs turned out pretty minimal, i.e. two units (out of 236) had to be replaced because of a failed PLL module. Rather, the majority of the issues were related to the communication between the BPMs to the IOCs as well as from the IOCs to the rest of the control system. Most of these issues were not anticipated prior to the commissioning but rather resulted from the evolution of the requirements from the BPM users, which naturally evolved during the commissioning.

Additional BPM system commissioning studies must be performed in the future. Even though the initial BPM resolution measurement results are very encouraging, to fully verify the compliance with the specs, similar measurements should be repeated at higher currents, as well as with long bunch trains (when stable). When larger amounts of dedicated beam time are provided, long term drift studies should also be performed. In addition, studies to characterize orbit sensitivity to the fill pattern changes and as well as to the changes of BPM attenuation should be performed (the latter have only been done with the pilot tone, not real beam). These will allow us to decide whether automated adjustments of BPM attenuation should be implemented in the control system, and if so, how. Another important issue for physics applications is the correction of the non-linearity at large transverse beam displacements (this is unrelated to the BPM electronics). So far the linearity is corrected using the coefficients obtained from BPM button geometry (essentially solving the Laplace equation). Experimental verification of these would be extremely beneficial, and it could be accomplished, for instance,

by comparing the BPM readout with large transverse beam offset vs. the positions on the nearby flag.

4.15 Measurements of the Local Vertical Kick Factor

The local bump method [1] has been applied for the vertical kick factor measurements of the DW straight sections, Cell 8 and Cell 18. Two straight sections have been chosen since their local vertical kick factor is higher than the kick factor of the standard arc sections of the storage ring and the kick factor of any other straight sections at this stage of the storage ring.

The local bump was applied to estimate the vertical kick factor of the straight section. As can be seen from Fig. 2 and Fig. 3 the local bump was not localized well. In Cell 08 the local bump is between BPMs 44 and 52. In Cell 18 the local bump is between BPMs 102 and 110. In both cases it is more wide bump than wanted. The available strength of the correctors was limited at that time locally and it was close to saturated value. Later the corrector strength was re-optimized by Lingyun around the ring keeping the orbit trajectory unchanged.

To estimate the local vertical kick factor, we used a model in which the beam trajectory deviation was fitted into the measured one. The orbit deviation is related to the kick factor by

$$\Delta y(s) = \frac{\Delta q}{E/e} k_{\perp} y_0 \frac{\sqrt{\beta(s_0)\beta(s)}}{2\sin\pi\nu} \cos\left(\left|\mu(s) - \mu(s_0)\right| - \pi\nu\right) \quad (1)$$

where Δq is the bunch charge difference, $k_{\perp}$ is the transverse kick factor, y_0 is the local bump height, $\beta(s_0)$ is the localized vertical beta function, $\beta(s)$ is the vertical beta function around the ring, ν is the betatron tune and $\Delta\mu = \mu(s) - \mu(s_0)$ is the betatron phase advance.

Some key parameters needed for the vertical kick factor measurements are given in Table 1.

Table 1: Parameters for the Kick Factor Measurements

Energy, E [GeV]	3
Localized vertical beta, $\beta(s_0)$ [m]	18.2
Vertical tune: ν	0.239
Bunch charge diference: Δq [nC]	1.6
Bump height: y_0 [mm]	2.3-2.5

The vertical beta function and the betatron phase advance difference are taken from the model. Based on the fitted data presented in Fig. 2 and Fig. 4 the measured vertical kick factor in both sections is $k_y = 235$ V/pC/m. As can be seen, the measured orbit trajectory deviation is oscillating too much in the region of the PETRA-III RF cavity location (Cell 24, between BPMs 143 and 144) and it is differed from the modeled trajectory.

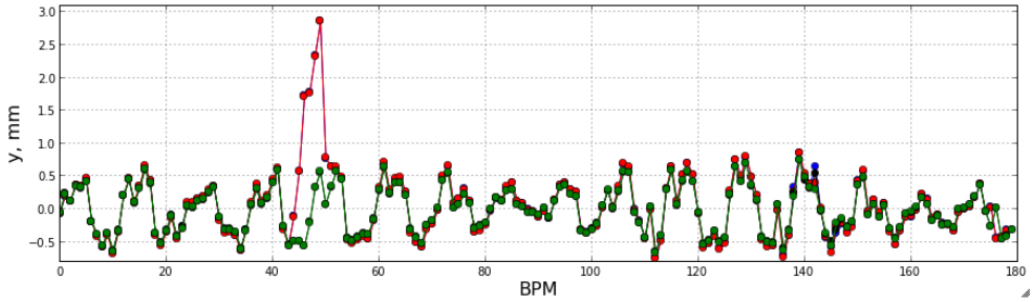

Fig. 1: Four orbit trajectories measured at low and at high single bunch currents without and with a 2.3 mm vertical local bump in the DW8 straight section.

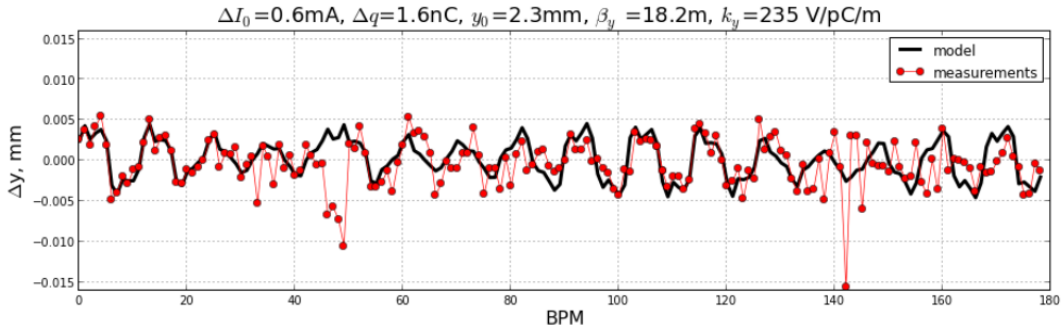

Fig. 2: Measured beam trajectory deviation (red) and fitted beam trajectory using the model (black).

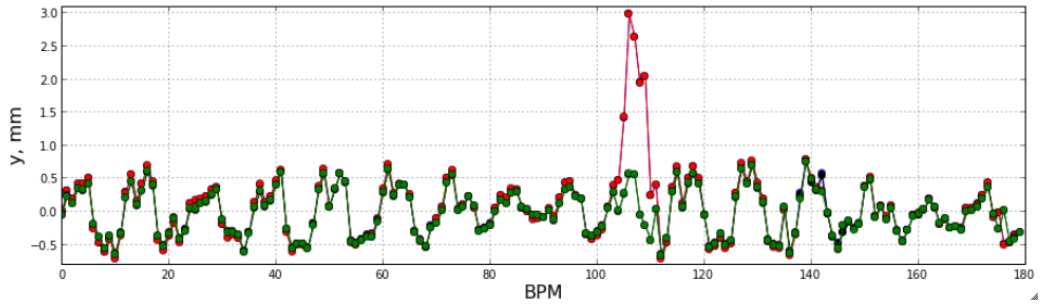

Fig. 3: Four orbit trajectories measured at low and at high single bunch currents without and with a 2.5mm vertical local bump in the DW18 straight section.

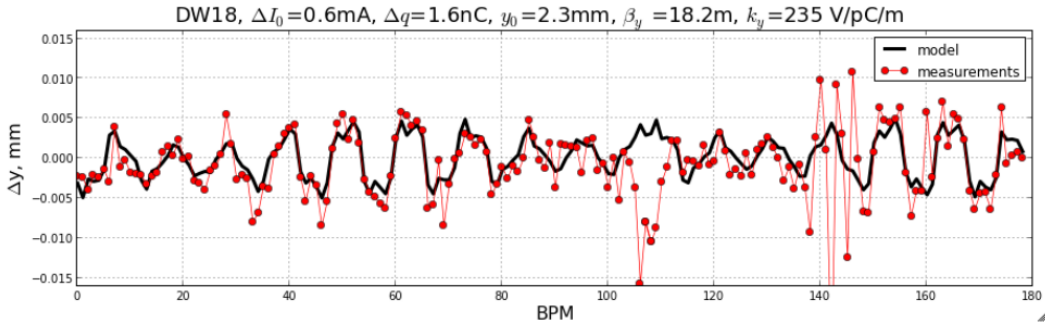

Fig. 4: Measured beam trajectory deviation (red) and fitted beam trajectory using the model (black).

The DW straight section is shown in Fig. 5. Two NEG coated aluminum vacuum chambers, 3.8m long each, joined together. The full vertical aperture of the chamber is 11.5mm. There are special tapered transitions on both sides of the section with RF shielded slots to hide the ion pump ports from the beam (Fig. 6).

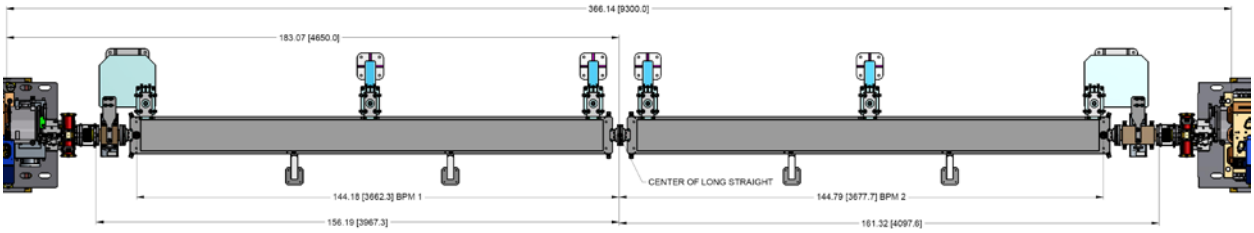

Fig. 5: Standard DW straight section. Cells 08, 10 and 18.

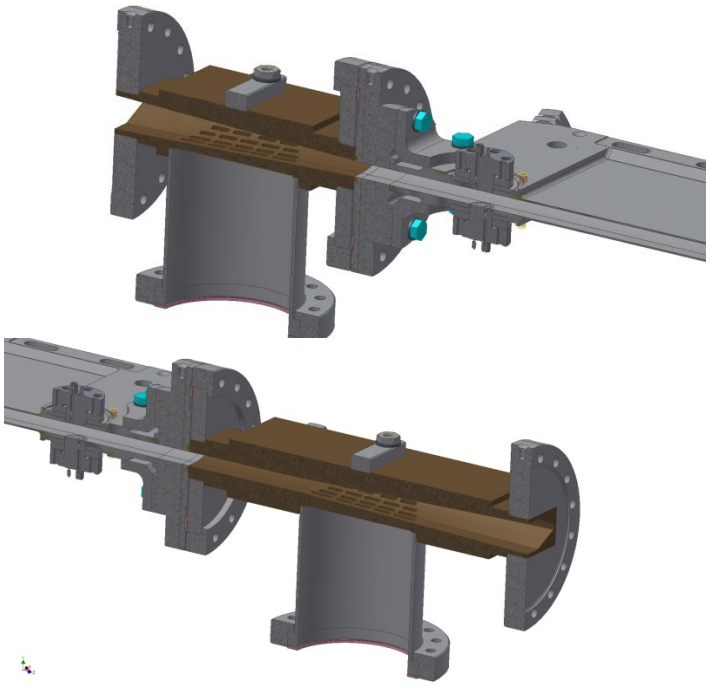

Fig. 6: Special tapered transitions with RF shielded slots to hide the ion pump ports from the beam.

Reference

[1] V. Kiselev and V. Smaluk, “Measurement of Local Impedance by an Orbit Bump Method”, NIMA 525 (2004), 433-438.

4.16 Single Bunch Current Limitation

We made first studies of the collective effects in the NSLS-II storage ring during operation with 500MHz PETRA-III RF cavity right before the accelerator was shut down for the planned maintenance. It is Phase 1 of the storage ring commissioning.

In the single bunch mode we studied bunch behavior at different chromaticities (0, +1/+1, +2/+2, +3/+3 and +4/+4) for both planes, horizontal and vertical. In post process regime we modeled the short range wakefields with broadband resonators (BBR) and estimated the BBR parameters form the measured growth rates and tune shifts as a function of current and chromaticity. In Appendix we outline the estimation method used.

Measurements of tunes have been done by kicking the beam horizontally via lowering the 4th injection kicker by 0.1kV. The BPM TBT data have been collected and Fourier analyzed for tune estimation. The envelope of the BPM TBT data have been fit by the function $(n) = ae^{-nT_0/\tau}$, where n is turn number, T_0 is the revolution period and τ the damping time.

Measured horizontal and vertical TbT data have been analyzed at different chromaticities. In Fig. 1b we plot the horizontal growth rate as a function of current for chromaticity +1/+1 and +2/+2.

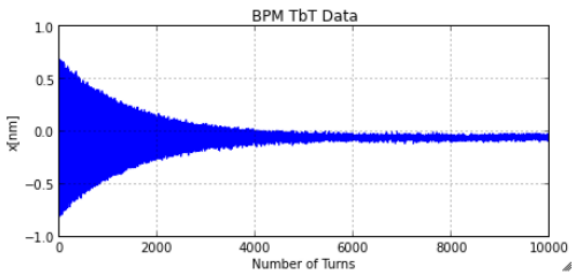

a) Measured horizontal Turn-by-Turn data at chromaticity +1/+1, BPM 6 (I=0.85mA).

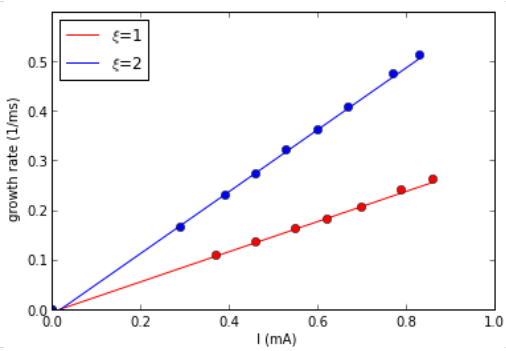

b) Measured horizontal growth rate as a function of current at +1/+1 and +2/+2 chromaticity

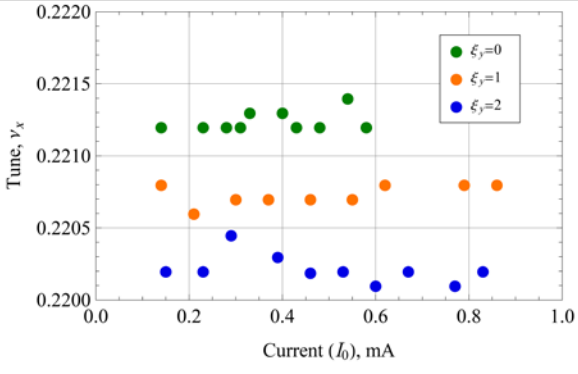

c) Measured horizontal tune as a function of current using FFT method (4000 TbT data).

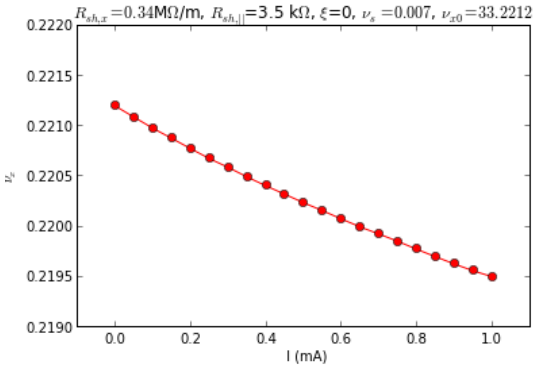

d) Simulated horizontal tune as a function of current by the OASIS code [1] applying the BBR model with parameters presented in Table 1.

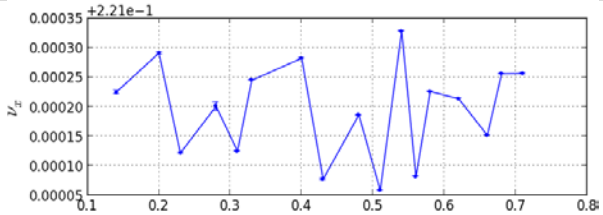

e) Measured Horizontal and Vertical Tune vs. Current using FFT (1000 TbT data) method with windowing following statistical analysis of all 180 BPMs.

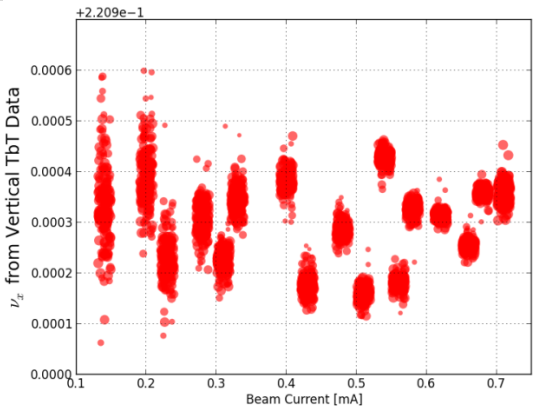

f) Horizontal tune statistic from 180 BPMs at different currents.

Fig. 1: Horizontal Turn-by Turn data analysis.

Table 1: Broadband Impedance Parameters

Longitudinal broadband impedance	$f_{r,\|\|} = 30GHz,\ R_{sh,\|\|} = 3.5\ k\Omega$, Q=1.
Horizontal broadband impedance	$f_{r,x} = 30GHz, R_{sh,x} = 0.34M\Omega/\text{m}$, Q=1.
Vertical broadband impedance	$f_{r,y} = 30GHz, R_{sh,y} = 0.67M\Omega/\text{m}$, Q=1.

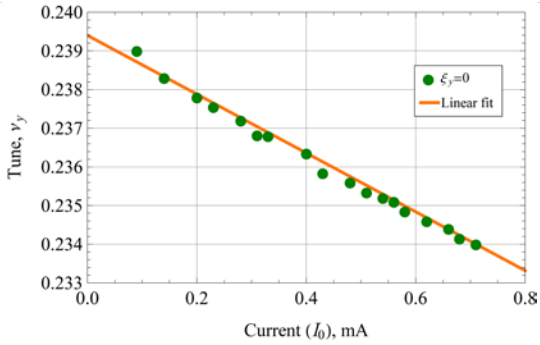

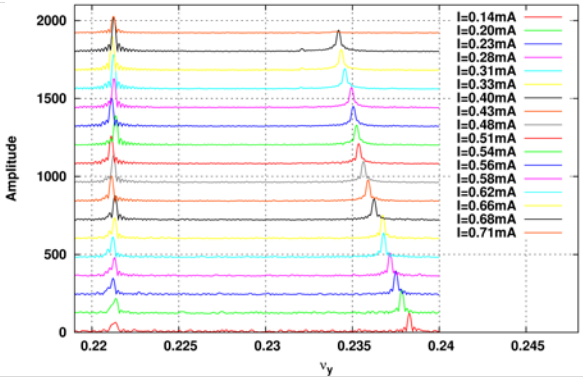

a) Zero Chromaticity

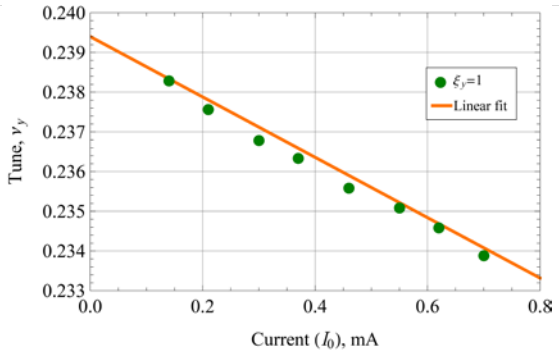

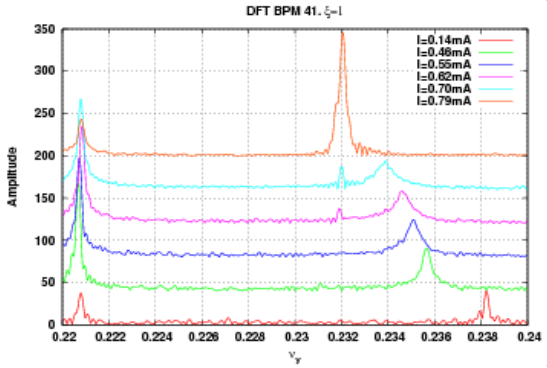

b) Both Planes (x/y) Chromaticity +1/+1

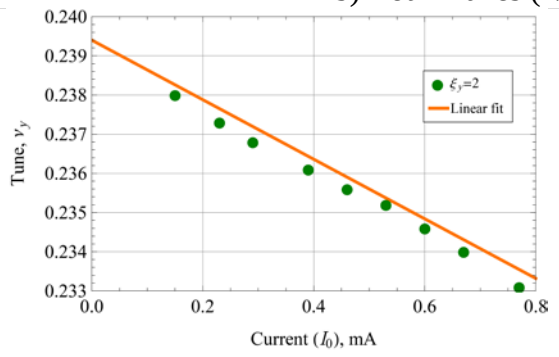

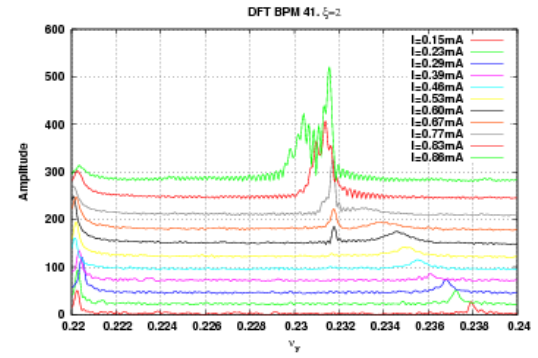

c) Both Planes (x/y) Chromaticity +2/+2

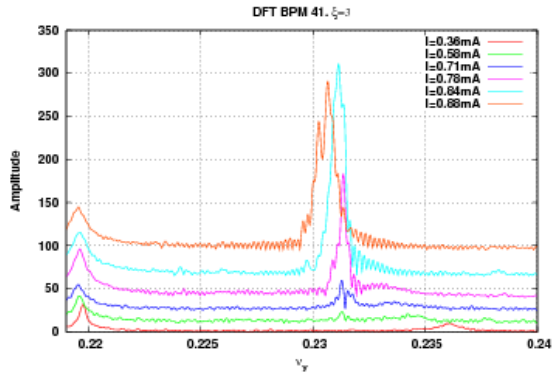

d) Both Planes (x/y) Chromaticity +3/+3

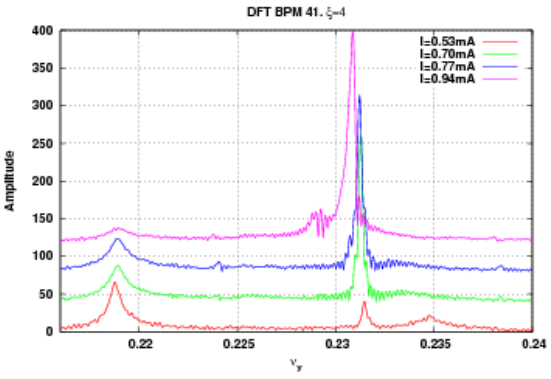

e) Both Planes (x/y) Chromaticity +4/+4

Fig. 2 Vertical Turn-by Turn data analysis. Vertical tune as function of current and spectra of BPM 41 TBT data for different chromaticities.

An approximate relation determining the threshold of the transverse coupled mode instability at zero chromaticity is given by [2] with an accuracy of about $\pm 30\%$

$$\left(\frac{\Delta\nu_y}{\nu_s}\right)^{av} \equiv \frac{e^2 N_e^{th} \beta_y}{4\pi\gamma mc^2 \nu_s} k_\perp \cong 0.7 \qquad (1)$$

where N_e^{th} is the number of electrons in a bunch at threshold, β_y is the average value of the betatron function, γmc^2 is the electron energy and ν_s is the synchrotron tune. For parameters in Table 2 and based on measurements data presented in Fig. 2a we can determine the global vertical kick factor of the NSLS-II storage ring. As can be seen from Fourier spectrum of TbT data in Fig. 2a two mode frequency peaks, m=0 and m=-1, can be recognized only at high beam intensity. They still do not merge at maximum accumulated current we achieved $I_0 = 0.71$mA at zero chromaticity.

Table 2: Parameters for Global Kick Factor Estimation

Energy, E [GeV]	3
Circumference, C [m]	791.9856
Revolution Period, T_0 [μs]	2.64
RF Voltage, V_{RF} [MV]	1.86
Synchrotron Tune, ν_s	7 x 10-3
Vertical/Horizontal Average beta-function: β_y, β_x [m]	7.7, 3.8
Damping Time: τ_x, τ_s [ms]	54, 27
Bunch Length, σ_τ [ps], σ_o [mm],	10, 3

The global kick factor of the NSLS-II storage ring is $k_y = 14$ kV/pC/m with a threshold of 0.81mA per bunch.

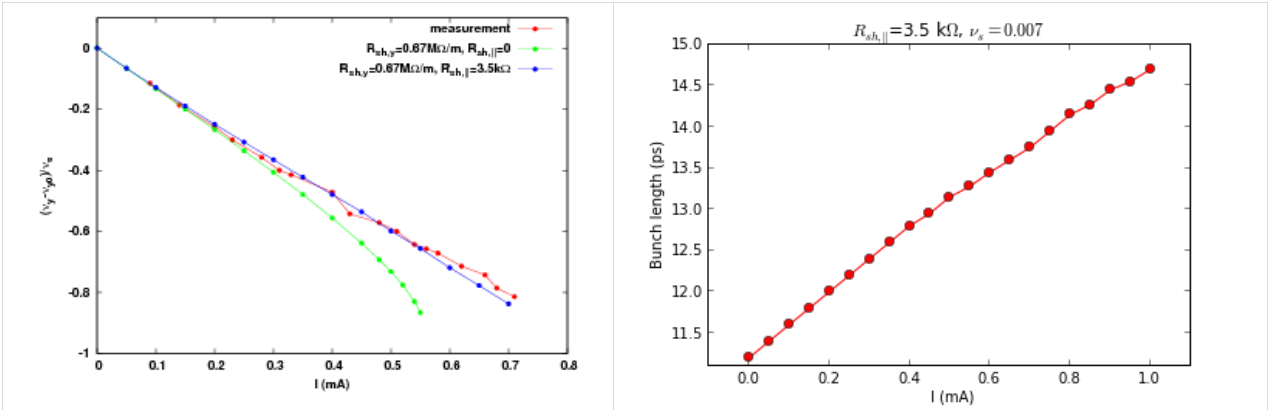

a) Vertical tune shit vs. current. In red measurement from TBT data. Numerical simulations with OASIS code with $R_{sh,y} = 0.67M\Omega/\text{m}$ and $R_{sh,||} = 0$ (green), and with $R_{sh,y} = 0.67M\Omega/\text{m}$ and $R_{sh,||} = 3.5\ k\Omega$ (blue).

b) Bunch lengthening vs. current with longitudinal broadband impedance parameters listed inTable 1.

Fig. 3: Analysis of the vertical tune as a function of current with bunch lengthening effect. a) Comparison of the measured vertical tune with numerically simulated using BBR models from Table 1. b) Simulated bunch lengthening effect using BBR models from Table 1 by the OASIS code.

Table 3: Turn-by-Turn data are shown from the first 12 BPMs for different currents at positive chromaticity +1/+1 and +2/+2.

	Chromaticity +1/+1	Chromaticity +2/+2
I_0=0.66mA	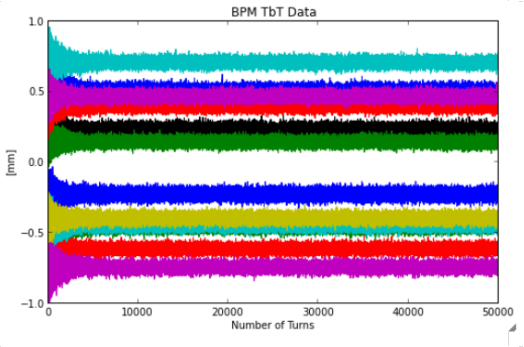	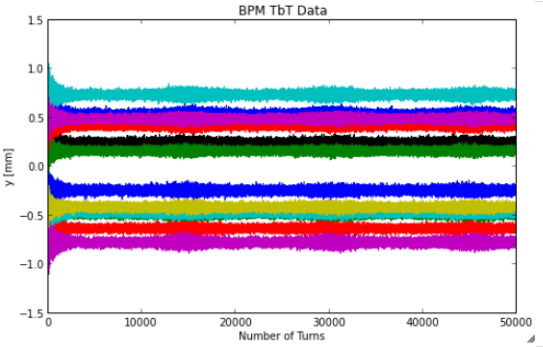
I_0=0.77mA	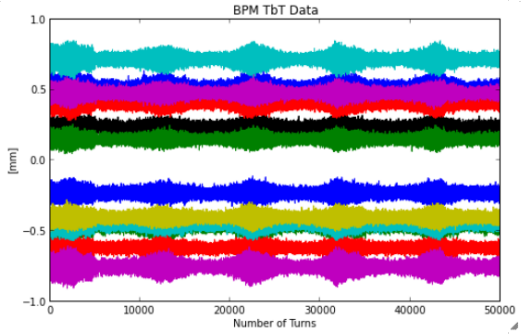	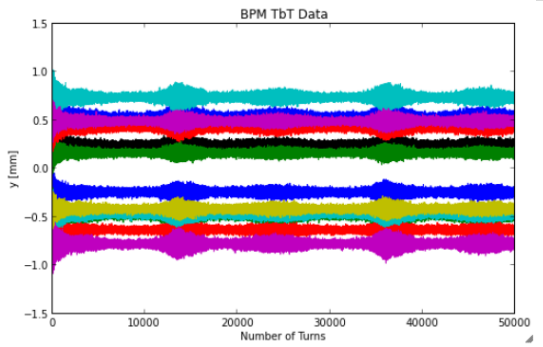
I_0=0.86mA	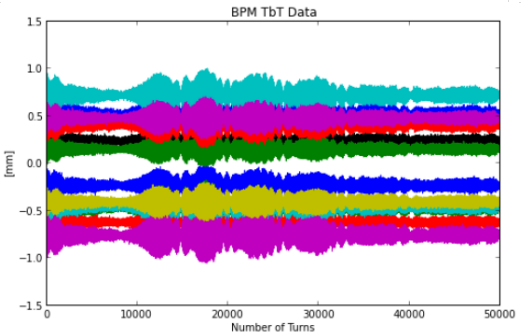	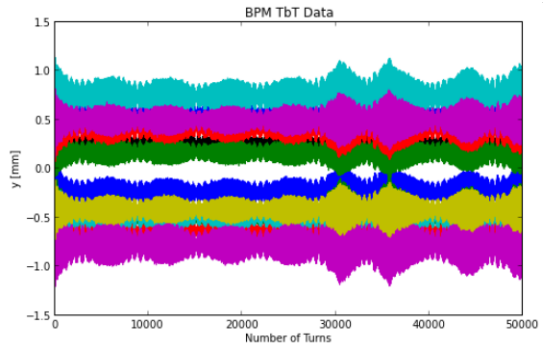

RF Voltage Ramp-Up

Studies of the single bunch current during the first phase of the commissioning showed that we can store about 0.9mA in a single bunch with positive chromaticity +2/+2 in both planes and at nominal RF voltage V_{RF}=1.86MV of the PETRA-III RF cavity. The measured bunch length at low current is 11ps. The intensity of the single bunch in the storage ring was accumulated by a small portion of the delivered charge from the booster (1.6nC per short???). After reaching 0.96mA no further accumulation was observed and the single bunch continued to circulate with high beam life time, about 20 hours. The beam starts to be vertically unstable at lower current 0.6mA, when some burst signals occur at vertical TbT data. The synchrotron light monitor shows how beam blow-up vertically at high current. In Figure 4 we present two

snapshots of the circulated single bunch in the storage ring from the synchrotron light monitor for two different currents, 0.96mA and 0.7mA, keeping the same aspect ratio for both images.

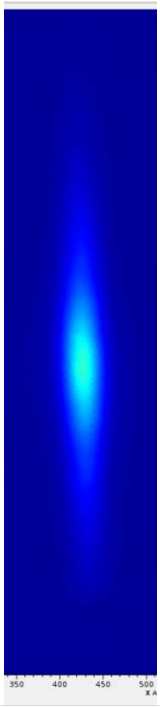

a) I_0=0.96mA

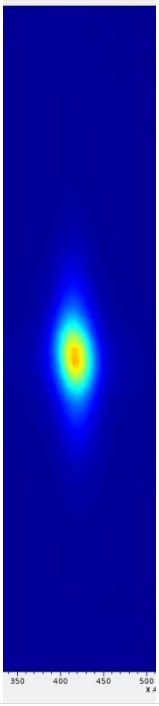

b) I_0=0.7mA

Fig. 4: Images of the single bunch profile from the synchrotron light monitor for two different currents, 0.96mA and 0.7mA. Vertical and horizontal axes are kept fixed for two snapshots.

To understand the course of instability in single bunch limitation we reduced the RF voltage of the cavity up to $0.2215 \times V_{RF}$ from its nominal value. In this case we immediately observed that the single bunch current can be accumulated up to 2.1mA (Fig.5a). Raising the RF voltage back to nominal value $0.8815 \times V_{RF}$ helped in the accumulation current increase up to 3.36mA. In Fig. 5 we plot bunch accumulation history for two different chromaticities +2/+2 (Fig. 5a) and +4.6/+4.6 (Fig. 5b).

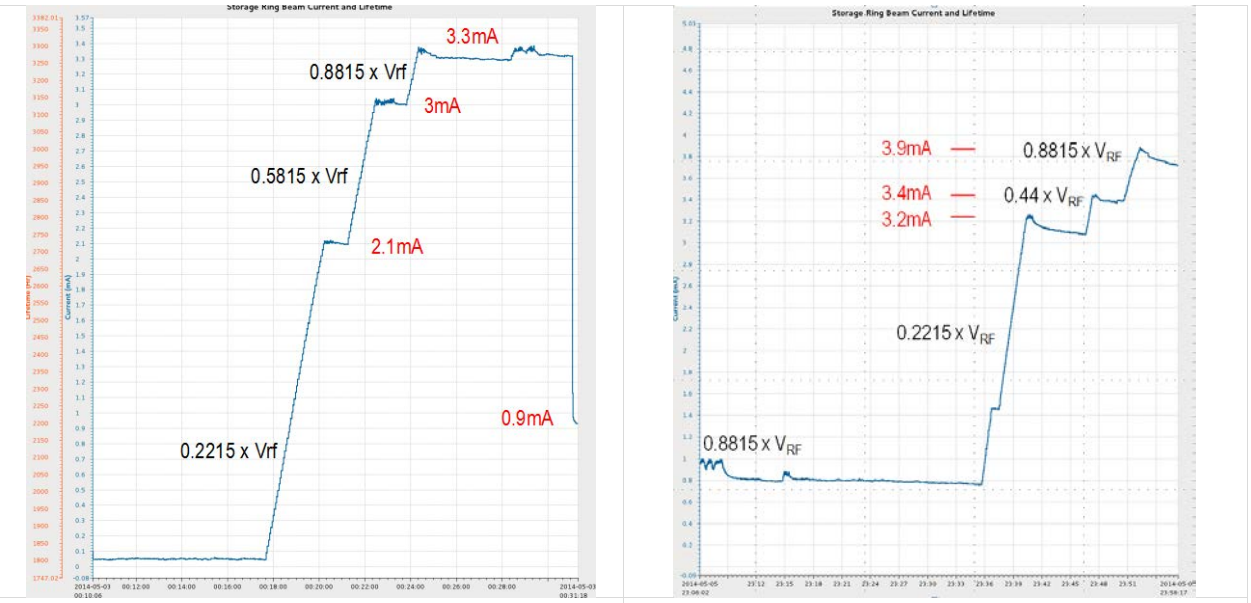

a) $\xi_{x,y} = +2/+2$ (1076 sr file) b) $\xi_{x,y} = +4.6/+4.6$

Fig. 5: Accumulation of the single bunch with high intensity due to lowering and ramp-up of the RF voltage.

References

[1] G. Bassi, OASIS code.
[2] See e.g., S. Krinsky, BNL-75019-2005-IR.

Appendix

$$\tau^{-1} = \mathrm{Im}(\Omega - \omega_\beta) = -\frac{eI\beta_x\omega_0 C}{8\pi^2 E\beta}\int_{-\infty}^{+\infty} dk\,\mathrm{Re}\,Z_\perp(k)e^{-\left(k-\frac{\omega_\xi}{c}\right)^2\sigma^2},$$

Growth rate τ^{-1} and frequency shift $\Delta\omega_\beta$

$$\Delta\omega_\beta = \mathrm{Re}(\Omega - \omega_\beta) = \frac{eI\beta_x\omega_0 C}{8\pi^2 E\beta}\int_{-\infty}^{+\infty} dk\,\mathrm{Im}\,Z_\perp(k)e^{-\left(k-\frac{\omega_\xi}{c}\right)^2\sigma^2}.$$

with chromaticity ξ for a Gaussian bunch

$$\omega_\xi = \frac{\xi}{\eta}\omega_0.$$

where

$\tilde{\lambda}(k) = e^{-\frac{k^2\sigma^2}{2}}$. $\Delta\nu_x = \frac{eI\beta_x C}{8\pi^2 E\beta}\int_{-\infty}^{+\infty} dk\left|\tilde{\lambda}(k)\right|^2 \mathrm{Im}\,Z_\perp(k)$, At zero chromaticity the tune shift formula reads

$\mathrm{Re}\,Z_\perp(k)$ where

At zero chromaticity $\tau^{-1} = 0$ since is odd and $\tilde{\lambda}(k)$ is even, but $\xi \neq 0 \rightarrow \tau^{-1} \neq 0.$

Approximate equation for τ^{-1}

$$\tau^{-1} = -\frac{eI\beta_x\omega_0 C}{8\pi^2 E\beta}\int_{-\infty}^{+\infty} dk\,\mathrm{Re}\,Z_\perp(k)e^{-\left(k-\frac{\omega_\xi}{c}\right)^2\sigma^2} = -\frac{eI\beta_x\omega_0 C}{8\pi^2 E\beta}\int_{-\infty}^{+\infty} dk\,\mathrm{Re}\,Z_\perp(k)e^{-k^2\sigma^2+\chi\sigma k-\frac{\omega_\xi^2\sigma^2}{c^2}}$$

where $\chi = \frac{\omega_\xi}{c}$ is the head-tail phase. For NSLS-II (Table2) $\chi = 0.13$ for $\chi = 1$.

$$\chi\ll 1 \quad \frac{eI\beta_x\omega_0 C\omega_0\sigma}{8\pi^2 E\beta\,\eta c^2}\int_{-\infty}^{+\infty} dk\,\mathrm{Re}\,Z_\perp(k)kc^{-k^2\sigma^2},$$

For a broadband resonator impedance with resonator frequency $\omega_r = 2\pi f_r$, shunt impedance R_{sh} and quality factor Q, the real part $Z_\perp$ reads

$ReZ_\perp(k) = \frac{k}{k_r}\frac{R_{sh}}{1+B^2}$, where $B = Q\left(\frac{k}{k_r}-\frac{k_r}{k}\right)$ and $k = \frac{\omega}{c}$, $k_r = \frac{\omega_r}{c}$.

For a given ω_r and Q, the shunt impedance R_{sh} can be estimated from Eq. (1) with the measured τ^{-1} (Fig. 1b)

$R_{sh} = \frac{\tau^{-1}}{\chi AF}$, where $A = \frac{eI\beta_x\omega_0 C\sigma}{8\pi^2 E\beta}$ and $= F(k_r, Q, \sigma) = \int_{-\infty}^{+\infty} dk\,\frac{k}{k_r(1+B^2)}$.

4.17 Subsystem Reliability and Performance

4.17.1 Recordable statistics

Duration of Phase 1 storage ring commissioning (3/28/2014-5/11/2014): 1056 hrs.
Total planned maintenance time during commissioning: 74 hrs.
Total available operating time: 982 hrs.
Total number of recorded faults: 374
Mean Time between failures (Total time/# faults): 2.63 hrs.
Lost time due to faults: 212 hrs.
Faults by group
Below is a summary of the number of faults and Mean Time Between Failures recorded during the first commissioning phase. The summary is separated by subsystem vertically and by date horizontally. Totals for each time period are shown at the bottom of each column.

total faults by sub-system																	
		start date	end date	start date	end date	start date	end date	start date	end date	start date	end date	start date	end date	start date	end date	start date	end date
		3/27/14	5/15/14	3/27/14	4/3/14	4/3/14	4/10/14	4/10/14	4/17/14	4/17/14	4/24/14	4/24/14	5/1/14	5/1/14	5/8/14	5/8/14	5/15/14
		Commissioning period 1		Week 1		Week 2		Week 3		Week 4		Week 5		Week 6		Week 7	
Accelerator Area	subsystem	number of faults	MTBF hrs	number of faults	MTBF hrs	number of faults	MTBF hrs	number of faults	MTBF hrs	number of faults	MTBF hrs	number of faults	MTBF hrs	number of faults	MTBF hrs	number of faults	MTBF hrs
Linac / LTB	Power Supplies	0	#DIV/0!	0	#DIV/0!	0	#DIV/0!	0	#DIV/0!	0	#DIV/0!	0	#DIV/0!	0	#DIV/0!	0	#DIV/0!
Linac / LTB	Vacuum	11	89	1	158	0	#DIV/0!	2	79	2	67	4	40	1	168	1	168
Linac / LTB	RF	85	12	7	23	6	26	10	16	13	10	9	18	35	5	5	34
Linac / LTB	EPS/PPS/Radmon	0	#DIV/0!	0	#DIV/0!	0	#DIV/0!	0	#DIV/0!	0	#DIV/0!	0	#DIV/0!	0	#DIV/0!	0	#DIV/0!
Linac / LTB	Utilities	2	491	0	#DIV/0!	0	#DIV/0!	0	#DIV/0!	1	134	0	#DIV/0!	0	#DIV/0!	1	168
Linac / LTB	Controls	5	196	0	#DIV/0!	5	32	0	#DIV/0!	0	#DIV/0!	0	#DIV/0!	0	#DIV/0!	0	#DIV/0!
Linac / LTB	Instrumentation	0	#DIV/0!	0	#DIV/0!	0	#DIV/0!	0	#DIV/0!	0	#DIV/0!	0	#DIV/0!	0	#DIV/0!	0	#DIV/0!
Linac / LTB	Other	1	982	0	#DIV/0!	0	#DIV/0!	0	#DIV/0!	0	#DIV/0!	1	158	0	#DIV/0!	0	#DIV/0!
Booster / BTS	Power Supplies	128	8	24	7	10	16	1	158	7	19	30	5	36	5	20	8
Booster / BTS	Vacuum	4	246	0	#DIV/0!	0	#DIV/0!	0	#DIV/0!	4	34	0	#DIV/0!	0	#DIV/0!	0	#DIV/0!
Booster / BTS	RF	42	23	5	32	5	32	17	9	3	45	1	158	6	28	5	34
Booster / BTS	EPS/PPS/Radmon	0	#DIV/0!	0	#DIV/0!	0	#DIV/0!	0	#DIV/0!	0	#DIV/0!	0	#DIV/0!	0	#DIV/0!	0	#DIV/0!
Booster / BTS	Utilities	1	982	1	158	0	#DIV/0!	0	#DIV/0!	0	#DIV/0!	0	#DIV/0!	0	#DIV/0!	0	#DIV/0!
Booster / BTS	Controls	1	982	1	158	0	#DIV/0!	0	#DIV/0!	0	#DIV/0!	0	#DIV/0!	0	#DIV/0!	0	#DIV/0!
Booster / BTS	Instrumentation	0	#DIV/0!	0	#DIV/0!	0	#DIV/0!	0	#DIV/0!	0	#DIV/0!	0	#DIV/0!	0	#DIV/0!	0	#DIV/0!
Booster / BTS	Other	2	491	0	#DIV/0!	0	#DIV/0!	1	158	1	134	0	#DIV/0!	0	#DIV/0!	0	#DIV/0!
storage ring	Power Supplies	34	29	3	53	3	53	6	26	1	134	3	53	6	28	12	14
storage ring	Vacuum	1	982	0	#DIV/0!	0	#DIV/0!	0	#DIV/0!	0	#DIV/0!	0	#DIV/0!	1	168	0	#DIV/0!
storage ring	RF	29	34	0	#DIV/0!	5	32	2	79	8	17	3	53	4	42	7	24
storage ring	EPS/PPS/Radmon	20	49	4	40	6	26	3	53	4	34	1	158	0	#DIV/0!	1	168
storage ring	Utilities	3	327	0	#DIV/0!	1	158	1	158	0	#DIV/0!	1	158	0	#DIV/0!	0	#DIV/0!
storage ring	Controls	0	#DIV/0!	0	#DIV/0!	0	#DIV/0!	0	#DIV/0!	0	#DIV/0!	0	#DIV/0!	0	#DIV/0!	0	#DIV/0!
storage ring	Instrumentation	0	#DIV/0!	0	#DIV/0!	0	#DIV/0!	0	#DIV/0!	0	#DIV/0!	0	#DIV/0!	0	#DIV/0!	0	#DIV/0!
storage ring	Other	1	982	0	#DIV/0!	0	#DIV/0!	0	#DIV/0!	1	134	0	#DIV/0!	0	#DIV/0!	0	#DIV/0!
Global	Controls	1	982	1	158	0	#DIV/0!	0	#DIV/0!	0	#DIV/0!	0	#DIV/0!	0	#DIV/0!	0	#DIV/0!
Global	Instrumentation	0	#DIV/0!	0	#DIV/0!	0	#DIV/0!	0	#DIV/0!	0	#DIV/0!	0	#DIV/0!	0	#DIV/0!	0	#DIV/0!
Global	Other	3	327	0	#DIV/0!	1	158	0	#DIV/0!	2	67	0	#DIV/0!	0	#DIV/0!	0	#DIV/0!
	total	374	3	47	3	42	4	43	4	47	3	53	3	89	2	52	3

Figure 1: Number of faults and Mean Time between Failures (MTBF) per week, and for entire commissioning phase I grouped by sub-system

The summary of faults listed below is sorted by quantity of faults per subsystem for the entire commissioning period. In addition to the number of faults recorded, the recorded time associated with the faults is listed. When the time period was recorded any fault that was restored in less than five minutes was assigned a zero time. Future recordings will use 5 minutes as a minimum recorded time if a manual reset or operator intervention is required.

Device faults sorted by # faults per subsystem							
Accelerator Area	subsystem	device	# faults	MTBF (hrs)	% of total faults	# faults with 0 minutes down time	# faults with >5 minutes down time
Storage Ring	Power Supplies	all kickers	130	8	35%	77	53
Booster / BTS	Power Supplies	Injection	67	15	18%	26	41
Booster / BTS	Power Supplies	extraction	38	26	10%	36	2
all	Power Supplies	all power	36	27	10%	0	36
Booster / BTS	RF	Transmitte	35	28	9%	20	15
Linac / LTB	RF	Modulator	28	35	7%	16	12
Linac / LTB	RF	Klystron 2	19	52	5%	17	2
Booster / BTS	Power Supplies	extraction	17	58	5%	12	5
Linac / LTB	RF	Klystron 3	12	82	3%	12	0
Linac / LTB	RF	Modulator	12	82	3%	11	1
Storage Ring	RF	RF	11	89	3%	0	11
Storage Ring	RF	Transmitte	10	98	3%	3	7
Linac / LTB	RF	Modulator	6	164	2%	6	0
Storage Ring	EPS/PPS/Radmon	Pentant 4	6	164	2%	0	6
Storage Ring	Power Supplies	C14-SM1B	6	164	2%	6	0
Booster / BTS	RF	Cavity	5	196	1%	4	1
Storage Ring	RF	Amplifier	5	196	1%	0	5
Linac / LTB	Controls	RF PLC	4	246	1%	0	4
Storage Ring	EPS/PPS/Radmon	MCC E-Stop	3	327	1%	0	3
Storage Ring	Power Supplies	C25 SM1A	3	327	1%	0	3
Booster / BTS	Vacuum	Arc 1 Ion	2	491	1%	1	1
Global	Other	SR:C23-	2	491	1%	2	0
Linac / LTB	RF	Klystron 1	2	491	1%	1	1
Storage Ring	EPS/PPS/Radmon	P5 security	2	491	1%	0	2
Storage Ring	Power Supplies	C16 SL10P4	2	491	1%	1	1
Storage Ring	Power Supplies	Dipole	2	491	1%	0	2
Storage Ring	Power Supplies	Injection	2	491	1%	0	2
Storage Ring	Power Supplies	Main	2	491	1%	0	2

Figure 2: Device faults with 2 or more faults per subsystem sorted by number of faults per subsystem

Faults have been manually recorded by the Machine Operators. Following the identification of a fault the Machine operators input data into a “New Fault Report” through SharePoint at https://ps.bnl.gov/acc/BeamOps/Reports/Lists/Fault%20Reports/NewForm.aspx?Source=https%3A%2F%2Fps%2Ebnl%2Egov%2Facc%2FBeamOps%2FReports%2FLists%2FFault%2520Reports%2FAllItems%2Easpx&RootFolder=

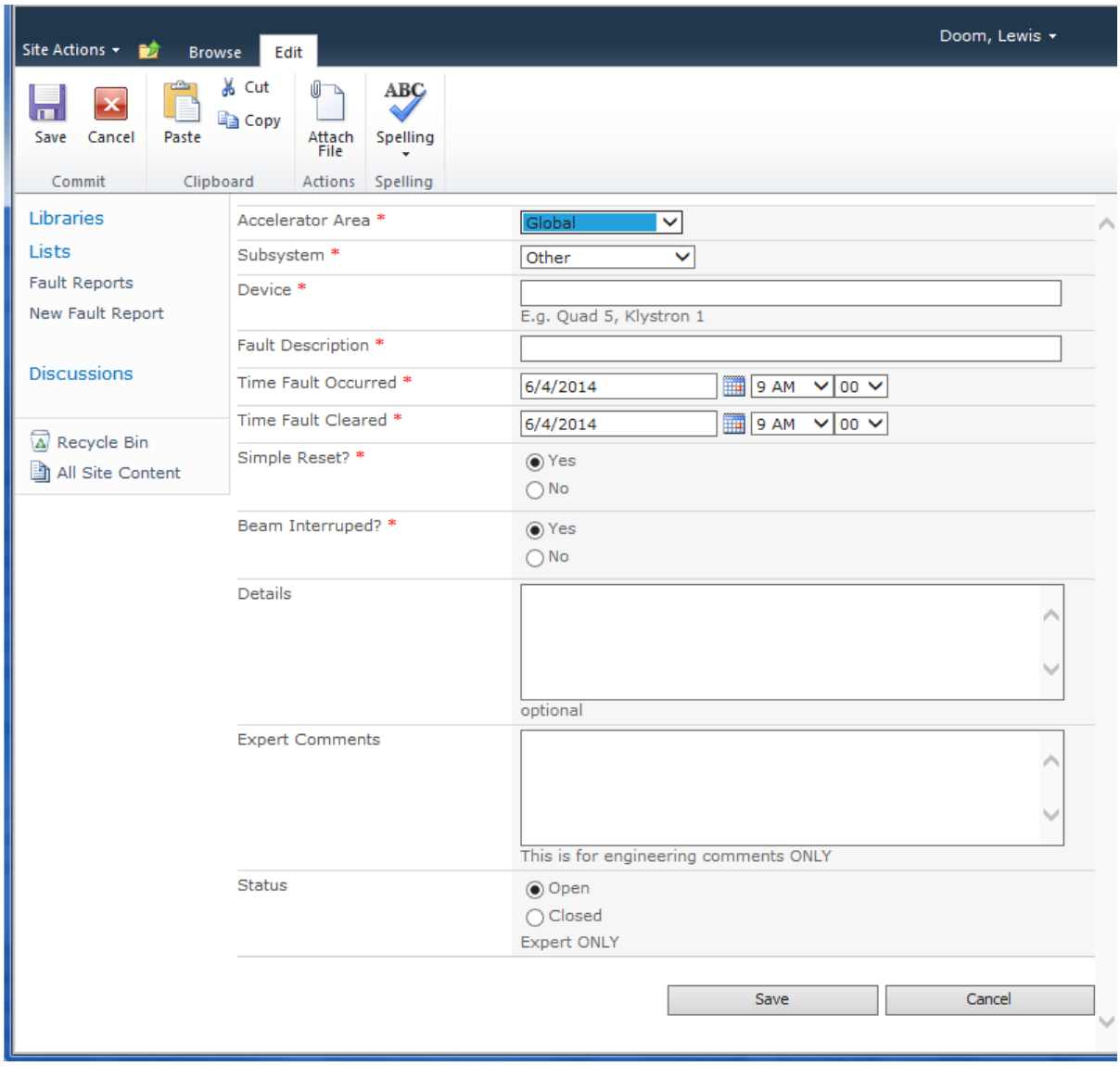

Figure 3: Blank Fault Report

Mean time to repair

Note, Due to the manual nature of the current fault recording system, data regarding the duration of faults should be used for reference only. In many case the fault event was cleared and the system was operable prior to the fault clearing being noted in the Fault Report. Accurate data is not available for mean time to repair.

Automatic Fault Recording

An automatic fault recording system and database is being developed by the controls group and is expected to be operable by 6/26/2014. The automatic fault recording system will be based on the BEAST - Best Ever Alarm System Toolkit storing data in a relational database (RDB). Reference information is available at: http://sourceforge.net/apps/trac/cs-studio/wiki/BEASTManual#a11JMS2RDB sections 11 and 12.

4.17.2 Performance by sub-system

Vacuum System:

The vacuum systems, covering over 1 km of beam channels, have been very reliable and have maintained ultrahigh vacuum throughout the whole commissioning period. There were 19 recordable fault events caused by vacuum systems during beam commissioning, with 13 events interrupted beam operation. Most events were attributed to failure of ion pump controllers, which either interlocked the gate valves or turned off Linac klystron power. A reset of AC power was usually sufficient to restore IPC operation. However, in three occasions, the IPC had to be replaced with spare units, thus causing down time longer than 1 hour. Through improved firmware and replacement of an eProm, these IPC will be upgraded in the coming shutdowns.

Aperture restriction and obstruction in the beam channel were identified at several locations in the storage ring using aperture scans with kickers and correctors. Four cells were subsequently opened for visual inspection, and RF contact springs were found protruding into beam channel at two locations, and were corrected. There are approximately 700 contact springs in storage ring. Among them, ~ 100 are of three-flange combination type, rather difficult to assembly and verify the integrity. In the future, we expect to identify and replace a few more springs with small protrusion into beam channel.

Controls

The overall performance of the control system was on specification and met all requirements during the first storage ring commissioning period. There were a minimal number of failure reports generated for control system components and network response issues. These issues were addressed at the time of failure and resolved by controls group staff. No systemic problems were identified.

The performance of the Network File System service was reported as being “slow”. To address this issue the NFS server will be augmented with two additional high performance servers in order to reduce the load on the single system. This upgrade will occur during the current maintenance period.

Diagnostics:

The overall performance of instrumentation systems was quite well. There were some hardware failure, but most of issues were in establishing the operating parameters of individual instrumentation systems.

RF BPMs – Out of ~200 RF BPMs, there were 4 RF BPM units which were swapped out due to hardware failure – 2 units with bad PLL chips in AFE module; 1 unit with slightly higher noise channel in AFE module; and 1 unit with failed DFE module. One PTC module was also found faulty. The investigation is in progress to perform further analysis to determine the root cause of these failures. There were several other faults where rebooting is required to clear the fault. One fault is when watch dog timer is timed out within RF BPM; and system reboots itself, but fully recovers. The root cause is being looked into.

Following is an example of troubleshooting a bad RF BPM with detailed report - C2BPM6 in this case.

During SR commissioning studies CH-C found to have a low amplitude noise. The source of noise was verified as being internal to the bpm electronics. Removed & replaced with ready spare SN 266.

Before: noisy CH-C, almost 200 counts pk-pk with no drive (definitely a subtle bit of noise, but still definitely a spurious waveform present with deterministic nature).

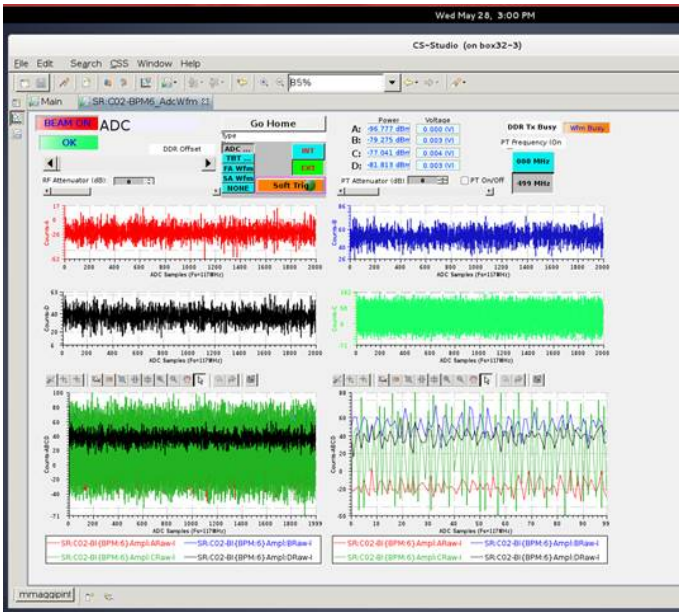

After (post replacement): nominal performance with no drive. Much nicer, all Gaussian-Brownian noise type stuff… no deterministic coupling.

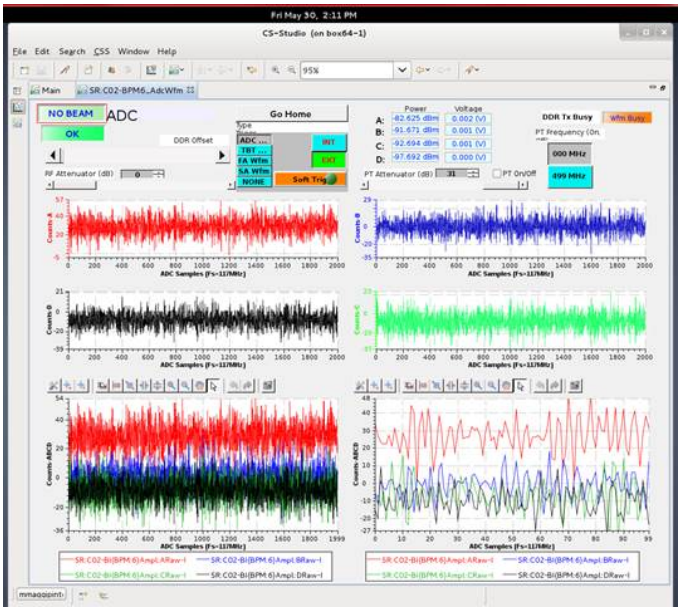

The removed unit (SN 123) will be brought back to the lab for troubleshooting.

Update: Troubleshooting complete.

BPM 6 from C2 (SN 123) with ready-spare SN 266 due to the low level noise present on CHC; troubleshot to find that 82nH inductor ref des L20, on the +5VDC bias for 1st stage receiver amplifier U39, was causing this problem.

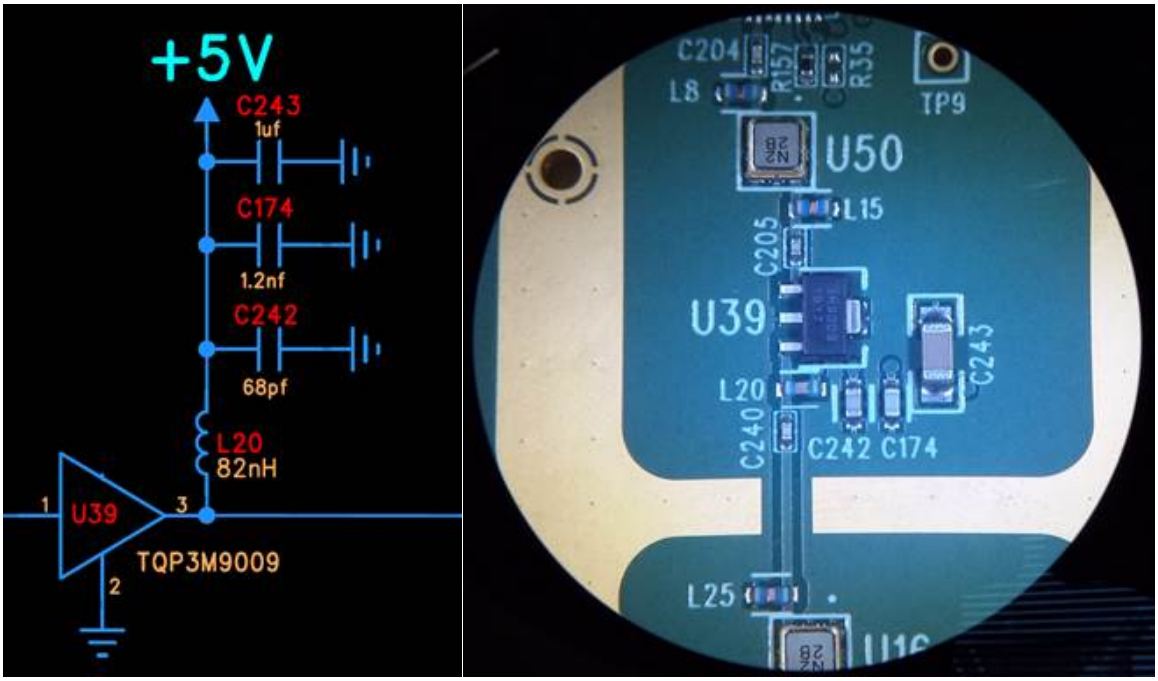

Before (low amplitude noise evident on CHC), counts/samples data per channel taken with no drive signal & each receiver terminated at SMA input to 50Ω:

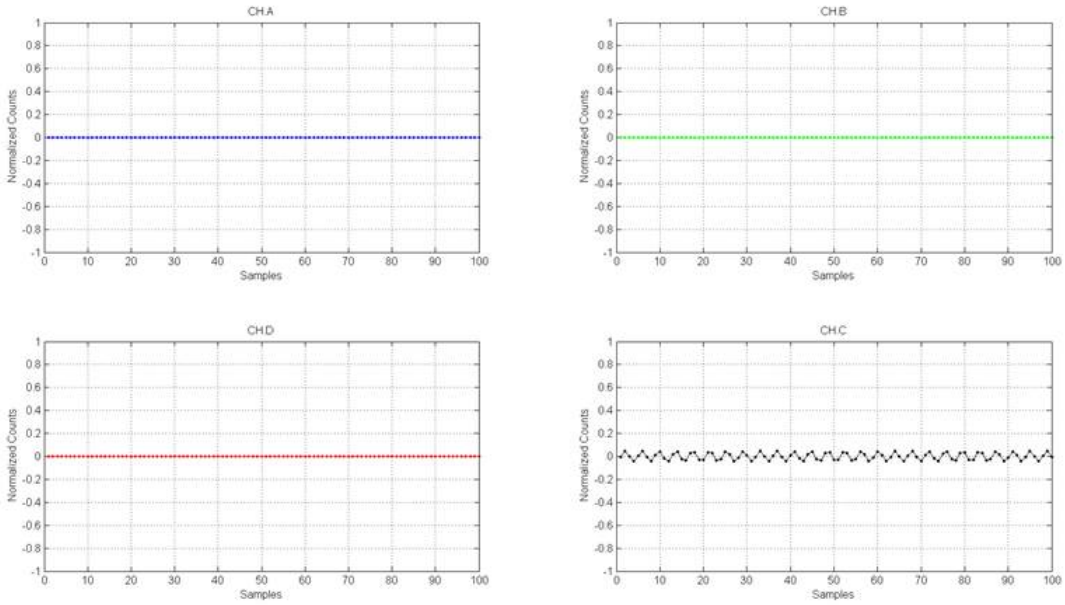

After rework:

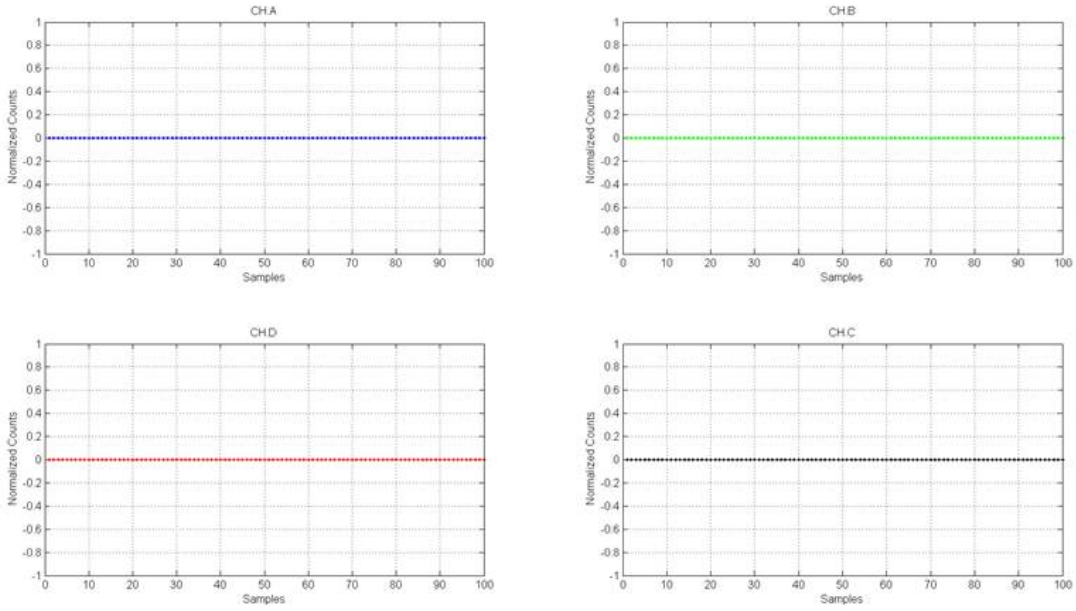

SR DCCT system – The overall system performed well, however, it was observed that measurement system had ~40 µamp noise level, which makes it difficult to calculate beam lifetime at low current. During shutdown, a low pass analog filter at 50Hz was installed, lowering the noise level to 3 µamp level. The remote AC power control was also added to individual DCCT system so that a remote AC power recycled could be performed to recover the system in case system hangs. This situation occurred 2 times during commissioning when operator had to walk to the mezzanine floor to restart.

Loss Control Monitor – This system consists of 3 horizontal and 3 vertical scrapers; and 7 loss monitors. The loss monitor electronics performed well and data was captured successfully. The high level programs are being worked on to perform full analysis on loss monitor signals. The scraper motor controls worked as expected, but the read back system for few scraper units has interference with magnetic coupling into the LVDT type read back systems. The recommendations are to replace the read back system to a system which has no coupling to the magnetic field. Also, vertical scrapers travel is restricted to 11.5 mm where a travel of more than 12.5 mm is required. It is recommended that vertical scrapers be replaced with a new design.

Other systems, SLM, BbB, TM and FPM monitor, are highly specialized systems. After initial tuning, all system performed as expected.

Mechanical:

The alignment tolerance is ±30 micron for multipole magnets on a common girder. Vibrating wire technique was used to align multipole magnets on each girder with an accuracy of better than ±10 micron. After fine adjustment, the RMS residuals was 6 micron in both X and Y direction. In order to reduce the impact of girder deformation due to transportation and supporting change, girder profile was established right after the vibrating wire alignment and was reproduced in tunnel by following dedicated procedures. The RMS residuals of girder profile reproduction was below 7 micron in both X and Y direction. With all the alignment error sources combined, the magnet alignment goal was well achieved.

The alignment tolerance is ±0.1 mm for adjacent girders and ±3 mm globally. The girder alignment depends on survey control network greatly. Survey control network has a global accuracy of ±0.6 mm and ±0.05 mm locally. The girder alignment is relative to adjacent monuments and the RMS residuals is below 0.05 mm in both X and Y direction. Although it took almost one year to accomplish girder alignment in tunnel with certain variations such as tunnel settlement, control network establishment, the global and local girder alignment goals were both well achieved.

The current survey technique is designed to monitor the girder location changes periodically and it allows touching up any outliers if necessary to maintain an optimal alignment status of the machine.

Magnets and Girders

Water leaks in magnets:

Water leaks from the storage ring magnets have been a continuing problem. The majority of leaks have been associated with the magnets from Buckley Systems and Tesla. Three types of leaks have been identified. The most common is leakage coming from the joint between the water manifold and one or more of the conductor fittings. Other leaks have been found at the swaged portion of the conductor fitting and along the conductor itself. Leaks along the conductor have been rare but required silver soldering to make the repair. Conductor leaks have been caused by machining errors during manufacture of the magnets. Leaks at the swaged portion of the conductor fitting typically require only tightening after appropriate access is

obtained. After review of the sealants used on the various NSLS-II magnets and that used at both APS and NSLS it was determined to repair any leaking magnets with the same procedure used at NSLS. This approach has historically proven to be very effective at NSLS. A new procedure was written and has been incorporated. During the extended maintenance period from 5/16/2014 through 6/26/2014 a total of 20 are being repaired. 14 dipoles and 6 quadrupoles. In addition to the repairs noted above, one Quadrupole manifold is being replaced with one made from PEEK.

Current leakage in dipoles:

The Power Supply Group identified excessive ground current losses on the dipole circuit. Testing was performed on each dipole to determine where the losses were coming from. It was found that there was a partial ground across the water manifold. The stainless steel braided hoses that attach each supply and return water line to the isolation manifold of all dipoles were replaced with radiation resistant rubber hose assemblies. Replacing the hose assemblies reduced the ground current to nearly zero. Monitoring will continue to identify if the ground current starts to rise.

Dipole magnet with stainless steel braided hose connection(left) and radiation resistant rubber hose connection (right)

One Water manifold was removed and cut in half after the hoses were installed. Analysis was done on the build up that was evident on the interior of the manifold. Below are photographs of the manifold interior and an X-ray spectra from a Scanning Electron Microscope W/ EDAX. The deposited material has a high concentration of Copper and Nickel.

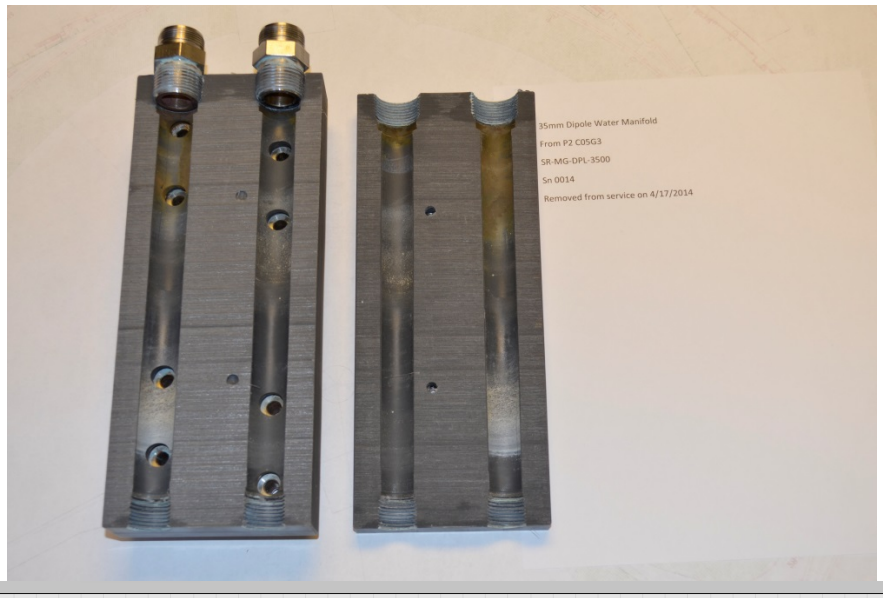

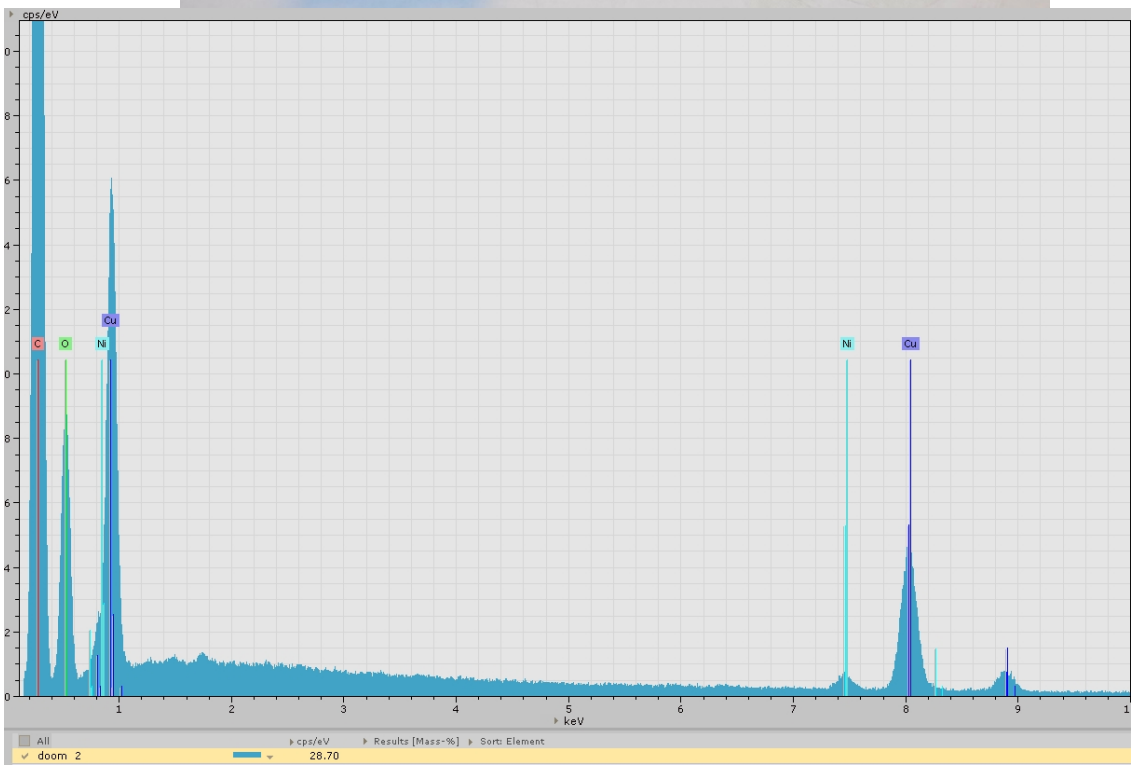

X-ray spectra from Scanning Electron Microscope W/ EDAX. Provided by John Warren.

The Utilities Group has been notified of these tests and is investigating possible causes and corrective action(s). Water Chemistry including % oxygen is one consideration of root cause.

4.18 SR fault studies summary

4.18.1 Shielding requirements and FLUKA simulations

It is required by the NSLS-II shielding policy [1] that the radiation dose rate in the continuously occupied areas should be less than 0.5mrem/hour for uncontrolled areas the integrated dose should not be greater than 20mrem during a fault.

The integrated dose should be kept within 100mrem for the controlled areas in an unplanned abnormal condition.

Radiation doses less than 100mrem/hour can be mitigated via administrative controls only when the use of area radiation monitors (ARM) is not practical. A secondary independent system is required if the does rate could be greater than 2000mem/hour.

Area radiation monitors are placed at the sensitive locations in the control areas. The ARMs are interlocked with the radiation sources and will shut down the operation of the accelerators in a few seconds following the exceeding of the radiation dose limits. The storage ring bulk shielding and the supplemental shielding are designed to reduce radiation levels to <0.5mrem/hour during normal operation and to meet the above criterion during incidental losses.

Various calculations have been performed to estimate the dose rates for the design shielding- configuration. The calculations are based on the loss rate of 15nC/s at 3 GeV, which is the maximum possible charge that the Booster could deliver at 1Hz repetition rate, and is also about 1% of the total charge when the storage ring operates at the full current of 500mA. The FLUKA calculations are listed in Table 1[2]. All the dose values are scaled to 15nC/s in this note.

Table 1 Summary Results of MCI Calculations for the Storage Ring (15 nC/s Loss at 3.0 GeV on a Thick Target (10 X_0 of Cu)

Area	Shielding (light concrete) (cm)	Distance (cm)	Analytical Total Dose Rate (mrem/hr)	FLUKA Total Dose Rate (mrem/hr)	FLUKA Neutron Dose Rate (mrem/hr)
Experimental Floor (InjectionLoses)	100	200		<40	
ISA	80	280		<40	
Road tunnel - pavement	71	688	189	60	17
Road tunnel – 3 m above pavement	71	388	596	200	50

Utility tunnel - floor	66	597	319	110	25
Utility tunnel – 2m above floor	66	397	720	230	60
Storage Ring Mezzanine	80	280	626*	200*	75*
Storage Ring Inboard	80	280	626*	200*	75*
Storage Ring Experimental Floor side	100	200	481*	150*	80*
ISA Labyrinth Entrance	80	240	60		40
Storage Ring RF Penetration	80	215		50	32

**Dose Rates are contact dose rates calculated on the shield surface*

4.18.2 Typical Loss Pattern

The fault studies were designed to verify the shielding effectiveness in areas such as labyrinths, shield doors, tunnel penetrations, and in general to prove that radiation doses on the experimental floor and work areas on the inside of the storage ring are within shielding limits. In order to simulate incidental losses, the beam was intentionally steered to a loss location, or intercepted by gate valves. Dose rates are then measured outside the downstream tunnel wall, at an interval of 3 feet. The measurement spots along the ratchet wall and the mezzanine are shown in Figure 1.

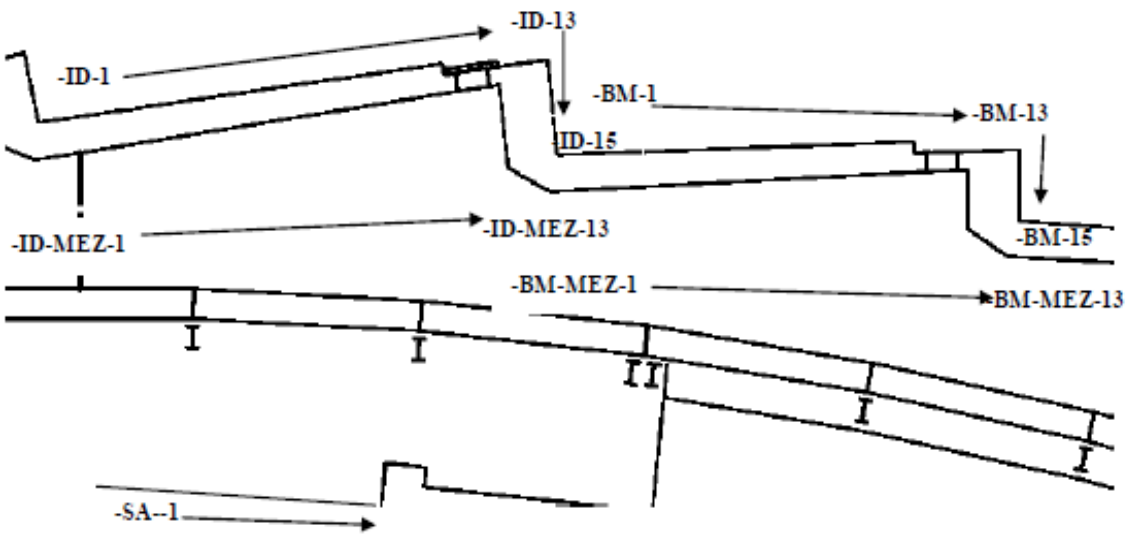

Fig. 1 The fault survey locations and names. As shown in the diagram the side wall is divided into sections and tagged as ID or BM according to the X-ray beam ports. The roof or the mezzanine was segmented as ID-MEZ and BM-MEZ, respectively. The measurement points are named as, for example, ID-1, ID-2, …, ID-15.

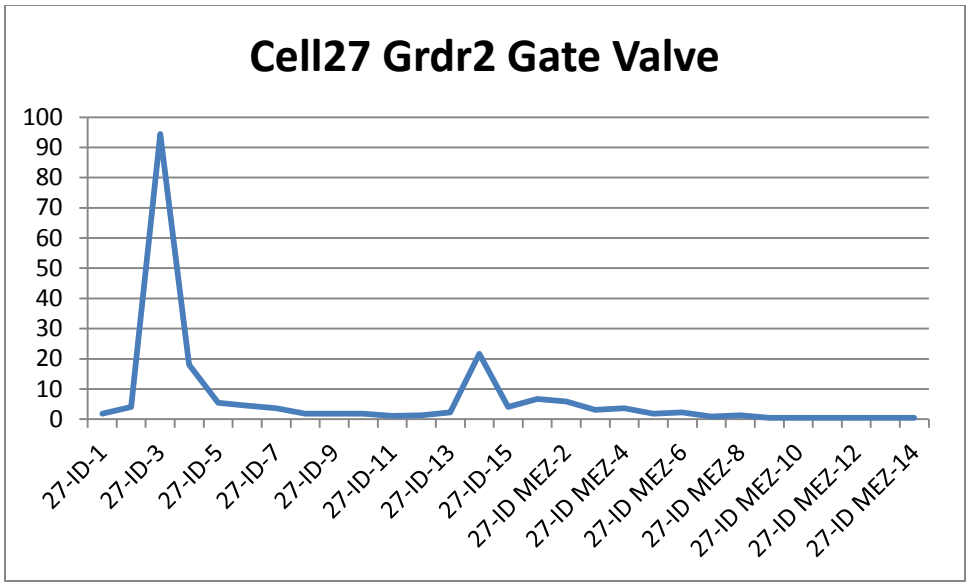

Fig. 2 Measured dose (scaled) when the gate valve at Cell27 Girder 2 was closed.

A typical loss pattern is shown in Figure 2[3]. The peak dose around 27-ID-4 is due to the scattering on the shadow shield downstream to the dipole B in Cell 27; and the second peak at 27-ID-14 on the front ratchet wall is due to the transmitted particles. In the following sections

the maximum doses are summarized for each case and compared with FLUKA estimation listed in Table 1.

4.18.3 Fault studies and maximum doses

Phase I Fault Studies [4]

Machine setup	Maximum dose (scaled) and location	FLUKA calculation
power B3 at 360A, or +44mr	**54**mrem/hour, ISA	<40mrem/hour
power B4 at 360A, or +33mr	18mrem/hour, ISA	<40mrem/hour
Close BS-SL1 slit	18mrem/hour, ISA	<40mrem/hour
BS-SP3 to 450A	6mrem/hour, ISA	<40mrem/hour
SR-IS-SP1 to 1000V	6mrem/hour, ISA	<40mrem/hour

Conclusions of Phase I fault study [4]:

With one exception, the dose rates measured during the phase I fault studies were less than the FLUKA estimated doses. The situation where the measured dose was in access of the FLUKA calculated dose occurred because the non-overlapped crack was not modeled by FLUKA.

Phase II Fault Studies [3]

Machine set-up	Maximum dose (scaled) and location	FLUKA calculation
SR-IS-VF1 interception	12mrem/hour, 29-BM-MEZ	<200mrem/hour
Scraper c30 v/h s1 interception	background, ISA	<40mrem/hour
Scraper c30 v/h s1 interception	2.25mrem/hour, ISA parking	<40mrem/hour
Scraper c30 v/h s1 interception	16mrem/hour, 30-ID-Mez	<200mrem/hour
Scraper C01 V s2 interception	11.3mrem/hour, SA2	<40mrem/hour
Scraper C01 V s2 interception	21.6mrem/hour, 1-ID MEZ	<200mrem/hour
Scraper C01 V s2 interception	20.7mrem/hour, 2-ID MEZ	<200mrem/hour
C02 Girder 4 steer inboard	**180**mrem/hour, 2-ID	<150mrem/hour
C02 Girder 4 steer inboard	20.7mrem/hour, 2-BM-MEZ	<200mrem/hour
C02 Girder 4 steer inboard	20.7mrem/hour, 1-ID-MEZ	<200mrem/hour
C02 Girder 6 steer	140mrem/hour, 3-ID	<150mrem/hour
C02 Girder 6 steer	20mrem/hour, 3-ID-MEZ	<200mrem/hour

C03 Girder 6 steer	18mrem/hour, 3-BM	<150mrem/hour
C03 Girder 6 steer	4mrem/hour, 3-BM-MEZ	<200mrem/hour
C03 Girder 6 steer	5.4mrem/hour, steam-tunnel	<110mrem/hour
C03 Girder 6 steer	17.1mrem/hour, 4-ID	<150mrem/hour
C03 Girder 6 steer	20mrem/hour, 4-ID-MEZ	<200mrem/hour
C17 Girder 2 Gate valve interception	3.15mrem/hour, Rd underpass	<60mrem/hour

C17 Girder 2 Gate valve interception	15.3mrem/hour, 16-BM	<150mrem/hour
C17 Girder 2 Gate valve interception	**160**mrem/hour, 17-ID	<150mrem/hour
C17 Girder 2 Gate valve interception	9mrem/hour, 17-ID-MEZ	<200mrem/hour
C19 Girder 6 steer	**64**mrem/hour, SA-5	<40mrem/hour
C19 Girder 6 steer	**225**mrem/hour, 19-ID	<150mrem/hour
C19 Girder 6 steer	21.2mrem/hour, 19-ID-MEZ	<200mrem/hour
C19 Girder 6 steer	1.35mrem/hour, 19-BM-MEZ	<200mrem/hour
C21 Girder 6 steer outboard	**270**mrem/hour, 20-ID	<150mrem/hour
C21 Girder 6 steer outboard	2.25mrem/hour, 20-ID-MEZ	<200mrem/hour
C21 Girder 6 steer outboard	17.1mrem/hour, 20-BM-MEZ	<200mrem/hour
C27 Girder 2 gate valve	94.5mrem/hour, 27-ID	<150mrem/hour
C27 Girder 2 gate valve	6.75mrem/hour, 27-ID-MEZ	<200mrem/hour
C27 Girder 2 gate valve	21.6mrem/hour, 26-BM	<150mrem/hour
C27 Girder 2 gate valve	18mrem/hour, 26-BM-MEZ	<200mrem/hour
C22 Girder 6 steer	Background, RF bldg. 1	<200mrem/hour
C22 Girder 6 steer	Background, RF bldg. 2	<200mrem/hour
C22 Girder 6 steer	10 mrem/hour, 22-BM	<150mrem/hour

C22 Girder 6 steer	2.25mrem/hour, 22-BM-MEZ	<200mrem/hour
C22 Girder 6 steer	**248** mrem/hour, 22-ID	<150mrem/hour
C22 Girder 6 steer	52mrem/hour, 22-ID-MEZ	<200mrem/hour
C24 Girder 6 steer	24mrem/hour, RF bldg. 1	<200mrem/hour
C24 Girder 6 steer	10mrem/hour, 24-BM	<150mrem/hour
C24 Girder 6 steer	Background, 24-BM-MEZ	<200mrem/hour
C24 Girder 6 steer	**317**mrem/hour, 24-ID	<150mrem/hour
C24 Girder 6 steer	20.3mrem/hour, 24-ID-MEZ	<200mrem/hour

4.18.4 Conclusions of the fault studies

1) The measured doses on the side walls, mezzanine, and the service buildings are all less than 100mrem/hour, except for that at the crack of the ratchet doors, of which the does could be several hundreds of mrem/hour.
2) Another measured value that is higher than expectation is at service building 5 when the beam was mis-steered to Girder 6 of Cell 19. The dose rate was 64mrem/hour, compared to the calculated value of 40mrem/hour.
3) FLUKA calculation predicted higher dose rates than the measurements in most cases. The exceptional cases are due to the incomplete modeling.
4) All doses rates are less than 2000mrem/hour therefore a second detecting system is not necessary.

Reference

[1] R. Lee, Photon Sciences Shielding Policy, PS-C-ASD-POL-005
[2]S. Walker, Fault study plan for the NSLS-II storage ring, PS-C-ASD-PLN-007, page 4.
[3] Survey data from R.Merkek, L. Summers, S. Townsend, F. Flanigan, S. Buckallew, and reviewd by F. Zafonte.
[4] S. Walker, Storage ring phase I fault study analysis

5. SR Phase II commissioning

The SR phase II commissioning goal was to achieve 25 mA with SRF cavity, which was installed after Phase I commissioning. The whole commissioning lasted half a month (June 27 to July 13). During the period, we conditioned SRF system, accumulated 50 mA beam, tested vertical pinger system and calibrated loss control monitor. The results are in the following section.

Prior to the tunnel installation, the SRF cavity was conditioned and tested in the block house and reached 1.4 MV voltage. The cavity tunnel conditioning took less than one week (June, 27-July 2) and reached 1.2 MV with 70 kW forward power, which was enough for 50 mA beam accumulation.

The machine showed stable and reliable operation after one and a half month shutdown. By reloading the saved MASAR file, it took a couple of hours to circulate the beam in SR for 300 turns (without RF on) by minor tuning injection element. On July 2nd, it took another couple of hours to accumulated beam up to 25 mA with SRF on. The beam property, such as tune, beta beat was comparable as before. On July 11th, we got the approval to store beam up to 50 mA. The result is shown in Figure 1. It was also very smooth process, except a few spot in front end showed a few degree temperature raise. The injection was paused every 5 mA for radiation survey and vacuum pressure. In between, the fast orbit feedback system was tested and will need more beam study after beam back.

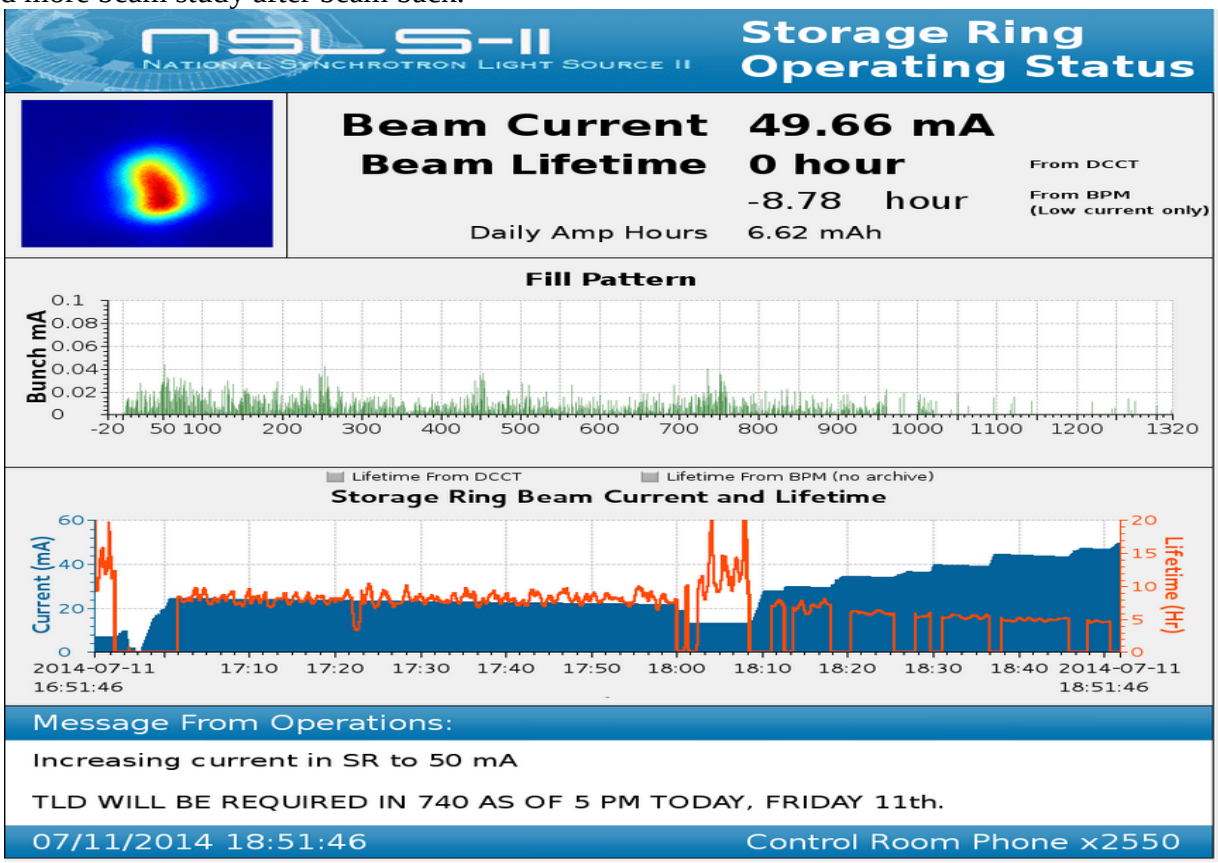

Figure 1: beam accumulation up to 50 mA

5.1 500 MHz Upstream Superconducting Cavity Commissioning

The NSLS-II storage ring RF system was designed to be equipped with up to four CESR-B type 500 MHz niobium superconducting cavities. The first one has been installed and commissioned with beam at the upstream location of Cell 24 RF straight.

Prior to tunnel installation, cryogenic and RF tests had been performed in the blockhouse to ensure the cavity can provide enough energy gain for electron beam current of 25 mA for commissioning, and up to ~300 mA for early operation depending upon the total energy loss per turn at that time. After the blockhouse test, the cavity was installed in the storage ring tunnel, where it was then cooled down, conditioned, and finally commissioned with up to 50 mA of beam current.

The NSLS-II LHe cryogenic plant was used to maintain the cavity temperature at 4.5K. The blockhouse is interfaced with the cryogenic manifold box via a vacuum jacketed line, while in the tunnel the cryomodule is fed by a valvebox which is supplied by the same manifold box. The helium gas is recovered by the close-loop LHe system, and the nitrogen gas is vented outside of the RF building through a vent line.

This report contains three parts: 5.1.1 describes cryogenic and RF tests in the blockhouse, while 5.1.2 describes cavity commissioning in the tunnel. Within 5.1.1 and 5.1.2 the cryogenic operation is introduced first then the RF test is described. 5.1.3 describes further studies proposed for the next operation period.

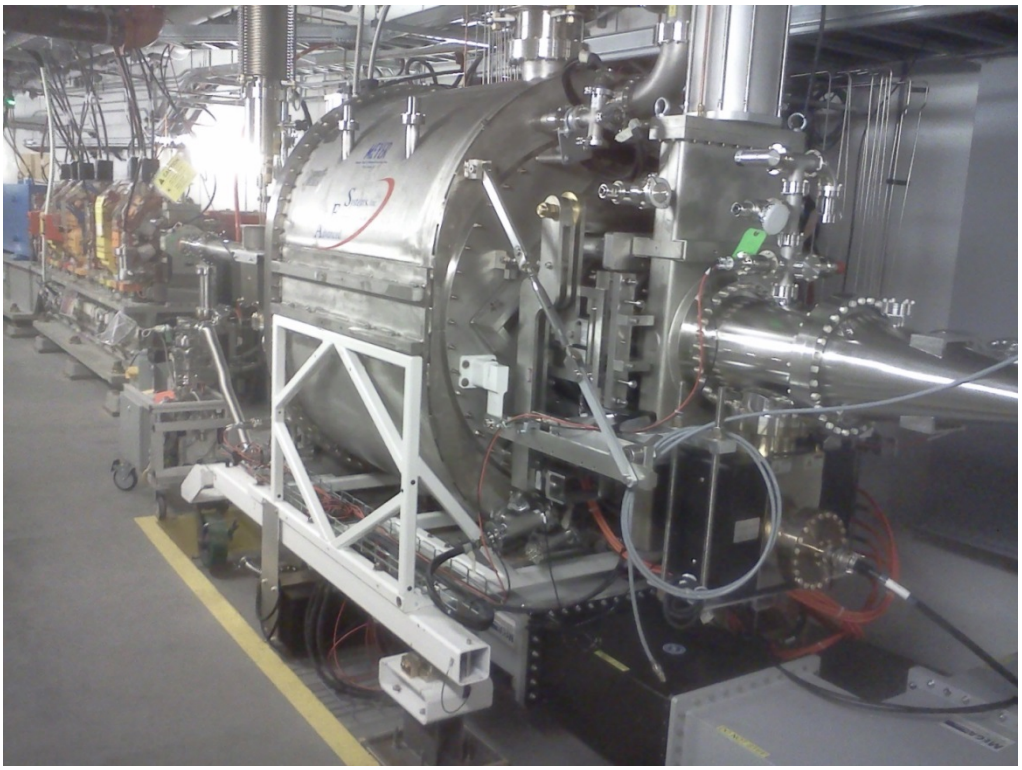

5.1.1 Blockhouse Test

Limited by less than 5 work days for tuner function verification, RF tests and high power conditioning (May 21st afternoon through 28th 5AM excluding Sunday and Memorial Day), the key RF parameters obtained during the blockhouse test are listed in Table 1. Section 1.1 will describe the blockhouse cavity cryogenic operation, while Section 1.2 will focus on the RF tests.

F0, resonant frequency with tuning range	499.68MHz ± 30kHz
Vc, cavity field conditioned up to	1.4 MV
Qext, external Q of the waveguide input port	79000
Q0, cavity Q conditioned up to	3.5e+8
R/Q according to design	44.5 Ohms

Table 1. Key RF parameters of the upstream cavity. These were limited by the time allocated for conditioning. See Section 1.2 for details.

Cavity cryogenic operation for the blockhouse test

LN2 cooldown and LN2 flow PID parameters

The graph in Fig. 1 shows the time-temperature response during the cool-down of the LN2 radiation shield of the SRF cavity. The blue curve corresponds to the temperature sensor on the bottom of the radiation shield and the green curve corresponds to the transition temperature on the wave-guide between the 77 K boundary and 300 K (insulated vacuum-jacket boundary).

To avoid thermal stresses caused by rapid cool-down, the norm is to restrict the cool-down rate to less than 30 K/hr for the LN2 shield and also the SRF cavity.

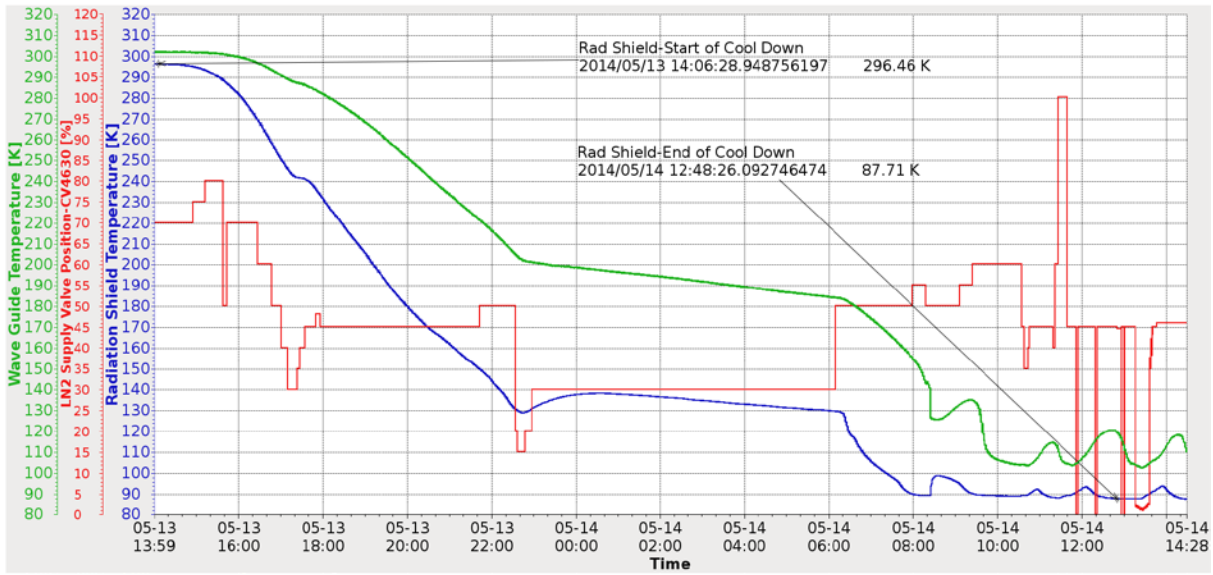

Figure 1. Cool-down of the Cavity LN2 Radiation Shield

For the manual cool-down of the LN2 shield, the optimum setting for the LN2 supply valve is between 45-50 %. For over-night operation (from 23:00 to 6:00), the LN2 supply was reduced to 30% which resulted in a slow cool-down rate of 2 K/hr. Hence for this first cool-down it took 18 hrs to cool-down the LN2 shield and to a reach the steady state temperature of 87 K.

Conclusion: For future operations, it is recommended to leave the LN2 supply valve in the auto PID LN2 Flow mode (LP3) with the "Max. Valve Opening" set to 45%. The other PID parameters for the auto PID LN2 flow controller is shown in Fig. 2 and summarized in Table 2.

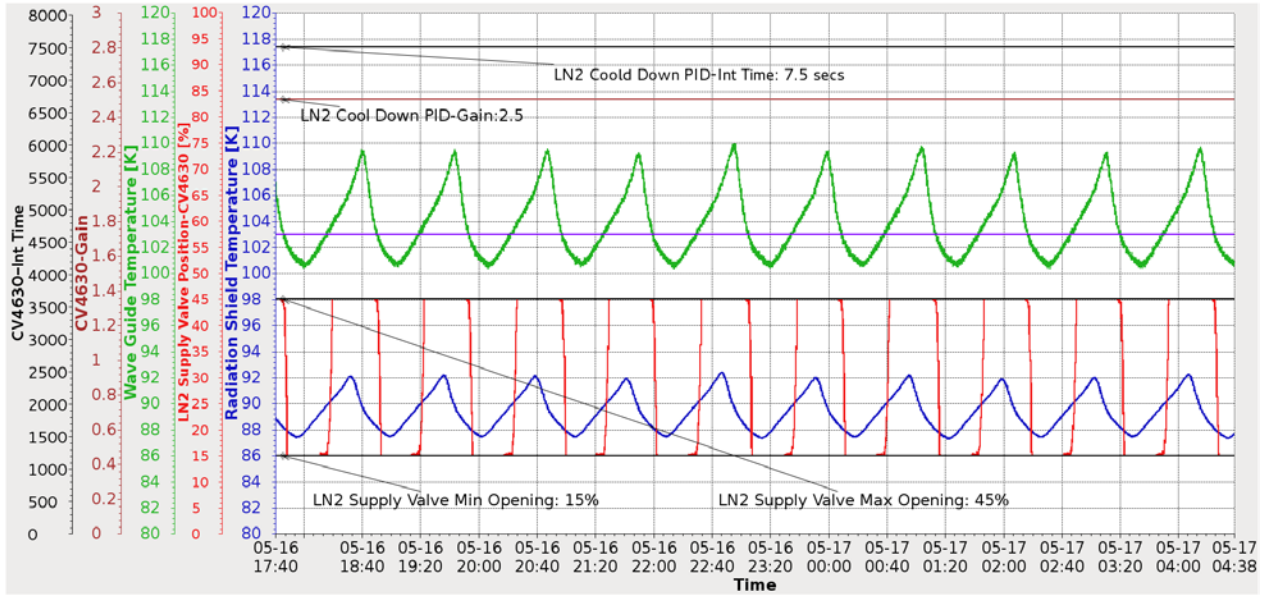

Figure 2. PID LN2 Flow Controller (LP3) Parameters for CV 4630

Table 2. PID LN2 Flow Controller (LP3) Parameters for CV 4630	
Temperature set point- T6600	103 K
Gain	2.5
Int Time	5000
Maximum Valve Opening	45 %
Minimum Valve Opening	15

Cool-down of SRF cavity with LHe and PID parameters for level and pressure control

The graph in Fig. 3 shows the time-temperature response during the cool-down of the SRF cavity with LHe. The cool-down of the SRF cavity with LHe was started five days after the cool-down of the LN2 shield. During this time the cavity temperature had gradually reduced due to conduction and radiation from the outer LN2 thermal shield and hence we see a starting temperature of 180 K for the temperature sensors mounted on the bottom (green curve) and the top (red curve) of the SRF cavity. The cool-down of the SRF cavity is dictated by the following two conditions:

a. The cool-down rate must be lower than 30 k/hr
b. The temperature gradient between the top and the bottom must be less than 70 K

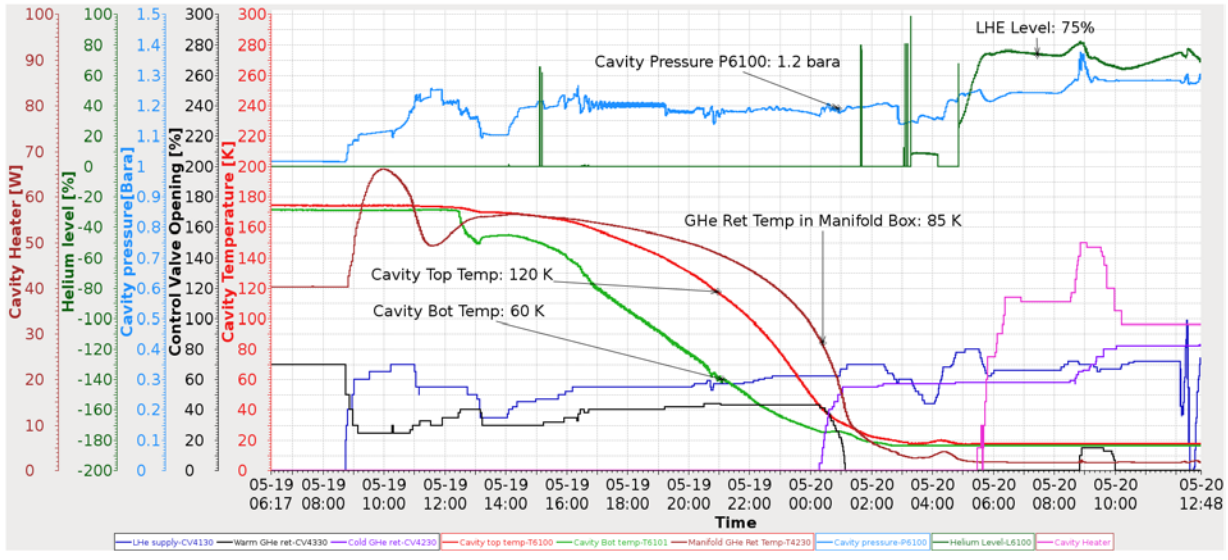

Figure 3: Cool Down of Cavity with LHe

For optimum cool-down of the SRF cavity the following initial valve settings are recommended:

1. Set the Warm Ghe supply valve-CV4330 to 45%
2. Set the LHe supply valve-CV4130 to 60% (gradually)
3. During the cool down of the cavity, adjust the warm gas return valve to maintain the cavity pressure in the range of 1.18-1.2 bara (cyan/light blue color).

During the cool-down the Ghe return temperature-T4230 in the Manifold box (shown by the reddish brown curve) was monitored. When the temperature reached 85 K (Time-00:10), we slowly opened the cold Ghe return valve-CV4230 (increments of 5%) while closing the warm Ghe return valve-CV4330. During the process, the cavity pressure P6100 was maintained at 1.2 bara. The cavity cool-down time is summarized below in Table 3.

Table 3. SRF cavity cool-down time summary	
Time between start of cool down and start of liquid level in the SRF cavity	18 hrs
Time to build 75% LHe level in the SRF cavity	3 hrs

Conclusion: For cool-down of the SRF cavity in future it is recommended to activate the cavity PID Ghe pressure controller-LP2 after the completion of the SRF cavity cool-down and before filling of the cavity with LHe. The LHe level PID controller-LP1 should be activated once the cavity is filled up to 70 %. The level set point for the LHe level PID controller-LP1 can then be ramped up to the desired set point of 82% which will ensure that the cavity is completely immersed in the liquid helium volume.

The PID parameters for the Ghe pressure (LP2) and LHe level (LP1) are shown in Fig. 4 and Fig. 5 respectively. These parameters are also summarized in Table 4 and Table 5.

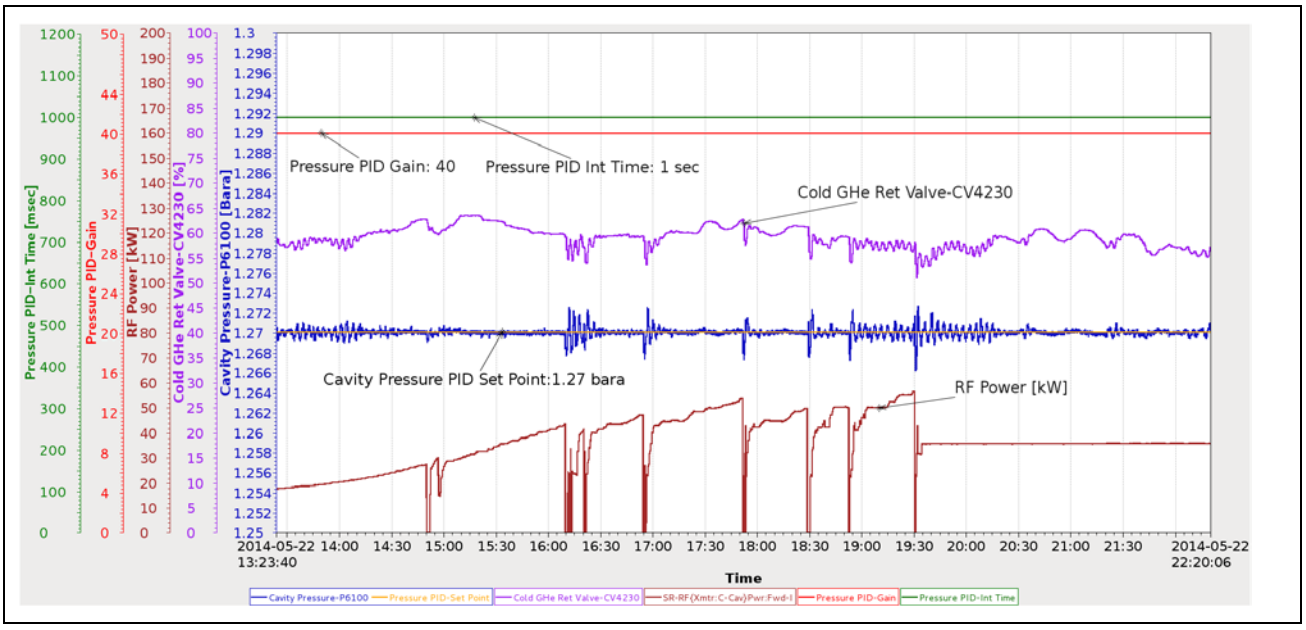

Figure 4. PID Ghe Pressure Controller (LP2) Parameters for CV 4230

Table 4. PID Ghe Pressure Controller (LP2) Parameters for CV 4230	
Pressure set point- P6100	1.27 bara
Gain	40
Int Time	1000 msec
Maximum Valve Opening	100 %
Minimum Valve Opening	0 %

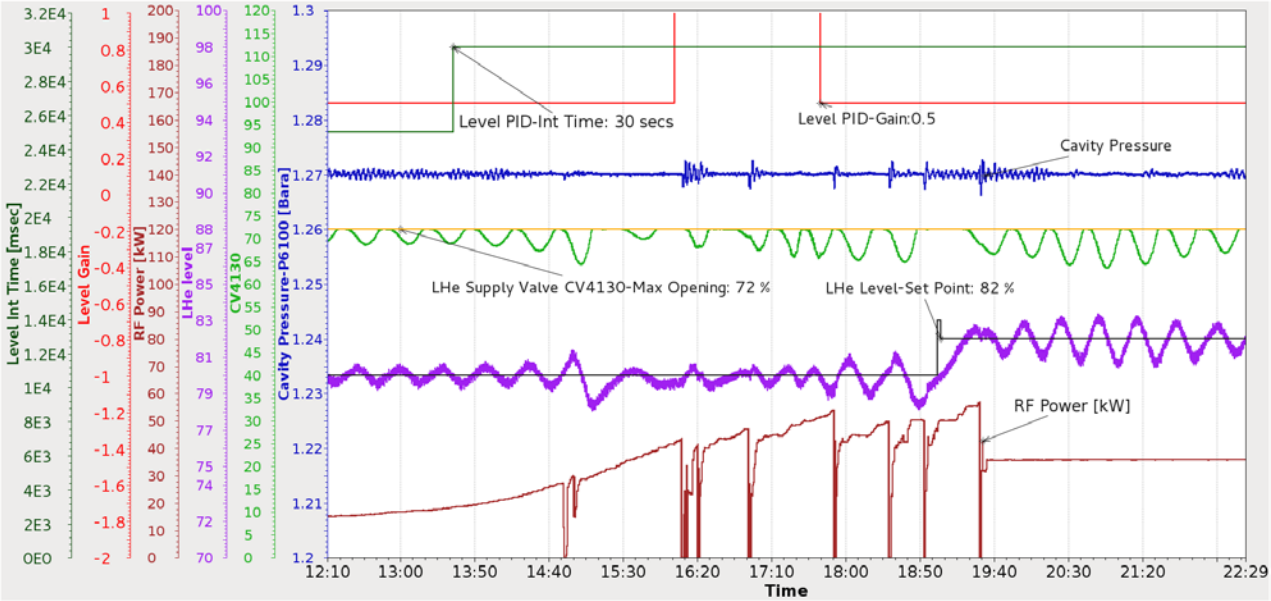

Figure 5. PID LHe Level Controller (LP1) Parameters for CV 4130

Table 5. PID LHe Level Controller (LP1) Parameters for CV 4130	
Level set point- L6100	82 bara

Gain	0.5
Int Time	30000 msec
Maximum Valve Opening	72
Minimum Valve Opening	0 %
	1

Cavity Heater Test

Calculation of Static Heat Load on the SRF Cavity

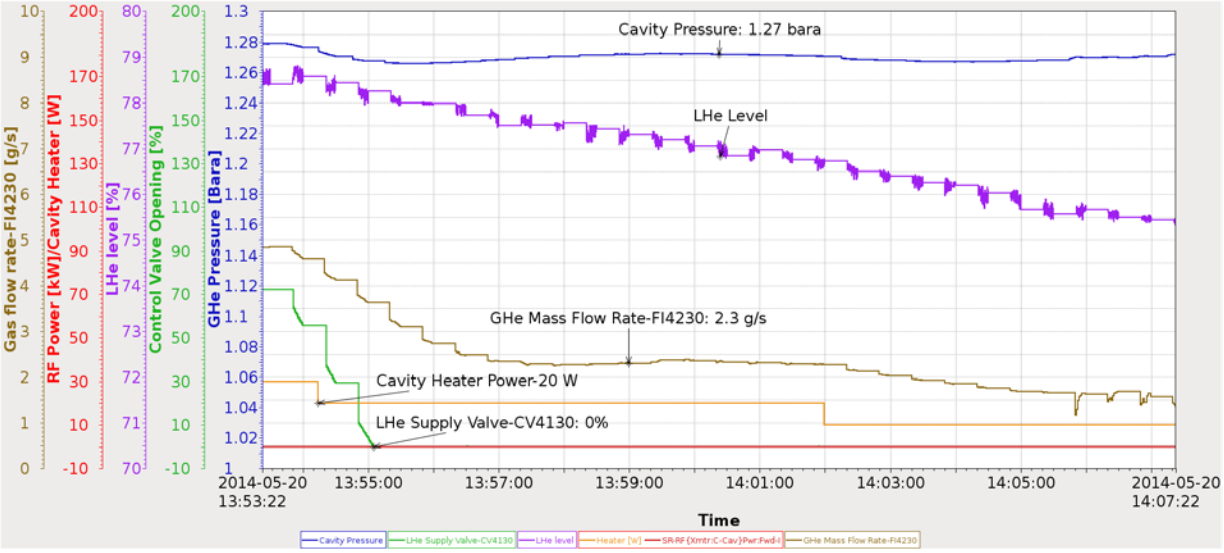

Figure 6. LHe Boil-off due to cavity heat load

The graph in Fig.6 corresponds to the following test conditions

Table 6. Test parameters			
CV4130	LHe supply valve open position (green curve)	0	%

P	Cavity Operating Pressure (blue curve)	1.27	bara
$\dot{m}_v$	Ghe mass flow rate measured by the venturimeter FI-4230 in the manifold box (brown curve)	2.3	g/s
Q_{HTR}	Cavity heater load (orange curve)	20	W

The boil off test was done with the fill valve closed. Therefore the flow-rate measured is what is boiled off in the cryostat.

The mass flow rate, $\dot{m}_v$ measured at the 199enture-meter is lower than the boil-off mass flow rate in the cryostat, due to the fact that a portion of the boil-off gas, $\dot{m}_{vl}$ will fill up the extra volume created by drop in liquid level due to the boil-off rate of LHe, $\dot{m}_l$, in the cryostat.

The boil-off mass flow rate in the cryostat can be calculated from the following equation

$$\dot{m}_l = \frac{\dot{m}_v}{\left(1 - \frac{\rho_v}{\rho_l}\right)} \tag{1}$$

Since,

$$\dot{m}_v = \dot{m}_l - \dot{m}_{vl} \tag{2}$$

and,

$$\dot{m}_{vl} = \frac{\rho_v}{\rho_l}\,(\dot{m}_l) \tag{3}$$

where,

ρ_v	Density of saturated vapor at 1.27 bara	21.5 kg/m^3
ρ_l	Density of saturated liquid at 1.27 bara	119.62 kg/m^3

The resulting boil-off rate in the superconducting cavity cryostat, $\dot{m}_l$ is 2.8 g/s.

The total heat load input to the SRF cavity can then be calculated from the boil-off mass flow rate, $\dot{m}_l$ by the following relationship:

$$Q_{cav} = \dot{m}_l \times L \tag{4}$$

where,

Qcav Total cavity heat load

L	Latent heat of vaporization at 1.27 bara	18.99 kJ/kg

The resulting total cavity heat load, Q_{cav} from Eq.4 is 53.25 W.

Conclusion: Since during this test the cavity heater was set to a constant value of 20 W, the static heat load, Q_s on the SRF cavity is calculated to be 33 W.

Calculation of static heat load on the transfer lines connecting the 3500 liters helium dewar and the SRF cavity in the block house via the manifold box.

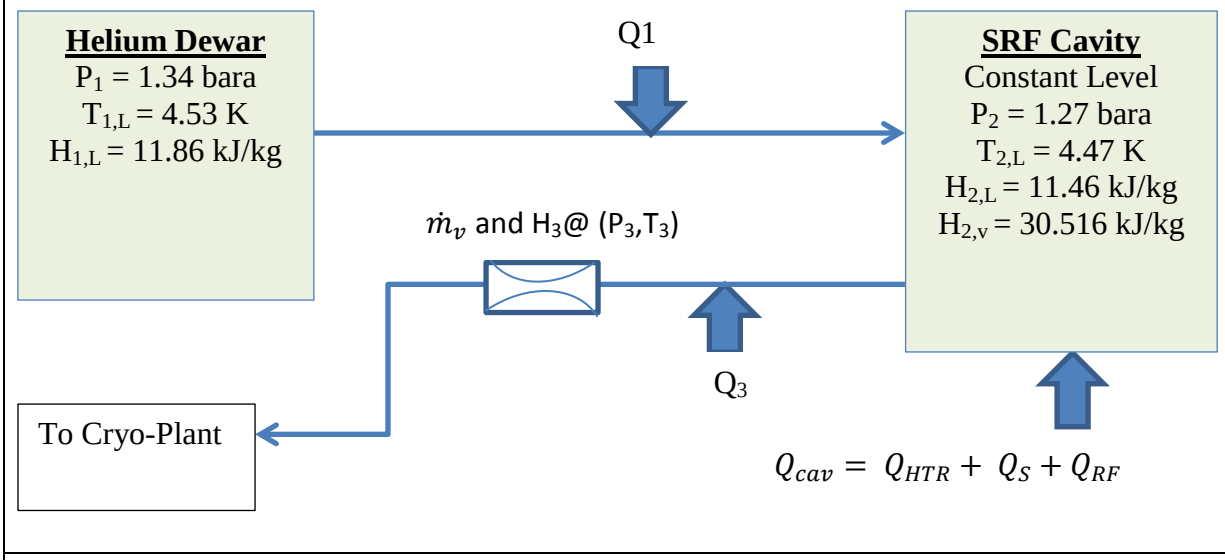

Figure 7. Boil-off Due to Static Heat Load

The total heat load for the system shown in Fig.7 can be expressed by the following equation:

$$Q_T = Q_1 + Q_3 + Q_{HTR} + Q_s + Q_{RF} = \dot{m}_v(H_3 - H_{1,L}) \quad (5)$$

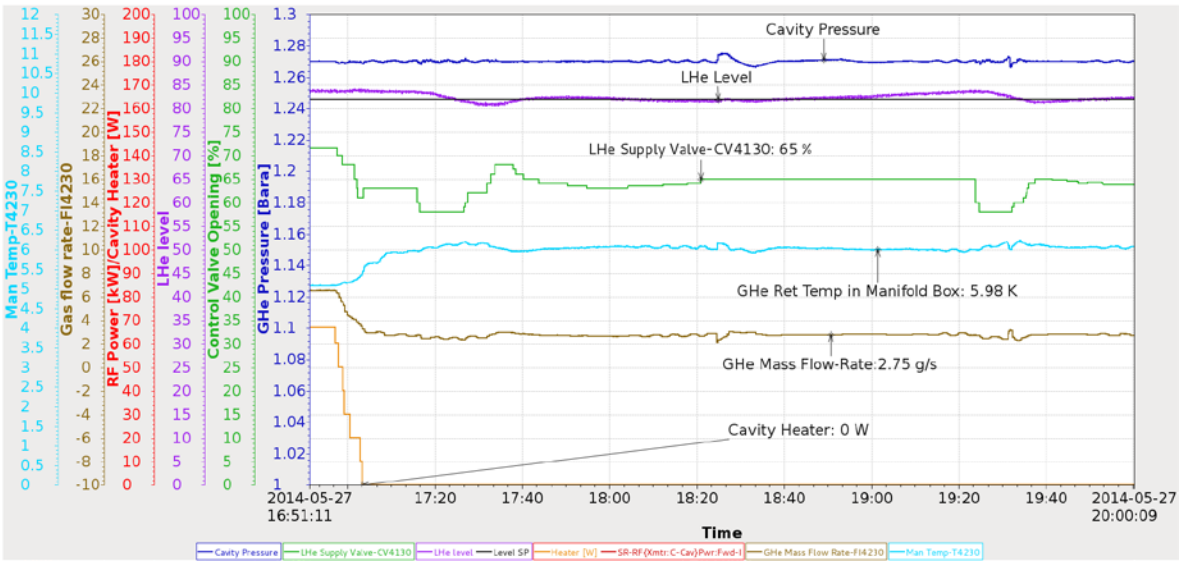

Figure 8. Boil-off Due to Static Heat Load

The relevant test parameters depicted in the graph in Fig. 8 and variables derived from these input conditions are shown in the table below:

Table 7. Test Parameters

P_1	Pressure in the Helium Dewar	1.34	Bara
$T_{1,L}$	Saturated LHe temperature in the dewar @ P_1	4.53	K
$H_{1,L}$	Saturated LHe Enthalpy in the dewar @ P_1	11.86	kJ/kg
P_2	Cavity operating pressure	1.27	bara
$T_{2,L}$	Saturated LHe temperature in the cavity @ P_2	4.47	K
$H_{2,L}$	Saturated LHe Enthalpy in the cavity @ P_2	11.46	kJ/kg
$H_{2,v}$	Saturated Ghe Enthalpy in the cavity @ P_2	30.52	kJ/kg
P_3	Ghe pressure at the venture-meter location	1.25	bara
T_3	Ghe temperature at the venture-meter location	6	K
H_3	Enthalpy of helium at P3 and T3	42.1	kJ/kg
$\dot{m}_v$	Mass flow rate measured at the venture-meter	2.75	g/s

Q_{RF}	RF Power	0	W
Q_{HTR}	Cavity Heater Power	0	W

Substituting the parameters shown in the table above in Eq. 5 yields a total heat load, Q_T of 83 W. The heat load, Q3 on the Ghe return line (Fig.7) can be calculated using the following equation:

$$Q_3 = \dot{m}_v(H_3 - H_{2,v}) \tag{6}$$

By substituting the values of $\dot{m}_v$, H_3 and $H_{2,v}$ (Table 7) in Eq. 6, the heat load, Q3 on the Ghe return line is calculated to be 32 W. Also we calculated the static heat load, Q_s on the SRF cavity cavity to be 33 W, explained in Sec. 1.1.3.1. Therefore we can estimate that the heat load, Q_1 on the liquid helium supply line to be 18 W.

Conclusion: The static heat load coming from the transfer lines between the 35,00 liters helium dewar and the SRF cavity in the block house is estimated to be 50 W.

Calibration of RF power and Verification of the mass flow rate calculated by the 202Venturi-meter

The goal of this test was to determine the dynamic power dissipated into the helium volume as a result of the "Forward RF Power" applied to the RF cavity.

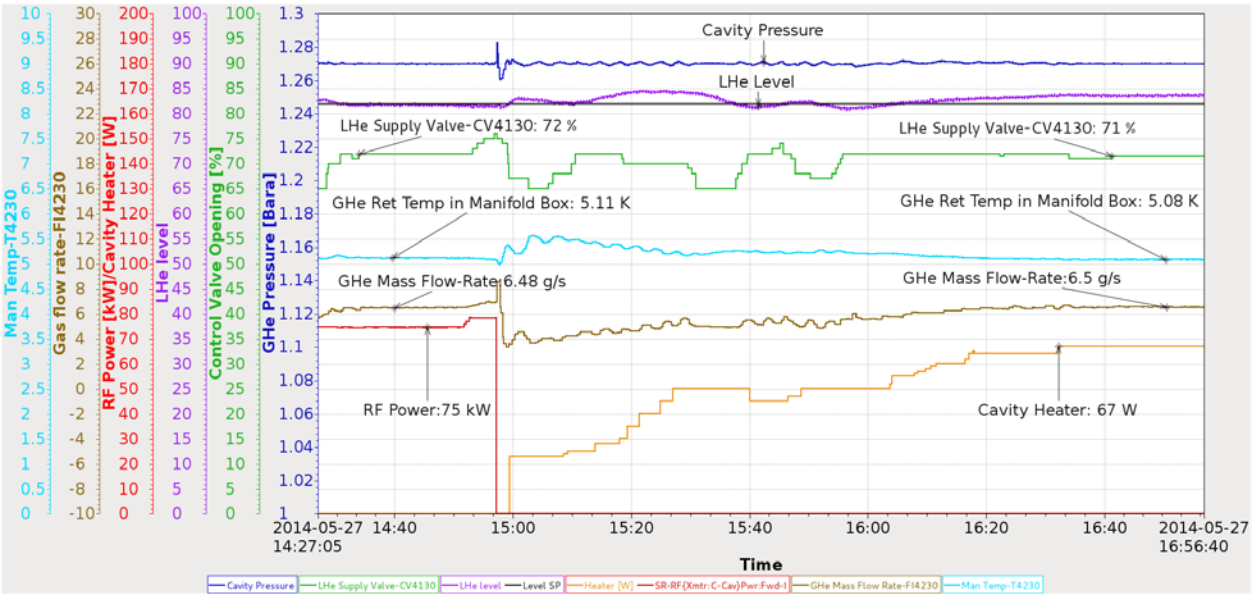

Figure 9. Calibration of Cavity Heater Power

The graph in Fig. 9 shows that by applying a "Forward RF Power" of 75 kW, resulted in a boil-off rate of 6.48 g/s. During this test the level in the RF cavity was maintained at a constant value of 82 % by putting the LHe supply control valve at 72 % open position. Also the cavity heater was set at 0 W.

In the next test, the "Forward RF Power", to the SRF cavity was turned off and the cavity heater power was manually ramped up to get the same boil-off rate as with the "Forward RF Power" on. The same amount of gas boil-off rate of 6.5 g/s was obtained with a cavity heater setting of 67 W.

Conclusion: The dynamic heat load on the SRF cavity corresponding to "Forward RF Power" of 75 kW is 67 W

The important test conditions corresponding to the graph in Fig.9 are summarized in the following Table 8.

Table 8. Test Parameters

P_1	Pressure in the Helium Dewar	1.34	Bara
$T_{1,L}$	Saturated LHe temperature in the dewar @ P_1	4.53	K
$H_{1,L}$	Saturated LHe Enthalpy in the dewar @ P_1	11.86	kJ/kg
P_2	Cavity operating pressure	1.27	bara
$T_{2,L}$	Saturated LHe temperature in the cavity @ P_2	4.47	K
$H_{2,L}$	Saturated LHe Enthalpy in the cavity @ P_2	11.46	kJ/kg
$H_{2,v}$	Saturated Ghe Enthalpy in the cavity @ P_2	30.52	kJ/kg
P_3	Ghe pressure at the venture-meter location	1.25	bara
T_3	Ghe temperature at the venture-meter location	5.08	K
H_3	Enthalpy of helium at P3 and T3	35.78	kJ/kg
$\dot{m}_v$	Mass flow rate measured at the venture-meter	6.45 ± 0.05	g/s
Q_{RF}	RF Power	0	W
Q_{HTR}	Cavity Heater Power	67	W

The 204enture-meter mass flow rate, $\dot{m}_v$ (shown by the brown curve in the graph in Fig. 9) is calculated in the Linde's PLC program from the measured differential pressure as per the following relationship:

$$\dot{m}_v = \frac{C}{\sqrt{1-\beta^4}} \epsilon \frac{\pi}{4} d^2 \sqrt{2\Delta P \rho_3} \tag{7}$$

where,

C	Discharge Coefficient	0.995
β	Diameter ratio, d/D	0.7274
ϵ	Expansion factor = $\epsilon = \sqrt{\left(\frac{K\tau^{2/K}}{K-1}\right)\left(\frac{1-\beta^4}{1-\beta^4\tau^{2/K}}\right)\left(\frac{1-\tau^{(K-1)/K}}{1-\tau}\right)}$	0.992
K	Isentropic exponent	2.365
τ	Pressure ratio = P2/P1	0.984
d	Venturi throat diameter	5.63 mm
D	Entrance diameter	7.75 mm
ΔP	Measured Pressure Difference	15.4 mbar
ρ_3	Fluid density at the 204enture inlet conditions (P3, T3)	15.7 kg/m^3

Since we know all the components of the total heat load on the system, we can now calculate the analytical mass flow rate using the following expression:

$$\dot{m}_v = \frac{Q_1 + Q_3 + Q_{HTR} + Q_s + Q_{RF}}{(H_3 - H_{1,L})} \tag{8}$$

Conclusion: Eq. 8 results in a mass flow rate of 6.3 g/s and the flow rate measured by the 204enture-meter is 6.45 ± 0.05 g/s. The error between the expected mass flow rate and the measured mass flow rate is less than 5%.

SRF cavity warm-up

Before the start of the cavity warm-up, maintenance work was planned for the water system, feeding water to the main compressor. Hence for the cavity warm-up we had to switch from the main compressor to the recovery compressor. For warming up the cavity, the warm Ghe return valve CV4330 was opened to 100%. This resulted in a lot of cold gas going back to compressor suction. Also the high pressure set point for the recovery compressor was set too high (13 barA). One of the trip conditions for all the compressors is that if the high pressure on the compressor discharge side is above 14.2 bara for sixty seconds then the compressor is shut down by the control system and a trip alarm, "PSAHH7160-High pressure too high" is generated. Consequently the recovery compressor tripped because of the incoming high cold gas volume and the pressure fluctuations on the compressor discharge (high) pressure side. This in turn caused pressure spikes on the cavity pressure. To mitigate this problem the high pressure set point for the recovery compressor was reduced from 13 bara to 11 bara. Also it was found that for the warm Ghe return valve CV4330, 30-40% valve open position is sufficient.

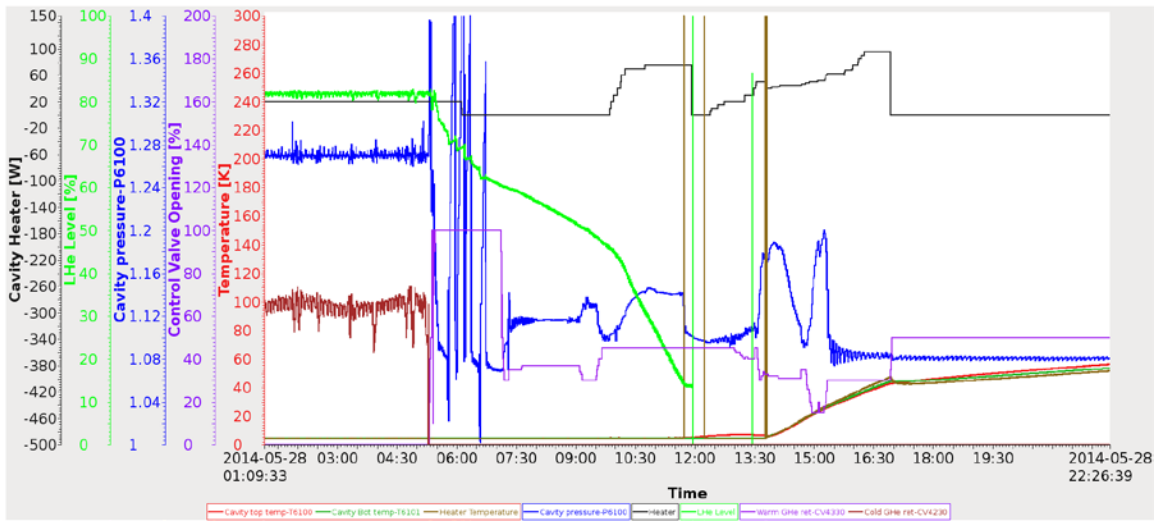

Figure 10. Warm-up of Cavity-LHe boil-off

The graph in Fig.11 shows the plot for the cavity warm-up. With the cavity heater set to 100%, the cavity warmed-up at a rate of 15 K/hr initially and then the warm-up rate reduced to 6 K/hr as the temperature approached-300 K. It took 5 days to completely warm up the cavity to 300 K. Please note at 19:00 on June 1st the heater tripped off, which caused cavity temperature to go down. The "Heater" curve in the figure shows the heater power setpoint, not the actual readback. The power readback should be implemented for future operation.

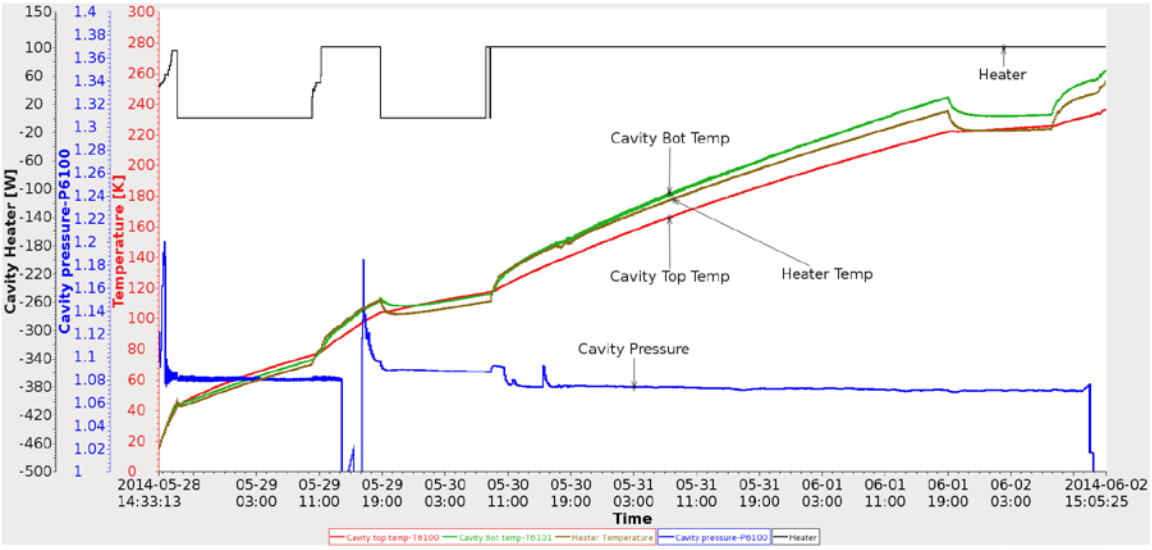

Figure 11. Warm-up of Cavity-up to 300 K

Blockhouse RF tests

Superconducting cavity RF basics

Superconducting RF cavities have become very popular for storage ring operations mainly for two reasons. First, in the superconducting state, the resistive loss on the cavity wall is minimal compared to power deliverable to the circulating beam, therefore it could be very energy efficient although there is a cost for a cryogenic plant. Second, the cavity's very high wall Q (Q0 ~ 10^8 – 10^9 at 500MHz) makes it possible to make the beam pipes bigger (which will reduce the fundamental mode R/Q) while still maintaining a fairly high shunt impedance for the fundamental mode. A bigger beam pipe generally helps reduce R/Qs of higher order modes (HOMs) and in many cases will allow HOMs to propagate to HOM loads, thus undesired beam-HOM coupling could be mitigated.

After the Nb cavity is fabricated, it is general practice to vertically test the cavity in a LHe dewar to verify Q0 prior to assembling the whole cryomodule. The vertical test of this upstream cryomodule was performed at Cornell University in August 2013. After conditioning the Q0 reached 6.8e+8 at an accelerating gradient of 10 MV/m (see Fig. 12).

In contrast to the vertical test where the waveguide port was blanked off and power was coupled to the cavity via an on-axis antenna with near-critical coupling, for the blockhouse test and future operations the cavity is connected to the transmitter via a waveguide port with very high coupling strength β on the order of 10000. The high β results from a high ratio of beam power to cavity power, unlike the case for a conventional normal conducting cavity, and this has simplified the calculation of the cavity voltage and the acceleration field.

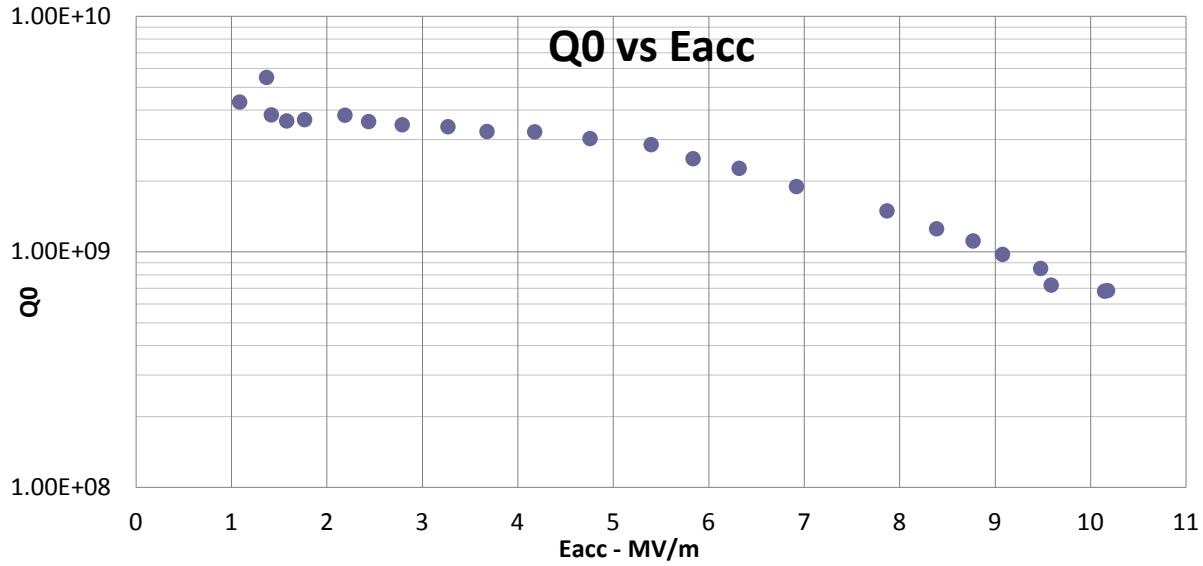

Figure 12. Vertical test data of the upstream superconducting cavity.

For an on-resonance cavity with a coupling strength β at the input port, the relation between the cavity power Pc and forward power Pf is

$$P_c = \frac{4\beta}{(1+\beta)^2} P_f \quad (9)$$

When β >> 1, Eq. 9 can be simplified as

$$P_c = \frac{4}{\beta} P_f \quad (10)$$

On the other hand, the cavity voltage Vc is

$$V_c = \sqrt{R_s P_c} = \sqrt{\frac{R}{Q} Q_0 P_c} \quad (11)$$

Eqs. 10 and 11 lead to

$$V_c = \sqrt{\frac{R}{Q} Q_0 \frac{4}{\beta} P_f} = \sqrt{4 P_f Q_{ext} \frac{R}{Q}} \quad (12)$$

where Qext is the external Q of the input port. Equation 12 shows that for a cavity with a highly over coupled input port, the cavity voltage can be calculated without knowing the value of Q0. However, Q0 will dictate the cavity wall loss thus affect the dynamic heat loss to the LHe plant. Since the R/Q is a known geometry parameter (89 Ohm), and Pf can be easily measured with a power meter, the critical parameters to be obtained are Qext and Q0.

The cavity has a weakly coupled field pickup antenna on the Nb round beam tube. Assuming the pickup port has an external Q of Qpu, and the pickup power is Ppu, with Eqs. 10 and 12 the relation between Ppu and Vc can be expressed as

$$\sqrt{P_{pu}} = \sqrt{\frac{Q_0 P_c}{Q_{pu}}} = \sqrt{\frac{4 P_f Q_0}{Q_{pu} \beta}} = \sqrt{\frac{4 P_f Q_{ext}}{Q_{pu}}} = \frac{V_c}{\sqrt{\frac{R}{Q} Q_{pu}}} \quad (13)$$

Since R/Q is known, and Qpu is fixed, Eq. 13 indicates the square root of the pickup power is proportional to cavity voltage Vc even though Q0 might be changing. For example, for a given Vc, if Q0 doubles, the cavity power will be cut by half, but the pickup coupling strength to the cavity βpu = Q0/Qpu will double so that Ppu = βpu*Pc remains the same. This means that on

the CFC, the cavity field channel is linear to the cavity voltage and acceleration gradient, regardless of change in βpu.

In order to obtain Q0, rewrite Eq. 10

$$P_c = \frac{4Q_{ext}}{Q_0} P_f \quad (14)$$

$$Q_0 = \frac{4Q_{ext}}{P_c} P_f \quad (15)$$

Since the cavity forward power Pf and the reverse power Pr are both three orders higher than Pc for such a high β, it is impossible to get accurate cavity power with Pc = Pf – Pr. The Pc, as a heat loss to the cryogenic system, can be obtained from the cryogenic instrumentations.

Test setup

Figure 13 shows the setup for the RF test, where the cavity tuner is not shown. At the left top corner, a phase lock loop (PLL) is set up to shift the drive frequency towards the cavity resonant frequency when the cavity tuner is locked; on the other hand the cavity tuner can shift the cavity resonant frequency towards the drive frequency if the PLL is not in use. Both the PLL and the tuner circuit compare the phase difference between the forward power signal and the cavity field signal, so the tuning mechanism is similar except that the PLL adjusts the signal generator side while the tuner adjusts the cavity side. The drive signal from the signal generator feeds the NSLS-II Frequency Standard chassis, which subsequently feeds the Cavity Field Controller (CFC). The CFC drive signal is amplified to watt level by a solid state pre-driver amplifier, which then drives the 310kW klystron amplifier. A circulator with a full power reject load is installed after the klystron to protect the tube from being damaged by reverse power. After the circulator, the RF power goes through a bi-directional coupler then feed the superconducting cavity. Both the forward and reverse power coupled signals go to the CFC and power meter channels, for measurement and monitoring purposes.

The cavity has a port on the Nb round beam tube (port C) for monitoring the cavity field, and a port on the Nb waveguide (port D) to monitor possible electron accumulation (e-cloud). There are also a few ports on the thermal transition fluted beam tube and the round beam tube but they are not monitored during this test.

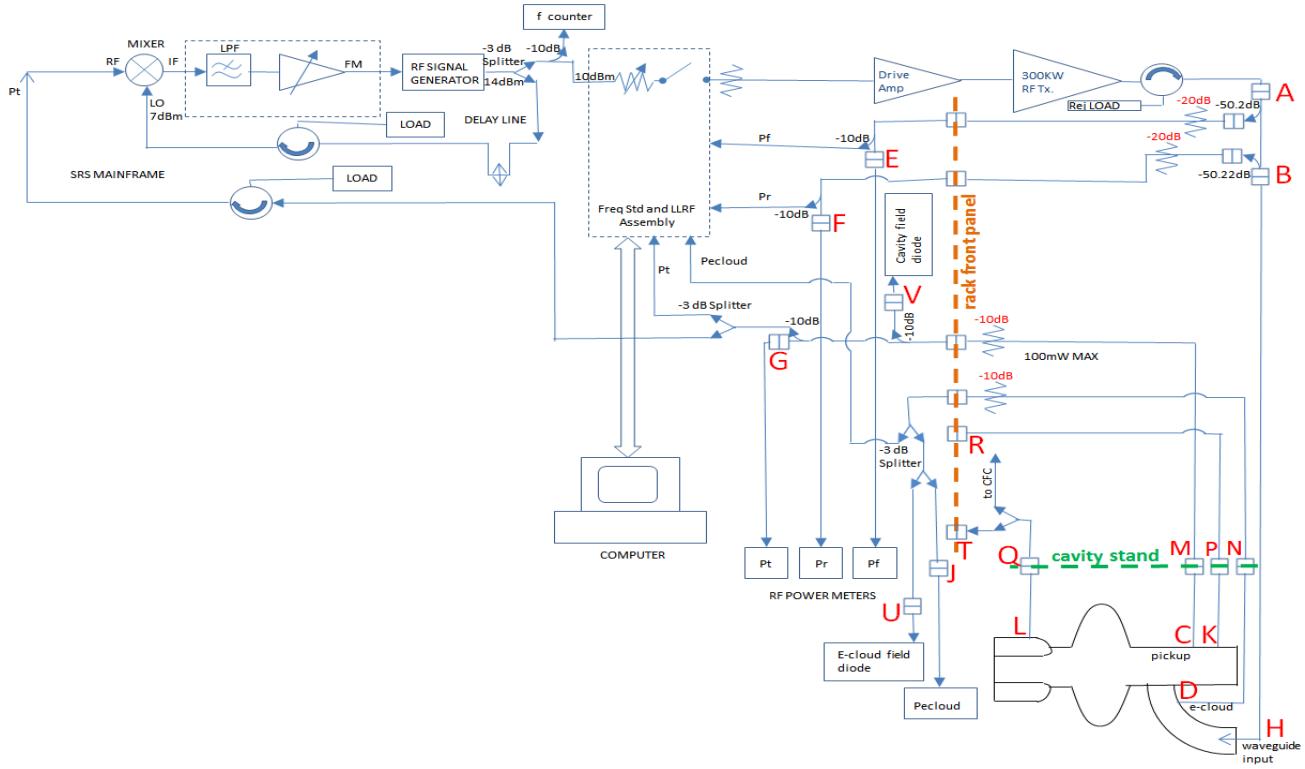

Figure 13. Setup for the blockhouse RR test (cavity tuner not shown).

The cavity frequency tuner

The cavity is specified to have a tuning range of 499.68MHz ± 150kHz. The tuner assembly allows the cavity to be stretched and compressed in the longitudinal direction so that the resonant frequency can be changed accordingly. A step motor pushes one side of the cavity outwards with levers and linkages, while the beam vacuum tries to pull the cavity back against the motor force. Two compensation bellows are installed as part of the tuner mechanism to account for variation of the pressure difference between beam vacuum and insulation vacuum. The step motor is controlled by a dedicated tuner PLC. Two strain gauges are used to monitor the tuner force and one linear variable differential transformer (LVDT) is used to monitor the tuner position. The tuner has soft limits (similar to door switches) and hard limits (locked nuts).

When the cavity is above the transition point 9.2K, the normal conducting Q0 is on the same order of magnitude as the Qext of the input port. Therefore it is possible to check the resonant peak with network analyzer S11 measurement. The Qext, which does not change with temperature, can also be measured at this time. The Qext measurement will be explained in the next section. After the cavity is cooled down to 4.5K, due to the large β it is no longer possible to see a clean peak with S11 measurement. Please note in this setup, the loaded Q of the cavity QL is essentially the same as Qext, which is about a few tens of thousands, and whose resonant peak is much wider than that of a superconducting cavity in a vertical test. Therefore, the S11 measurement is not limited by the width of the peak, but by the large β. On the contrary, during a vertical test, the β is close to unity, but because QL and Q0 are on the same order of magnitude, the cavity will have a bandwidth less than 1Hz – therefore in a vertical test the S11 measurement is not limited by the β, but by the peak width. Figure 14 shows S11 of the cavity waveguide input port before and after LHe cooldown. One can see after the LHe cooldown, the resonant peak is not clean anymore.

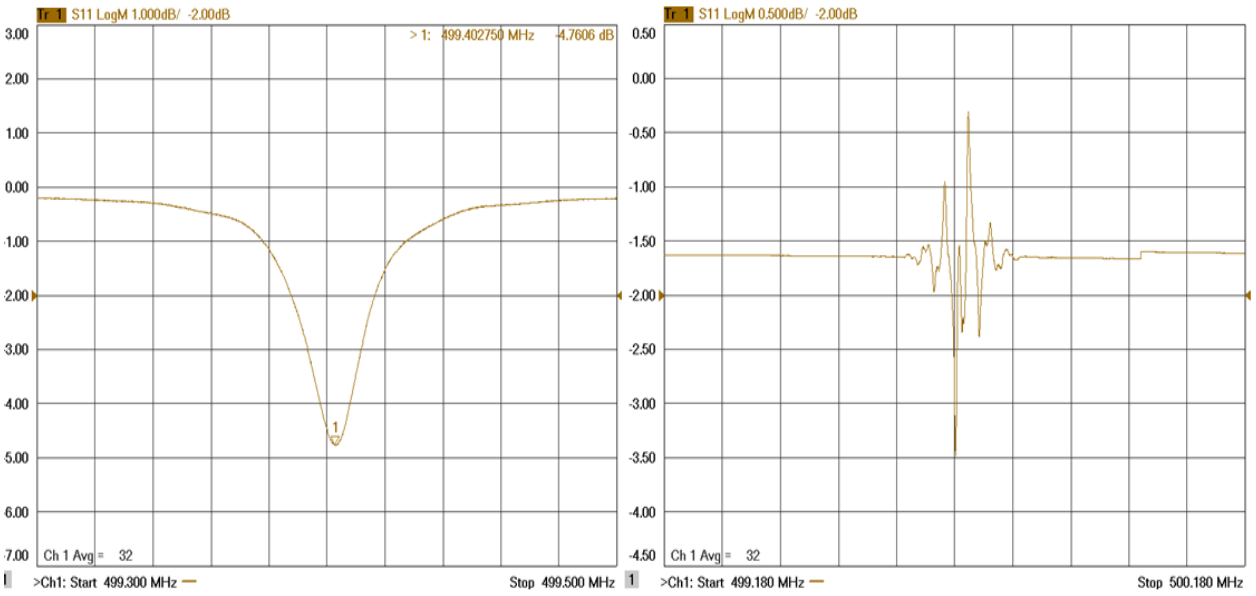

Figure 14. S11 of the cavity waveguide input port before (left) and after (right) LHe cooldown.

After cavity cooldown, waveguide installation between the cavity and the circulator was completed. It was attempted to search for the cavity resonant peak via the cavity pickup port and the e-cloud port, however no visible resonant peak was found, possibly due to the significant undercoupling of the probes to the cavity.

After a few kilowatts of Pf applied to the cavity, the PLL was successfully closed, where the drive signal frequency was monitored by a frequency counter. Then by using phase shifters, the cavity resonant frequency was found and adjusted to 499.68MHz. It was determined that a tuning range of 499.68MHz ± 30kHz is sufficient for NSLS-II operation without unnecessary stress to the cavity, then the soft and hard tuner limits were adjusted accordingly.

Through a few attempts to close the tuner loop, it was found that the phase error sent to the tuner PLC by the CFC is only around one of the two zero crossings of a cycle. If the zero crossing is sitting on an unstable slope, the tuner loop will not close and the cavity resonant frequency will run away. A solution for this scenario is to reverse the motor direction.

It happened one time that when the tuner hit the inner soft limit (lower frequency limit) but not the hard limit, it got stuck there and the manual control was not able to bring the tuner back to the middle range. The solution was to remove the power and communication plug to the motor controller, then move the tuner back by hand, then reconnect the power and communication plug. This problem cannot be repeated.

Qext measurements of the waveguide input port

Equation 12 shows Qext is a very critical quantity for determining the cavity voltage. During the test three different methods were used independently to measure the Qext: using a network analyzer to measure S11 through the waveguide input port at warm temperature (~150K); using the pickup port to measure the 3dB bandwidth of cavity power giving constant Pf at 4.5K; and using a power meter to measure the decay time of the cavity emitted power after a transmitter trip. All three of them give a Qext ~ 79000.

The S11 method for Qext measurement

There are mainly two ways to do Q measurements via S11: using a Smith chart and using the log-mag curve. Using a Smith chart is easier if the serial resistive loss is negligible; otherwise the correction on a Smith chart is not very straightforward. On the contrary, it is fairly easy to use the log-mag curve when there is significant serial resistive loss.

The Smith chart approach was attempted first due to its simplicity. However, as shown in Fig 15 it was found the separation between the resonant circle and the chart perimeter is comparable to the size of the resonant circle, which means the serial resistive loss is non-negligible and will make the measurement less accurate. Therefore, the log-mag curve approach was adopted later for more accurate results.

Figure 16 shows how the log-mag approach was performed. When an input port to the cavity does not have serial resistive loss, the far-off-resonance S11 magnitude should be unity and the corresponding dB reading should be zero. However, due to the serial loss, the log-mag curve here had a nonzero offset dS11, shown on the left plot of Fig. 16. For accurate measurements, the offset was then subtracted from the on-resonance S11, i.e. S0. With the corrected S0, reflection coefficient Γ and coupling strength β were calculated. Furthermore, the dB level to be used to determine QL (BWS11), as a function of Γ or β, was calculated. Finally, the offset dS11 was added back to BWS11 for easier marker search on the network analyzer, and the bandwidth for QL was found, as shown on the right plot of Fig. 16. Then Qext can be calculated with QL and β.

Nine sets of data were taken during the cooldown, while the cavity was still not superconducting, and the result is Qext = 79046 ± 569.

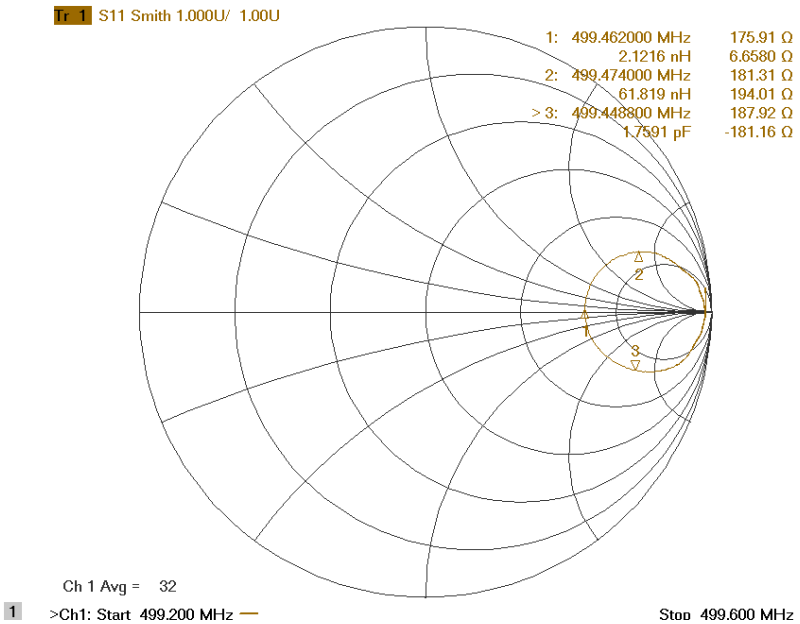

Figure 15. S11 of the input port on a Smith chart where non-negligible serial resistive loss is present.

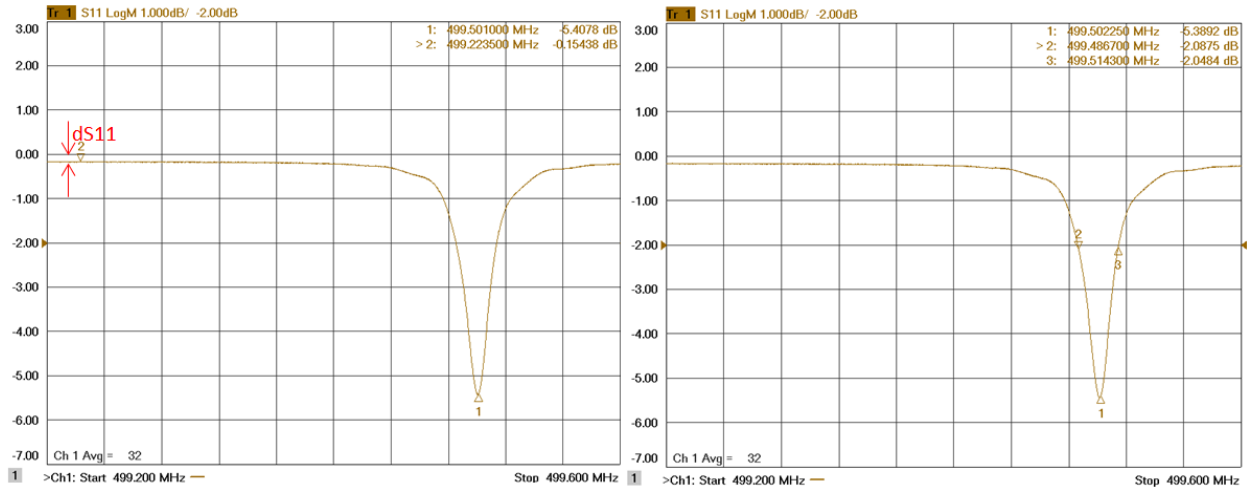

Figure 16. S11 on the log-mag curve with offset measured (left) and QL markers identified (right).

Probing cavity power for Qext measurement

After the cavity temperature reached 4.5K, the Q0 is on the order of 10^8 to 10^9. This Q0 is much larger than Qext which is on the order of 10^4. In this case, Qext = QL. As shown in Fig. 17, the phase shifters of the PLL was adjusted to change the drive frequency while the cavity resonant frequency was fixed, then the pickup port power will vary given a constant Pf. The bandwidth fH-fL was found for QL and Qext calculation.

Two sets of data were obtained and the result is Qext = 79750 ± 1061.

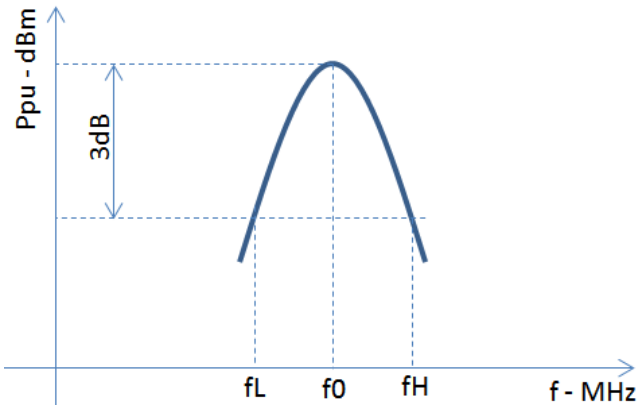

Figure 17. Using cavity power to measure QL, which is the same as Qext for high β.

Using the cavity field decay time for Qext measurement

When the transmitter trips, both the waveguide port and the pickup port will emit power whose time constant can be used to calculate QL and Qext. Figure 18 shows the power decay curve on semilog scale, where ideally the curve should be a straight line. While section A-B is nearly straight, section B-C is a little curved. With Section A-B, QL and Qext was calculated as 78450; and with A-C, QL and Qext was calculated as 77000. The latter is lower than former because of the line is curved.

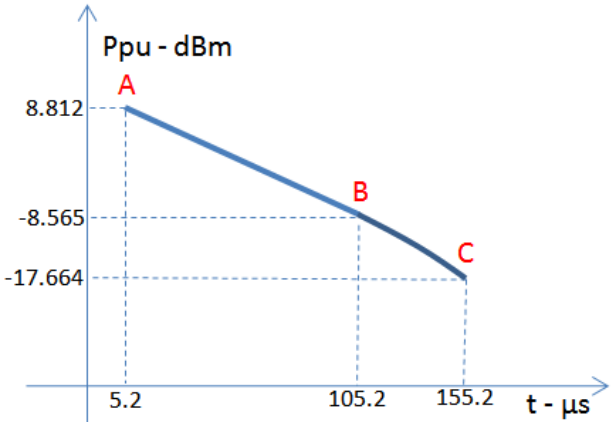

Figure 18. Using cavity power decay curve time constant to measure QL, which is the same as Qext for high β.

Higher power conditioning to increase Vc

Based on Eq. 12, Vc is determined by Pf, Qext and R/Q. Therefore, it is necessary to keep increasing Pf until desired Vc is reached. In the meantime, conditioning is necessary to obstacles such as vacuum burps and window arcs. Figure 19 shows Vc as a function of Pf. The highest Pf read by a power meter was 68.55kW, which yielded a Vc of 1.4MV corresponding to an acceleration gradient of 4.63MV/m.

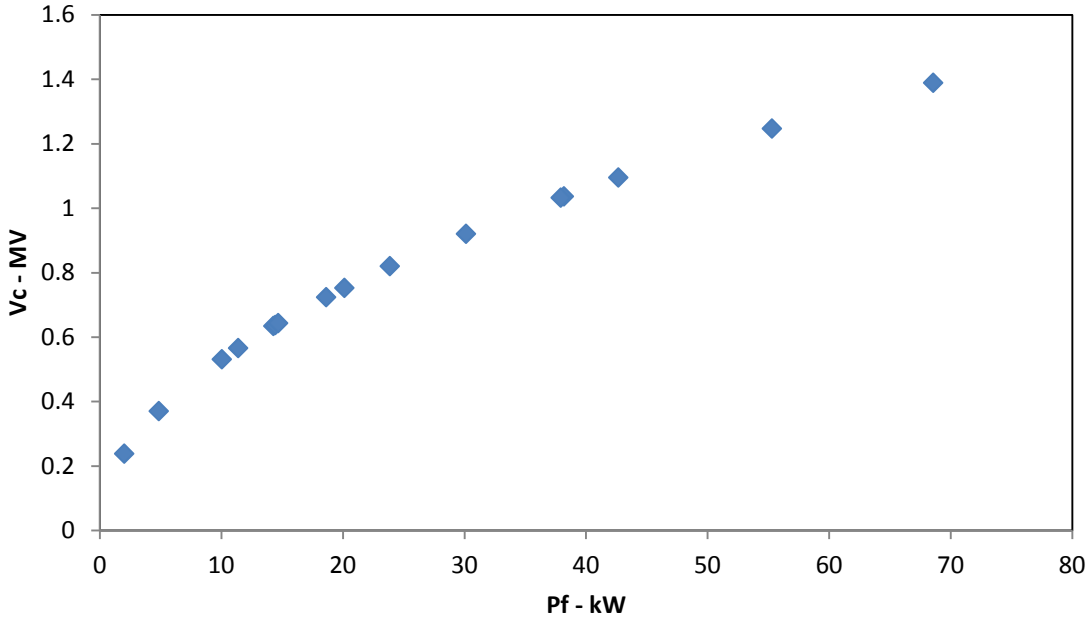

Figure 19. Cavity voltage Vc calculated from Pf read by a power meter.

Figure 20 plots Pf with waveguide pumpout box ion pump pressure reading. Generally Pf was increased during a manned shift against pressure bursts and arc trips, and was kept at a lower level when unattended. Sometimes Pf had dips and went back by itself, and Figure 21 gives an example. Figure 22 shows attempts to go beyond Pf of 68.55kW during the final shift. The highest Pf should be a few kilowatts higher however the Vc will not be affected

dramatically. Various trips, mainly vacuum and arc trips prevented Pf from going higher. The test had to stop in the early morning of May 28th because of the scheduled shutdown.

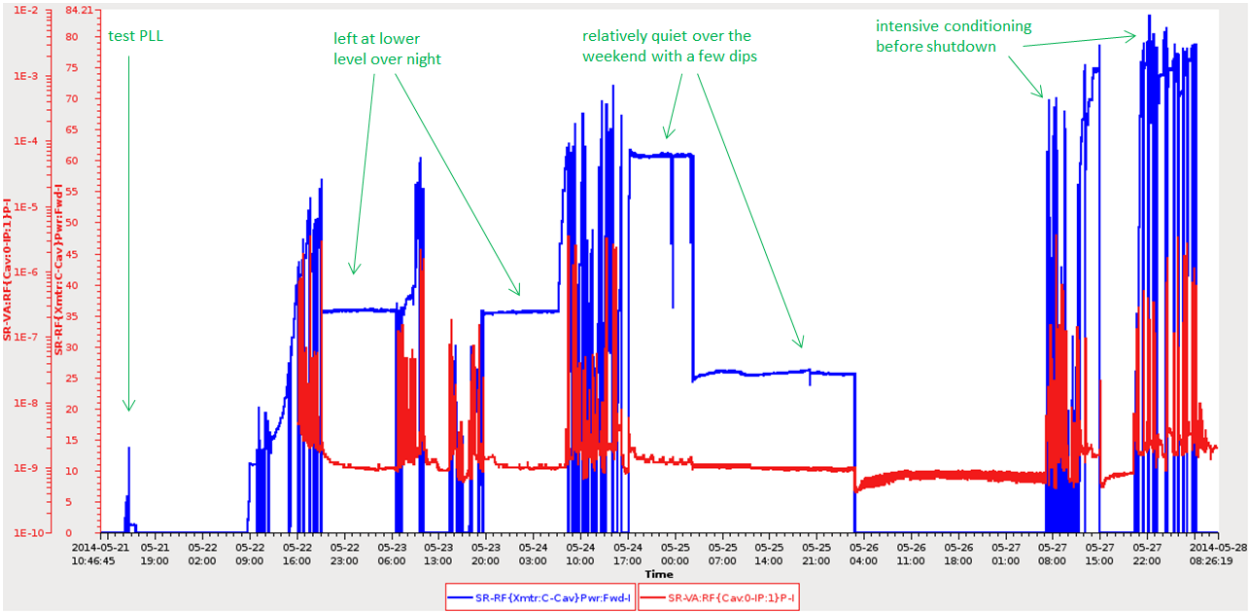

Figure 20. Pf with waveguide pumpout box ion pump pressure reading throughout conditioning.

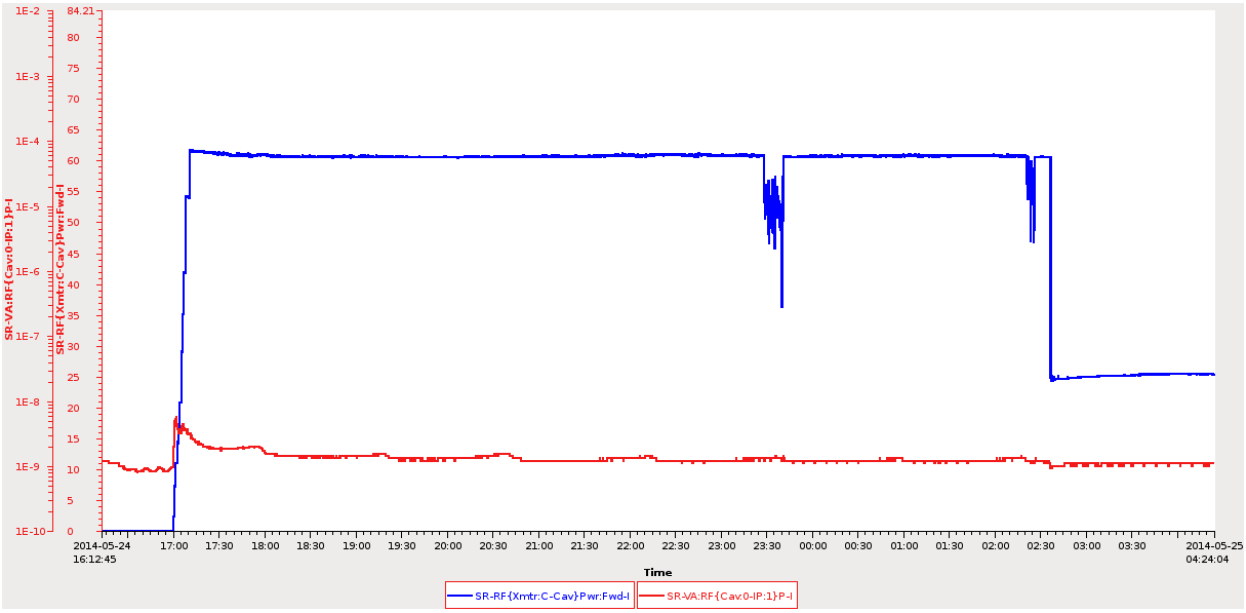

Figure 21. Power dips in Pf.

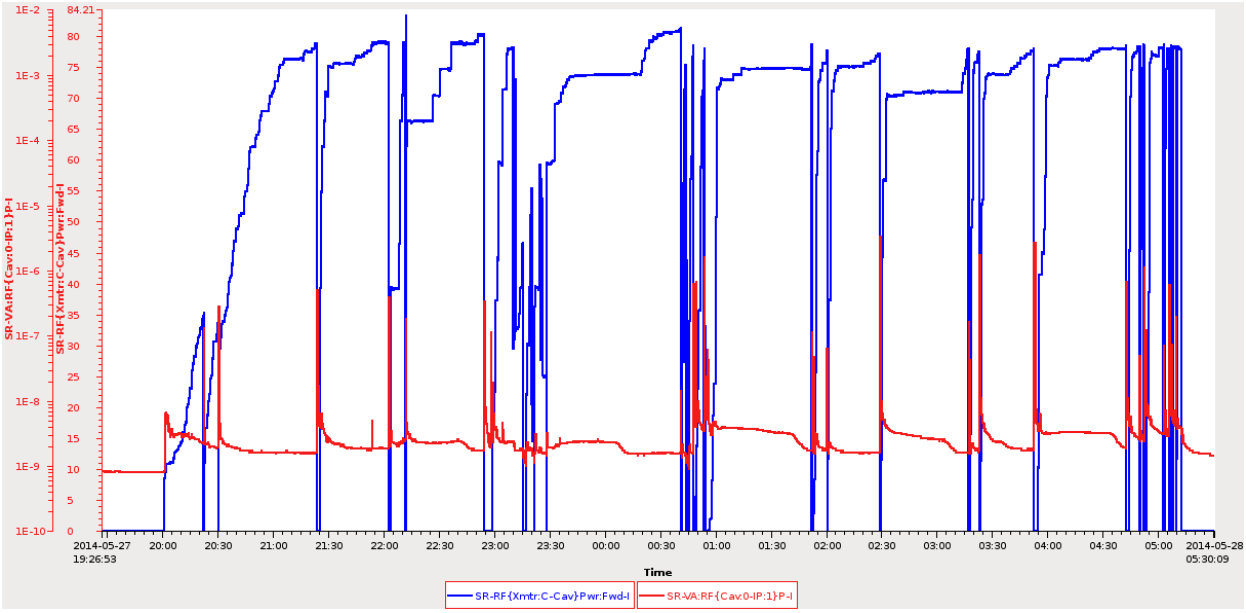

Figure 22. Forward power Pf and vacuum during the last conditioning shift.

Q0 measurement of the cavity

As described in Section 1.2.1, the cavity power Pc is needed for Q0 calculation. For our measurement Pc was obtained as follows:

First the cavity voltage was set to 1.4MV by Pf, where Pc contributed to the heat loss inside the LHe vessel. The LHe vessel heater was kept off and the Ghe warm return valve was closed. The LHe level and Ghe pressure within the LHe vessel were kept constant. In this case the total heat loss inside the LHe vessel consisted of the cavity power Pc and static loss, and the total loss was reflected by the mass flow rate (MFR) of the Ghe cold return line. The MFR was measured to be 6.54 g/s.

Then while the other conditions remained the same, the RF was turned off and the LHe heater was turn on. The heater power was manually adjusted until the MFR had minimal ripples and matched the value of the case when RF power alone was applied earlier. At this moment the heater power should be the same as Pc applied earlier. The Pc was determined to be 62.8W. Use Eq. 15 with Pc = 62.8W, the cavity Q0 at Vc = 1.4MV (Eacc = 4.63MV/m) was found to be 3.5e+8.

Figure 23 compares the cavity condition with that from the vertical test. The green ellipse represents where the cavity is now, and it closely resembles the Q0 values in the vertical test when the cavity had not been fully conditioned. It is expected that with more conditioning, the cavity Q0 would move higher towards the purple dots, where the cavity was fully conditioned.

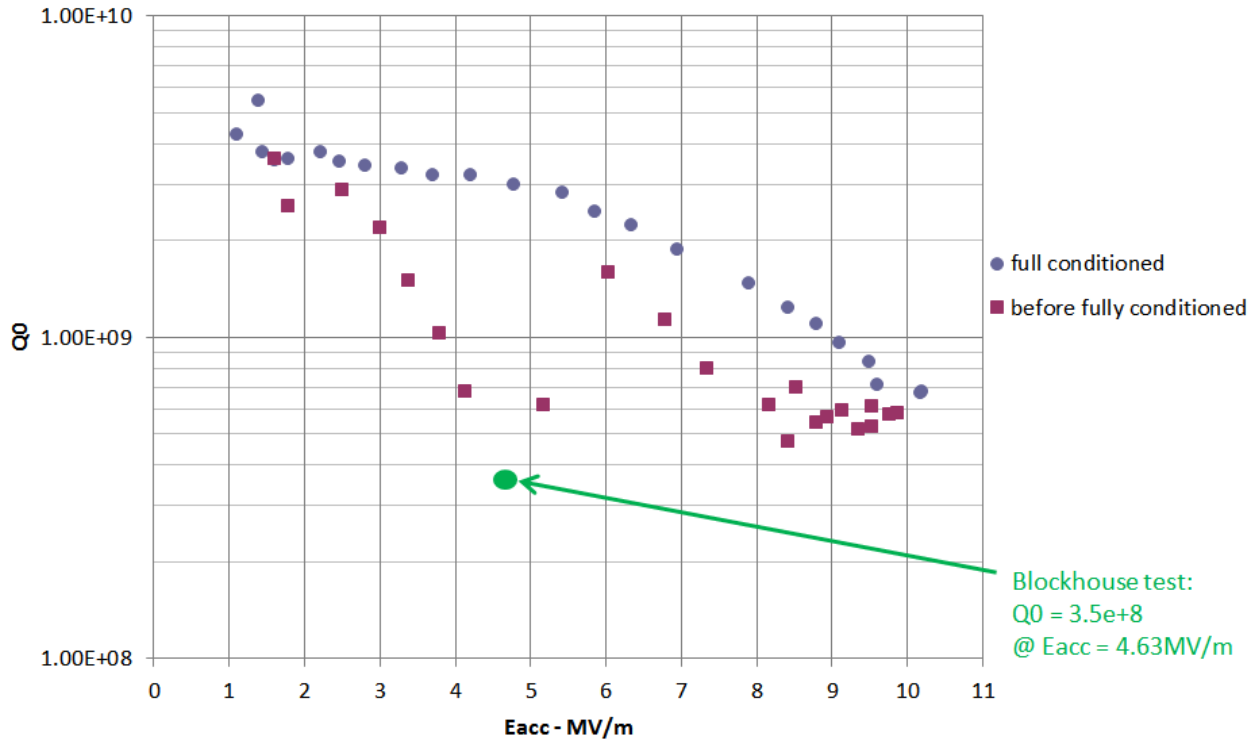

Figure 23. The present Q0 of the cavity (the green dot) compared to the vertical test data. The magenta dots represent Q0 values before full conditioning during the vertical test, while the purple dots represent Q0 values after full conditioning.

5.1.2 Tunnel Commissioning

After the blockhouse test, the cavity was installed at the upstream location of the Cell 24 RF straight. Conditioning the cavity up to 2MV has been attempted, however due to symptoms of possible quenching the cavity voltage was finally lowered to 1.2 MV for reliable operation. During commissioning it was noticed that the Ghe flow through the cavity waveguide heat exchanger (HEX) was blocked, then after the commissioning it was confirmed a Ghe check valve did not function properly. The lack of Ghe flow would increase the heat leak to the niobium cavity through the waveguide and it might be related to the possible quenching. The RF parameters are listed in Table 9. The cavity Q0 was not checked during tunnel operation due to the tight schedule, thus the result from blockhouse test was used.

Section 2.1 will describe the tunnel cavity cryogenic operation, while Section 2.2 will focus on the RF tests.

Frequency (MHz)	499.68 nominal
r/Q (Ω)	44.5
Q0	3.5e+8 from blockhouse
Rsh (MΩ)	15600
Voltage for commissioning Vc (MV)	1.2

Input port coupling strength β	4430
QL	79000
Cavity power (W)	46.2
Beam energy (GeV)	3.0
Beam energy loss per turn Va (kV)	288
Beam current (mA)	50
Momentum compaction	3.7e-4
Synchronous phase $\cos^{-1}$(Va/Vc)	76.11°
Beam power (kW)	14.4
Forward power (kW)	58.68
Reverse power (kW)	44.23
Detuning angle	-15.87°
Detuning frequency (kHz)	-0.899
Synchrotron frequency (Hz)	2080
Synchrotron tune	5.49e-3

Table 9. 500MHz superconducting cavity RF parameters for commissioning

Cavity cryogenic **operation for tunnel commissioning**

Cool-down of Cold-Box

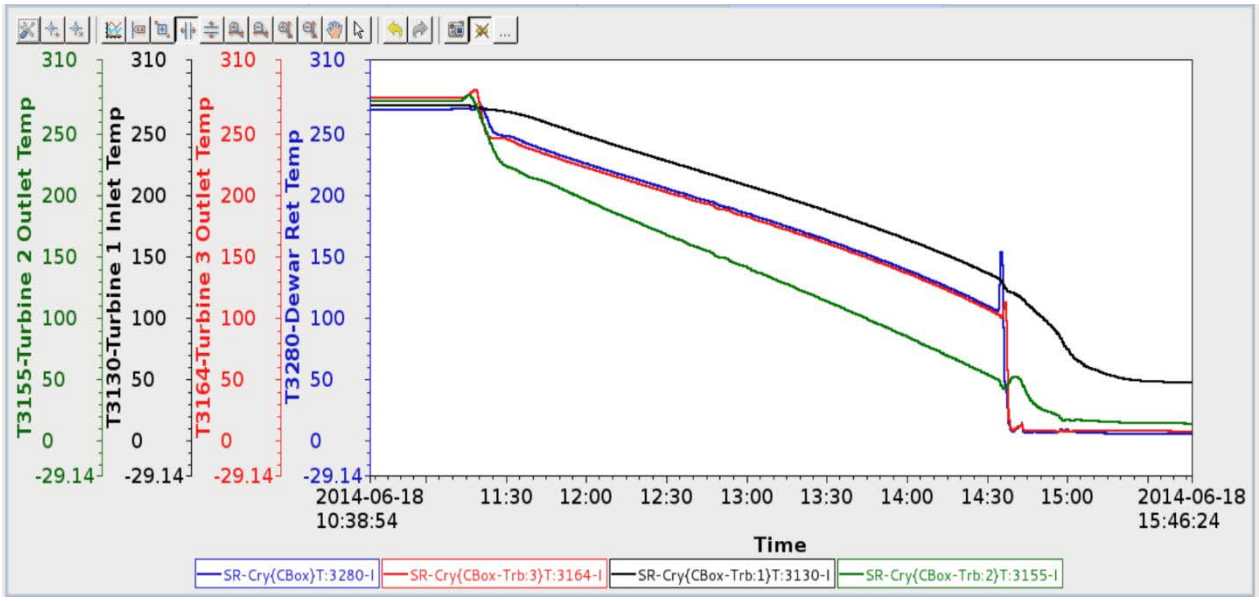

Figure 24. Cool-down of Cold-Box

1. Cool-down of cold box started at 10:38 on 06/18/2014
2. End of cold-box cool down indicated when the temperature of helium gas returning from the Dewar (TI3280-blue curve) reaches a steady state temperature of 4.6-4.7 K.
3. The cold box takes ~4-5 hrs to reach stable conditions

Building helium level in the 3500 LTs Dewar

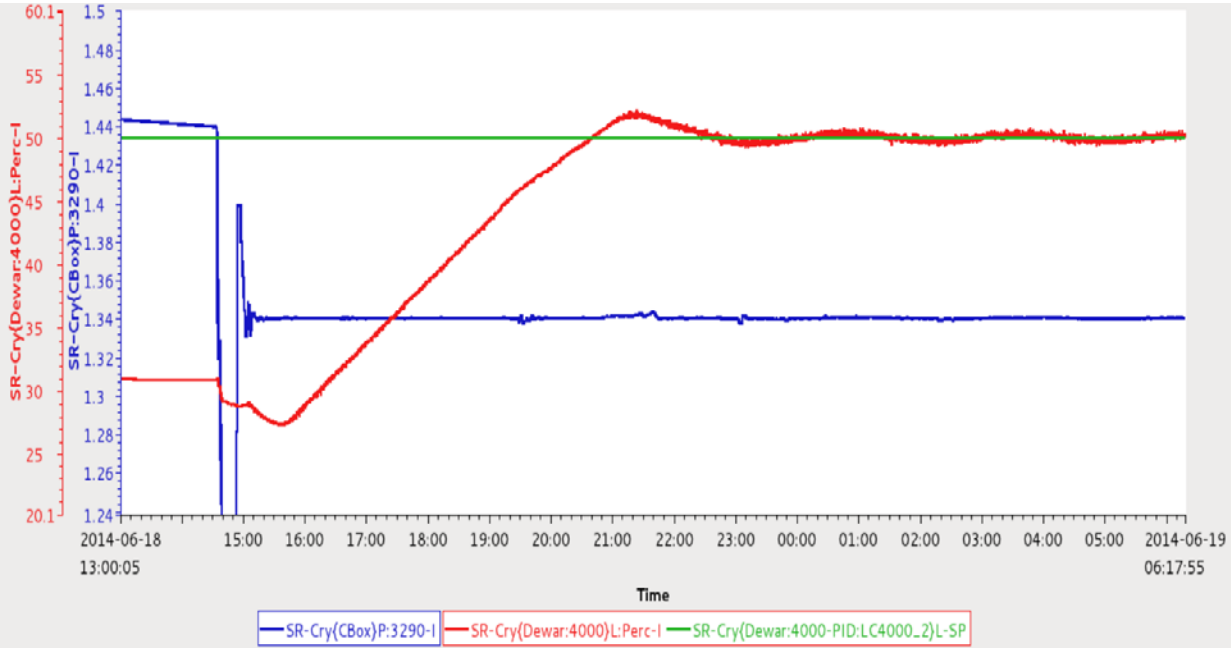

Figure 25. Building helium level in the 3500 LTs Dewar

1. Before starting the cool-down of the cold box the helium level in the 3500 lts dewar had dropped to 30%. It took another 7-8 hrs for the helium level to build up to the set point of 50%
2. Note (as per Linde's recommendation, different level set points for the two controllers control the dewar level, otherwise the two controllers with fight against each other)

a. The level set point for the (LC4000B-1) for the compressor B HP was set to 40%

b. The level set point for the (LC4000-2) for the dewar heater (R4000A) was set to 50%

Relationship between liquid helium level and the buffer tank pressure

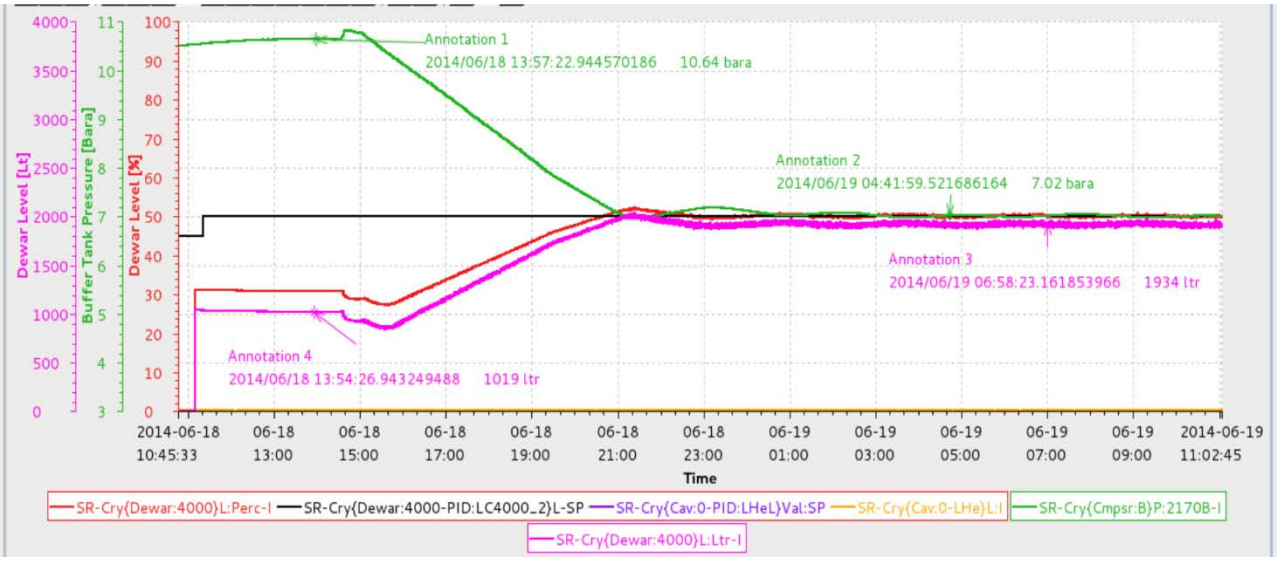

Figure 26. Relationship between liquid helium level and the buffer tank pressure

Note: The helium gas was delivered from two gas tanks (Tank B and Tank C)

1. Initial Buffer Tank pressure = 10.64 bara
2. Initial level in the helium dewar = 1000 ltr
3. Final buffer tank pressure = 7.02 bara
4. Final level in the helium dewar = 2000 ltr
5. Conclusion: 1 bar of helium gas pressure in the buffer tank yields ~140 lts of liquid helium volume in the Dewar.
6. Note: A minimum of 2.5 bara pressure is required in the buffer tanks
7. Before starting the cryo-plant ensure that the pressure in the gas tank is greater than 4 bar in all three tanks

8. If there is not enough gas in the tube trailer try increasing the pressure in the gas tank by lowering the level set point of the 3500 liquid helium dewar

9. When refilling the gas tank, fill two tanks to a maximum pressure of 9 bara and the third tank to ~4 bara.

Cool-Down of Manifold box LN2 Shield

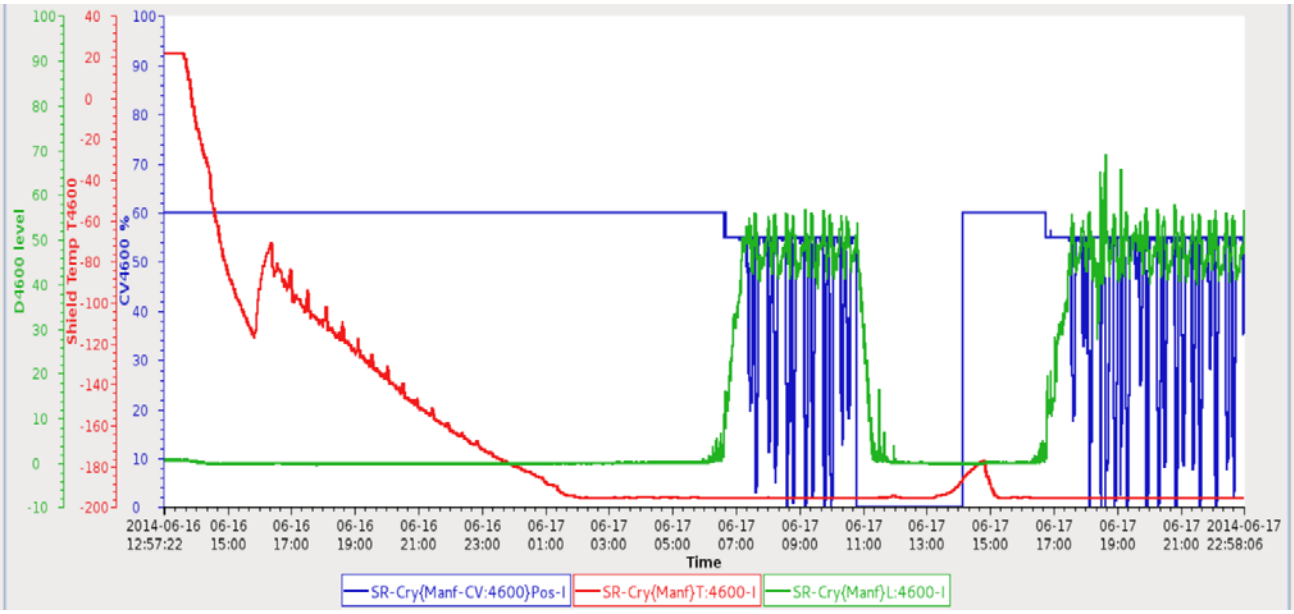

Figure 27. Cool-Down of Manifold box LN2 Shield

1. The cool-down of the manifold box was started at ~13:00 on 06-16-2014. The cool-down of the LN2 shield of the manifold box takes about 16 hrs to complete.

2. After cool-down of the LN2 shield, it takes another 20 hrs for the level in the LN2 phase separator D4600 to build up to the set point and then stabilize.

Cool-Down of Valve box LN2 Shield

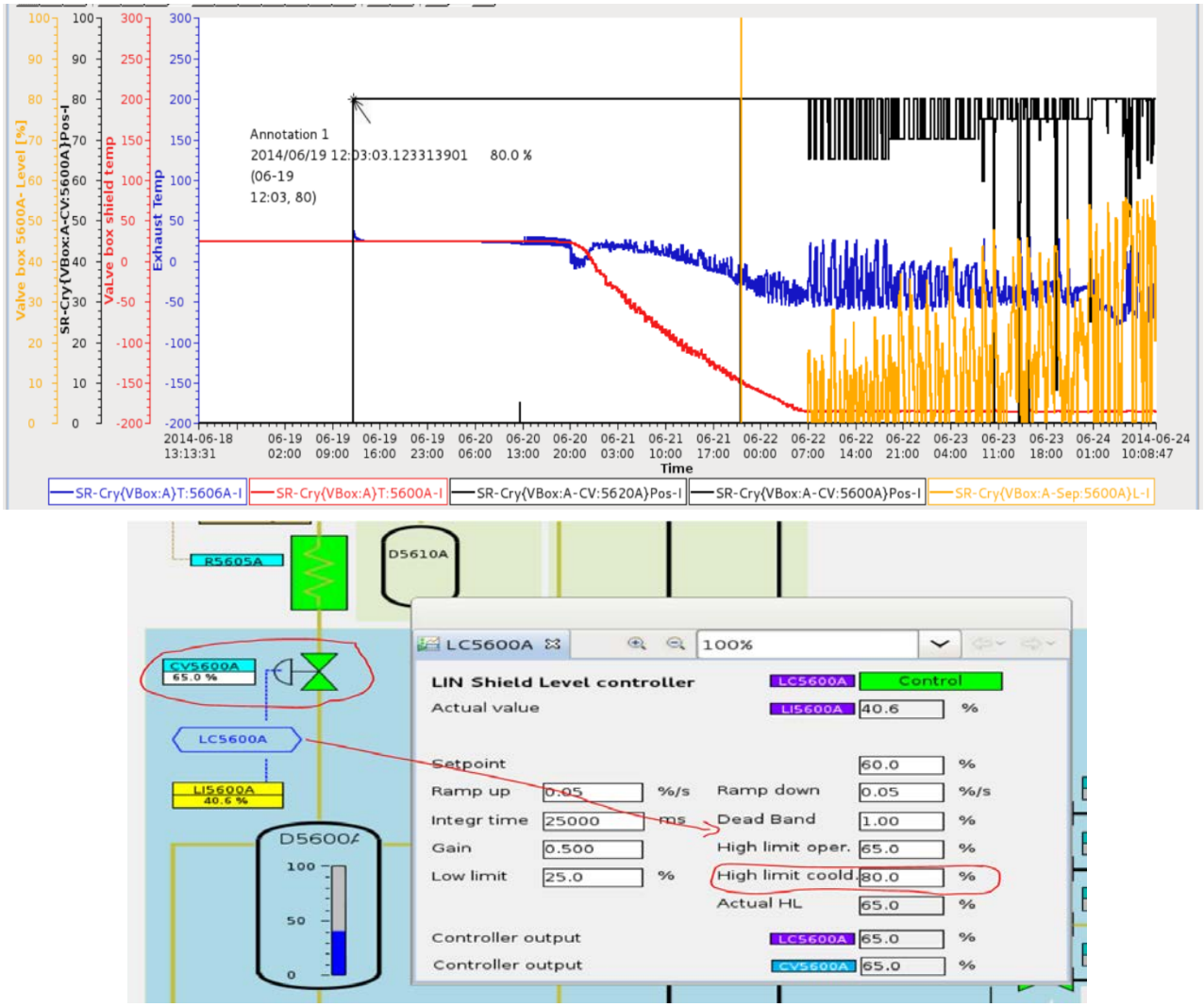

Figure 28. Cool-Down of Valve box LN2 Shield

1. The cool-down of the valve box was started at 12:03 on 06-19-2014.

   Note: CV5600A is an exhaust valve. During cool-down this valve has a maximum opening of 80%. To speed up the start of the valve box LN2 shield cool-down, the set point for the "high limit coold" can perhaps be set to 90-95%
2. As shown by the red curve, it took about 36 hrs before the temperature of valve box LN2 shield started dropping. This slow response is limitation set by the small size (DN6) for CV5600A which controls the gas exhausting from the valve box.

3. It takes another 48 hrs for the valve box LN2 shield temperature to reach steady state and to build LN2 level in the vessel D5600A.

Cavity LN2 Cool-Down

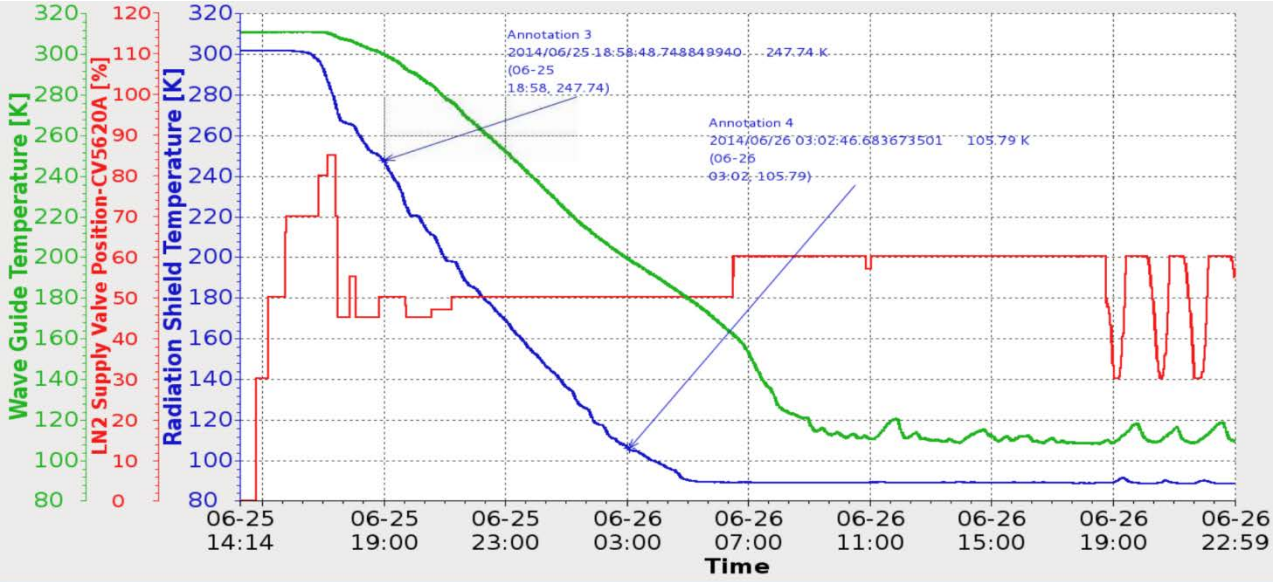

Figure 29. Cavity LN2 Cool-Down

NOTE: Refer to the cavity cool-down procedure for all the steps involved in the cool-down process

1. The cool-down of the cavity LN2 shield was started at 14:00 on 06-25-2014.

2. To speed up the start of the cool-down process the LN2 supply valve (CV5620A-red curve) was initially open to 80-85% and also the back pressure regulator (RV6620-refer to cavity PID) on the exhaust side was left wide open (the flow meter FI6601 on the downstream side of the back pressure regulator indicated a flow reading of 6 scfm. The normal operating flow reading is 1.5-2 scfm.

3. Once the radiation shield showed a drop of ~30 K the LN2 supply valve-C5620A opening was reduced to 50% and the back pressure regulator was adjusted to match the following conditions:

    a. Pressure on the inlet side of the back pressure regulator = 20 psi

    b. GN2 Flow = 1.5-2 scfm

4. With the above settings, the radiation shield cooled down at a rate of 20 K/hr.

Cavity Helium Cool-Down

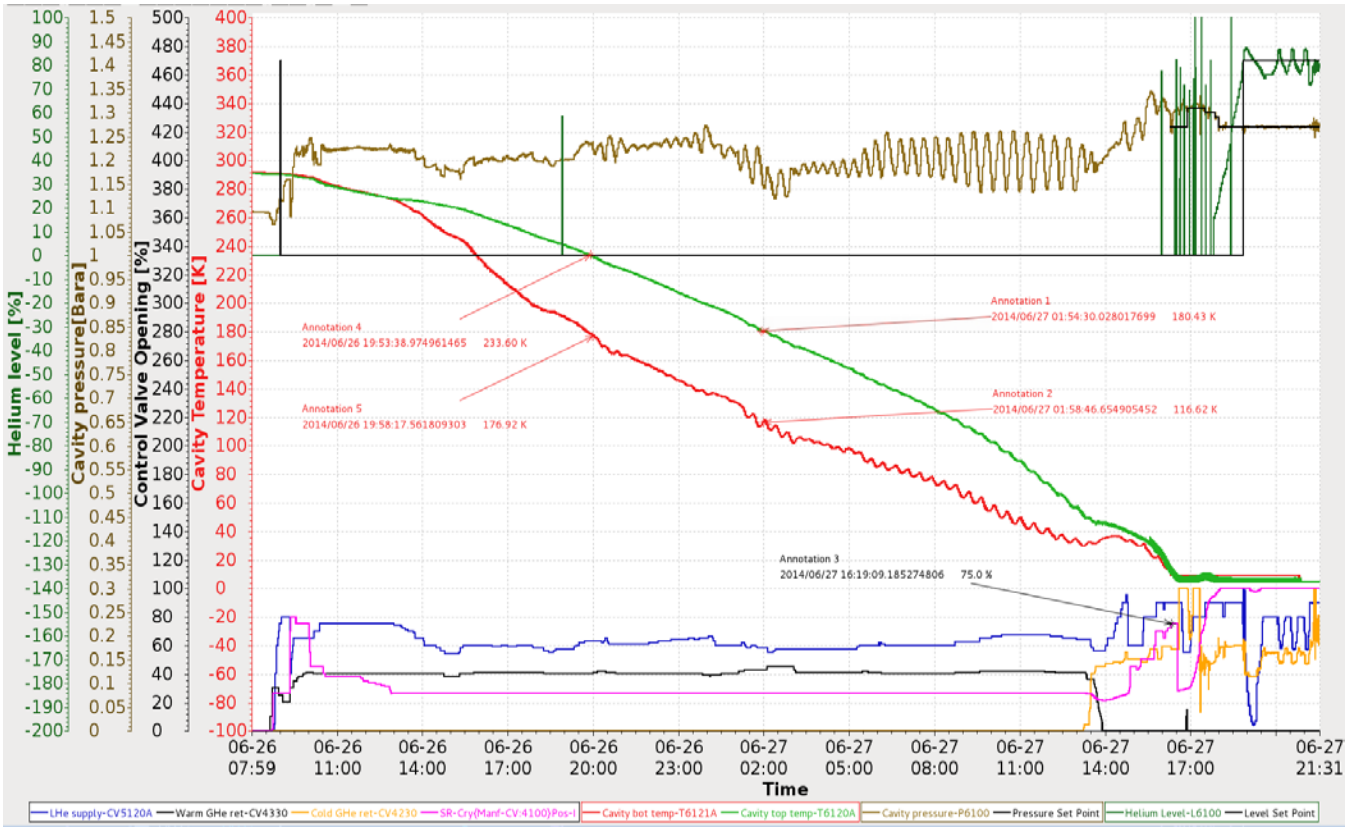

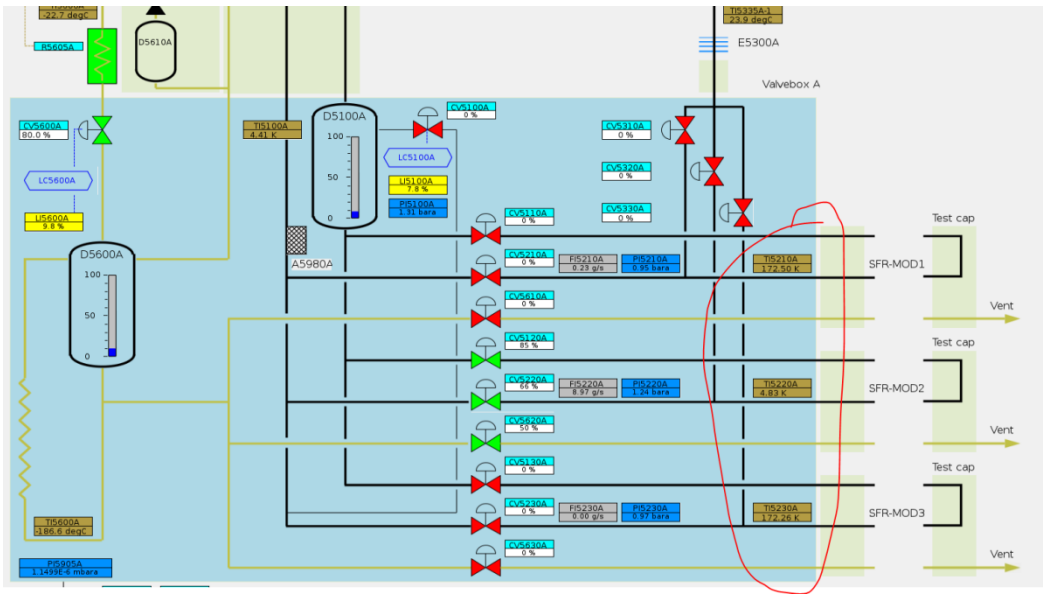

Figure 29. Cavity Helium Cool-Down

a. Cavity Helium Cool-Down

2. The cavity cool down with liquid helium was started at 8:00 on 06-25-2014. It took about 33 hrs to cool down the cavity including the ~150 feet long helium supply and return transfer lines from the manifold box to valve box. The cavity was cooled-down at a rate of 9 K/hr.

3. The liquid helium supply valve CV4100 (pink curve) was put in manual mode and set to 75-80% in the beginning of the cool down and also towards the end of the cool down and this helped in speeding up the cool down process. However cool-down was dictated by the temperature difference criteria of less than 70 K between the cavity top and bottom.

4. Lessons learned and suggestions for future cool-down

    a. Cool-down of the first cavity including the transfer line from the manifold box to the valve box (150 ft long)

        Try the following before starting the LHe Distribution from the Manifold box permissive page

        i. Start with 30-40% opening for the warm gas return valve

        ii. Set the liquid helium supply valve to 100%

        iii. Turn on the Liquid Helium distribution from the "Manifold Box Permissive" page

        iv. Treat the CV4100 (in the manifold box) as the main liquid helium supply valve. Put this valve in manual mode and adjust the opening % (perhaps 45 %) to get ~1.3 bara pressure in the cavity

            NOTE: For the opening % for CV4100, it is probably better to start slow otherwise the temperature difference will increase to the maximum allowable limit of 70 K in the beginning of the cool down process and then remain as a bottleneck throughout the process.

        v. Adjust the cool-down rate and maintain the temperature difference between the cavity top and bottom temperature by adjusting CV4100 opening %.

        vi. Do the switch between the warm gas return valve and the cold gas return valve as per the cavity cool-down procedure

        vii. Once the cavity top and bottom temperature have reached steady state temperature then put the cold gas return valve in pressure control auto loop (LP2)

        viii. Put CV4100 in auto mode

ix. Reduce the liquid helium supply valve to 80 % and monitor the helium level in the cavity.

b. Cool-down of second cavity

Note: During this step the transfer line from the manifold box to the valve box would have already cooled down and CV4100 would be fully open.

i. Start with 30-40% opening for the warm gas return valve

ii. Turn on the Liquid Helium distribution from the "Manifold Box Permissive" page

iii. Set the liquid helium supply valve to 20% and adjust the opening % (perhaps 45%) to get ~1.3 bara pressure in the cavity

iv. Adjust the cool-down rate and maintain the temperature difference between the cavity top and bottom temperature by adjusting the liquid helium supply control valve opening %.

v. Do the switch between the warm gas return valve and the cold gas return valve when the gas return temperature in the valve box (TI5210A/5220A/5230A) reaches 5 K

Note: If the switch over is done at a higher temperature then it will warm up the return line and CV4100 will start to close.

vi. Once the cavity top and bottom temperature has reached steady state temperature then put the cold gas return valve in pressure control auto loop (LP2)

Cavity RF operation in the tunnel

After the cryomodule cooldown and filled with LHe in the tunnel, RF conditioning and commissioning with beam were performed. The steps were largely the same as those for the blockhouse test, except for a few extra actions: readjusting the tuning range, adding the function

of heater compensation for the cavity power, and commissioning the cavity with up to 50mA of beam.

Tuning range adjustment

After the cooldown, the cavity frequency tuning range was found too high above the nominal NSLS-II master oscillator frequency. The plate spacing of the tuner was then adjusted several times in order to set the cavity frequency in the proper range. Figure 30 shows the estimated upper and lower frequency limits as a function of plate spacing, based on limited number of samples. The estimated tuning range is 110 kHz. Finally the spacing was set to 1.107 inch, as shown in Fig. 31.

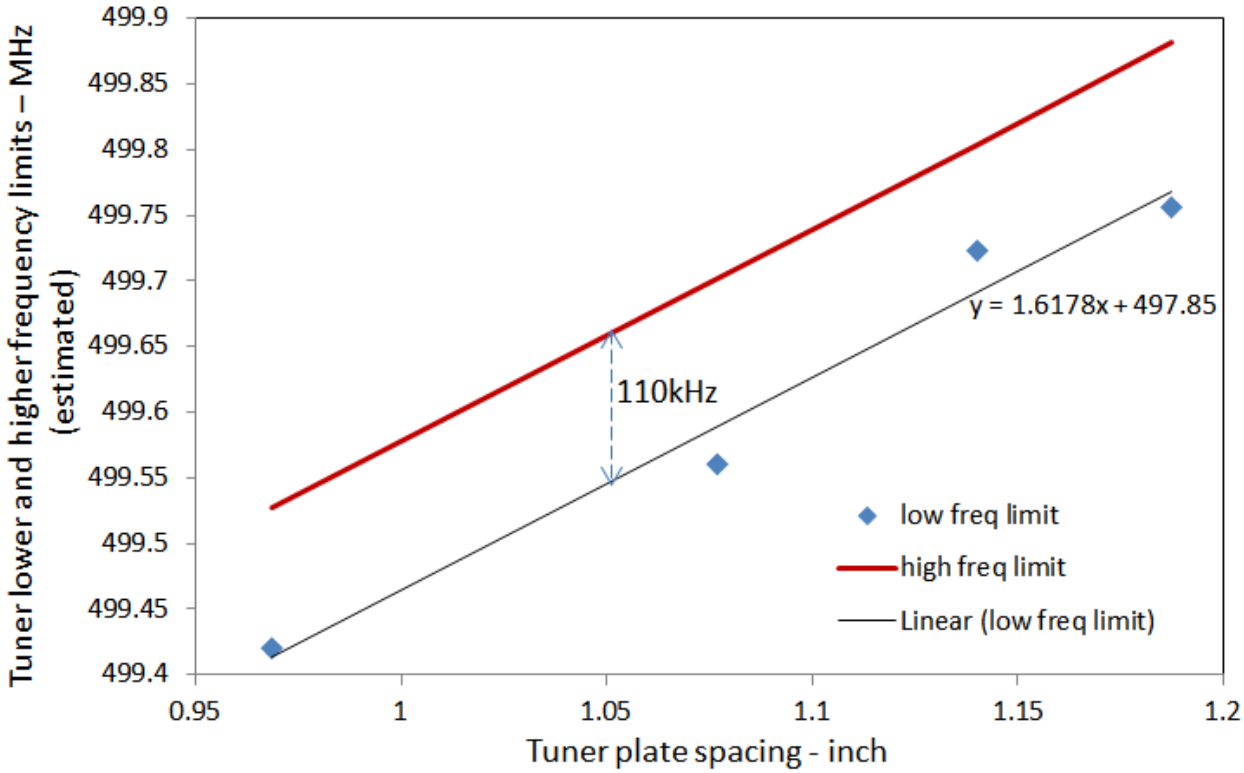

Figure 30. Estimated cavity frequency limits as functions of tuner plate spacing

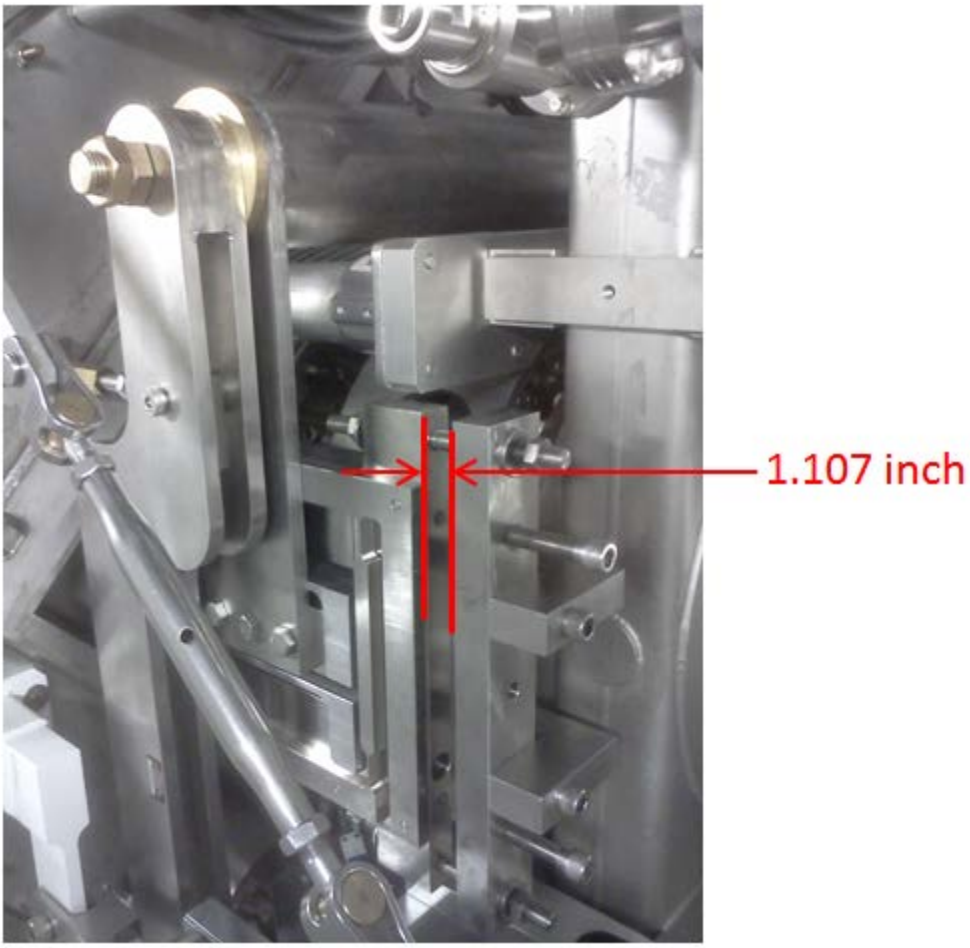

Figure 31. The tuner plate spacing was set to 1.107 inch.

LHe vessel compensation heater setup

It is good practice to keep the heat load constant to the cryogenic system to minimize Ghe pressure, LHe level and Ghe flow variation. The heat load of the cryomodule consists of two parts: static loss which does not change over time, and dynamic loss which is a combination of cavity power (wall loss) and the heater power inside the LHe vessel. When the cavity RF trips, the cavity power will drop to zero and the LHe vessel heater is needed to make up the total heat load. Figure 32 shows the configuration of this heater compensation scheme. The cavity voltage is detected with the cavity pickup and a detector circuit, then the cavity power is calculated by the PLC with the nominal Q0, finally the heater power to be applied is set as the total dynamic loss budget (100 W) minus the cavity power. Figure 33 shows the cavity power as a function of the detector voltage based on the nominal Q0 = 3.5e+8. Figure 34 shows when the cavity power changed between 46W and 11.5W, both the Ghe pressure and LHe level stayed stable.

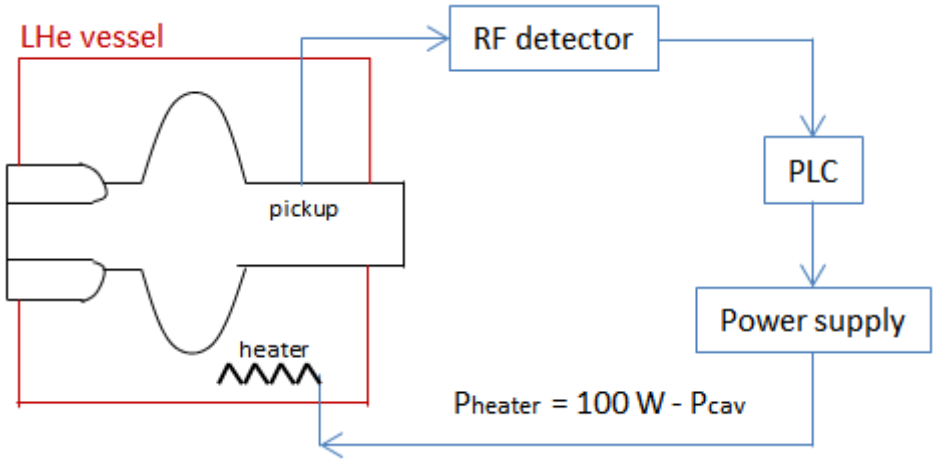

Figure 32. The LHe vessel compensation heater

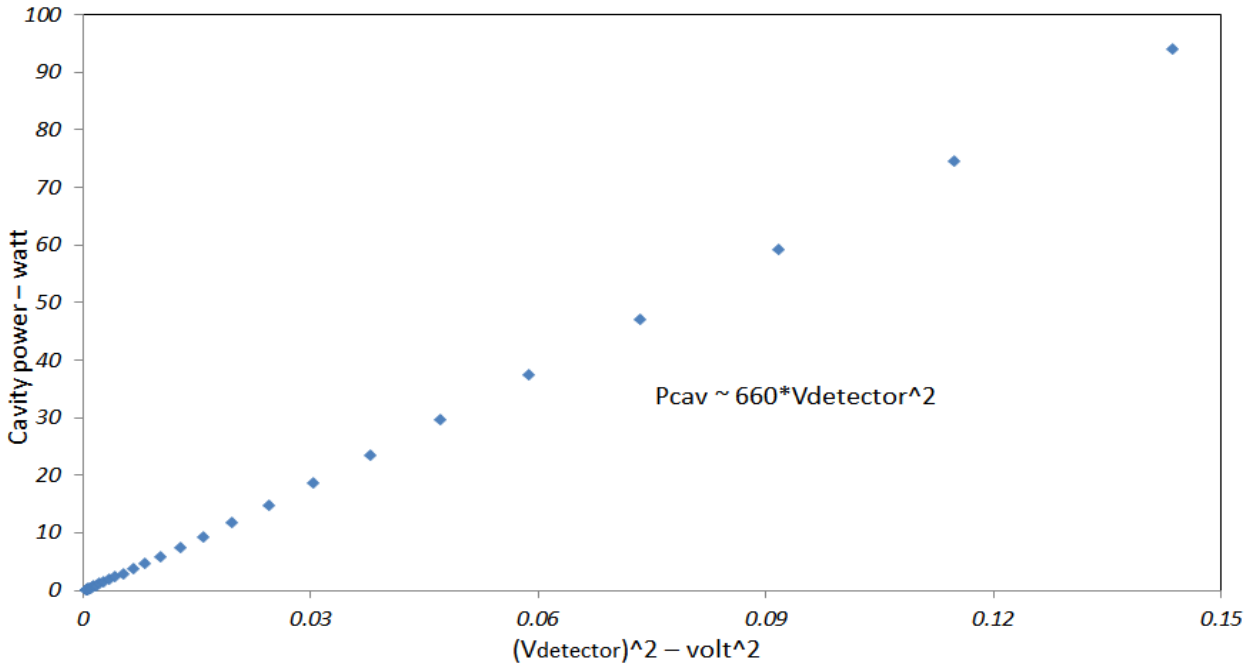

Figure 33. The cavity power as a function of the square of the detector voltage

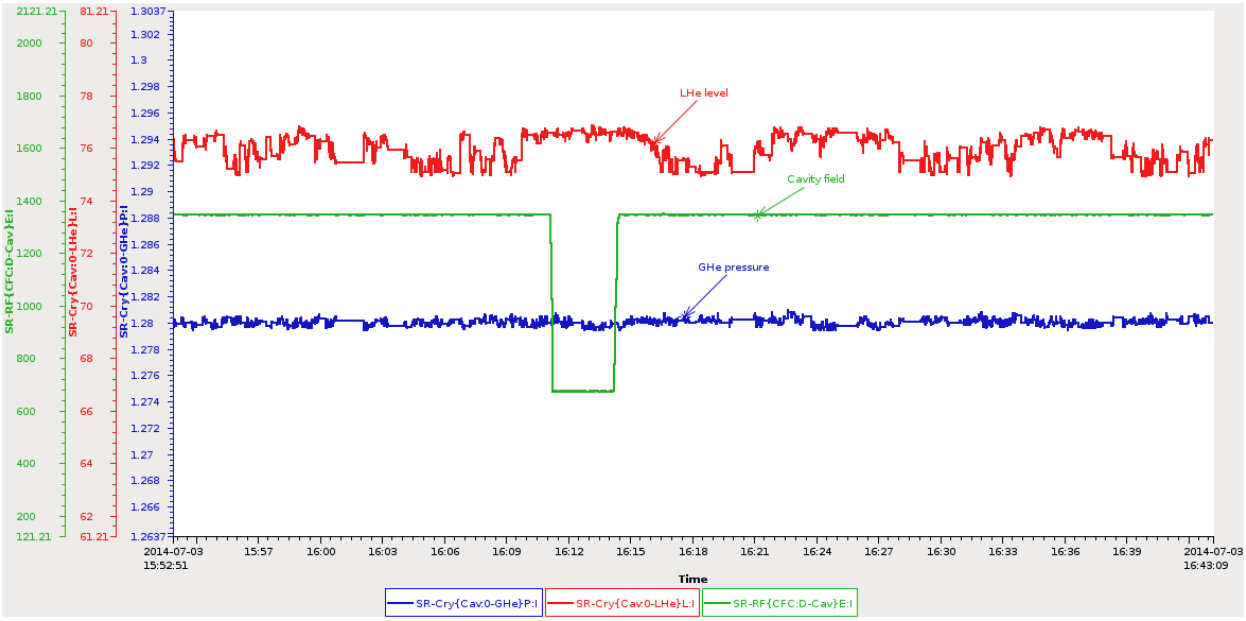

Figure 34. The Ghe pressure and LHe level stay stable when Pcav changes between 46W and 11.5W.

Cavity conditioning in the tunnel

The cavity voltage was initially set to 1.2MV for beam operation during the daylight and evening shifts, and was set to conditioning mode by the control room throughout the night shift. Before the compensation heater was implemented, turning on and off the RF power caused large variation of Ghe pressure and LHe level, especially when the cavity voltage was set high. Figure 35 shows the highest cavity field it has ever been set to, approximately 1.9MV. As shown by the traces, the Ghe pressure and LHe level varied so much that even the quench detector, a device that monitor the cavity pressure, annunciated quench alarms several times. The waveguide vacuum level was moderate in this case, with some variation. After the parameter history was reviewed, more conservative conditioning actions were taken since this is the only cavity available for beam studies, which had higher priority at that time.

Figure 36 shows another scenario. One time the cavity field was raised to 1.45MV, slightly higher than the highest level reached during the blockhouse test, 1.4MV. For the first 20 minutes the systems ran well, however at about 20 minutes the transmitter forward power showed a dip, which is not visible on the cavity field trace (possibly limited by sampling rate). At about the same time the Ghe pressure and LHe level start to oscillate. The cause has not been identified yet.

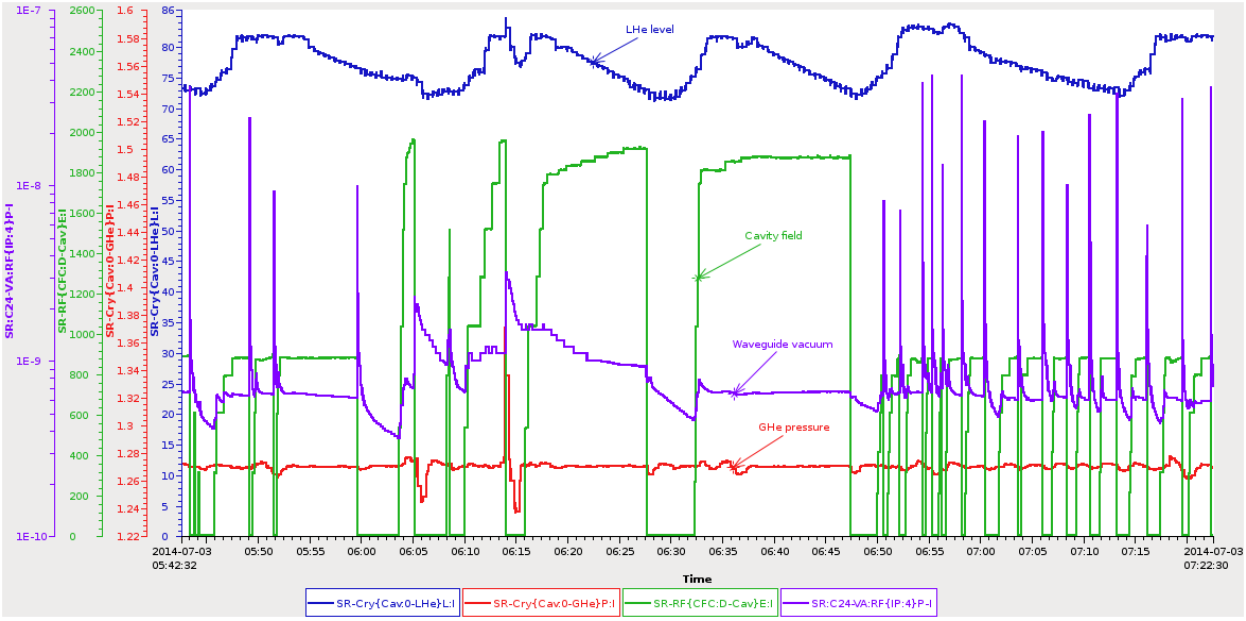

Figure 35. Attempts to raise cavity voltage leads to numerous trips together with large variation of Ghe pressure and LHe level (compensation heater had not been implemented at that time).

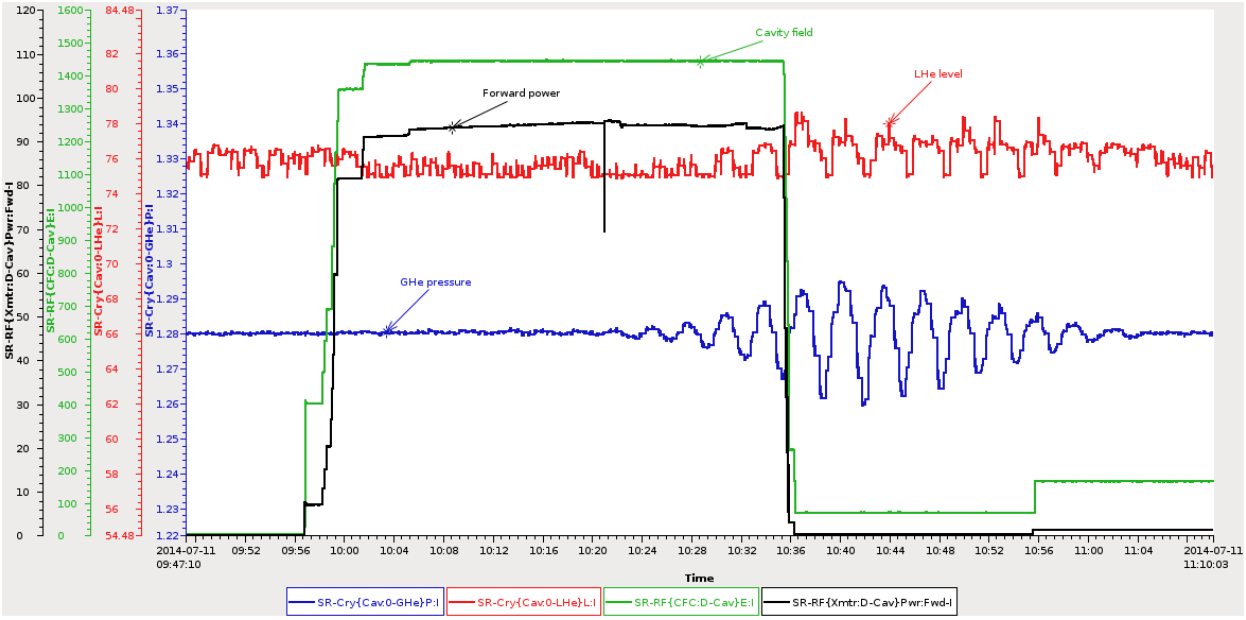

Figure 36. A forward power dip followed by oscillation of Ghe pressure and LHe level (the compensation heater was on). The RF was manual turn off to mitigate the problem.

Quench detection

The cavity is equipped with two pressure based quench detector circuits which would trip the RF transmitter should the GHe pressure reached the threshold, 5.17 psig (0.36 bara). The Quench detector utilizes a pressure transducer with a 1 ms time response. The pressure rise of the helium vessel during a quench is of the order of a few ms to reach the trip pressure of 0.36

bara. The pressure transducer is fed into a comparator circuit with a response time of a few microseconds, and the transmitter shuts down in ~10 microseconds so the overall response time is determined by the propagation of the quench and subsequent pressure rise. Figure 37 shows a possible quenching event. In Fig 37, when the RF power was turned on, the cavity field lags the forward power by approximately 2 seconds, which was due to the granularity in the PLC scanning by EPICS. Based on the granularity of the system sampling the uncertainty of the data with respect to an absolute clock was later estimated to be approximately 3 seconds. Once the rising edge of the cavity field is shifted to overlap with the rising edge of the forward power, with delay corrected, it can be seen on the falling edge the cavity field collapsed first, then the forward power went up trying to maintain the field but it was unsuccessful. Then the Ghe pressure and LHe level went up and the transmitter was tripped. The cold gas return flow also shows a spike therefore the pressure relief valve might not be opened at that time.

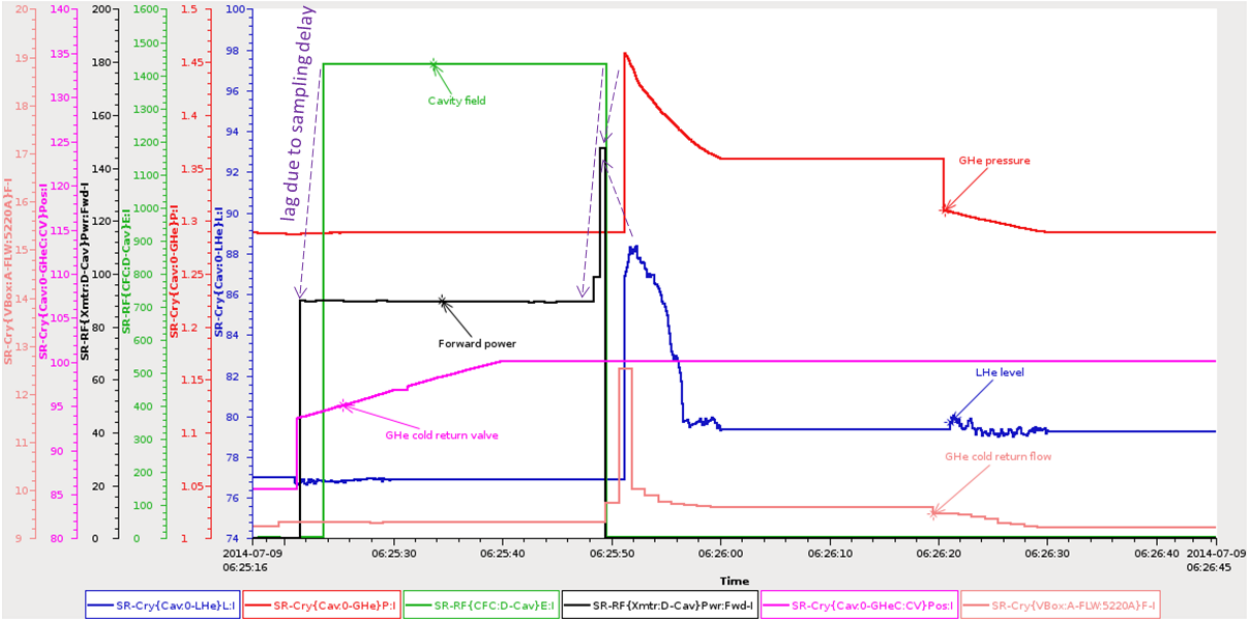

Figure 36. Quench detector tripped RF transmitter

Beam oscillation sensitive to CFC PI loop parameters

It was also observed one time the beam was not stable (large oscillation) at PI parameter settings Ki = 0.05, Kp = 0.05; and the oscillation disappeared when Kp was lowered to 0.03. This might be related to impedance reduction by higher CFC gain, and it needs further investigation.

Beam current reached 50mA with this cavity

In the afternoon of July 11th, 2014, the beam current was gradually increased to 50mA. Figure 38 shows the cavity field, forward power and reverse power when the beam current was approaching 50mA. The cavity detuning was checked to ensure the forward power was minimized for 50mA. No problem was experienced during the fill and the cavity successfully met its goal for beam operation at 50mA.

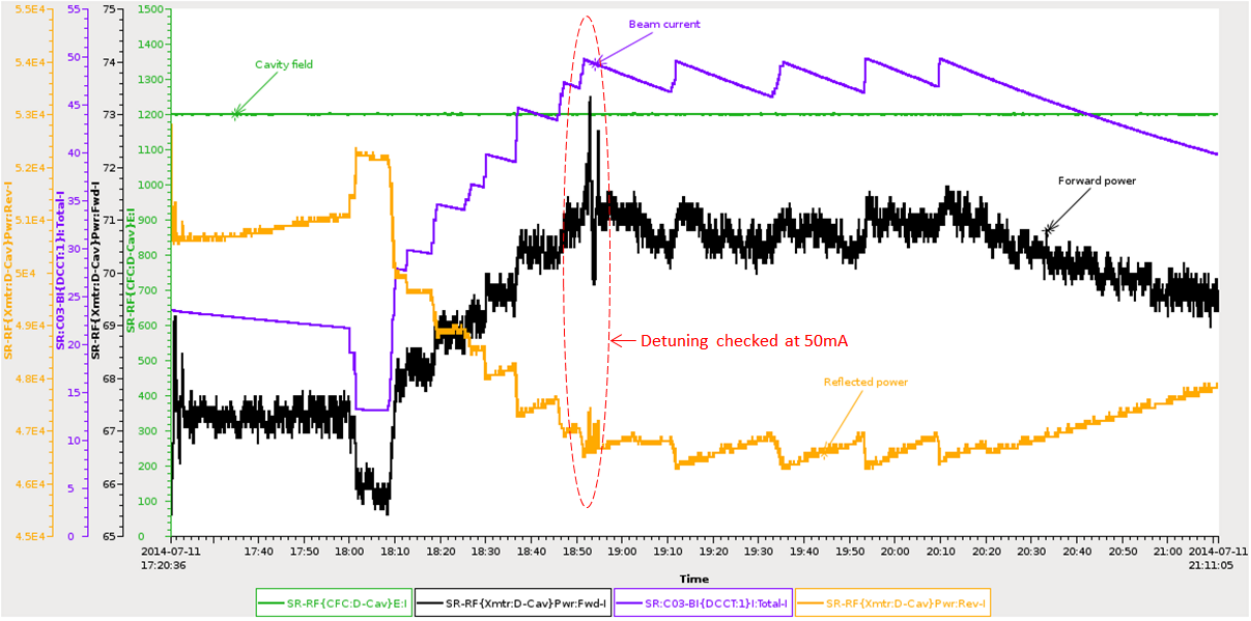

Figure 38. Cavity field, forward power and reverse power when beam current approaching 50mA. There is some calibration difference between the transmitter readbacks and a power meter. The power readings shown from the transmitter are relative not absolute, while the readings from a power meter are regarded accurate.

5.1.3 Further studies

Proposed RF studies for the next operation period

Cavity Q0 re-measurement

The Q0 of the cavity was measured in the blockhouse at 1.4 MV voltage, as described in Section 1.1.6.3 and Section 1.2.6. It needs to be re-measured after various conditioning activities were performed during commissioning, and it probably needs to be measured after every significant event which could possibly change the Q0.

Time estimate: 3 hours for one Q0 - Vcav data point. Maybe 12hours for a curve.

Three-stub tuner studies

A three-stub tuner will be installed between Transmitter D circulator and the cavity. Studies need to be performed to understand stub setpoints for different beamloading scenarios.

Time estimate: 8 hours.

CFC feedforward table phase modulation

Similar to what was done with the 7-cell cavity, the effects of CFC feedforward phase modulation on beam orbits and spectra need to be studied.

Time estimate: 3 hours.

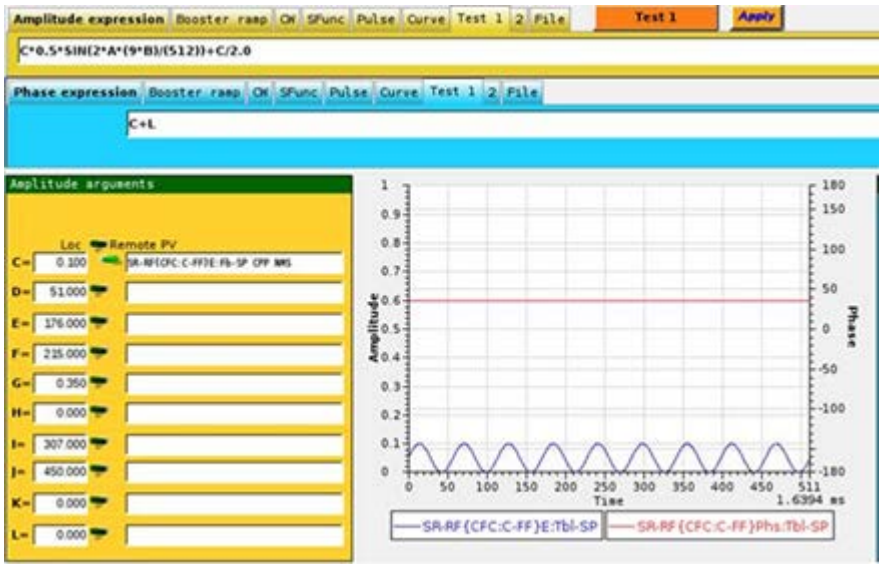

Figure 39. CFC feedforward phase modulation

CFC circular buffer

The CFC has a circular buffer function with which the RF signals near the trip point were recorded for postmortem investigation.

Time estimate: 4 hours.

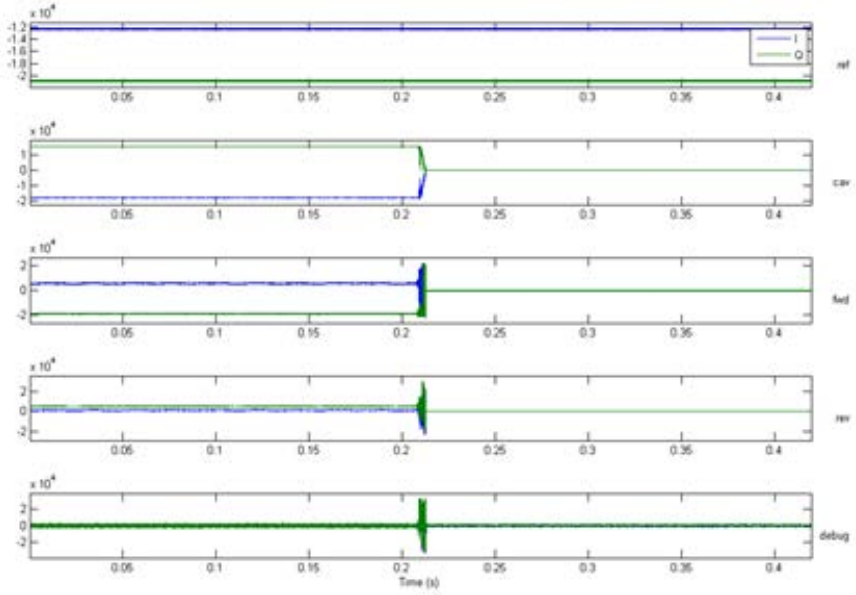

Figure 40. CFC circular buffer.

Transmitter HVPS switching lines

The Klystron Supply Unit (KSU) High Voltage Power Supply (HVPS) is a switching supply with a switching frequency of approximately 112 kHz. There are 86 switching modules and the RF forward power of the klystron has very low sidebands of the switching sub-harmonic of F_switching/86. For the current configuration the subharmonics are multiples of 1.3 kHz: 1.3,2.6,3.9……..

The subharmonics are over -80 dBc (eight orders of magnitude below the carrier) but never the less the 1.3kHz and 2.6 kHz are seen on the BPM responses. The design of the switching supply allows for the change of the switching frequency to change these subharmonics. Beam studies are required to determine the best setup.

Time Estimate: 4 hours

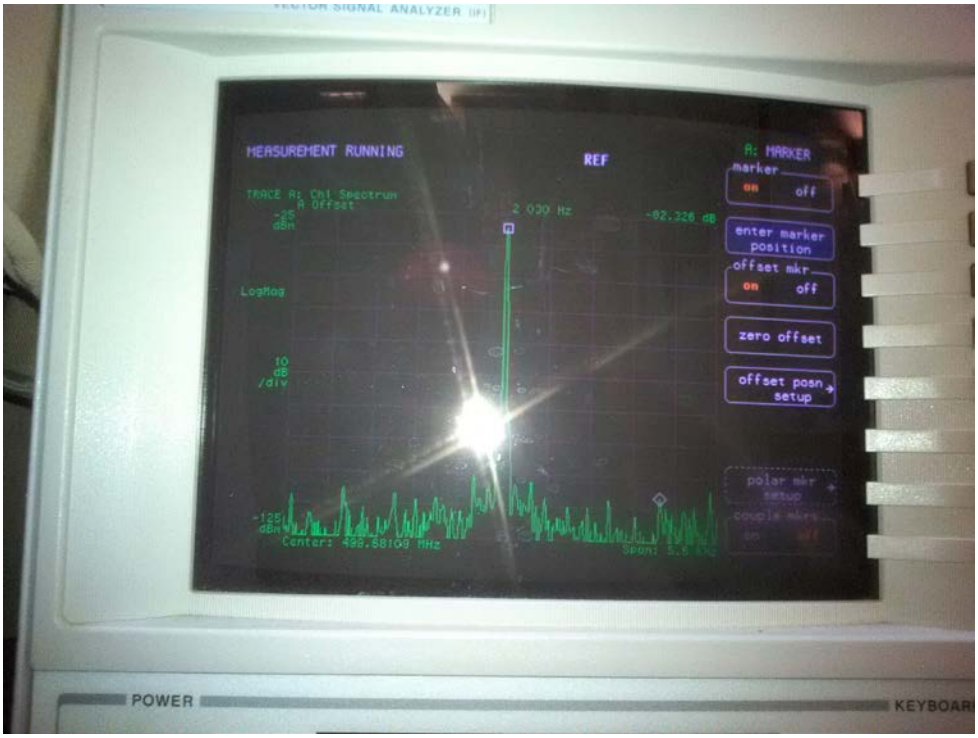

Figure 41. Cavity field showing ~2.03 kHz synchrotron sidebands and the 1.3kHz and 2.3 kHz switching lines.

Transmitter HVPS AC power lines

Similar to the switching power supply lines the HVPS has AC power line harmonics of 60, 120, 240, 360…..720Hz. The switching algorithm for the modules has weights that can be set to minimize these harmonics. There is some indication that as the 3-phase AC power balance changes this algorithm may need to be adjusted. This too needs to be studied.

Time estimate: 4 hours.

5.2 Storage Ring Loss Control and Monitoring System Commissioning

Two partial shifts of commissioning were run on July 2, and 10, and a quick test on 12th, 2014. This allowed commissioning with injection beam and some initial testing of the stored beam operation of the LCM but no calibration.

5.2.1 Testing and calibration of the Neutron Beam Loss Monitors (NBLM) for the injection septum

The two NBLM were mounted above the injection septum and tested to see if they saw the neutron signals (long decay time of their signal due to slower neutron particle propagation from septum to detector) from beam hitting the septum, when the septum is turned off. Both PMT's had 1200V applied and their signals appeared quite similar in amplitude. NBLM1 signal has less gamma ray signal and longer decay time resulting from longer and more backward angles subtended to the loss point than the NBLM2 signal. The GUI interface to these detectors was tested which included: instrument noise subtraction, and integration of signal in region of interest (ROI). However the calibration was performed by eyeball averaging of signal integration and dividing by average of ICT2 data. Calibration data stored: NBLM1 =2.22e-4 and NBLM2= 2.436e-4 nC/sum[Vi(I in ROI)]. A PV for the Qnblm =Aver(Qnblm1, Qnblm2) wasn't available but as the septum was ramped to full field this average charge loss went to a smaller value for both NBLM1 and 2, consistent with ~15-18% beam loss in the septum region, in agreement with the injection charge inefficiency. On July 12th this value measurement of septum charge loss after ramping to full field went to a small value of < 1% (dominated by septum noise pickup), as shown in Figure 2.

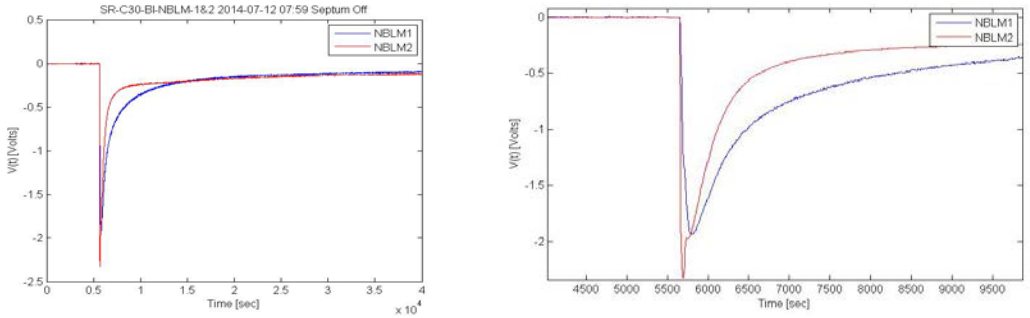

Figure 1: Beam loss signals from NBLM1(upstream) and 2(downstream) detectors for injection beam hitting the septum(off). Right signal is magnified region after beam hits septum.

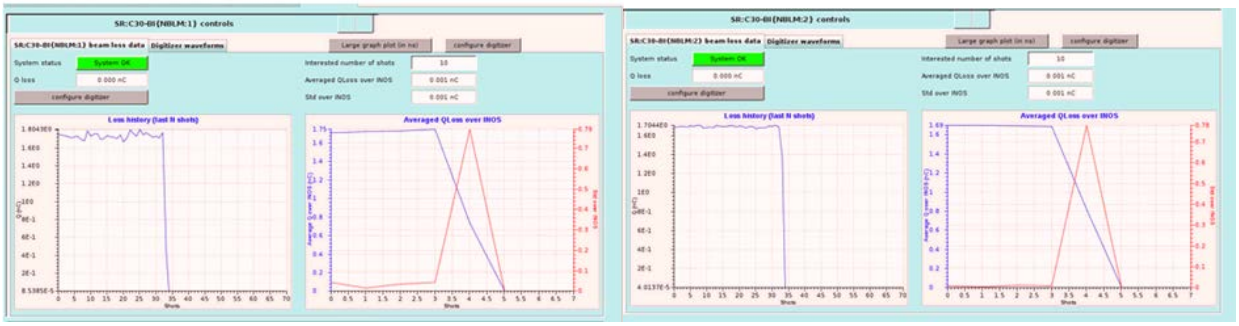

Figure 2: The integrated signal for NBLM1 and 2, as the septum was ramped from off to full field, on July 12, 2014, indicating beam loss in septum < 1% of the ICT2 charge.

5.2.2 Testing and calibration of the Cherenkov Beam Loss Monitors (CBLM) for the injection loss

The Cherenkov Beam Loss Monitors (CBLM) are designed to measure the amount of beam loss intercepted by the SR scrapers using the output low energy electron spectrum generated in the scraper and bent by the dipole into the Cherenkov radiator rods installed in theses dipoles. The CBLM will measure both stored beam and injection beam losses. Since time was limited the injection losses was the only mode that was calibrated. However if the system proves to be linear over the large dynamic range, from high intensity pulsed beam losses to the lower rate stored beam losses, these calibrations will be very similar in values.

For stored beam losses the voltage output of the CBLM detectors will be directly proportional to the dQ/dt beam loss on the upstream scraper. Calibrating this to the DCCT loss signal will be challenging, since the NSLS-II lifetime measurement shows large level of instrumentation noise. The present calibration for injection beam loss, assumes all of the BS-ICT2 charge, Qict2, is intercepted by the scraper and the integrated CBLM signal is then proportional to this charge loss. A PV will be added that subtracts the charge lost in the injection septum, Qnblm from the ICT2 charge signal to yield a better calibration value for the intercepted charge, but this wasn't used here. Figure 3 shows the CBLM signals for the injected beam (~1.05nC/pulse) hitting the Hscraper1. All CBLMs are plotted but only the subsequent monitors CBLM2 and CBLM3 show any significant signal. The CBLM1 shows some small signal possibly from booster beam halo, while CBLM4 and 5 show almost zero signal coming from the higher momentum component off the scraper that could be transported to that region. The two ranges of the CBLM2 and 3 amplifier gain settings were calibrated by integrating the V(t) signals over the pulse duration and dividing by the BS-ICT2 charge (Qict2). This was done by measuring one V(t) trace and dividing by the average charge Qict2. The GUI will be improved to allow the IOC to average a number of measurements of the integral V(T) divided by the (Qict2 – Qnblm). This calibration should better agree with the stored beam loss calibration. The resulting calibration values for injected beam loss are listed in the table below.

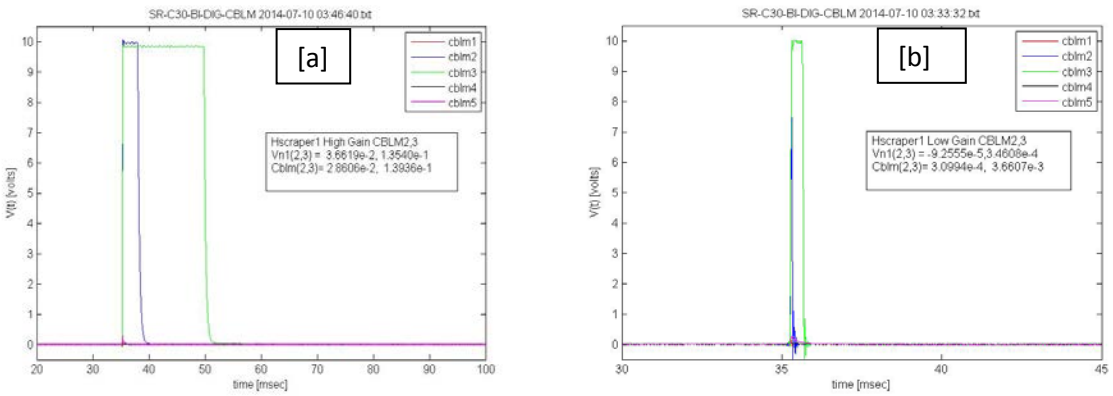

Figure 3: The CBLM2 and 3 signals for ~1.05 nC of charge hitting the Hscraper1 for [a] high gain/low bandwidth and [b] low gain/high bandwidth amplifier settings.

After calibrating the new GUI feature of plotting integral V(t) versus Qict2 was tested to look at the linearity of the signal. Figure 4 show this data for Hscraper1 and CBLM 2 and 3. Both CBLM2 and 3 were calibrated and show linearity, except that the one zero ICT2 value set the scale making it hard to see for CBLM3. However the CBLM2 shows several zero values for the integrated signal that had ICT2 charge. This may result from a greater sensitivity of the signal

from CBLM2 due to booster beam steering that may affect the electron steering in the quadurupole and sextupole fields that steer beam ahead of the CBLM2 detector.

Table1: The CBLM calibration values determined for Injected Beam loss on the scrapers

Scraper	Gain	CBLM	Vn1[V]	IntV/Q[V-s/nC]	SRQloss[nC]	Filename
HScraper2	high	5	5.39E-2	1.56E-1	1.90E-3	_03%15%27.txt
Qict2=1.0	high	4	4.82E-2	3.99E-2	2.84E-3	
Qict2 =1.28	low	5	-3.04E-4	2.43E-3	1.32E-2	_02%54%02.txt
Qict2 =1.28	low	4	-1.42E-4	3.27E-4	-2.46E-1	
HScraper1	high	3	1.35E-1	1.39E-1	6.75E-3	_03%46%40.txt
Qict2=1.05	high	2	3.66E-2	2.86E-2	6.13E-3	
Qict2=1.05	low	3	3.46E-4	3.66E-3	-2.58E-3	_03%33%32.txt
Qict2=1.05	low	2	-9.26E-5	3.10E-4	6.87E-2	
HScraperX	low	1	-1.70E-4	2.17E-3	-1.59E-3	_04%05%04.txt
Qict2=1.05	high	1	1.04E-1	1.39E-1	3.29E-4	_04%10%31.txt

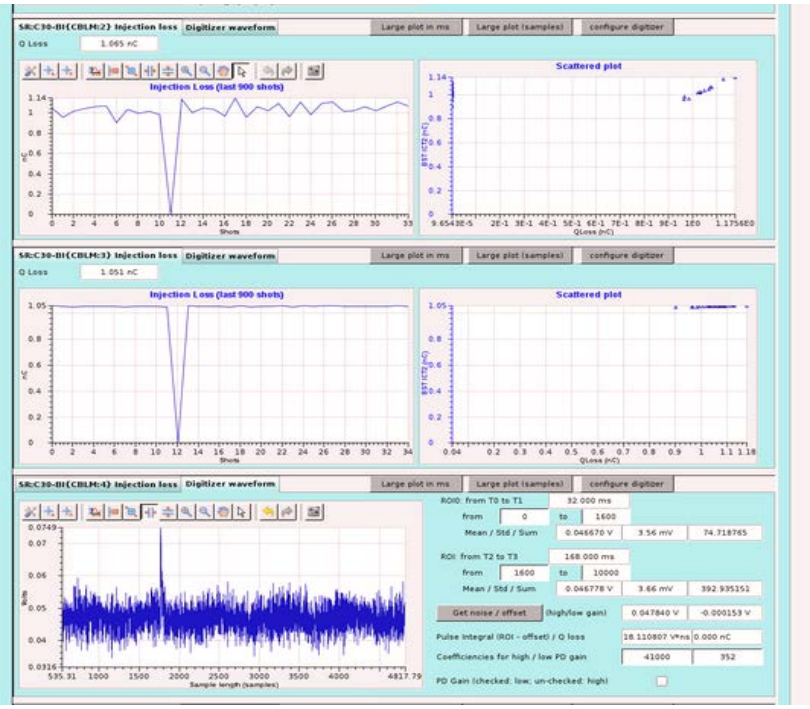

Figure 4: The CBLM2 and 3 integrated charge loss value linearity versus the Qict2 value for injection beam hitting Hscraper1.

5.2.3 Testing the CBLM for stored beam losses

The GUI interface for calibrating with stored beam wasn't available but testing of the control of stored beam losses with the scrapers was run using the functional LCM interface GUI. Figure 5 shows the Hscraper2 inner blade inserted into about -5mm and the resulting increase of the CBLM5 signal is shown. However over most of this range the Q' seen by the V(t) for CBLM5 is due to collecting the lifetime beam losses that occur around the SR at the Hscraper2 determined aperture. As it is inserted more of the distributed beam loss occurs at the scraper and CBLM5. The GUI interface will have to correlate this Q' loss with the <V(t)> level once the scraper starts to reduce the lifetime loss of the ring. This insures that the scraper is dominating the aperture limit of the ring and all additional beam loss rate occurs from the scraper aperture reduction.

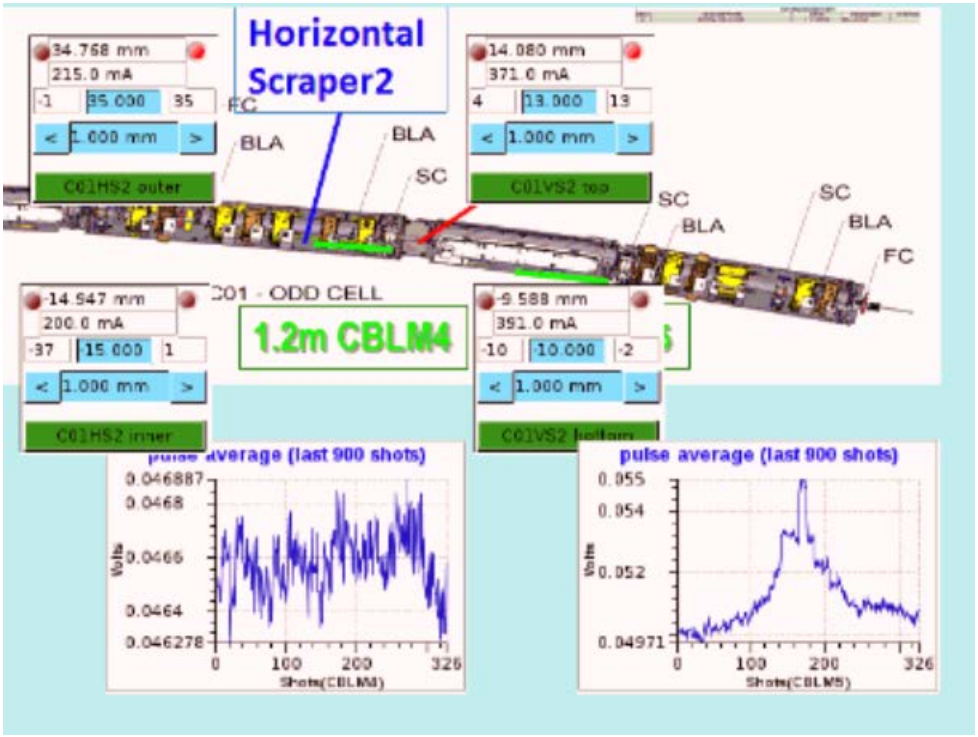

Figure 5: The local stored beam loss rate controlled by scraper Hscraper2 and this loss seen by CBLM5, lower right curve

5.3 Pinger

There are two Pinger magnets in the Storage Ring cell 22, one for horizontal Pinger and the other for vertical pinger. It is to provide very fast dipole magnets to intentionally perturb the beam orbit in a single pass. The effects of this controlled transverse "kick" will be monitored by BPM system for validation and improvement of beam optics and dynamic aperture. In phase II commissioning, only vertical pinger was ready for commissioning.

The Pinger pulsed power systems consists of the following: A Spellman HV Power Supply and ACICM Box D, VME Crate (for timing), Pulser Box (located at the magnet), the Spellman Power Supply Controls Interface Chassis, and Power Supply Interface (PSI).

The Pinger parameters are listed in Table 1. The magnetic length is 0.3 m. The pulse length is ~ 1.6 us half sine waveform, less than SR revolution.

Table 1 Vertical Pinger parameters

Vertical Pinger		
Parameter	Value	Unit
Deflection Angle	2.5	mR
Pulse length	2 ½	½ sine
Magnet length	300	mm
Required Field	830	Gauss
Magnetic Inductance	0.156	uH
Drive Capacitor	2.6	uF
Current	7	kA

The Pinger operation interface is shown in Figure 1. User can adjust the delay and voltage. During commissioning, its timing trigger is synchronized with the injection kicker and SR BPMs for convenience, so that user can have the freedom to combine horizontal (borrow from IS kickers) and vertical perturbation. The timing delay was calibrated by monitoring BPM TBT data amplitude from the betatron oscillation. Only short bunch train was stored in SR for the delay optimization. The pinger voltage is limited as 3 kV, which is big enough for vertical dynamic aperture study.

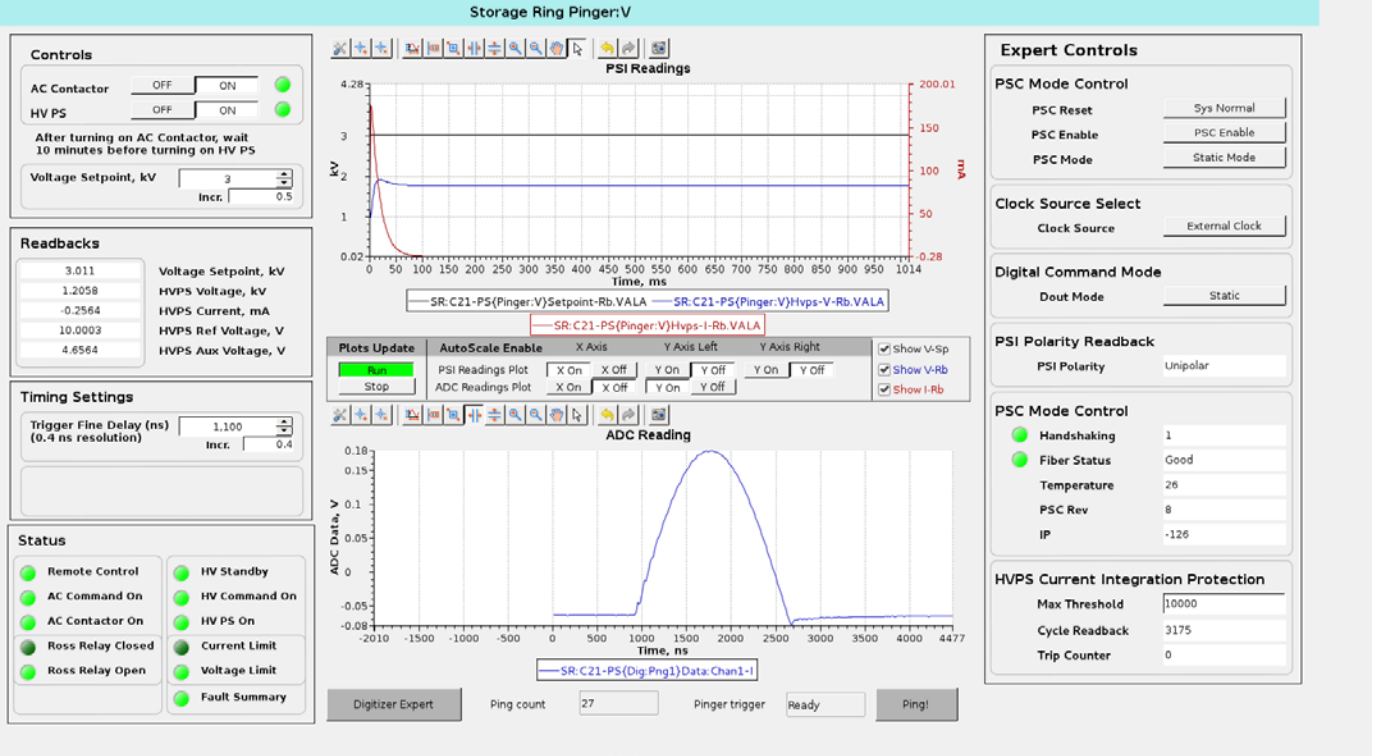

Figure1: Pinger operation page

With the pinger, the vertical beta beat was well characterized. Figure 2 shows one BPM vertical plane TBT data and its spectrum. The tune is 0.219.

With 180 BPMs TBT data, the beta beat can be fitted. Figure 3 shows the vertical plane beta beat. The RMS beta beat is 4.7%.

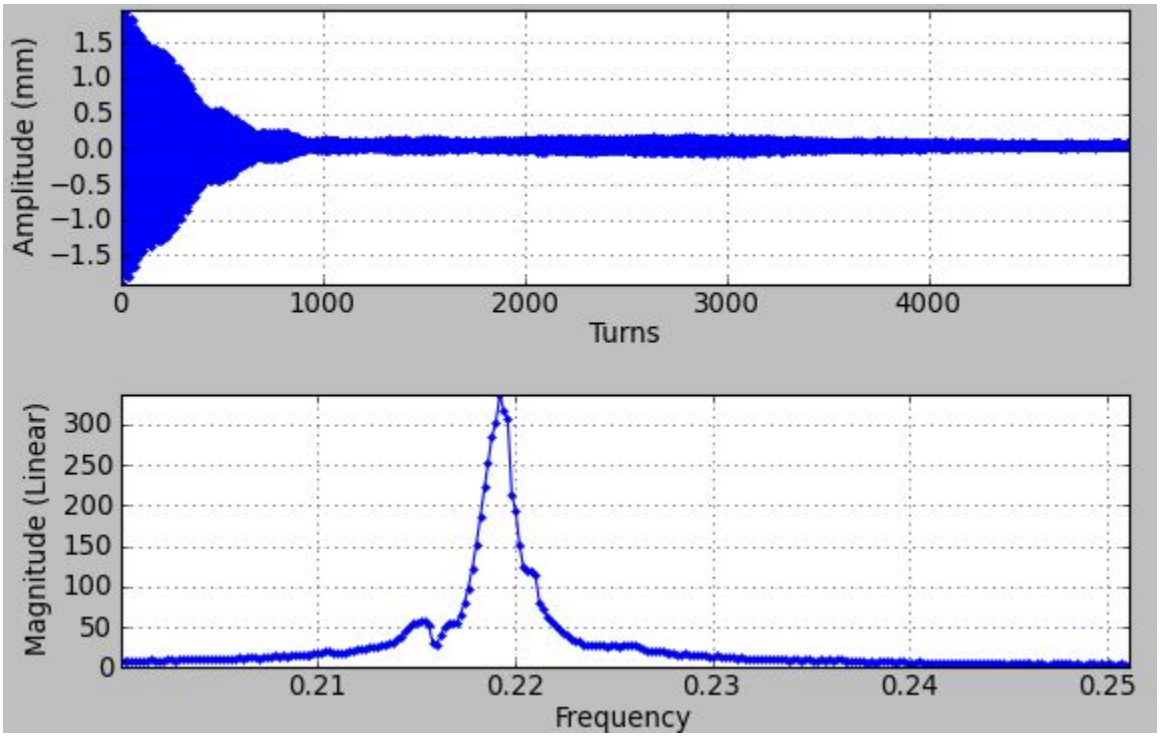

Figure 2: one BPM TBT data and spectrum in vertical plane

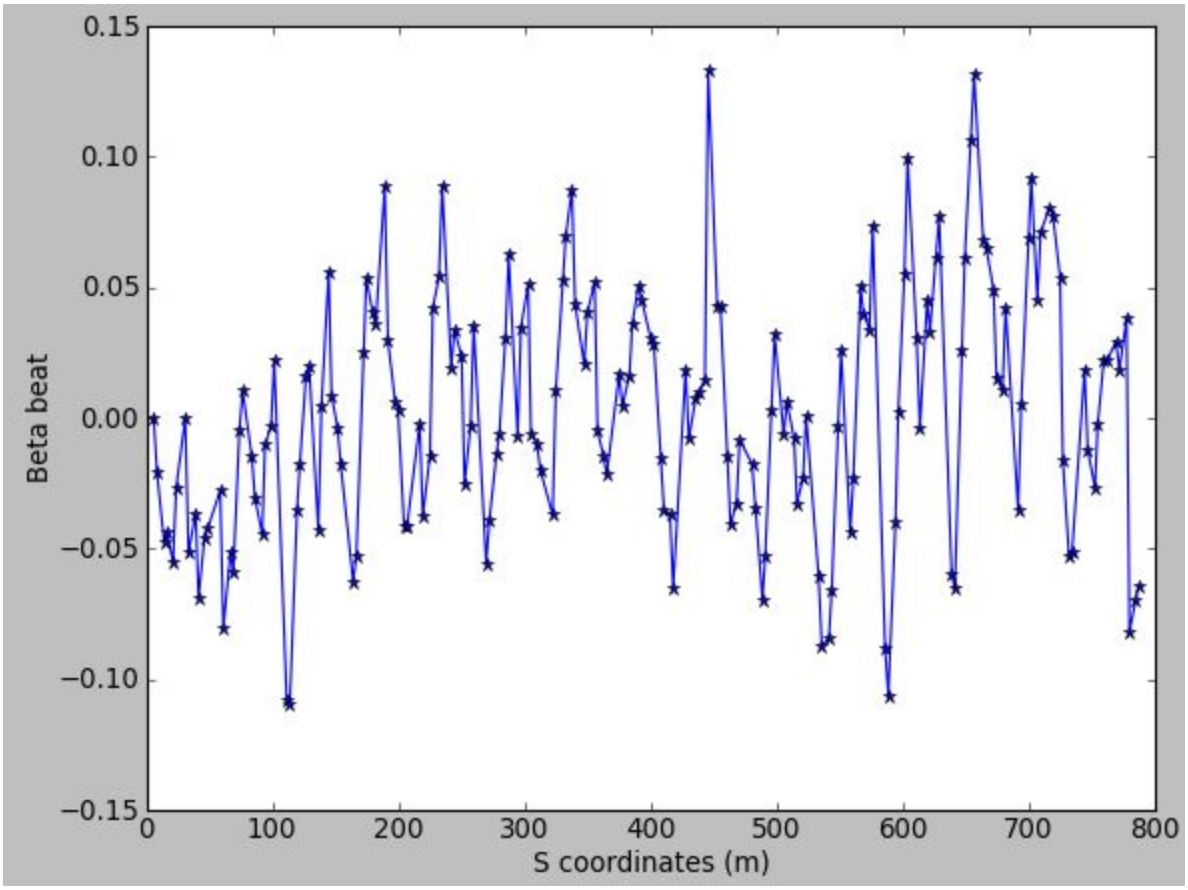

Figure 3: Beta beat in vertical plane

The beam oscillation amplitude with the pinger voltage was retrieved from 180 BPMs turn by turn data, as shown in figure 4. The response matrix is from ideal model. It shows linear relation, except at very low voltage due to big noise signal ratio. The beam centroid at the injection straight was plotted is figure 5 with multi-TBT data. Different color is for different pinger voltage. The vertical dynamic aperture was studied by scanning pinger up to the pinger voltage limit, as shown in Figure 6 for on momentum beam.

More study will continue with the new pinger pulser, which is designed to kick beam up to 2.5 mrad.

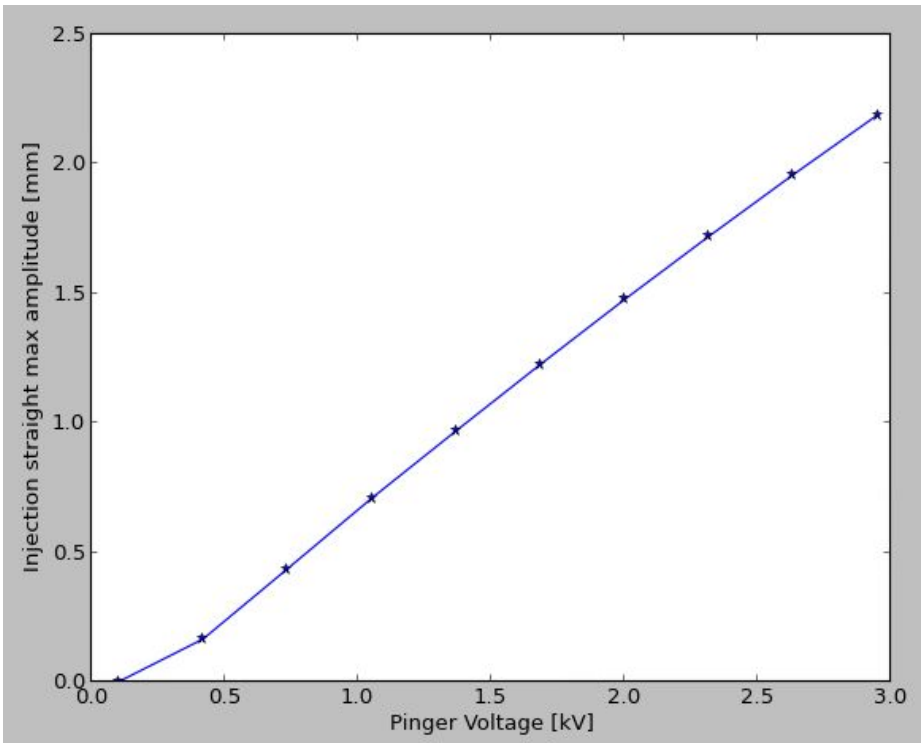

Figure 4: Oscillation amplitude VS pinger voltage

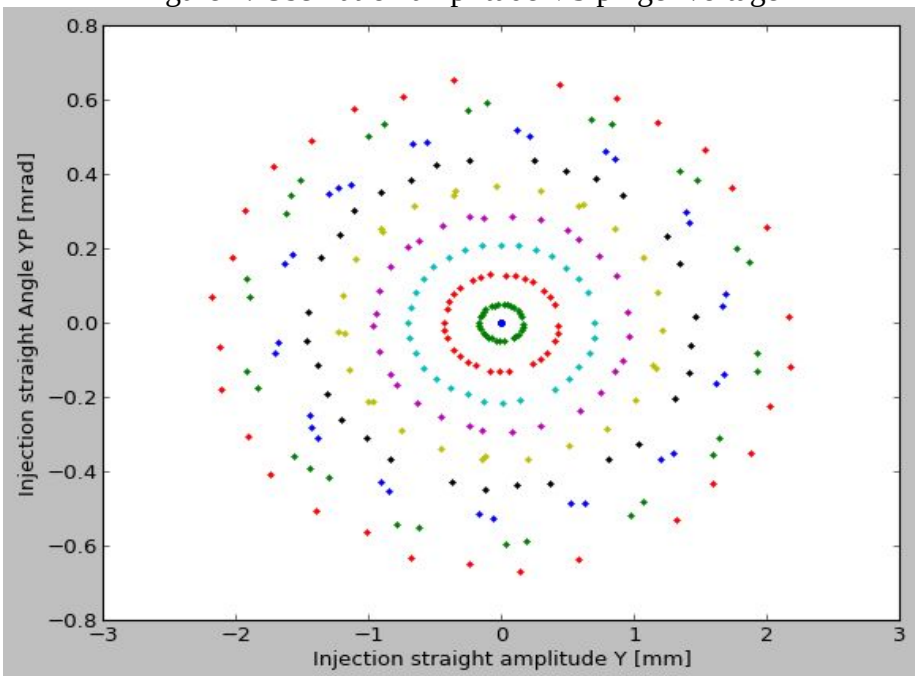

Figure 5: The beam centroid at injection straight (Different color is for different pinger voltage)

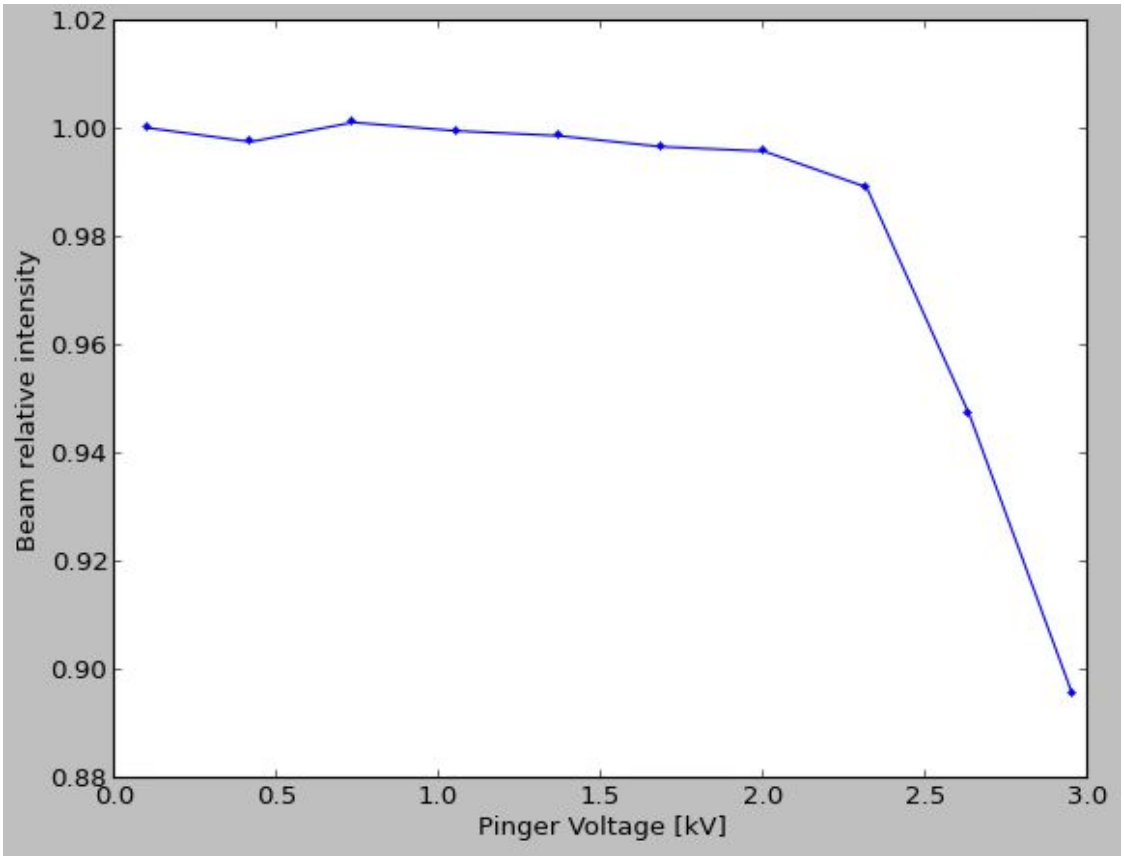

Figure 6: Vertical beam dynamic aperture study

6. Outlook of remaining studies

On May 11 the first phase of the NSLS-II Storage Ring Commissioning was completed. The machine entered shutdown for installation of front-ends, insertion devices and superconducting RF cavity. At the end of June, machine was restarted and took two weeks to reach 50 mA with superconducting RF cavity, reaching the Project Key Performance Parameters. The plan is to restart beam studies in Oct. with the goal to commissioning 6 project beamlines and fast orbit feedback improve the beam stability.